NUMERICAL PREDICTION OF FLOW IN CURVED DUCTS AND VOLUTE CASINGS

by

Reazul Gafur Mahmud Hasan

BSc (Engg.), MSc (Engg.)

Thesis submitted for the degree of Doctor of Philosophy of
the University of London and for the
Diploma of Imperial College

Department of Mechanical Engineering,
Imperial College of Science, Technology and Medicine, London.
May, 1990.

ABSTRACT

The present study is a numerical investigation of steady, incompressible, isothermal flow through different types of curved ducts including nozzle-less, single-entry volute casings such as found in small radial inflow turbines. The main objective was to produce a prediction method for the study of the effects of geometrical characteristics of curved ducts on flow parameters. This then provided a technique for the design and analysis of the flow in volute casings based on a more fundamental approach than previously available.

A computer code was developed using finite volume method to solve the three-dimensional, elliptic governing partial differential equations . The equations were first transformed from cylindrical-polar to a general non-orthogonal curvilinear coordinate system. Discretisation was then carried out in the computational domain using a staggered arrangement of flow variables. The SIMPLE algorithm was adapted for the present boundary conforming coordinate to handle pressure-velocity coupling. In order to close the time-averaged equations of motion for turbulent flow, a two equation ($k - \varepsilon$) model was employed. The developed code, capable of calculating flow in ducts of arbitrary curvature and arbitrary cross-section, was tested for several flow situations (both laminar and turbulent) in which either 'exact' or experimental results with bench-mark accuracy were available. In all cases, emphasis was placed on the accuracy of prediction of the viscous secondary flows in the duct cross-section induced by curvature.

Three duct types were considered: viz., i) constant curvature and constant cross-section, ii) constant curvature and variable cross-sectional area and iii) variable curvature and variable cross-section. The laminar flow development through the first type of duct with and without tangents was studied in detail. The streamwise velocity shows a distinct two-step plateau like profile for higher Reynolds number, and the isovelocity contours exhibit double peaks with a consequent distortion of the secondary velocity vortex. A circular 45-degree C-diffuser (representing the second type) was studied to determine the effects of area-variation. The turbulent flows through the above types of ducts were also characterized by the presence of a strong secondary velocity. However, in comparison with laminar flows the thickness of the outer wall boundary layer was found to be increased relative to that on the inner wall.

The predicted flows through the volute like duct near the entrance region displayed basically similar pattern in comparison with curved ducts, but they are further complicated by the combined effect of very tight curvature and area reduction. As the flow moves downstream, the typical two-vortex secondary flow breaks up, resulting in four vortices. Tests were made in various volute shapes to determine the ability of the code to handle different cross-sections as found in practice. The level of agreement of the predicted results with experiments suggests that the method can serve as a useful design tool for turbine scrolls or other similar curved ducts of practical importance such as aircraft inlet ducts.

ACKNOWLEDGEMENTS

I would like to express my deepest gratitude to my supervisor, Dr. J. J. McGuirk for his guidance, constant encouragement and invaluable suggestions throughout this project and also for his always friendly and patient attitude in achieving every minute detail of the thesis.

I would also like to thank other members of the Fluids Section from whom I have been benefitted over the last few years. I appreciate the inspirations and suggestions that I have received and since they are too numerous it is better not to name any lest one is omitted.

This is an opportunity to thank the Association of Commonwealth Universities in U.K. and also the Department of Mechanical Engineering of this College for providing financial support towards the completion of this work. Sincere thanks are due to Bangladesh University of Engineering and Technology for granting me leave for this rather too long period.

Finally, I am profoundly grateful to my wife for her constant encouragement during the course of the work. This thesis is dedicated to my wife and our parents for their sacrifices.

CONTENTS

NOMENCLATURE

The following list is a summary of the nomenclature used. In some cases the variants of a particular symbol are not included.

Latin letters

a	coefficients in the discretised equations; pipe radius
A	area; coefficient matrix
b	metric derivatives ; residual of pressure-correction equation
B	coefficients in the transformed differential equations
C	coefficients in the turbulence model; constants
Cp	static pressure coefficient, defined as $(p-p_{ref})/0.5\rho u_0^2$
D	transformation parameter; hydraulic diameter; cross-derivative terms
$\overline{D}$	deformation tensor
De	Dean number
Dp	Dean number
$\overline{e}$	base vectors
E	coefficients in cross-derivatives; constants
f	ratio; factor; function
g	determinant of the metric tensor
G	rate of production of turbulent kinetic energy; convection part of the 'a' coefficients; constant pressure gradient
H	diffusion contribution of 'a' coefficients
$\overline{i}$	Cartesian base vectors
I	grid number index
$\overline{I}$	unit tensor
J	Jacobian of transformation; grid number index
k	kinetic energy of turbulence; Dean number
K	constant; grid number index
l	length
L	length
LP1	No. of grids in I direction
$\dot{m}$	mass flow rate
MP1	No. of grids in J direction
$\overline{n}$	a unit normal
N	total number of computational nodes; rpm
NP1	No. of grids in K direction
p	static pressure
P	total pressure

$\bar{q}$	flux vector
r	radial coordinate
R	radius
Re	Reynolds number
RI	inside radius
RO	outside radius
S	source terms
t	time
T	total temperature
$\bar{T}$	stress tensor
u	streamwise velocity component (in the direction of x or θ)
U	contravariant velocity in ζ direction
v	radial velocity component (in the direction of y or r)
V	contravariant velocity in η direction
$\bar{V}$	velocity vector
w	axial or transverse velocity component (z direction)
W	contravariant velocity in ξ direction
WD	volute exit width
x	Cartesian coordinate
y	Cartesian coordinate
z	coordinate direction
Z	normalized distance

Greek letters

α	Cartesian component of dual natural base vectors; under-relaxation factors; flow-angle
β	coordinate transformation factors
γ	coefficients of transformed equations
Γ	diffusivity coefficients
∂	differential operator
δ	Kronecker's delta; radius-ratio
ε	rate of dissipation of turbulent kinetic energy; mass source residual
κ	von Karman's constant
λ	friction factor ; convergence limit
μ	dynamic viscosity
ρ	density
θ	coordinate direction
ϕ	circumferential coordinate; angle
ψ	general variable

η	coordinate direction
ζ	coordinate direction (usually streamwise)
ξ	coordinate direction
$\bar{\tau}$	shear stress

Subscripts

c	related to curved duct; critical or mean value
e,w,n,s,l,r	at the centre of cell face: e,w,n,s,l,r
E,W,N,S,L,R	grid-node points
eff	effective value
exit	exit location
i,j	index
in	inlet
max	maximum
min	minimum
o	bulk value; related to upstream tangent
out	outlet
p	related to pressure
P	related to grid node P
ref	reference value
res	resultant
t	rotor-tip; related to turbulence
th	throat
u,v	related to velocity
W	related to wall
ψ	related to variable ψ
η,ζ,ξ	differentiated with respect to these coordinate directions
1,2,3	indices

Superscripts

i,j	indices
n	index; iteration counter
u,v,w	related to particular velocity component
1,2,3	indices
$*$	guessed value ; normalized coordinate
$'$	fluctuating component; corrector part
$+$	normalized quantity in wall function ; positive side of cell face
$-$	negative side of computational cell face

CHAPTER 1

INTRODUCTION

1.1 Background

Flow through turning channels has become an important research topic during the past few decades. One reason for this is that this type of flow is frequently encountered in many practical flow applications. For example, flow through air-conditioning duct bends, aircraft engine intake systems (Anderson, 1988), turbine flow passages, heat exchangers etc. Apart from these, the entry flow in a curved geometry tube has recently become of physiological concern because of its relevance to phenomena like mixing of injected substances in arteries and the deposition on arterial walls of suspended material such as Cholesterol (Pedley, 1980).

Before the rapid development of computer technology, scientists had to depend primarily on experimental techniques in order to know the flow details in practical engineering devices containing complex duct flows. Since the mid-1960's, it has become possible to obtain numerical solutions to many problems for which, although the mathematical formulations were laid down long ago, solutions were impossible to obtain analytically except for a very limited number of special cases; curved duct flows are an example of one such area where Computational Fluid Dynamics (CFD) studies have begun to provide insights useful to designers. In comparison to experimental investigations, numerical predictions offer several advantages in respect of cost, time and flexibility. On the other hand, predictions also suffer from some limitations such as insufficient computer resources (leading to insufficiently fine meshes and hence numerical accuracy is reduced), simplifications necessary for handling complex practical geometries (these were very common, but since the early 1980's are not essential; more discussion on this point is deferred until §2.3) and simplifications necessary to simulate the complex flow structures found in turbulent flow (i.e., turbulence model assumptions ; more details to be given in §2.6). Nevertheless, prediction codes have begun to contribute to improved understanding of complex fluid flows, although usually only after comprehensive comparison against reliable and 'bench-mark' data (usually experimental). The importance of curved ducts as a common feature of many engineering devices and the highly complicated nature of the associated flows make up a demanding but attractive target for the application of CFD techniques.

Although the detailed application examples of curved ducts vary widely and hence also the details of the type of duct employed, some general features describing duct geometries can be identified. Two important geometrical characteristics of turning channels are:

i) The mean radius of curvature and

ii) The cross-sectional area and shape.

The mean radius of curvature (or the ratio of hydraulic radius of the cross-section to the mean radius of curvature of the duct) is an indication of how tight a bend is and is often used as a parameter for the comparison of different bends. Another aspect is that the spatial locus of the mean centre-line of curvature may or may not have inflexion points. This leads to a further classification of curved ducts as once-curved (a simple bend as used in pipeline), twice-curved (an S-diffuser as used in aircraft inlets) or multiply-curved (piping in heat exchangers) (Murata et al, 1976).

The shape of the duct cross-section also varies widely, from regular (such as circular, rectangular and triangular) to irregular shapes. For simple engineering applications circular shapes are often preferred because it is easy to fabricate and offers maximum rigidity. On the other hand, special engineering devices such as aircraft inlets, volute casings etc., must resort to other shapes as will be outlined later. The shape may also remain unchanged throughout the length of the duct or it may change. The area of the cross-section represents the flow-area and is clearly determined by its shape; this also may or may not vary along the duct.

From the brief discussion presented so far, it appears that once-curved ducts (on which emphasis will be placed in the present study) can be further divided into the following types (see Fig.1.1a) :

i) Constant curvature and constant cross-section

ii) Constant curvature but variable cross-section and

iii) Variable curvature and variable cross-section.

Similar classifications may also be applied to the twice-curved and multiply-curved ducts.

The most striking flow feature in a curved duct is the presence of a secondary velocity field (significant transverse velocities in a cross-sectional plane) producing a flow pattern which may be far removed from that found in a straight duct (Ward-Smith, 1980). As the flow traverses a curved duct, a centripetal acceleration is experienced, driven by an inwardly acting radial pressure gradient. The magnitude of this gradient is set by the bulk fluid velocity in the core of the flow. It thus represents an excessive force, out of balance with the local acceleration, for the slower moving fluid in the boundary layers on the walls of the pipe. These are caused to move inwards and, by continuity, outward flow is induced in the duct centre. These curvature-induced secondary flows must be superimposed on the general through-flow. This gives rise to counter-rotating helical vortices as typically observed in curved ducts (see Fig.1.1b). In addition to this, several other curvature promoted flow features such as bifurcation of secondary velocity vortex (Nandakumar and Masliyah, 1982), flow separation and reattachment (Stewartson et al, 1980), growth of the internal boundary layers etc., may be of importance to designers.

In this thesis, a systematic investigation of flow in a specific type of curved ducts is made. The type has been chosen to be typical of that found in the inlet volute casing of small automobile turbochargers. The final objective of this work was thus the development of a numerical technique for predicting flow in turbocharger inlet volutes. However, before going on to define more specific objectives, a brief description of the kind of curved duct found in this application is given in the next section, together with a literature review on previous work. It is important to note here that much relevant information is contained in papers on simpler curved duct flows; and will be reviewed later in the thesis, as necessary. The application of CFD codes to similar complex internal flow problems will also be mentioned in later chapters.

1.2 The Inlet Volute Casing

Current design trends in the automotive industry have led to an upsurge of interest in the application of turbocharging to both petrol and diesel engines of all sizes (Watson and Janota, 1982). Using this technique, some of the energy of the exhaust gases (which would otherwise be wasted) is used to increase the intake air pressure and mass flow and hence the amount of fuel that can be burnt in the engine cylinder is also increased. The turbocharger consists of a turbine driven by the exhaust gases and a compressor coupled to the same shaft. The turbine used for this purpose is usually radial for small and medium size turbochargers and axial for larger applications. The radial turbine is cheaper and simpler to manufacture and provides a high level of efficiency for various sizes.

1.2.1 Geometry and Relevant Terminology

A schematic diagram of a typical turbocharger turbine is given in Fig.1.2a. It consists essentially of two components viz., i) a scroll-shaped casing (stationary part), which is fitted with the exhaust manifold of the engine and ii) the rotor, which carries the blades. The casing distributes the hot exhaust gases from the engine cylinder onto the rotor blades where as much as possible of the kinetic energy of the working fluid is converted to mechanical energy to drive the compressor.

The volute casing can be divided into two parts: the inlet duct and the spiral part. Usually the inlet section acts as an adaptor for directing fluid into the spiral distributor part. In many cases, the inlet duct is of constant cross-section and in several other situations, it is a converging duct which helps to accelerate the flow as it enters the spiral part. The junction of the inlet duct and the spiral part is usually termed as the 'throat'. The other important geometrical characteristic is the lower profile of the inlet duct at the throat where the flow has to separate from the wall, and is known as the 'tongue' as shown in the Fig.1.2a. A certain amount of mass usually recirculates under the tongue and mixes with the incoming fluid stream from the engine exhaust manifold. The function of the volute is to transform some of the fluid static enthalpy into kinetic energy and also to distribute the working fluid at a uniform rate and with a suitable flow angle around the rotor periphery. An incorrect or non-uniform angle of the fluid particles at the inlet of the rotor blades can be the cause of inefficiencies, possible separations and non-uniform loading. Since the blades are rotating at speeds anywhere between 25,000 and 200,000 rpm, this will ultimately reduce the life of the turbine. For this reason, some casings are fitted with a set of nozzles or guide vanes (Fig.1.2b) to achieve improved angular control of the flow onto the blades. Unfortunately, in most practical applications, since the operating conditions vary over a wide range, fixed nozzles are of little beneficial effect, at least for smaller turbines. Nozzle-less casings (Fig.1.2b) have more freedom in adjusting to rotor entry over a wider range of operating speeds, although this can clearly be achieved by a proper design of the volute, based on good understanding of the flow processes in the casing itself.

Often, the cross-sectional area of the volute is divided into two chambers by incorporating a 'separating wall' when it is called twin-entry (Fig.1.2b). If the separating wall is absent, it is termed as single-entry. The former is more common because it provides higher efficiency than the latter. However, for the purpose of the present study only the single-entry volute casings are considered, because it still retains the essential features of the flow phenemena of interest. As far as the cross-sectional shapes are concerned, it is generally governed by the mechanical constraints and the ease of manufacture. Hence, various shapes ranging from regular to irregular are common as shown in Fig.1.2c. One way of classifying the shapes is the relative area distribution over the cross-section, on the basis of which, some volutes are found to be symmetric (Fig.1.2a and 1.2b) and some are non-symmetric (Fig.1.2c).

While the rotor speed is obviously described by the rpm, the amount of mass which flows through the turbine is usually indicated by the overall pressure-ratio across the turbine. This is defined as the ratio of static or total pressure at the inlet plane of the volute inlet duct or at the throat to the static pressure at the exit from the rotor which is often known to be atmospheric. In general, the higher is the pressure ratio, the higher will be the mass flow rate. The fluid velocity at the exit from the volute or at the rotor tip is often expressed in terms of the Mach number and is also an indication of the flow rate.

1.2.2 Literature Review

Out of the two major parts of a turbocharger turbine, the rotor is obviously of prior importance and a large number of papers have appeared in the past. Due to the highly competitive nature of turbine design, it is only recently that the emphasis is found to be directed to the study of the stationary part of the turbine. As mentioned in §1.1, the present investigation is on curved geometry flows including those found in typical volute casings. What follows is a relevant survey of the past research on the stationary part of the turbocharger.

It may be recalled that one of the most important functions of nozzle-less volute casings (which are considered in this study) is to ensure uniformity of flow at exit from the rotor in terms of flow rate as well as flow direction. Hence, the majority of the previous experimental and theoretical works were concerned with the variation of flow angle at exit for various types of volutes. On the theoretical side, most of the early work on volute design are found to have employed one-dimensional inviscid, incompressible flow analysis (for example, Kastner et al, 1975). Assuming a constant angular momentum (or so-called free-vortex flow) along the radius at any cross-section, some elementary derivations can be made (Watson and Janota, 1982). With reference to Fig.1.2a, this analysis gives the following relation between flow angle α and the geometrical parameter $(A/R_c)_{th}$ and WD as:

$$\tan\alpha=(A/R_c)_{th}(1/2\pi WD) \tag{1.1}$$

where, A is the cross-sectional area, R_c is the distance measured from the centre of the rotor to the centroid of the cross-section and WD is the exit width (or commonly called the rotor-tip width) of the volute. The subscript 'th' refers to the throat.

The above relation shows that, for a specified rotor-tip width 'WD', the volute exit flow angle is defined by A/R_c at the throat. This ratio is often used to define the casing geometry. Further it implies that i) the flow angle is independent of mass flow rate and ii) the shape of the cross-section is also unimportant. Needless to say such an analysis is far from reality because it does not take into account most of the aerothermodynamic processes occuring in such a complex geometry flow situation. For example, the effects of geometrical shape, effect of viscosity, effect of compressibility are all excluded from this derivation.

Bhinder (1970) has essentially followed the same type of analysis based on conservation of mass and momentum. An improvement was made to the existing constant angular momentum approach by making use of isentropic one-dimensional relations in his flow model, whereby he was able to derive an expression relating $(A/R_c)_{th}$ with some rotor parameters and operating conditions. The relation can be expressed as :

$$(A/R_c)_{th}=f\{A_{exit},R_t,\alpha,N,T,m\} \tag{1.2}$$

In the above functional relation, A_{exit} represents the discharge area from the volute ($=2\pi R_t WD$, see Fig.1.2a), N is the rpm of the rotor, T is the total temperature of the fluid at the inlet plane and m stands for the mass flow rate. R_t is the rotor-tip radius and hence a rotor parameter. This analysis is an improvement in the sense that it is a parametric relation which gives certain design guidelines, but from the point of view of flow analysis, it still suffers from the above mentioned limitations. This paper reported the flow angle measurements on three proprietary volute casings having the same $(A/R_c)_{th}$ ratio, but the results showed large variations of flow angle among each other around the azimuthal direction. This is clearly an expected behaviour and several reasons can be associated with it as mentioned in the previous paragraph. However, the parametric relation of Bhinder (1970) showed that the dependence of flow angle for a specific volute casing on the operating conditions such as mass flow rate, total temperature, rpm etc., is very small. In other words, the geometrical details are the determining factors for the flow angle. Gubarev et al (1961) has also reported experimental investigation of flow angle and pressure loss for a nearly circular volute designed on a one-dimensional inviscid, incompressible flow. He also observed significant flow angle variations along the circumference of the rotor.

Hussain (1982) has conducted an experimental study on an essentially circular cross-section, symmetric, single-entry, nozzle-less volute casing designed on the basis of one-dimensional, inviscid approach. The findings agree well with Bhinder's (1970) observation that the flow angle does not remain uniform around the rotor periphery for a volute designed on such elementary assumptions and also it (flow angle) shows very little dependence on operating conditions such as pressure ratios (i.e., mass flow rates). The results put emphasis on the design of the inlet duct of the volute, especially the length and azimuthal location of the 'tongue' (see Fig.1.2a) in order that the desired free-vortex profile (i.e., highest velocity at the rotor-tip) is attained. Hussain developed a flow model by considering two velocity components (azimuthal and radial) and using one-dimensional isentropic relations. The effect of wall friction in the azimuthal direction was included in his flow model using empirical friction factors for curved pipes (Ito, 1959). An attempt has also been made to take care of the cross-sectional shape variation by taking components of shear force along the inclined surfaces of the cross-section. The results show some improvements over the free-vortex theory in respect of prediction of pressure and velocity at exit from the volute. However, a large discrepancy was still found between experimental and theoretical results. Although the author cast doubt on his own experimental data in order to explain the reasons behind the discrepancies, some comments were made about the inadequate treatment of shape as well as the other velocity component (the axial component). It is therefore very difficult to make a conclusive judgement but obviously the use of pipe friction factor for the volute geometry flow is of limited accuracy. The effect of viscosity may also have contributed to the discrepancies.

Miller et al (1988) have measured the flow parameters (total velocity, flow angle and pressure) for a symmetric, nozzle-less proprietary turbine (with an essentially linear area variation in the azimuthal direction) by means of a five-port cobra probe. Apart from the tongue region, in the range of $60<\theta<300$ deg (see Fig.1.2a), the results showed fairly uniform distribution of flow angle and static pressure. However, due to the mixing of the two streams at the tongue, significant flow disturbances were observed there. The paper also reported measurements of flow parameters at different axial positions (z-direction in Fig.1.2a) at the volute exit for each azimuthal section. Significant disturbances in the axial direction were observed, which confirms the presence of strong axial velocity component even at the volute exit. The results put emphasis on the design of the tongue region which is in accordance with the findings of Hussain (1982).

Barnard and Benson (1969) have carried out experimental investigations on three volute casings with equal inlet areas but different cross-sectional shapes and two other volutes with similar cross-sectional shape but different inlet areas. It has been found that the efficiency of the turbine stage reduced significantly just because of the change of shape. However, no comment about why this happened was found in the discussion.

The work of Ellison and Partridge (1978) is worthy of special attention. They have measured the blade vibration of the rotor for turbocharger turbines. The amplitude of vibration was found to be considerable which, they believed, was due to unequal pressure fields set up by the casing (especially near the tongue region) around the rotor. They have shown that if the inlet duct of the volute were curved and if the 'tongue' was extended further into the spiral part, the vibration characteristics could be significantly improved. It was further emphasised that an understanding of the flow pattern inside the scroll is a pre-requisite for successfully identifying and eliminating the sources of excitation of vibrations.

Scrimshaw (1981) has reported the 'size scale effect' of small geometrically similar, radial gas turbines. Three turbines having rotor diameters of 50.8, 67.73 and 101.6mm and two more proprietary turbines were studied experimentally. The volute casings of the first three had a trapezoidal cross-section and all other dimensions were scaled accordingly such that they could be called as geometrically similar. It has been found that the turbine flow capacity (or swallowing capacity) per unit flow-area decreased with decreasing size of the machine which ultimately affected the peak efficiency. A maximum of 5% drop in peak efficiency was reported for the smallest turbine at an overall total/static pressure ratio of 1.5 across the turbine. The reasons were attributed to the varying degrees of stagnation pressure loss in the vicinity of the 'tongue', where strong static pressure irregularities were observed due to the stream mixing. It has also been found that this pressure irregularity gave rise to an 'injection effect' (suction) for the fluid immediately below the volute. This was evidenced by the negative value of the measured flow angle at this location. It should be mentioned here that since Scrimshaw's measurements were supplied with complete, detailed geometrical information of the volute, they form the validation test case for the volute in the current research programme.

In another investigation on the same three geometrically similar turbines as mentioned above, Tindal et al (1987) have shown that apart from the 'size effect', a significant Reynolds number effect can be present in the volute casings. The growth of the boundary layers within the volute casing can reduce the swallowing capacity per unit area of the turbine which decreases as the size is reduced.The reduction of the swallowing capacity was shown to be related to the boundary layer growth. By defining the blockage with the displacement thickness of the boundary layer, they have shown that the swallowing capacity reduced by about 3% for the smallest turbine. The paper also reported the flow pattern under pulsating conditions which showed essentially similar nature as observed under steady state condition. This observation is of particular significance, because although the flow inside volutes is known to be pulsating, the assumption of steady flow is a reasonable simplification. A tendency of flow separation was also observed at lower pressure ratios. This tendency was most pronounced at the 'throat' on the outer wall and is a consequence of an adverse pressure gradient experienced by the flow. At all other locations, the tendency to flow separation was much less pronounced even at lower flow rates. At higher pressure ratios, since the boundary layer thickness becomes smaller due to increased mass flow rate, the tendency towards separation was found to have reduced.

As far as the experimental results on flow details in volute casings are concerned, it is only recently that a few papers have appeared. The main reason being the complicated shape of the cross-section which hinders measurements to be taken by both intrusive and non-intrusive techniques. Tabakoff et al (1980) have reported the through-flow velocity data for three cross-sections in the azimuthal direction. A non-symmetric nearly circular scroll was investigated with flow Mach number within the incompressible range (below 0.2). This study paid particular attention to identifying the parameters for dynamic similarity of turbines. These include the local Reynolds number based on the local hydraulic diameter of the volute cross-section and the ratio of the mean radius of curvature to the hydraulic radius of the cross-section. The second parameter incorporates the two geometrical characteristics of curved ducts as mentioned in §1.1.[1] The secondary velocity pattern was only extrapolated qualitatively from the measured through-flow velocity contours. In another accompanying paper Tabakoff, Vittal and Wood (1984) have reported some secondary velocity measurements on the same scroll-nozzle assembly. Instead of the familiar counter-rotating helical vortices found in curved ducts (Fig.1.1b), they have observed two secondary loops (since these cannot be considered as a true vortex) over the cross-section (see Fig.1.3a). No proper explanation as to why this pattern occurred was mentioned in the paper, but the most likely reason is a combined effect of curvature and discharge flow on flow development.

Another set of data has been reported by Malak et al (1986) on a nozzle-less, nearly square, non-symmetric scroll using a two colour LDV system. The cross-sectional area of the volute was reduced approximately linearly with azimuth angle. All three components of velocity were reported for eight uniformly spaced azimuthal locations. The through-flow velocities show that the flow pattern is strongly influenced by the geometry of the cross-section and scroll area variation around the circumference. The secondary velocity characteristics at two locations are given in Fig.1.3b. Again, similar to the observation of Tabakoff et al (1984), no counter-rotating vortices were observed for this particular flow configuration. These results indicate that the flow development inside volute casings is more complicated due to the radially exiting discharge flow. Also noteworthy is the fact that at exit from the casing, all three components of velocity are significant and hence justifies a three-dimensional analysis of such flow.

All the above, in brief, constituted representative experimental studies of volute flows. During the past three decades, the application of CFD to turbomachinery flow has also grown considerably. However, relatively few papers have appeared on computational flow modelling of turbine volutes perhaps because of the complex geometry of this component.

---

[1] The Reynolds number and radius-ratio of curved duct can be combined to make a non-dimensional number called the Dean number; this will be shown in Chapter 4.

Hamed, Baskharone and Tabakoff (1978) have reported an analysis of a scroll-nozzle assembly by making a two-dimensional simplification of the flow. Potential function was taken to be the primary dependent variable rather than the stream function because the former was found to be more suitable for handling the boundary conditions. In another contemporary paper, Hamed and Baskharone (1980) have reported three-dimensional finite element computations of compressible, inviscid flow through scroll and nozzle of a radial inflow turbine. Both symmetric and non-symmetric scrolls were investigated. Comparisons of through-flow velocities with experimental data show only qualitative agreement. The authors believe that the discrepancies were probably due to viscosity which was not taken into account in their numerical scheme.

Baskharone (1984) has solved three-dimensional inviscid, compressible flow in a scroll-nozzle assembly for a Mach number of up to 0.986. The same finite element technique has been employed. The findings highlighted the fact that the flow angle can be controlled by changing the cross-sectional area around the azimuthal direction. The variation of flow angle around the volute exit, as calculated by his numerical procedure, is shown in Fig.1.4a. Large variations can be seen, which is clearly undesirable as discussed before.

Khalil and Weber (1984) have applied finite difference techniques using primitive variables (i.e., velocity components and pressure rather than the velocity potential and stream function as the previous cases) for solving the flow through a proprietary turbocharger volute having symmetric cross-section. By employing a transformation from cylindrical-polar to general non-orthogonal curvilinear coordinate system, they were able to simulate the static pressure variation around the rotor-tip of a turbine. However, instead of using the fully elliptic form of equations, a repeated space marching integration technique has been employed for the purpose of economy. No velocity data or any details about the boundary conditions were reported. This work is superior to other works in the sense that viscosity effect has been incorporated by using a turbulence model. On the other hand, since the method is space marching, any possibility of a streamwise separation is excluded from the initial derivation. It has already been shown that although the boundary layers are expected to remain attached for the most part of the spiral section, just at the throat, such a possibility cannot be ruled out (Tindal et al, 1987).

One interesting numerical work has been reported by Chen, Lee and Huang (1986). The scroll geometry (consisting only of the spiral part) was first described with reference to cylindrical-polar coordinate and then transformed into a spherical coordinate system. Only the Laplace's equation employing velocity potential was solved assuming the flow to be inviscid, irrotational. Three symmetric, circular cross-section, nozzle-less volute casings with different azimuthal area variations were studied using finite difference techniques. Results were presented in the form of velocity vectors for the through-flow direction and for secondary velocities over one cross-section for each of the three model volutes. The secondary velocities for all cases exhibit a radially inward pattern, unlike the experimental observations of Tabakoff et al (1980) for a circular cross-section, non-symmetric volute (Fig.1.3a). The authors did not mention any particular reason for the differences, but probably the viscous effects may have been responsible for it. Although the main emphasis of the work was on the potential robustness of the mathematical formulation, which has been demonstrated for circular cross-section only, for practical applications it does not appear to be so convenient, especially when the full Navier-Stokes equations are considered. In the preliminary stages of the current research programme, this transformation has been tried for the full Navier-Stokes equations and it has been found that the number of terms appearing in the transport equations become prohibitively large for computational purposes, and would be larger if additional transformations were required for a non-circular geometry. Modelling of the inlet duct (which is almost always present in practical cases) will also need special attention.

Finally, Lymberopoulos (1987) has used finite difference calculation techniques in order to predict two-dimensional (and also quasi three-dimensional, where the area variation over the cross-section was accounted for, but the axial velocity component was always neglected) inviscid flow through single- and twin-entry turbocharger volute casings. He has solved Euler equations using the widely used time marching technique of Denton (1975) for blade flow calculations. Three single-entry volute casings (one of which was of a proprietary type) were investigated. The validity of the computations were judged mostly on the basis of pressure data and flow angle measurements; the latter, however, was usually overpredicted (by about 25%). The reasons for the discrepancies were attributed to the inaccuracies in reproducing the exact three-dimensional geometry of the volutes (and also partly due to experimental uncertainty). It is apparent from his work that accurate geometrical information must be available for the successful prediction of such type of complex flows. A typical velocity distribution on a through-flow surface, as predicted by his code, is shown in Fig.1.4b.

In the following section, the conclusions which can be drawn from the literature review is highlighted, on the basis of which the specific objectives of the current research were extracted.

1.2.3 Conclusions Drawn from the Survey

Previous experimental investigations of the flow in volute casings have shown significant variations of flow properties around the rotor inlet. However, due to limitations arising out of complicated geometry of the volute and the associated access problems, very few detailed and systematic measurements of the flow have been obtained and hence the fundamental reasons causing these non-uniformities are unexplored in most of the cases and usually only a qualitative comment was made. On the other hand, most of the numerical studies have employed two-dimensional or even one-dimensional approximations to this highly complex three-dimensional flow. The viscous effects which may be quite strong are also excluded from the prediction methods except for one or two research programmes. No work has come to the notice of the author which solves the fully elliptic Navier-Stokes equations for these flow situations.

It is therefore obvious that more work is necessary on this type of curved duct flow. A systematic investigation which solves governing differental equations in their full form (rather than using various truncated forms such as inviscid, partially parabolic etc., which excludes some of the physical flow phenomena) for a range of ducts from simple bend up to the volute would certainly be more fundamental than any other existing approach. The rationale behind this lies in the essential geometrical similarity of a volute casing and a curved duct, and has been the guiding principle for the current study, the objectives of which are presented in the next section.

1.3 Objectives

On the basis of the discussion presented so far, the volute casing can be identified as a once-curved duct having variable curvature and variable cross-section with radial exit along one boundary. The flow in such type of duct is known to be three-dimensional, viscous, compressible and usually the fluid is at a high temperature. Clearly, a predictive tool has to have several desirable properties in order that the practical flow situations are fully realized computationally. These are as follows:

i) It should be three-dimensional;
ii) It should be capable of describing the proper geometry (i.e., body conforming);
iii) It should allow viscosity (i.e., for low flow rates, the laminar viscosity should be considered and for high flow rates of interest, must use a turbulence model);
iv) It should be capable of simulating the main effects known to take place in bend flows;
v) It should be compressible;
vi) It should be capable of taking care of heat transfer.

So, the strategy of handling the problem by checking each of these aspects separately in a step-by-step development manner would be the most appropriate one.

In the current reseach programme, the compressibility effect has not been considered because, it is believed that eliminating this effect does not remove the essential problem and for most cases the effect of compressiblity is not very large for real operating conditions. Assumption of constant total temperature eliminates the need for solving an enthalpy equation.

The main objectives of this work are therefore :

i) To develop a general computer code which solves the fully elliptic Navier-Stokes equations and can handle the geometrical complexity of a range of ducts up to and including typical volute shapes.

ii) To study the flow through constant curvature and constant cross-section ducts, identify the basic features of such flows and demonstrate that the code is capable of resolving these adequately.

iii) To study the flow in constant (and variable) curvature and variable cross-section ducts, and thus to ascertain the individual effects of curvature and cross-section, as predicted by the code.

iv) To apply the developed code to the study of flow in volute casings.

1.4 Contents of the Thesis

The first requirement for the development of a suitable code is the formulation of a mathematical model which should be sufficiently general to allow the analysis of the complex geometry systems, typical of volute flows. In Chapter 2, the governing differential equations are therefore presented in a coordinate free form. The transformation to a general coordinate system is then shown and the equations presented in the general coordinate system. Since all real volute flows are turbulent, the time-averaged equations of turbulent flow, and the turbulence model adopted for this study are then described.

In Chapter 3, the detailed methodology of the solution procedure is given. The physical significance of the general transformation is outlined. Discretisation practices are described for a scalar variable and the final form of the discretised equation is shown. The convection scheme, boundary conditions, grid generation techniques etc., are also presented here.

Chapter 4 describes the results from a study of laminar flow in constant curvature and constant cross-section (circular and square) toroidal ducts. Both fully-developed and developing flows were studied and comparisons with experimental data are presented.

In Chapter 5, the developed computer code employing a non-orthogonal curvilinear coordinate system is assessed by applying it to some simple inviscid, laminar and turbulent flows for which either analytic, numerical or experimental data of bench-mark accuracy were available. Effects of grid density and under-relaxation factors on the accuracy of results and the rate of convergence are shown. In addition to this, laminar and turbulent flows through a constant curvature and constant cross-section 90-deg bend with upstream and downstream tangents are studied. Finally, flow in a 45-deg C-diffuser is solved. The objectives of these studies are, apart from showing the ability of the computer code to handle such three-dimensional complex flows, to study the effects of curvature and area variation for such ducts.

Chapter 6 deals with flows in volute casings. First, in order to bridge the gap between a duct and a volute, a trumpet-shaped (volute-like) duct is solved. Next, the laminar flow in a symmetric, circular cross-section volute is presented. Lastly, flow through a non-symmetric, trapezoidal cross-section volute is studied for which experimental data were available to assess the quality of the predictions.

Finally, conclusions and suggestions for future work are presented in Chapter 7.

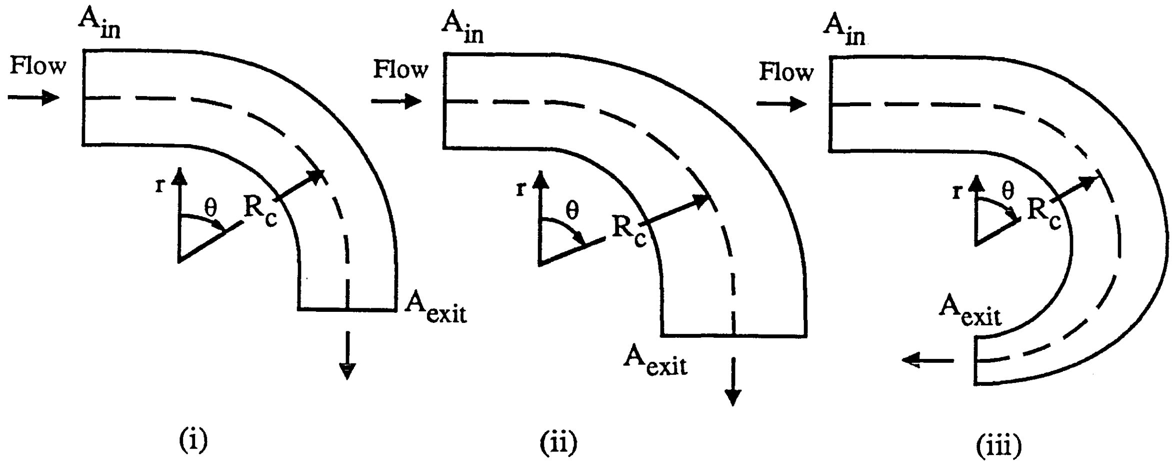

Fig. 1.1a Schematic diagram of once-curved ducts in two dimensions:

(i) Constant curvature, constant cross-section; R_c=constant, $A_{in} = A_{exit}$

(ii) Constant curvature, variable cross-section; R_c=constant, $A_{in} < A_{exit}$

(iii) Variable curvature, variable cross-section; $R_c = R_c(\theta)$, $A_{in} > A_{exit}$

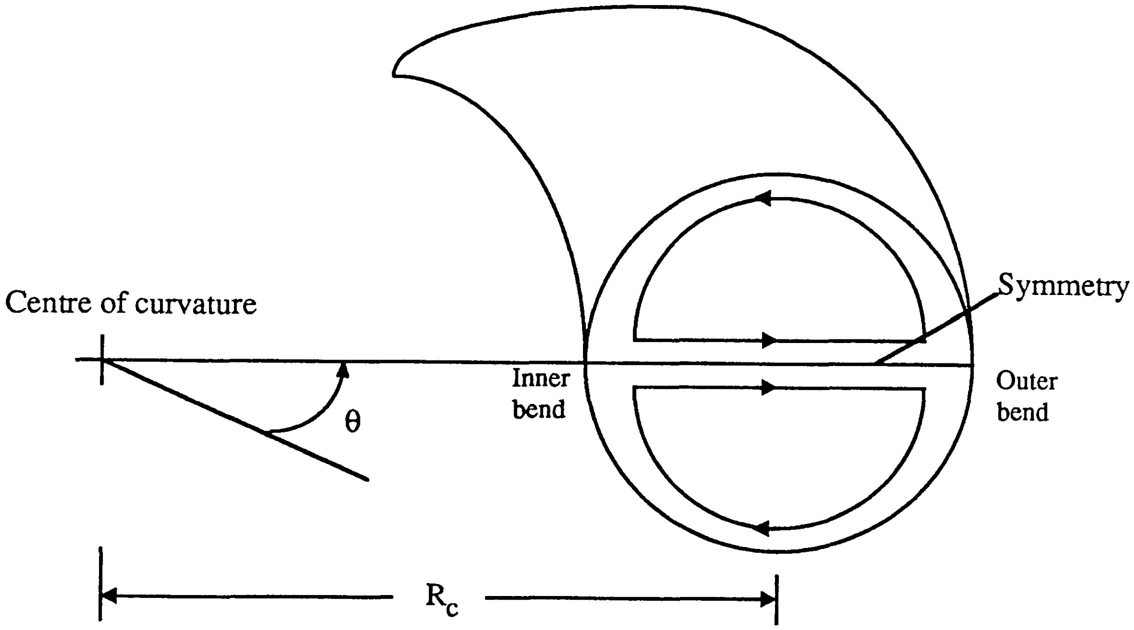

Fig. 1.1b Typical secondary flow in the cross-section of a curved pipe.

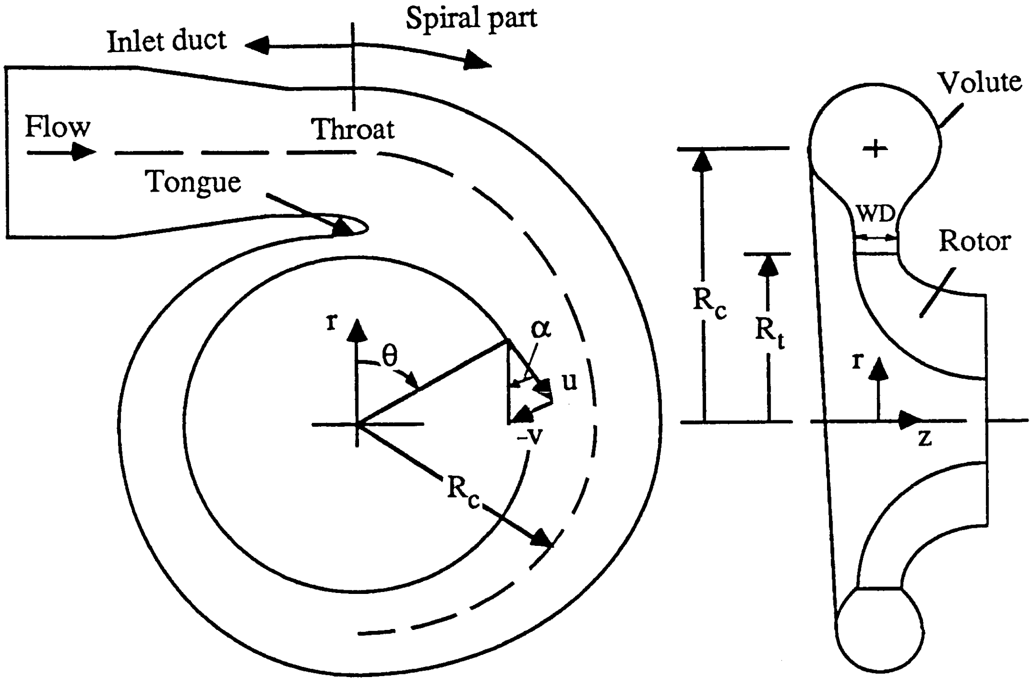

Fig. 1.2a Diagram of turbocharger turbine.

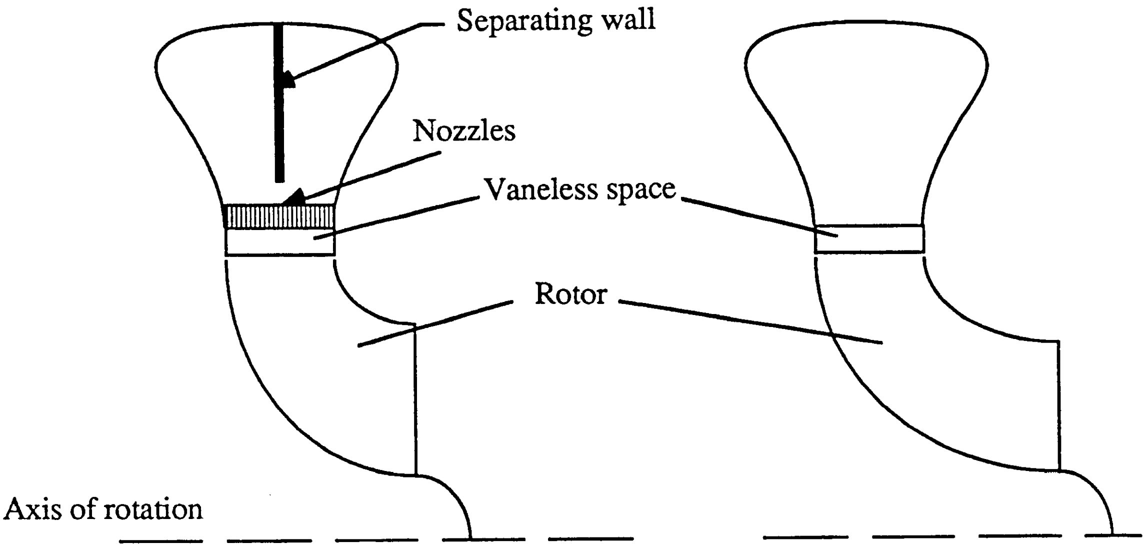

Twin-entry volute with nozzles

Nozzle-less, single-entry volute

Fig. 1.2b Single and Twin-entry, symmetric volutes.

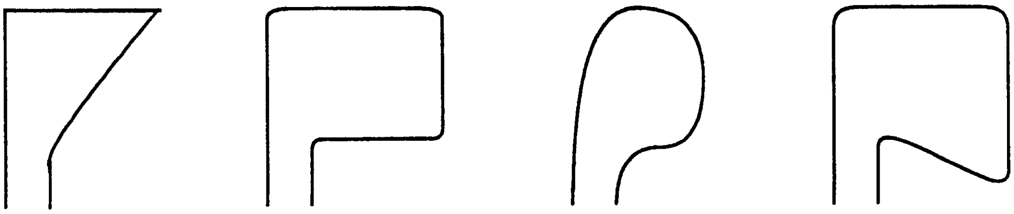

Fig. 1.2c Common shapes of non-symmetric volute casings

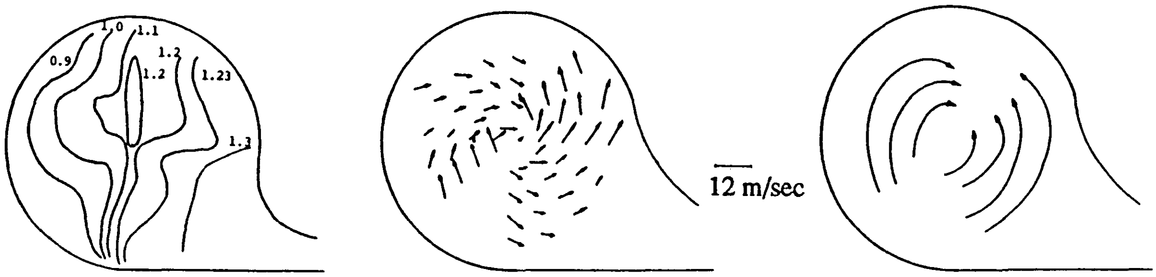

Normalized through-flow velocity contour

Secondary velocity vector

Vortex pattern of secondary velocity

Fig. 1.3a Measured velocity distribution in a cross-section of a volute at $\theta=139$ deg (Tabakoff et al, 1980)

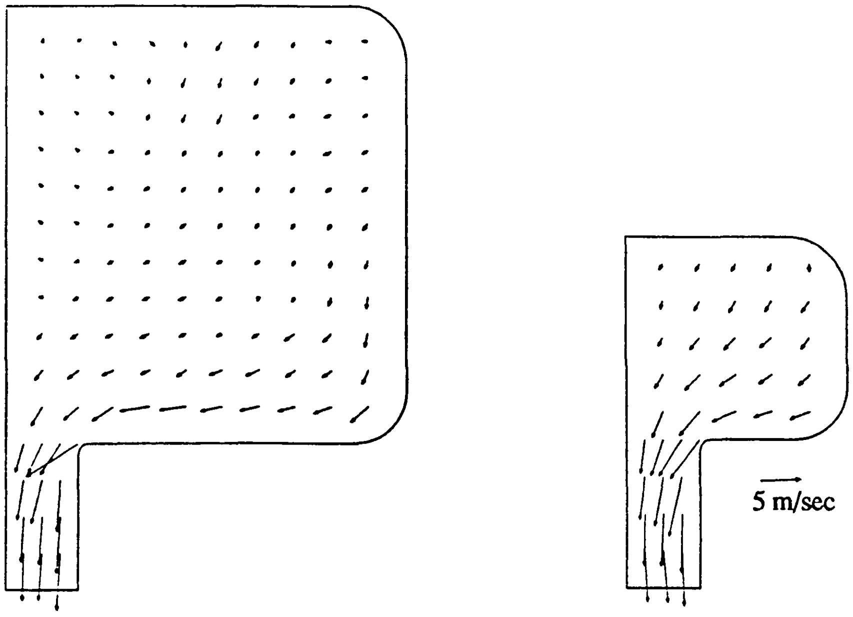

$\theta=90^{o}$

$\theta=270^{o}$

Fig. 1.3b Measured secondary velocity for a non-symmetric, nearly square scroll (Malak et al, 1986)

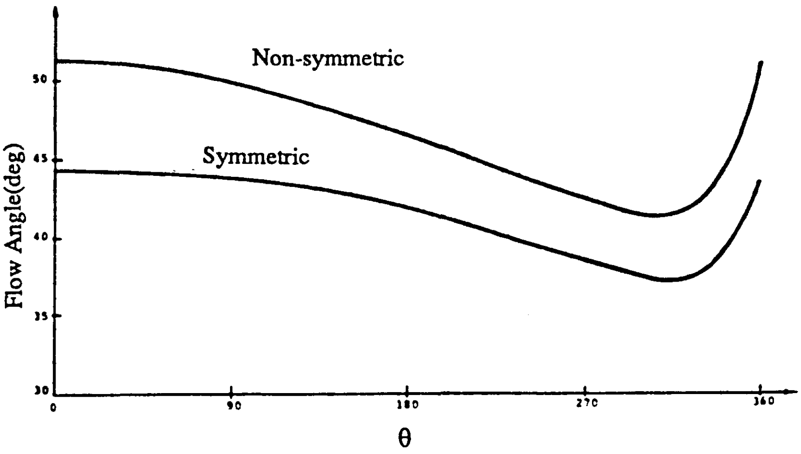

Fig. 1.4a Predicted flow angle at scroll exit (symmetric and non-symmetric, circular cross-sectional volutes), Hamed and Baskharone (1980)

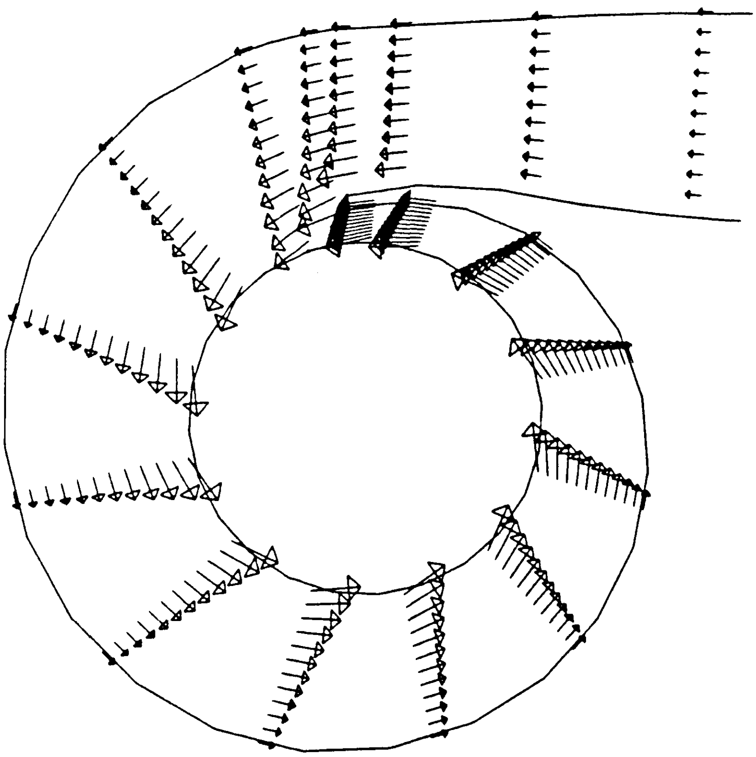

Fig. 1.4b Predicted velocity vectors on a through-flow surface, Lymberopolous (1987)

CHAPTER 2

THE MATHEMATICAL MODEL

2.1 Introduction

The flow through any duct geometry is governed by the set of partial differential equations known as the Navier-Stokes equations. They represent nothing more than the mathematical statements of the conservation of momentum (Newton's 2nd Law of Motion), of energy (1st Law of Thermodynamics) and of mass etc.; and are long established. Due to their complex nature, very few analytical solutions can be obtained. With the development of high speed computers, a wide range of flows have been investigated numerically by employing simple and regular coordinate versions of these equations (Cartesian, for example). For these systems the choice of vector and tensor components, and therefore the form of equations, is obvious. However, these simple coordinates are often found to be inadequate for the calculations of flow through complex geometries and one has to resort to more general systems which offer the flexibility of curvilinear coordinates. For the latter case, there are various possible ways of deriving the equations and each particular form offers several advantages and disadvantages in comparison to the others. While all forms of conservation equations describe the same laws and from a mathematical point of view are equivalent, different forms have different properties from the viewpoint of a numerical solution of the equations, and this must therefore be considered in detail when the particular form is adopted.

The remainder of this chapter consists of six sections. First in section 2, the conservation equations are presented in a coordinate-free form. In section 3, the different types of coordinates that can be employed for the description of the flow domain are briefly discussed and the choice for the present investigation is made. Then, in section 4, the various forms of equations that can be derived in the chosen coordinate system are outlined. In section 5, the equations are first presented in a cylindrical-polar coordinate system; by employing a transformation, the conservation equations are then derived in a general coordinate system. Time-averaged versions of the equations suitable for turbulent flow problems and the turbulence closure model chosen are presented in section 6. Finally, section 7 summarizes the main points of the current chapter.

2.2 Coordinate-free Form of Governing Equations

The conservation equations of mass, momentum and scalar quantities (such as enthalpy, mass fraction etc.) can be expressed in the following form, which is independent of coordinate system employed:

$$\frac{\partial \rho}{\partial t} + \mathrm{div}\,(\rho\bar{V}) = 0$$

$$\frac{\partial (\rho\bar{V})}{\partial t} + \mathrm{div}\,(\rho\bar{V} \otimes \bar{V} - \bar{T}) = \bar{S_V}$$

$$\frac{\partial (\rho\psi)}{\partial t} + \mathrm{div}\,(\rho\psi\bar{V} - \bar{q}) = S_\psi \qquad (2.1)$$

Here, ρ is the density, $\bar{V}$ is the velocity vector, $\bar{T}$ is the stress tensor, $\bar{q}$ is the scalar flux vector and ψ is any dependent scalar variable. $\bar{S_V}$ and S_ψ are the source terms for momentum and scalar equation respectively. 'div' is the divergence operator and $\otimes$ represents the tensor product. The first term of each equation represents the time dependent term which is equal to zero in the steady state.

For a Newtonian fluid, the stress tensor is defined as:

$$\bar{T} = (-p+\frac{2}{3}\,\mu\,\mathrm{div}(\bar{V}))\bar{I} + 2\,\mu\,\bar{D} \qquad (2.2)$$

where, p is the pressure, μ is the dynamic viscosity of the transporting fluid, $\bar{I}$ is the unit tensor of second order, and $\bar{D}$ is the deformation tensor (rate of strain).

The deformation tensor is defined to be the symmetric part of the velocity gradient:

$$\bar{D}=\frac{1}{2}\{\mathrm{grad}\,(\bar{V}) + [\mathrm{grad}\,(\bar{V})]^T\} \qquad (2.3)$$

where 'grad' is the gradient operator and superscript 'T' represents the transpose.

The flux vector $\bar{q}$ is usually given by the Fourier-type law:

$$\bar{q} = -\,\Gamma\ \mathrm{grad}\,\psi \qquad (2.4)$$

where Γ represents a diffusion coefficient and is usually a property of the fluid.

In order to devise a numerical technique of finite difference or finite volume type for solving the above set of Eqs.(2.1), it is usual for reasons of practicality to select a single coordinate system appropriate to the needs. In the next section, the different types of coordinate systems as found in literature are briefly discussed and the choice for the present problem is made.

2.3 Types of Coordinate Systems

The commonly employed coordinate systems for the finite volume solution of conservation equations are mainly of three types viz., i) Cartesian or Cylindrical-polar, ii) Curvilinear Orthogonal and iii) Curvilinear Non-orthogonal. An illustration of these coordinates in conjunction with an irregular domain such as the cross-section of a volute casing is given in Fig.2.1. Strictly speaking, any of the above-mentioned systems can be employed for the analysis of arbitrarily -shaped flow domains. However, much evidence is available in the literature that the quality of prediction for a given flow situation and the effort required can be significantly different depending on the particular choice.

Historically, by far the most popular is the first type. The main reason being that the governing transport equations assume their simplest form and hence the computer codes. The interpretation of results is also very simple. However, apart from their straightforward application to regular geometries, some special techniques such as 'blocking-off' cells (Patankar,1980) or a 'piecewise linear' approximation (Koutmos et al, 1990) are always necessary for handling the complex geometries of engineering importance. These treatments are somewhat wasteful of computer storage and time for two reasons. Firstly, trivial computations are still carried out for the blocked-off regions and the results have to be stored. Secondly, the introduction of fine grids in the regions of steep gradients (such as near the walls) results in unnecessary refinement elsewhere in the domain. Although these apparently crude approximations often lead to fairly accurate predictions for the bulk of the domain, for obvious reasons, the near-wall behaviour cannot be correctly predicted as described by, among others, Koutmos and McGuirk (1983). From a user's point of view, this approach appears to be cumbersome because for every new arrangement of grid, some tedious 'flagging' is necessary for boundary cells.

These problems can be greatly overcome by making use of curvilinear systems (also known as body-fitted) because, here the geometry of the flow domain 'dictates' the coordinate lines unlike the previously discussed Cartesian coordinate where the flow-domain is super-imposed on a regular mesh. The use of type (ii) involves the derivation of the governing differential equations in a general orthogonal coordinate system. The resulting equations are much more complex in comparison to the Cartesian but the discretised forms look very similar. The calculations of various lengths, areas and volumes for the numerical cells are not as simple as in the previous case and involves some additional programming. The main disadvantage is that these methods are particularly very demanding on grid properties (to be described in §3.8.1) because of the stringent requirement of having orthogonality at every grid node. Hence an elaborate grid generation technique must be available which itself is a substantial task. Besides, in some parts of the flow domain such as near the corners (see Fig.2.1b), the 'unavoidable' deviation from orthogonality causes inaccuracy. These methods are also sometimes wasteful in terms of computational effort because of unnecessary clustering of grids in some regions (core region, for example). Employment of this class of coordinates has widened the scope of Computational Fluid Dynamics by its ability to handle a variety of practical flow configuratuions. Several works can be found in literature which fall into this category (e.g., Manners, 1988; Humphrey et al 1985; Coupland and Priddin, 1986 etc.).

As is evident from its name, the methods which employ non-orthogonal curvilinear coordinates are much more flexible in respect of grid generation, because in this case the grid lines need not be orthogonal. Also the grid layout can be conveniently rearranged enabling higher resolution in the regions of steeper gradients. The superiorities in resolution can be obtained at the extra effort required in programming the large number of terms which appear in the general coordinate systems. During the last decade or so, a number of workers have employed these methods for the analysis of flow through complex geometries viz., Karki and Patankar (1989), Braaten and Shyy (1986), Peric (1985), Khalil and Weber (1984) etc.

Considering the aspects described above and keeping in mind the objective of the current research, the non-orthogonal curvilinear coordinate system has been chosen for the bulk[1] of this study.

---

[1] The study of flow through constant curvature and constant cross-section ducts (Chapter 4) does employ a curvilinear orthogonal mesh since this is easy to generate for these ducts. However, non-orthogonal curvilinear coordinate systems are equally applicable for such flows as will be evident from Chapter 5.

2.4 Discussion on Various Forms of Equations in General Coordinate System

Having decided that the non-orthogonal curvilinear coordinate system will be employed for the complex flow geometries, the next obvious question is what the form of the governing equation will be. As mentioned earlier in the chapter, there are several possible ways of expanding the governing transport Eqs.(2.1) for such a general system. In fact, the resulting form of equation depends on two basic factors viz.,

i) the definition of spatial operators or base vectors and
ii) the way the divergence operators featuring in Eqs.(2.1) are expanded.

Demirdzic (1982) has conducted an extensive study on various possible forms of the governing partial differential equations and recently Manners (1988) has also reported a similar study highlighting the relative advantages and disadvantages of various forms from the viewpoint of a numerical analyst. There is therefore no need for a detailed discussion on this topic; only a brief summary of the two factors is mentioned for completeness. Readers interested in more details about these aspects are directed to the above and other references (e.g., Sokolnikoff,1964; Aris,1962 etc.). In the following sections, Cartesian tensor notations and Einstein summation conventions are adopted as usual. The relevant information of tensor calculus can be found in the above references.

2.4.1 Spatial Operators in General Coordinates

Fig.2.2 is a schematic representation of the two types of coordinate systems viz., Cartesian, denoted by x^i ($x^1=x, x^2=y, x^3=z$) and general, denoted by η^i ($\eta^1=\zeta, \eta^2=\eta, \eta^3=\xi$). For the Cartesian frame, the base vectors $\bar{i}_i$ are obvious and are described along each of the coordinate lines. Whereas for the frame η^i, there exists more than one possibility.

The natural choice for the latter system would be to use the vectors $\bar{e}_i$ directed along the tangents; these are shown in Fig.2.2b. The other set of base vectors are the 'dual natural' base vectors $\bar{e}^i$ which are normal to the corresponding coordinate surface of constant η^i.

The relationship of $\bar{e}_i$ and $\bar{e}^i$ with the reference Cartesian base vectors are:

$$\bar{e}_i = \frac{\partial x^m}{\partial \eta^i} \bar{i}_m \tag{2.5}$$

$$\bar{e}^i = \frac{\partial \eta^i}{\partial x^m} \bar{i}^m \tag{2.6}$$

These are the two basic forms of base vectors and are conventionally called the Covariant and Contravariant forms. (Quantities which transform like natural base vectors (Eq.2.5) are called 'covariant' and those which transform like dual natural base vectors (Eq.2.6) are called 'contravariant'). Superscripts are associated with contravariant quantities and subscripts are related to covariant components. For Cartesian coordinates there is no difference between contravariant and covariant components of the base vectors.

2.4.2 Non-physical Base Vectors

In order to convert the transport Eqs.(2.1) presented in §2.2 into computationally soluble component equations, the vector and tensor components appearing in Eqs.(2.1) are to be expressed with respect to a set of base vectors. If the contravariant vector and tensor components are used:

$$\begin{aligned}
&\bar{T} = T^{ij}\, \bar{e}_i \otimes \bar{e}_j \\
&\bar{V} = V^i\, \bar{e}_i \\
&\bar{S} = S^i\, \bar{e}_i \\
&\bar{q} = q^i\, \bar{e}_i
\end{aligned} \tag{2.7}$$

where $\bar{e}_i$ are the natural base vectors defined by Eq.(2.5).

The divergence operators featuring in Eqs.(2.1) can be expanded in the following two ways:

$$\begin{aligned}
&\operatorname{div} \bar{V} = \bar{e}^j \cdot \frac{\partial \bar{V}}{\partial \eta^j} = \frac{\partial V^j}{\partial \eta^j} + V^m \left\{ {j \atop j\ m} \right\} \\
&\operatorname{div} \bar{T} = \bar{e}^k \cdot \frac{\partial \bar{T}}{\partial \eta^k} = \frac{\partial T^{ij}}{\partial \eta^j} + T^{mj} \left\{ {i \atop m\ j} \right\} + T^{im} \left\{ {j \atop j\ m} \right\}
\end{aligned} \tag{2.8}$$

or, in a more compact form as:

$$\operatorname{div}\bar{V}=\frac{1}{\sqrt{g}}\frac{\partial}{\partial\eta^j}\{\sqrt{g}\,V^j\}$$

$$\operatorname{div}\bar{T}=\frac{1}{\sqrt{g}}\frac{\partial}{\partial\eta^j}\{\sqrt{g}\,(T^{ij}\bar{e}_i\} \tag{2.9}$$

In the above expressions $\{{}_j{}^i{}_k\}$ represents the Christoffel symbols of the second kind, and are given by:

$$\{{}_j{}^i{}_k\}=\frac{1}{2}g^{im}\left(\frac{\partial g_{jm}}{\partial\eta^k}+\frac{\partial g_{km}}{\partial\eta^j}-\frac{\partial g_{jk}}{\partial\eta^m}\right) \tag{2.10}$$

where, g^{ij} and g_{ij} are the covariant and contravariant metric tensor components respectively and g is the determinant.

Dropping the time-dependent term for steady-state situation, and adopting the above two forms of the divergence expressions (Eqs.2.8 and 2.9), the following forms of equations may result.

Weak Conservation Form (using Eq.2.8)

$$\frac{\partial}{\partial\eta^j}(\rho V^j)+\{{}_j{}^j{}_m\}\,\rho V^m=0$$

$$\frac{\partial}{\partial\eta^j}(\rho V^i V^j-T^{ij})+\{{}_m{}^i{}_j\}\,(\rho V^m V^j-T^{mj})+\{{}_j{}^j{}_m\}\,(\rho V^i V^m-T^{im})=S_v^i$$

$$\frac{\partial}{\partial\eta^j}(\rho\psi V^j-q^j)+\{{}_j{}^j{}_m\}\,(\rho\psi V^m-q^m)=S_\psi \tag{2.11}$$

Strong Conservation Form (using Eq.2.9)

$$\frac{1}{\sqrt{g}}\frac{\partial}{\partial\eta^j}(\sqrt{g}\;\rho V^j)=0$$

$$\frac{1}{\sqrt{g}}\frac{\partial}{\partial\eta^j}[\sqrt{g}\;(\rho V^i V^j - T^{ij})\,\bar{e}_i]=S_V^i\,\bar{e}_i$$

$$\frac{1}{\sqrt{g}}\frac{\partial}{\partial\eta^j}[\sqrt{g}\;(\rho\psi V^j - q^j)]=S_\psi \qquad (2.12)$$

By comparing the two sets (Eqs.2.11 and 2.12), it can be observed that the weak conservation form contains many more extra terms (there can be a maximum of nine non-vanishing Christoffel symbols and, for each of these there will be more than one term) than the strong conservation form. The other important point is that all the terms of Eqs.(2.12) appear under the differential operator. So, when an integration is performed over a control volume by applying Gauss' Theorem, the flux terms cancel in pairs at the cell faces in the interior of the solution domain, so that only the boundary fluxes remain (Roache,1976). In the case of Eqs.(2.11), there is no obvious way of discretising the undifferentiated terms which would assure cancellation from cell to cell and consequently produce overall conservation of the corresponding quantity. Hence the strong conservation form is usually attractive to a numerical analyst.

The momentum equation in strong conservation form is still a vector equation and must therefore be resolved into component equations for computational purposes. The difficulty lies in the fact that in this case a vector (the momentum vector), and not its components, is the quantity that is physically conserved. Hence, if the directions of resolution are not spatially invariant, the resolved equations must have terms (associated with Christoffel symbols) which redistribute this vector from one direction to the other.

The most obvious way would be to resolve the equations in the direction of natural base vectors $\bar{e}_i$ (Fig.2.2). The momentum equation then assumes the following form:

$$\frac{1}{\sqrt{g}}\frac{\partial}{\partial\eta^j}(\rho V^i V^j - T^{ij})+\left\{{i \atop m\;j}\right\}(\rho V^m V^j - T^{mj})=S_v^i \qquad (2.13)$$

This form of equation offers some advantages over the weak conservation form in that it contains fewer terms and hence requires less computational effort and interpolation errors are also less. This is usually preferred when an orthogonal curvilinear coordinate system is employed[1] (such as Humphrey et al, 1985; Manners,1988). But for non-orthogonal curvilinear coordinate system, this approach proved to be very sensitive to grid-continuity and smoothness as shown by Demirdzic (1982). The reason can be attributed to the fact that the Christoffel symbols involve the second derivatives of the grid lines and hence cannot be calculated accurately unless a very smooth mesh is used.

The non-differentiable terms appearing in Eq.(2.13) will disappear and a strong conservation form will result if the base vectors are expressed in terms of 'fixed' Cartesian base vectors $\bar{i}$. The equations now express the transport of the Cartesian components of momentum:

$$\frac{1}{\sqrt{g}}\frac{\partial}{\partial\eta^j}[\sqrt{g}\,(\rho V^m V^j - T^{mj})\,\alpha^i_m] = S^m\,\alpha^i_m \qquad (i = 1,3) \qquad (2.14)$$

where,

$$\alpha^i_m = \frac{\partial\eta^i}{\partial x^m} \qquad (2.15)$$

Although this form of equation is a strong conservation form, it suffers from the disadvantage that a large number of terms have appeared due to summation on 'm' . However, because of the conservative nature of the terms, this form of equation finds highest popularity among researchers employing non-orthogonal curvilinear coordinate system (such as Shyy et al ,1985; Peric,1985 etc.). The other disadvantage in using fixed basis for the resolution of momentum equations is the so-called 'decoupling' problem, which requires special attention; these matters will be discussed in the next chapter.

In a different approach for obtaining a strong conservation form, Vinokur (1974) resolved the momentum equations with respect to a locally fixed basis. For each computational cell, there can be assumed a fixed base vector at the centre of the cell. With such a definition of discrete reference of base vector, a much simpler form of equation with prominent velocity component will result, but on each cell face a discontinuity problem will arise. That is, the flux from one cell is not generally equal to the flux into the neighbouring cell. This is why the current research programme does not consider this approach.

---

[1] This set of equations has been used for the study of flow through constant curvature and constant cross-section ducts (Chapter 4), where a toroidal (orthogonal curvilinear) coordinate has been employed. The derivation of equations employing physical components will be shown later in the thesis.

The above discussion has been conducted in terms of contravariant vector and tensor components. Similar forms of equations can be obtained if covariant vector and tensor components along with 'dual natural' base vectors (Eq.2.6) are used. These forms, however, did not gain popularity because of larger number of terms appearing in the equations. However, they offer one advantage in that they have only one pressure gradient for each of the momentum equations unlike three for the contravariant case (for example, in Eq.2.14 the stress term T^{mj} which contains pressure (Eq.2.2) is summed on i=1,3). The PHOENICS code (Malin et al, 1989) employs the covariant form of equations mainly because of this reason.

2.4.3 Physical Components

The base vectors $\bar{e}_i$ and $\bar{e}^i$ (defined in Eqs.2.5 and 2.6) are usually neither non-dimensional nor unit vectors. In many cases, the associated vector quantities (contravariant and covariant) may have dimensions which are different from the physical meaning of velocity. (For example, in cylindrical polar coordinate, $V^\theta=d\theta/dt$ is the contravariant velocity which does not conform to the usual dimension of velocity i.e., length/time). This makes understanding of results extremely complicated and may introduce singularity problem. (For example, if a plane polar coordinate is used to describe uniform parallel flow, then $r\,\{d\theta/dt\}=r\,V^\theta$=constant. Hence, for $r\rightarrow0$, $V^\theta\rightarrow\infty$).

To get rid of these anomalies, researchers are usually found to have applied the non-dimensional base vectors such that the associated vectors have the conventional meaning of vector (such as velocity). The corresponding base vectors in non-dimensional form are:

$$\bar{e}_{(i)}=\frac{\bar{e}_i}{\sqrt{g_{ii}}} \qquad \text{(No summation)} \qquad (2.16)$$

$$\overline{e^{(i)}}=\bar{e}^i\sqrt{g_{ii}} \qquad \text{(No summation)} \qquad (2.17)$$

where $\sqrt{g_{ii}}$ is the magnitude of $\bar{e}_i$.

A vector $\overline{V}$ can now be expressed with physical base vector:

$$\overline{V}=V^{(i)}\overline{e_{(i)}} \tag{2.18}$$

In the above Eq.(2.18), $V^{(i)}$ bears the same dimension as a vector. The main advantage of using these bases are that the 'vectors' and 'tensors' are found to behave in a physically meaningful manner and hence the results are easy to interpret.

2.4.4 The Chosen Form

From the brief discussion presented in the previous sections, it appears that the strong conservation form with physical base vectors should be preferred. Also noteworthy is the fact that when using non-orthogonal curvilinear coordinate system, the strong conservation form is only viable if a fixed frame of reference is retained. The governing equations can be obtained in two ways:

i) Starting from the basic form (Eqs.2.1) and employing knowledge of tensor calculus (Aris,1962; Sokolnikoff,1964).

ii) Starting from the Cartesian form of equations (or Cylindrical-polar which is Cartesian-like) and employing the chain rule of differentiation.

For convenience, the second approach appears to be popular such as Shyy et al (1985), Nakayama (1985) etc. Recently, Karki and Patankar (1989) have shown that the discretised forms of governing equations may be conveniently obtained in the general coordinate system from the discretised forms of the equations in Cartesian coordinate. This is clearly analogous to the second approach, although from practical programming point of view, it has been shown to be more convenient.

For the present study, the more popular, the second, has been followed with the difference that instead of Cartesian, a Cylindrical-polar frame of reference has been chosen in order to handle pressure-velocity decoupling (this will be shown in the next chapter). This derivation is similar to that followed by Khalil and Weber (1984).

2.5 Derivation of Conservation Equations in General Coordinate System

Since the objective of the present investigation is to handle flow through complex geometry curved ducts, the transport equations were derived, following Khalil and Weber (1984), starting from the original form in Cylindrical-polar (r,θ,z) coordinate system. These equations are as follows:

Continuity

$$\frac{1}{r}\frac{\partial}{\partial r}(\rho r\, v) + \frac{1}{r}\frac{\partial}{\partial \theta}(\rho u) + \frac{\partial}{\partial z}(\rho w) = 0 \tag{2.19}$$

Scalar Quantity

$$\frac{1}{r}\frac{\partial}{\partial r}(\rho r\, v\, \psi) + \frac{1}{r}\frac{\partial}{\partial \theta}(\rho u\, \psi) + \frac{\partial}{\partial z}(\rho w\, \psi)$$
$$= \frac{1}{r}\frac{\partial}{\partial r}\{r\mu \frac{\partial \psi}{\partial r}\} + \frac{1}{r^2}\frac{\partial}{\partial \theta}\{\mu \frac{\partial \psi}{\partial \theta}\} + \frac{\partial}{\partial z}\{\mu \frac{\partial \psi}{\partial z}\} + S_\psi \tag{2.20}$$

Momentum Equations

v-momentum (r-direction):

$$\frac{1}{r}\frac{\partial}{\partial r}(\rho r\, v^2) + \frac{1}{r}\frac{\partial}{\partial \theta}(\rho u\, v) + \frac{\partial}{\partial z}(\rho w\, v) - \frac{1}{r}\rho u^2$$
$$= -\frac{\partial p}{\partial r} + \frac{2}{r}\frac{\partial}{\partial r}\{r\mu \frac{\partial v}{\partial r}\} + \frac{1}{r}\frac{\partial}{\partial \theta}\{\mu(\frac{1}{r}\frac{\partial v}{\partial \theta} + r\frac{\partial u/r}{\partial r})\}$$
$$+ \frac{\partial}{\partial z}\{\mu(\frac{\partial v}{\partial z} + \frac{\partial w}{\partial r})\} - \frac{2\mu}{r}\{\frac{1}{r}\frac{\partial u}{\partial \theta} + \frac{v}{r}\} \tag{2.21}$$

u-momentum (θ-direction):

$$\frac{1}{r}\frac{\partial}{\partial r}(\rho r\, v\, u) + \frac{1}{r}\frac{\partial}{\partial \theta}(\rho u^2) + \frac{\partial}{\partial z}(\rho\, w\, u) + \frac{1}{r}\rho v u$$
$$= -\frac{1}{r}\frac{\partial p}{\partial \theta} + \frac{1}{r}\frac{\partial}{\partial r}\{\, r\mu\, (\frac{1}{r}\frac{\partial v}{\partial \theta} + r\frac{\partial u/r}{\partial r})\} + \frac{2}{r}\frac{\partial}{\partial \theta}\{\mu(\frac{1}{r}\frac{\partial u}{\partial \theta} + \frac{v}{r})\}$$
$$+ \frac{\partial}{\partial z}\{\mu(\frac{\partial u}{\partial z} + \frac{1}{r}\frac{\partial w}{\partial \theta})\} + \frac{\mu}{r}\{\frac{1}{r}\frac{\partial v}{\partial \theta} + \frac{\partial u}{\partial r} - \frac{u}{r}\} \tag{2.22}$$

w-momentum (z-direction):

$$\frac{1}{r}\frac{\partial}{\partial r}(\rho r\, v\, w) + \frac{1}{r}\frac{\partial}{\partial \theta}(\rho u\, w) + \frac{\partial}{\partial z}(\rho\, w^2)$$
$$= -\frac{\partial p}{\partial z} + \frac{1}{r}\frac{\partial}{\partial r}\{r\mu(\frac{\partial v}{\partial z} + \frac{\partial w}{\partial r})\} + \frac{1}{r}\frac{\partial}{\partial \theta}\{\mu(\frac{\partial u}{\partial z} + \frac{1}{r}\frac{\partial w}{\partial \theta})\} + 2\frac{\partial}{\partial z}\{\mu \frac{\partial w}{\partial z}\} \tag{2.23}$$

All of the above Eqs. (2.19-2.23) can be expressed in a more compact form as given by the equation for the scalar variable (Eq.2.20):

$$\frac{1}{r}\frac{\partial}{\partial r}(\rho r v \psi)+\frac{1}{r}\frac{\partial}{\partial \theta}(\rho u \psi)+\frac{\partial}{\partial z}(\rho w \psi)$$
$$=\frac{1}{r}\frac{\partial}{\partial r}\{r\mu\frac{\partial \psi}{\partial r}\}+\frac{1}{r^2}\frac{\partial}{\partial \theta}\{\mu\frac{\partial \psi}{\partial \theta}\}+\frac{\partial}{\partial z}\{\mu\frac{\partial \psi}{\partial z}\}+S_\psi \qquad (2.20)$$

In the above equation, ψ represents a general variable and S_ψ are the corresponding source terms (the extra terms in momentum Eqs.2.21-2.23). If $\psi=1$, the continuity Eq.2.19 will result.

By taking the limit $r\to\infty$ and $rd\theta=dz$ in Eqs.2.19-2.23 one can obtain the equations of motion with reference to the Cartesian base vectors. It can be seen that only few terms of the momentum equations are outside the differential operator and hence strictly speaking, this is not a strong conservation form. It should be mentioned that since the base vectors are not spatially invariant, it is not possible to bring all the terms of the governing equations under the differential operator. However, all such terms disappear if the Cartesian counterparts are obtained as above.

If new independent variables η,ζ,ξ are introduced, the form of conservation law (Eq.2.20) can be changed according to the following general transformation[1]:

$$\begin{aligned}\eta&=\eta(r,\theta,z)\\ \zeta&=\zeta(r,\theta,z)\\ \xi&=\xi(r,\theta,z)\end{aligned} \qquad (2.24)$$

By using the chain-rule of differentiation, the following relations between the operators in two systems can be obtained:

$$\begin{aligned}\frac{\partial}{\partial r}&=\frac{1}{J}[B_{11}\frac{\partial}{\partial \eta}+B_{21}\frac{\partial}{\partial \zeta}+B_{31}\frac{\partial}{\partial \xi}]\\ \frac{\partial}{\partial \theta}&=\frac{1}{J}[B_{12}\frac{\partial}{\partial \eta}+B_{22}\frac{\partial}{\partial \zeta}+B_{32}\frac{\partial}{\partial \xi}]\\ \frac{\partial}{\partial z}&=\frac{1}{J}[B_{13}\frac{\partial}{\partial \eta}+B_{23}\frac{\partial}{\partial \zeta}+B_{33}\frac{\partial}{\partial \xi}]\end{aligned} \qquad (2.25)$$

---

[1] Usually, for the duct type of flows presented in this thesis, ζ is taken to be the streamwise coordinate and η and ξ are the coordinates over the cross-section.

where, 'J' is the Jacobian of transformation. The above transformation between the two coordinates is only possible if the determinant of the Jacobian is non-zero. 'J' is given by:

$$J = \begin{vmatrix} r_\eta & \theta_\eta & z_\eta \\ r_\zeta & \theta_\zeta & z_\zeta \\ r_\xi & \theta_\xi & z_\xi \end{vmatrix} \tag{2.26}$$

The metric components B_{ij}, appearing in Eq.(2.25) are given by:

$$\begin{array}{lll} B_{11} = \theta_\zeta z_\xi - \theta_\xi z_\zeta & B_{21} = \theta_\xi z_\eta - \theta_\eta z_\xi & B_{31} = \theta_\eta z_\zeta - \theta_\zeta z_\eta \\ B_{12} = z_\zeta r_\xi - z_\xi r_\zeta & B_{22} = z_\xi r_\eta - z_\eta r_\xi & B_{32} = z_\eta r_\zeta - z_\zeta r_\eta \\ B_{13} = r_\zeta \theta_\xi - r_\xi \theta_\zeta & B_{23} = r_\xi \theta_\eta - r_\eta \theta_\xi & B_{33} = r_\eta \theta_\zeta - r_\zeta \theta_\eta \end{array} \tag{2.27}$$

Using the above transformation relation, the conservation equations of mass, momentum and scalar variable (Eqs.2.19-2.23) assume the following forms:

Continuity

$$\frac{\partial}{\partial \eta}(\rho V) + \frac{\partial}{\partial \zeta}(\rho U) + \frac{\partial}{\partial \xi}(\rho W) = 0 \tag{2.28}$$

Scalar Quantity

$$\frac{\partial}{\partial \eta}(\rho V \psi) + \frac{\partial}{\partial \zeta}(\rho U \psi) + \frac{\partial}{\partial \xi}(\rho W \psi) = \frac{\partial}{\partial \eta}\left[\frac{\mu}{rJ}(\beta_{11}\psi_\eta + \beta_{12}\psi_\zeta + \beta_{13}\psi_\xi)\right]$$

$$+ \frac{\partial}{\partial \zeta}\left[\frac{\mu}{rJ}(\beta_{21}\psi_\eta + \beta_{22}\psi_\zeta + \beta_{23}\psi_\xi)\right] + \frac{\partial}{\partial \xi}\left[\frac{\mu}{rJ}(\beta_{31}\psi_\eta + \beta_{32}\psi_\zeta + \beta_{33}\psi_\xi)\right] + rJ\, S_\psi \tag{2.29}$$

Momentum Equations

v-momentum (r-direction)

$$
\begin{aligned}
&\frac{\partial}{\partial\eta}(\rho Vv)+\frac{\partial}{\partial\zeta}(\rho Uv)+\frac{\partial}{\partial\xi}(\rho Wv)\\
&=\frac{\partial}{\partial\eta}[\frac{\mu}{rJ}\{\beta_{11}\frac{\partial v}{\partial\eta}+\beta_{12}\frac{\partial v}{\partial\zeta}+\beta_{13}\frac{\partial v}{\partial\xi}+rB_{11}\gamma_{11}+B_{12}\gamma_{21}+rB_{13}\gamma_{31}\}-rB_{11}p]\\
&+\frac{\partial}{\partial\zeta}[\frac{\mu}{rJ}\{\beta_{21}\frac{\partial v}{\partial\eta}+\beta_{22}\frac{\partial v}{\partial\zeta}+\beta_{23}\frac{\partial v}{\partial\xi}+rB_{21}\gamma_{11}+B_{22}\gamma_{21}+rB_{23}\gamma_{31}\}-rB_{21}p]\\
&+\frac{\partial}{\partial\xi}[\frac{\mu}{rJ}\{\beta_{31}\frac{\partial v}{\partial\eta}+\beta_{32}\frac{\partial v}{\partial\zeta}+\beta_{33}\frac{\partial v}{\partial\xi}+rB_{31}\gamma_{11}+B_{32}\gamma_{21}+rB_{33}\gamma_{31}\}-rB_{31}p]\\
&+[\rho u^2-\frac{2\mu}{r}\{\frac{1}{J}(B_{12}\frac{\partial u}{\partial\eta}+B_{22}\frac{\partial u}{\partial\zeta}+B_{32}\frac{\partial u}{\partial\xi})+v].J \qquad (2.30)
\end{aligned}
$$

u-momentum (θ-direction)

$$
\begin{aligned}
&\frac{\partial}{\partial\eta}(\rho Vu)+\frac{\partial}{\partial\zeta}(\rho Uu)+\frac{\partial}{\partial\xi}(\rho Wu)\\
&=\frac{\partial}{\partial\eta}[\frac{\mu}{rJ}\{\beta_{11}\frac{\partial u}{\partial\eta}+\beta_{12}\frac{\partial u}{\partial\zeta}+\beta_{13}\frac{\partial u}{\partial\xi}+rB_{11}\gamma_{12}+B_{12}\gamma_{22}+rB_{13}\gamma_{32}+2Jv\}-B_{12}p]\\
&+\frac{\partial}{\partial\zeta}[\frac{\mu}{rJ}\{\beta_{21}\frac{\partial u}{\partial\eta}+\beta_{22}\frac{\partial u}{\partial\zeta}+\beta_{23}\frac{\partial u}{\partial\xi}+rB_{21}\gamma_{12}+B_{22}\gamma_{22}+rB_{23}\gamma_{32}+2Jv]-B_{22}p]\\
&+\frac{\partial}{\partial\xi}[\frac{\mu}{rJ}\{\beta_{31}\frac{\partial u}{\partial\eta}+\beta_{32}\frac{\partial u}{\partial\zeta}+\beta_{33}\frac{\partial u}{\partial\xi}+rB_{31}\gamma_{12}+B_{32}\gamma_{22}+rB_{33}\gamma_{32}+2Jv\}-B_{32}p]\\
&+[-\rho vu+\frac{\mu}{r}\{\frac{1}{J}(B_{12}\frac{\partial v}{\partial\eta}+B_{22}\frac{\partial v}{\partial\zeta}+B_{32}\frac{\partial v}{\partial\xi})-u].J \qquad (2.31)
\end{aligned}
$$

w-momentum equation (z-direction)

$$
\begin{aligned}
&\frac{\partial}{\partial\eta}(\rho Vw)+\frac{\partial}{\partial\zeta}(\rho Uw)+\frac{\partial}{\partial\xi}(\rho Ww)\\
&=\frac{\partial}{\partial\eta}[\frac{\mu}{rJ}\{\beta_{11}\frac{\partial w}{\partial\eta}+\beta_{12}\frac{\partial w}{\partial\zeta}+\beta_{13}\frac{\partial w}{\partial\xi}+rB_{11}\gamma_{13}+B_{12}\gamma_{23}+rB_{13}\gamma_{33}\}-rB_{13}p]\\
&+\frac{\partial}{\partial\zeta}[\frac{\mu}{rJ}\{\beta_{21}\frac{\partial w}{\partial\eta}+\beta_{22}\frac{\partial w}{\partial\zeta}+\beta_{23}\frac{\partial w}{\partial\xi}+rB_{21}\gamma_{13}+B_{22}\gamma_{23}+rB_{23}\gamma_{33}\}-rB_{23}p]\\
&+\frac{\partial}{\partial\xi}[\frac{\mu}{rJ}\{\beta_{31}\frac{\partial w}{\partial\eta}+\beta_{32}\frac{\partial w}{\partial\zeta}+\beta_{33}\frac{\partial w}{\partial\xi}+rB_{31}\gamma_{13}+B_{32}\gamma_{23}+rB_{33}\gamma_{33}\}-rB_{33}p] \quad (2.32)
\end{aligned}
$$

In the above expressions (Eqs.2.30-2.32) the γ 's are defined as:

$$\gamma_{kj}=\frac{\partial V^k}{\partial \eta^m} B_{mj}\,(r)^{1-\delta_{2j}} \tag{2.33}$$

Here, the exponent δ_{2j} is the Kronecker's delta which is one when j=2 and zero for j≠2. When expanded for one term in the v-momentum Eq.(2.30):

$$\gamma_{11}=\frac{\partial v}{\partial \eta} r\, B_{11}+\frac{\partial v}{\partial \zeta} r\, B_{21}+\frac{\partial v}{\partial \xi} r\, B_{31} \tag{2.34}$$

Similar expressions will follow for other γ terms from Eq.(2.33). The other new variables appearing in Eqs.(2.28-2.32) are defined as follows:

$$V= r\, B_{11}v + B_{12}u + r\, B_{13}w$$

$$U= r\, B_{21}v + B_{22}u + r\, B_{23}w$$

$$W= r\, B_{31}v + B_{32}u + r\, B_{33}w \tag{2.35}$$

U,V,W represent the contravariant variables scaled by the Jacobian (The physical significance of these quantities will be given in the next chapter).

β_{ij} (Eq.2.29-2.32) represent other metric components defined as:

$$\beta_{11}= r^2 B_{11}^2 + B_{12}^2 + r^2 B_{13}^2$$

$$\beta_{22}= r^2 B_{21}^2 + B_{22}^2 + r^2 B_{23}^2$$

$$\beta_{33}= r^2 B_{31}^2 + B_{32}^2 + r^2 B_{33}^2$$

$$\beta_{12}= \beta_{21}= r^2 B_{11}B_{21}+ B_{12}B_{22}+ r^2 B_{13}B_{23}$$

$$\beta_{23}= \beta_{32}= r^2 B_{21}B_{31}+ B_{22}B_{32}+ r^2 B_{23}B_{33}$$

$$\beta_{31}= \beta_{13}= r^2 B_{31}B_{11}+ B_{32}B_{12}+ r^2 B_{33}B_{13} \tag{2.36}$$

As can be seen from above, the momentum Eqs.(2.30-2.32) are much more complex than the scalar Eq.(2.29) because of the expansion of the stress term in the general coordinates. However, apart from a few terms featuring in the v- and u-momentum Eqs.(2.30 and 2.31), all of them are in the desired strong conservation form and hence, are easy to discretise. If the basic equations were written in the Cartesian frame of reference, all such terms would disappear.

A further important aspect of the momentum equations is that each of them (Eqs.2.30-2.32) contains three pressure derivatives, as against only one pressure derivative for the Cylindrical-polar frame (Eqs.2.21-2.23). This, however, does not appear to be problematic for the present solution technique as will be shown in the next chapter.

The set of Eqs.(2.28-2.32) presented above are the final forms which can be discretised and cast into a set of algebraic equations suitable for numerical solution. Similar to Eq.2.20 in cylindrical-polar coordinate, the transformed Eqs.(2.28-2.32) can be conveniently expressed by a general equation which is same as Eq.(2.29).

2.6 Turbulence Closure Model

The conservation Eqs.(2.28-2.32) when taken together with the appropriate boundary and initial conditions, form a closed set; the solution of which would in principle provide a complete description of any flow. In real engineering problems however, the flows are usually turbulent. In these situations, fluctuations of flow variables are always present. Further, with different Reynolds number, there are various ranges of 'eddy-size' and frequencies present in the flow (Tennekes and Lumley, 1972). Therefore, unless special steps are taken, the full three-dimensional time-dependent form of equations are to be solved numerically by employing a very fine mesh with grid-spacing smaller than the characteristic length of the smallest turbulent eddies and time-step small enough to resolve the fastest frequency. This is not currently a practical approach because of the enormous computer resources needed for such a solution for the high Reynolds numbers of practical interest.

In order to make the turbulent flow problem tractable, the conventional approach is to obtain equations for 'average' quantities (e.g., time-averaging, see Schlichting, 1979). The time-averaging process consists of expressing each variable through its mean value

ψ and fluctuating component ψ', thus :

$$\psi=\psi+\psi' \qquad (2.37)$$

Now, if the dependent variable ψ of Eq.(2.29) is decomposed into mean and fluctuating components by using Eq.(2.37) (neglecting the fluctuations of viscosity and density of fluid for non-reacting, incompressible flow), and the equations ensemble averaged, then unknown correlations between the fluctuating components appear for the momentum and scalar equations. These extra terms are traditionally called the 'Reynolds stresses' (Schlichting, 1979). Additional equations for these stresses may be derived by manipulation of the Navier-Stokes equations but further unknowns are then introduced. This procedure may be repeated for the new correlations, but the number of unknowns increases at a greater rate than the number of equations and so rigorous closure is just not possible. At some stage it is necessary to curtail derivation of further equations and to approximate the unknown correlations in terms of known quantities. Such approximations are individually termed as 'closure approximations' and when taken collectively to form a closed set of equations constitute a 'turbulence model'.

A wide range of 'turbulence models' have been proposed in literature (e.g., Gibson et al, 1988; Launder and Spalding, 1974 etc.). These vary both in complexity and in the physical realism which they embody. Also, some models have been subjected to far greater use and subsequently compared with experiments than others. For this study, the most widely used 'k-ε' model of turbulence (Jones and Launder, 1972) has been used.

Without going into further details (these may be found in several references, such as Jones and Launder,1972; Launder and Spalding,1974 etc.), this model uses a gradient diffusion approximation for the Reynolds stresses i.e., involves a linear stress vs. strain rate relationship analogous to that of a Newtonian fluid, with the molecular viscosity replaced by a turbulent viscosity. The eddy viscosity is calculated by solving two more conservation equations; one for the 'kinetic energy of turbulence, k and the other for its dissipation rate ε. These two quantities are defined as :

$$k=\frac{1}{2}\overline{V_i' V_i'}$$

$$\varepsilon=\frac{\mu}{\rho}\overline{[\frac{\partial V_i'}{\partial \eta^n}\alpha_j^n][\frac{\partial V_i'}{\partial \eta^n}\alpha_j^n]} \qquad (2.38)$$

where $\alpha^n{}_j$ is given by Eq.(2.15).

The differential equations for k and ε are exactly of the same form as that of the scalar Eq.(2.29) with the following differences.

i) The dynamic viscosity μ should be replaced by μ_{eff} (for all of the conservation equations), which is defined as :

$$\mu_{eff} = \mu + \mu_t \tag{2.39}$$

where,

$$\mu_t = C_\mu \rho k^2/\varepsilon \tag{2.40}$$

ii) In the equations for k and ε, the turbulent transport coefficient μ_{eff} should be replaced by μ_{eff}/σ_k and $\mu_{eff}/\sigma_\varepsilon$ respectively.

iii) The new source terms are to be calculated as :

$$S_k = G - \rho\varepsilon \tag{2.41}$$

$$S_\varepsilon = C_1 \frac{\varepsilon}{k} G - C_2 \rho \frac{\varepsilon^2}{k} \tag{2.42}$$

where 'G' represents the rate of production of turbulent kinetic energy.

In the above expressions (Eqs.2.40-2.42), C_μ , C_1, C_2, σ_k and σ_ε represent empirical constants and the set of values were taken from Launder and Spalding (1974) (C_μ=0.09; C_1=1.44; C_2=1.92; σ_k=1.0 and σ_ε=1.3).

The rate of production term 'G' in Cylindrical polar coordinates is given by:

$$\begin{aligned} G = \mu_{eff} [\, & 2\{ (\frac{\partial v}{\partial r})^2 + (\frac{\partial w}{\partial z})^2 + (\frac{\partial u}{r\partial\theta} + \frac{v}{r})^2 \} + \{ \frac{\partial w}{\partial r} + \frac{\partial z}{\partial z} \}^2 \\ & + \{ \frac{\partial v}{r\partial\theta} + r \frac{\partial}{\partial r}(\frac{u}{r}) \}^2 + \{ \frac{\partial w}{r\partial\theta} + \frac{\partial u}{\partial z} \}^2] \end{aligned} \tag{2.43}$$

By applying the transformation relation among the operators (Eq.2.25), the generation term assumes the following form in the general coordinate system:

$$
\begin{aligned}
G=\frac{\mu_{eff}}{r\,J}[\,2\{\, r\,B_{11}\frac{\partial v}{\partial \eta}+r\,B_{21}\frac{\partial v}{\partial \zeta}+r\,B_{31}\frac{\partial v}{\partial \xi}\,\}^2+&\\
+2\{\; B_{12}\frac{\partial u}{\partial \eta}+\; B_{22}\frac{\partial u}{\partial \zeta}+\; B_{32}\frac{\partial u}{\partial \xi}+J\,v\}^2+&\\
+2\{\, r\,B_{13}\frac{\partial w}{\partial \eta}+r\,B_{23}\frac{\partial w}{\partial \zeta}+r\,B_{33}\frac{\partial w}{\partial \xi}\,\}^2+&\\
+\{\, r\,B_{11}\frac{\partial w}{\partial \eta}+r\,B_{21}\frac{\partial w}{\partial \zeta}+r\,B_{31}\frac{\partial w}{\partial \xi}+r\,B_{13}\frac{\partial v}{\partial \eta}+r\,B_{23}\frac{\partial v}{\partial \zeta}+r\,B_{33}\frac{\partial v}{\partial \xi}\,\}^2+&\\
+\{\, B_{12}\frac{\partial v}{\partial \eta}+B_{22}\frac{\partial v}{\partial \zeta}+B_{32}\frac{\partial v}{\partial \xi}+r\,B_{11}\frac{\partial u}{\partial \eta}+r\,B_{21}\frac{\partial u}{\partial \zeta}+r\,B_{31}\frac{\partial u}{\partial \xi}-J\,u\,\}^2+&\\
+\{\, r\,B_{13}\frac{\partial u}{\partial \eta}+r\,B_{23}\frac{\partial u}{\partial \zeta}+r\,B_{33}\frac{\partial u}{\partial \xi}+B_{12}\frac{\partial w}{\partial \eta}+B_{22}\frac{\partial w}{\partial \zeta}+B_{32}\frac{\partial w}{\partial \xi}\,\}^2 &\qquad (2.44)
\end{aligned}
$$

Hence, for the prediction of turbulent flows the equations to be solved are continuity (Eq.2.28), momentum (Eqs.2.30-2.32) and kinetic energy and dissipation rate (Eq.2.29 with respective source terms S_k and S_ε given by Eqs.2.41 and 2.42 respectively). For laminar flow predictions, only the continuity (Eq.2.28) and momentum (Eqs.2.30-2.32) equations are to be solved.

2.7 Closing Remarks

In this chapter, the mathematical basis for the present investigation is described. Different possible forms of governing transport equations in the chosen body-fitted coordinate system are briefly discussed. Conservation equations for mass, momentum and scalar variables are presented in a form suitable for discretisation.

The most widely used 'k-ε' model of turbulence has been adopted for handling the high Reynolds number flows. The equations for k and ε have the same form as that of a scalar variable with new source terms. The diffusion coefficients featuring in the conservation equations are modified according to the standard practice. The empirical constants which appear in the k and ε equations were taken to be those proposed by Launder and Spalding (1974).

In order to solve the exact transport equations presented in this chapter by a numerical technique, they are to be cast in an algebraic form through discretisation. The other incidental topics include the boundary conditions, solution algorithm, grid generation procedure etc., which will be described in the next chapter.

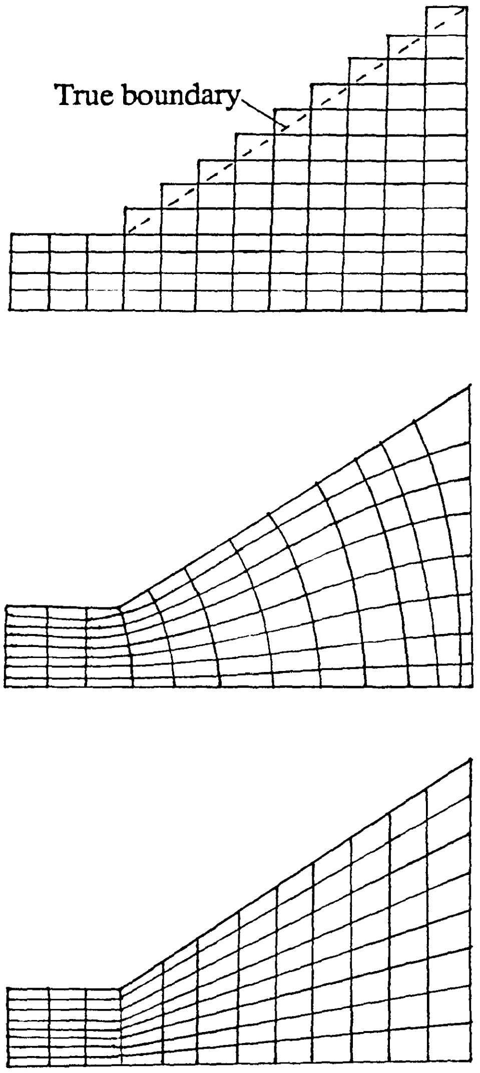

(a) Cartesian

(b) Curvilinear orthogonal

(c) Curvilinear non-orthogonal

Fig. 2.1 Description of volute geometry by different types of coordinates.

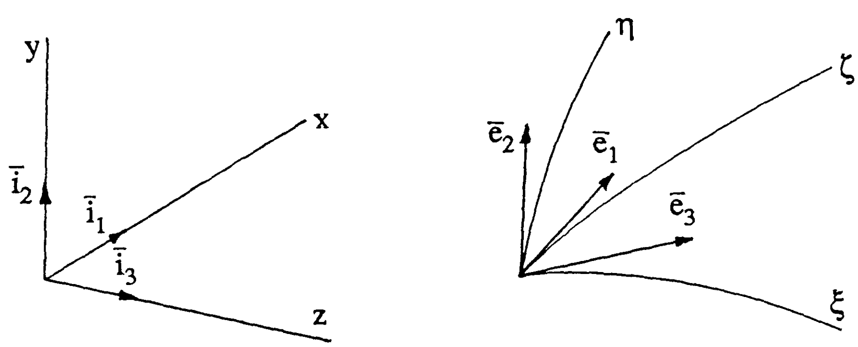

(a) Cartesian, x^i ($x^1=x$, $x^2=y$, $x^3=z$)

(b) General, η^i ($\eta^1=\zeta$, $\eta^2=\eta$, $\eta^3=\xi$)

Fig. 2.2 Cartesian (x^i) and general (η^i) coordinate systems and tangent vectors.

CHAPTER 3

METHODOLOGY OF NUMERICAL SOLUTION

3.1 Introduction

In order to obtain a numerical solution for any fluid flow situation, the governing equations presented in the previous chapter are to be transformed into corresponding discrete forms. In the finite volume method, the domain is first overlaid with grid nodes; as a result of which the whole domain is divided into a number of 'computational cells' surrounding each node. For each cell, the transport equations are integrated and all of these equations are cast into algebraic forms which are solved using linear algebraic relations and iterative processes. As the size of the cell volume becomes vanishingly small, the discrete transport equations should regain their 'exact' nature.

Firstly in section 2 of this chapter, the various possible types of computational cells and the corresponding location of flow variables (such as u, v, w, p etc.) are briefly discussed and the present choice is outlined.

Section 3 discusses the calculation technique and interpretation of metric derivatives arising out of the general transformation (Eq.2.24) described in the previous chapter. The physical meaning of the contravariant variables (Eq.2.35) are shown by constructing a simple two-dimensional flow configuration.

The discretisation procedure for all other quantinties are briefly discussed in section 4. The final form of the algebraic equations resulting from such discretisations are also given.

The SIMPLE (Semi-Implicit Pressure Linked Equations) algorithm (Patankar,1980) adopted for the present study requires pressure to be calculated in an indirect way. This needs the derivation of an equation called the pressure-correction equation, which is described in section 5. The material presented in sections 3, 4 and 5 follows similar lines to that described by Shyy et al (1985).

The interpolation practice for the present study and the common boundary conditions along with their implementation techniques are described in section 6.

Next, in section 7 the other details regarding the solution technique is outlined and a brief summary of the algorithm is presented.

The grid generation technique along with the desired properties of grid lines are discussed in section 8. Finally, closing remarks are given in section 9.

3.2 The Computational Cell and Location of Variables

The choice of computational cell and the relative locations of flow variables for a regular coordinate system are fairly well established (Patankar, 1980), but for a general system, it needs special attention. In this section, the type of computational cell employed for the current study is briefly described.

3.2.1 Types of Computational Cell

With respect to the location of flow variables, there are basically two types of computational cells, viz.,

i) the non-staggered arrangement, where all the variables are located at the centre of the cell or at the node, and
ii) the staggered arrangement, where the scalar variables are usually stored at the grid node or cell-centre and the velocities are stored at the cell faces of the scalar control volumes.

An illustration of the two types are shown in Fig.3.1 for a simple rectangular two-dimensional cell structure.

For the non-staggered arrangement, the grids are first generated by a suitable technique and variable locations are fixed by calculating the centre (P, for example, in Fig.3.1a) of the cell. One of the biggest advantages of this arrangement is that only one control volume is needed for all the variables (velocity components, scalars etc.), which makes the programming significantly simpler. The boundary cells can also be kept uniform at the cost of an 'extra' quashed (zero-thickness) or overlapping cell (Peric, 1985). However, since pressure is calculated from a coarser grid ('alternate' rather than 'adjacent') than the one actually employed, there is, apart from diminished accuracy, a chance of zig-zag pressure field (Patankar, 1980), commonly termed as the 'pressure-velocity decoupling'. In order to obtain a meaningful and smooth pressure, some sort of post-processing is usually necessary (Sani et al, 1981).

On the other hand, the second arrangement does not suffer from a possibility of producing a 'checker-board' pressure field (because the velocities which are stored at the cell faces are always driven by pressures on adjacent nodes). From accuracy point of view, this arrangement of variables offers second order accuracy in terms of Taylor

Series Truncation Error (Roache, 1976) even if the grid is non-uniform. However, for every velocity component, there will be a different control volume and in the case of three-dimensional situation, a minimum of four (u, v, w and pressure) control volumes are involved. Hence, the programming is much more elaborate. Another small disadvantage is that the cells near the boundaries become irregular (either half or one-and-a-half) which requires special treatment. But, due to the above mentioned advantages, the number of works employing staggered arrangement of flow variables appears to be much more in comparison to the former. Few other (less popular) variable arrangements have also been reported in the literature as can be found in Manners (1988).

The above comments were made with reference to a regular Cartesian mesh. For curvilinear systems, if one uses grid oriented velocity vectors (§2.4), all the advantages of the staggered arrangement are equally valid and this is therefore commonly employed (Humphrey et al, 1985; Manners, 1988; Demirdzic, 1982). However, when a non-orthogonal curvilinear grid is employed in conjunction with fixed base vectors (§2.4), there is still a possibility of having a checker-board pressure field (in other words, the velocities not being driven by pressures at adjacent nodes). Hence, the chance of reaching a zig-zag pressure field must be eliminated for non-orthogonal curvilinear grid and fixed base vector situation. Different remedies have been proposed in literature as described by Sani et al (1981). The other alternative is to move back to the non-staggered arrangement (Rhie, 1985) and employ some sort of pressure post-processing. This problem is discussed in the next section.

3.2.2 Pressure-Velocity Decoupling

Fig. 3.2 shows a two dimensional turning flow through a 90-degree bend. The frame of reference for the velocity vectors is shown to be Cartesian in Fig.3.2a. It can be observed that when the grid lines turn through 90^0 as at position (ii), the velocities are no longer driven by the pressures stored at the main grid nodes, but rather by the interpolated values at the corners of the control volume. Since the corner pressures are the averages of pressures at adjacent grid nodes (six for three-dimension), any checker-board pressure field that gives constant values for the corner pressures will be felt as a uniform pressure field by the momentum equations.

One of the methods of extracting a physically meaningful pressure field, as done by Braaten and Shyy (1986), is to post-process the computed pressure field by a suitable averaging. For example, the pressure at node P can be smoothed as :

$$p_P=0.25(p_N+p_S+p_E+p_W) \tag{3.1}$$

for a uniform mesh as shown in Fig.3.2a. The averaging can be done in several ways as described by Sani et al (1981). For the case of grid lines aligned with vector direction, this post-processing means an additional smoothing and may degrade the accuracy.

In the present formulation, a different approach has been followed. If, as shown in Fig.3.2b, a Cylindrical-polar reference is used, the velocities are always driven by pressure, and as such, no situation involving the pressure-velocity decoupling can arise. It is clear that this procedure is restricted to the present problem of strongly curved ducts, nevertheless it does allow the staggered approach with all its inherent advantages to be retained.

3.2.3 The Chosen Cell

From what has been discussed above, the staggered arrangement of flow variables was chosen for the present study. First, the flow domain was laid out by grid nodes by following a suitable grid generation technique (to be described in §3.8). The pressure and other scalar variables were stored at the grid nodes and the velocity components (u, v, w) and contravariant variables (U, V, W) were stored halfway between the grid nodes along the corresponding coordinate lines (for example, u and U were stored along the ζ and x-coordinate lines). For the calculation of curved ducts, a cylindrical-polar frame of reference has been used. However, the Cartesian references could also be used along with the special techniques for pressure-velocity coupling as mentioned in the previous section.

3.3 Calculation and Interpretation of Metric Derivatives and Contravariant Variables

A direct result of the transformation employed for the derivation of governing transport equations in general coordinate system is the appearance of 'nine' metric derivatives (shown in the expression for the Jacobian in Eq.2.26) relating the two coordinates (r,θ,z and η,ζ,ξ). The method of calculation of these quantities is vital for a successful solution of any fluid flow. In order to illustrate the calculation technique employed for the present study, for the sake of simplicity but without loss of generality, the two-dimensional configuration as shown in Fig.3.3a is considered.

One of the metrics r_η is considered for illustration. This is calculated by taking the quotient as follows:

$$r_{\eta,P}=(r_N - r_S)/(\eta_N - \eta_S) \qquad (3.2)$$

All such values are calculated in the same way at each of the grid nodes and stored for later use. On the boundaries, (the North-boundary-node NB in Fig.3.3a), it is calculated from adjacent internal nodes. That is :

$$r_{\eta,NB}=(r_{NB} - r_{PB})/(\eta_{NB} - \eta_{PB}) \qquad (3.3)$$

The coordinates of r represent the actual physical dimension given with respect to the Cylindrical-polar (or Cartesian) frame of reference, while the coordinates in the computational plane (η-direction, for example) are just arbitrary numbers in an order. (The actual values of the computational coordinate are immaterial, and in the transformed space (η,ζ,ξ) all these spacings such as ($\eta_{NB} - \eta_{PB}$) can be taken as unity. These matters have been discussed in details by other authors such as Peric, 1985; Shyy et al, 1985; Rhie, 1985).

A slightly more accurate way of evaluating the metric components would be to calculate the values at the mid-point between the grid nodes. For example, with reference to Fig.3.3a, at location n, the metric derivative can be calculated as:

$$r_{\eta,n}=(r_N - r_P)/(\eta_N - \eta_P) \qquad (3.4)$$

However, as the size of the control volume tends to vanishingly small, both of these techniques will recover the governing differential equations and become equally correct (Shyy et al, 1985).

Once the metric derivatives are calculated and stored, all other quantities relating the two spaces such as J, B_{ij}, β_{ij} (given by Eqs.2.26, 2.27 and 2.36 respectively) etc., can be calculated whenever required. In fact, it is convenient to calculate the Jacobian once and store it because it features in several places of the programme.

The next important quantitities to be calculated are the contravariant variables U, V, W (defined by Eq.2.35). The calculation technique can be shown with reference to Fig.3.3b. In the physical plane, the velocity components v are located at points 'n' and 's', while the components w are stored at 'w' (west) and 'e'. Their counterparts in the computational plane, V and W are stored at corresponding positions in Fig.3.3b. The expression for the contravariant velocity V and W for the two-dimensional configuration (in the r-z plane) can be obtained from the general expression (Eqn.2.35) by making use of the following assumptions :

$r\theta_\zeta=1$

No variation along ζ and θ coordinate. (3.5)

The expressions for V and W then become:

$$V=vz_\xi-wr_\xi$$
$$W=wr_\eta-vz_\eta \qquad (3.6)$$

If v_n represent the 'v' velocity component at location 'n' and using the same notation, the mass fluxes across the cell-face 1-2 are :

Physical plane: $\rho v_n(z_1- z_2) - \rho w_n(r_1-r_2)$
Computational plane: $\rho V_n(\xi_1- \xi_2)$

Equating the two fluxes one gets :

$$V_n=v_n(z_1- z_2) /(\xi_1- \xi_2) - w_n (r_1-r_2) /(\xi_1- \xi_2)$$

$$\text{i.e., } V\approx v\, z_\xi- w\, r_\xi \qquad (3.7)$$

Hence, ρV represents the mass flux across the face 1-2 in the computational plane. A similar relation for W can be obtained following the above procedure.

Hence, the metric derivatives can be interpreted as the projected lengths of the computational cell surface in the physical space, otherwise the conservation laws will not be maintained. Since the fluxes determined by the contravariant variables ρV, ρU and ρW in the computational space are normal to the surfaces given by η, ζ and ξ respectively, it is clear that the computational space can be imagined to be a rectangular parallelopiped bounded by the coordinate lines.

A three-dimensional extension to the above interpretation is straightforward and easily understandable. The only difference is that instead of length (for two-dimension) a surface-area is involved and instead of surface area (for two-dimension), a volume is to be considered.

3.4 Discretisation Procedure

The finite volume method which is used in the present formulation requires the conservation equations of mass, momentum and scalar variables to be integrated over a finite number of control volumes. The interpretation of the metric derivatives and the so-called contravariant variables presented in the previous section suggests that all the integrations can be performed in the computational space. Since a staggered grid system has been chosen for all the velocity components, a separate control volume is to be considered (see Fig.3.4), for the integration of each of the conservation equations. However, the method of integration is exactly the same for all of them. Here, the discretisation procedure for a scalar variable ψ whose control volume is the same as that of pressure (around node P in Fig.3.4) is briefly described. More details can be found in several other references (Peric, 1985; Patankar,1980; Roache,1976 etc.).

The elementary volume of a pressure cell (Fig.3.4b) is equal to $\Delta\eta\Delta\zeta\Delta\xi$. Each term of the conservation equation is integrated over this cell. By making use of Gauss' theorem, the volume integral is split into surface integrals (six for three-dimensions). The convection parts of Eq.(2.29) are integrated as:

$$\frac{1}{\Delta\eta\Delta\zeta\Delta\xi}\int_{l}^{r}\int_{w}^{e}\int_{s}^{n}\frac{\partial}{\partial\eta}(\rho V\psi)\,d\eta d\zeta d\xi \approx G_{\eta}^{+}(\psi_N+\psi_P)-G_{\eta}^{-}(\psi_P+\psi_S) \qquad (3.8)$$

where,

$$G_{\eta}^{+}=\frac{(\rho_N+\rho_P)V_n}{4\Delta\eta_P} \qquad G_{\eta}^{-}=\frac{(\rho_P+\rho_S)V_s}{4\Delta\eta_P} \qquad (3.9)$$

To obtain the above formula, a linear interpolation (central-differencing) has been used to calculate unknown values of the dependent variables on the cell faces; section 3.6 returns to this point later.

Similarly the other terms of the convection part of the equation can be integrated. Thus the continuity Eq.(2.28) which contains only convection terms can be discretised as :

$$2[(G_{\eta}^{+}-G_{\eta}^{-})+(G_{\zeta}^{+}-G_{\zeta}^{-})+(G_{\xi}^{+}-G_{\xi}^{-})]=0 \qquad (3.10)$$

The right hand side of the other conservation equations contain diffusion-like terms as well as other source terms. All of the second derivative terms on the right hand side of the conservation Eq.(2.29) have the coefficients β_{ij}. The diffusion terms for which i=j are grouped as 'normal diffusion' terms whereas the others for which i≠j are termed as 'cross-diffusion' terms. In an orthogonal coordinate system these cross-diffusion terms are absent. The normal diffusion terms are integrated over the control volume as :

$$\frac{1}{\Delta\eta\Delta\zeta\Delta\xi}\int_{w}^{e}\int_{l}^{r}\int_{s}^{n}\frac{\partial}{\partial\eta}[\frac{\mu}{rJ}(\beta_{11}\frac{\partial\psi}{\partial\eta})]d\eta d\zeta d\xi \cong H_{\eta}^{+}(\psi_N-\psi_P)-H_{\eta}^{-}(\psi_P-\psi_S) \qquad (3.11)$$

where,

$$H^{+}_{\eta}=\frac{\beta_{11n}(\mu_N+\mu_P)}{2(rJ)_n\Delta\eta_P(\eta_N-\eta_P)} \qquad H^{-}_{\eta}=\frac{\beta_{11s}(\mu_P+\mu_S)}{2(rJ)_s\Delta\eta_P(\eta_P-\eta_S)} \tag{3.12}$$

$$\beta_{11n}=\frac{1}{2}(\beta_{11N}+\beta_{11P}) \qquad \beta_{11s}=\frac{1}{2}(\beta_{11P}+\beta_{11S}) \tag{3.13}$$

Again, linear interpolation has been used. The two other normal diffusion terms can be similarly discretised. The cross diffusion terms are treated explicitly as source terms and are evaluated at the grid node. The integration of these terms (together with any 'real' source for ψ, S^{Ψ}) are obtained as follows:

$$\frac{1}{\Delta\eta\Delta\zeta\Delta\xi}\int_{w}^{e}\int_{l}^{r}\int_{s}^{n} S^{\Psi}\,d\eta d\zeta d\xi \cong S_{\psi P}=S'_{\psi P}+S''_{\psi P}\psi_P \tag{3.14}$$

where, the same linearisation practice as recommended by Patankar (1980) has been adopted.

Following the procedure outlined above and collecting all the terms obtained therefrom (Eqs. 3.8,3.11 and 3.14), and by making some use of the discretised form of the continuity Eq. (3.10), one can obtain an algebraic equation which is an approximation of the nonlinear partial differential Eq. (2.29). The final form of the algebraic equation can be written as:

$$a_P\psi_P=a_N\psi_N+a_S\psi_S+a_E\psi_E+a_W\,\psi_W+a_R\psi_R+a_L\psi_L+S'_{\psi P}$$

$$\text{i.e., } a_P\psi_P=\sum_{i=m}a_i\psi_i+S'_{\psi P} \tag{3.15}$$

where,

$$a_P=\sum_{i=m}a_i-S''_{\psi P}$$

In the above expressions, i=m represents the six neighbour nodes (N,S,E,W,R,L). The coefficients 'a_i' are given as follows :

$$
\begin{aligned}
a_N &= H^+_\eta - G^+_\eta \qquad & a_S &= H^-_\eta + G^-_\eta \\
a_E &= H^+_\xi - G^+_\xi \qquad & a_W &= H^-_\xi + G^-_\xi \\
a_R &= H^+_\zeta - G^+_\zeta \qquad & a_L &= H^-_\zeta + G^-_\zeta
\end{aligned}
\tag{3.16}
$$

It can be seen that the 'a' coefficients contain the convection and the normal diffusion parts of the Eq.(2.29). All other terms including the cross-diffusion terms are treated via the source terms 'S' of Eq.(3.15).

The momentum Eqns.(2.30-2.32) can be similarly discretised over the respective control volumes (see Fig.3.4). The only difference is that for each case three pressure derivatives and a few other extra terms (featuring in Eqs.2.30 and 2.31) are present. Using the same approach outlined above, for the discretisation of the general scalar variable ψ, an algebraic expression similar to Eq.(3.15) can be obtained for each of the momentum equations.

3.5 Derivation of the Pressure-Correction Equation

The pressure derivatives appearing in the momentum Eqs.(2.30-2.32) represent an additional variable for pressure. Hence, when a numerical solution of the transport Eqs.(2.28-2.32) is attempted, these pressure gradients must be known. The problem is that for pressure there is no obvious equation for obtaining it. For a given pressure field, however, there is no particular difficulty in solving the momentum equations. But, unfortunately, for most of the fluid flow situations this pressure field cannot be known beforehand.

One of the remedies to this problem is to use the vorticity/stream-function method (Gosman et al, 1969), which eliminates the pressure derivative terms from the equations. For two-dimensional flows, this method appears to be fairly simple and has been employed by many workers. But for three-dimensional cases, such a method is very complicated and often the results are harder to visualise, which make them unattractive.

The alternative method is to use some indirect way of calculating pressure at every iteration during the solution procedure and updating it at the next iteration. This can be done by modifying the continuity equation and extracting a relation in terms of pressure.

The SIMPLE (Semi-Implicit Pressure Linked Equations) algorithm of Patankar and Spalding (1972) employs this principle of solving the momentum equations and this has been adopted in the present study. The relation, originally developed for a rectangular coordinate system, is commonly known as the Pressure-Correction Equation. Following the same approach (Patankar, 1980), the pressure-correction equation has been reformulated for the general coordinate system and is described below.

The discretised continuity Eq.(3.10) can be rewritten in the following form:

$$(1/\Delta\eta)_P\{(\rho V)_n-(\rho V)_s\}-(1/\Delta\zeta)_P\{(\rho U)_r-(\rho U)_l\}-(1/\Delta\xi)_P\{(\rho W)_e-(\rho W)_w\}=0 \quad (3.17)$$

Let, u^*, v^*, w^* be guessed velocities that satisfy the momentum equations with a given pressure field p^*. Since these guessed velocities will not in general satisfy the continuity Eq.(3.17), the pressure field must be corrected. In SIMPLE procedure, the pressure p is obtained from

$$p=p^*+p' \qquad (3.18)$$

where p' is called the pressure correction. The corresponding velocity corrections u', v', w' can be introduced in a similar manner.

$$\begin{aligned} u&=u^*+u' \\ v&=v^*+v' \\ w&=w^*+w' \end{aligned} \qquad (3.19)$$

To derive the pressure correction equation, it is assumed that u^*, v^*, w^* are obtained from the momentum equations as follows:

$$u_P^*=\sum_{i=m}\frac{a_i^u}{a_P^u}u_i^*+D^u+(E^u p_\eta^*+F^u p_\zeta^*+G^u p_\xi^*)$$

$$v_P^*=\sum_{i=m}\frac{a_i^v}{a_P^v}v_i^*+D^v+(E^v p_\eta^*+F^v p_\zeta^*+G^v p_\xi^*)$$

$$w_P^*=\sum_{i=m}\frac{a_i^w}{a_P^w}w_i^*+D^w+(E^w p_\eta^*+F^w p_\zeta^*+G^w p_\xi^*) \qquad (3.20)$$

The above expressions are a different way of representing Eq.(3.15) for momentum. The three pressure derivatives appearing in the above equations are related to the expression for the exact form of the momentum Eqs.(2.30-2.32). In addition, D^u, D^v,

D^w represent the cross-derivative viscous terms in the u, v, w momentum equations respectively. The coefficients in the pressure derivatives are:

$$E^v = -\,r\,B_{11}/\,a_P^v \qquad F^v = -\,r\,B_{21}/\,a_P^v \qquad G^v = -\,r\,B_{31}/\,a_P^v$$

$$E^u = -\,B_{12}\,/\,a_P^u \qquad F^u = -\,B_{22}\,/\,a_P^u \qquad G^u = -\,B_{32}\,/\,a_P^u$$

$$E^w = -\,r\,B_{13}/\,a_P^w \qquad F^w = -\,r\,B_{23}/\,a_P^w \qquad G^w = -\,r\,B_{33}/\,a_P^w \qquad (3.21)$$

The correction equations for the velocity components can be written (by dropping the cross-diffusion terms and $\Sigma a_i u_i/a_P$, following Patankar,1980) as :

$$u = u^* + (E^u\,p'_\eta + F^u\,p'_\zeta + G^u\,p'_\xi$$

$$v = v^* + (E^v\,p'_\eta + F^v\,p'_\zeta + G^v\,p'_\xi\,)$$

$$w = w^* + (E^w\,p'_\eta + F^w\,p'_\zeta + G^w\,p'_\xi\,) \qquad (3.22)$$

By substituting these expressions (Eq.3.22) into the relations for contravariant variables (Eqs.2.35), the correction formulae for U, V, W become :

$$\begin{aligned}
V = V^* &+ \{\, r\,B_{11}E^v + B_{12}E^u + r\,B_{13}E^w \}\, p_\eta' + \\
&+ \{\, r\,B_{11}F^v + B_{12}F^u + r\,B_{13}F^w \,\}\, p_\zeta' + \\
&+ \{\, r\,B_{11}G^v + B_{12}G^u + r\,B_{13}G^w \}\, p_\xi' \\
U = U^* &+ \{\, r\,B_{21}E^v + B_{22}E^u + r\,B_{23}E^w \}\, p_\eta' + \\
&+ \{\, r\,B_{21}F^v + B_{22}F^u + r\,B_{23}F^w \,\}\, p_\zeta' + \\
&+ \{\, r\,B_{21}G^v + B_{22}G^u + r\,B_{23}G^w \}\, p_\xi' \\
W = W^* &+ \{\, r\,B_{31}E^v + B_{32}E^u + r\,B_{33}E^w \}\, p_\eta' + \\
&+ \{\, r\,B_{31}F^v + B_{32}F^u + r\,B_{33}F^w \,\}\, p_\zeta' + \\
&+ \{\, r\,B_{31}G^v + B_{32}G^u + r\,B_{33}G^w \}\, p_\xi' \qquad (3.23)
\end{aligned}$$

In the above expressions U*, V*, W* represent the contravariant velocity components based on u*, v*, w*. These equations can now be rewritten by dropping the cross-derivatives of pressure-correction (for example, in the expression for U, by dropping the p_η' and p_ξ' terms). This is done in order to obtain the final algebraic equation in the same form as the other equations (Eq.3.15). The simplified velocity correction equations now assume the following form:

$$V=V^*+E^\eta p_\eta' \qquad U=U^*+F^\zeta p_\zeta' \qquad W=W^*+G^\xi p_\xi' \tag{3.24}$$

where, E^η, F^ζ and G^ξ are defined as :

$$\begin{aligned} E^\eta &= r\,B_{11}E^v + B_{12}E^u + r\,B_{13}E^w \\ F^\zeta &= r\,B_{21}F^v + B_{22}F^u + r\,B_{23}F^w \\ G^\xi &= r\,B_{31}G^v + B_{32}G^u + r\,B_{33}G^w \end{aligned} \tag{3.25}$$

The magnitudes of the contravariant components V, U, W are evaluated at the cell faces of the pressure control volume in the transformed domain as shown in Fig.3.4.

For example, the values of V, U and W at locations n, e and r are respectively :

$$\begin{aligned} V_n &= V_n^* + E_n^\eta(p_P'-p_N')/(\eta_P-\eta_N) \\ U_r &= U_r^* + F_r^\zeta(p_P'-p_R')/(\zeta_P-\zeta_R) \\ W_e &= W_e^* + G_e^\xi(p_P'-p_E')/(\xi_P-\xi_E) \end{aligned} \tag{3.26}$$

Similar expressions can be obtained for three other cell faces (s,l,w) of the control volume. These expressions are now substituted in the discretised form of the continuity Eqn.(3.17). After some rearrangement, the equation can be written as :

$$a_P p_P' = \sum_{i=m} a_i p_i' + b \tag{3.27}$$

where, i=m stands for the neighbour nodes viz., N,S,R,L,E,W. The coefficients a_i and the value of 'b' are :

$$\begin{aligned} a_N &= (\rho_n E_n^\eta)/\{\Delta\eta(\eta_P-\eta_N)\} \\ a_R &= (\rho_r F_r^\zeta)/\{\Delta\zeta(\zeta_P-\zeta_R)\} \\ a_E &= (\rho_e G_e^\xi)/\{\Delta\xi(\xi_P-\xi_E)\} \end{aligned} \tag{3.28}$$

$$b=-[(1/\Delta\eta)_P\{(\rho V^*)_n-(\rho V^*)_s\}+(1/\Delta\zeta)_P\{(\rho U^*)_r-(\rho U^*)_l\}+(1/\Delta\xi)_P\{(\rho W^*)_e-(\rho W^*)_w\}]$$

It can be seen that the pressure-correction equation derived above is of the same form as the other algebraic equations derived previously (Eq.3.15). Hence, the same solution technique can be used for the solution of the pressure-correction equation.

3.6 Interpolation Practice and Boundary Conditions

3.6.1 Interpolation Practice

During discretisation, it is often desirable to calculate the values of the dependent variables at the cell faces which lie between the nodal points. Depending on the type of interpolation practice (also called the differencing scheme) used to accomplish this task both the stability of the numerical algorithm and the accuracy of the solution are influenced. In the literature, various types of interpolation practices can be found (Lai,1982; Patankar,1980 etc.). However, if the size of the computational cell tends to zero, the discretised equations (e.g.,Eq.3.15) will regain their 'exact' nature irrespective of the differencing scheme. In practice, one can only use a finite number of control volumes (because of computer limitations) and hence the interpolation practice which describes the transport phenomena more closely for these finite cells will produce a better solution. In other words, the interpolation practice should be such that the three important properties of transport equations namely, conservativeness, boundedness and transportiveness (Patankar,1980) are properly maintained. Numerous references can be found in the literature regarding these aspects and hence, these are not discussed further in this thesis. Readers interested in these matters are directed to the above and other references such as Leonard (1979), Wilkes and Thompson (1983) etc.

For the purpose of this study the most widely used interpolation practice known as the 'Hybrid Differencing Scheme' (Spalding,1972) has been followed. It is a combination of the Central Differencing Scheme and the Upwind Differencing Scheme; in which the switching from CDS to UDS is controlled by the magnitude of the cell Reynolds number. These aspects are well established and can be found in the above references.

3.6.2 Boundary Conditions

The finite difference form of the conservation Eqs.(3.15) can only be solved for a given set of boundary conditions. In many cases, these conditions are well defined, but situations may occur when the boundary conditions are to be estimated by some indirect procedure. In this section, the most frequently encountered boundary conditions and the treatment necessary to incorporate them into the discretised equation are briefly described.

3.6.2.1 Inlet Boundary

At an inflow the values of the dependent variables (u,v,w etc.) are nomally known (Dirichlet boundary conditions). In most cases, these are obtained by reference to experimental data for the particular flow configuration or from experimental evidences. If no data are available, then these values are to be estimated which is justifiable only when the inlet values are not expected to significantly influence the flow domain of interest. When using the two-equation (k-ε) turbulence model, it is usually necessary to calculate the dissipation rate of turbulence ε from the measured k values and estimates of the length scale 'l'. In this thesis, the inlet value of ε is obtained as:

$$\varepsilon \infty k^{3/2}/l \qquad (3.29)$$

where, 'l' is a characteristic length. (e.g., the characteristic dimension of flow domain).

Fig.3.5a shows a two-dimensional sketch of a solution domain in the (η,ζ) plane near the inlet boundary. L represents a grid node on the boundary plane. The scalar variables are located at node L while the velocity component in that direction, for example u, is staggered a further half-cell and it is also located at L. Calculations always start from the node adjacent to the boundary such as u_R cell shown in Fig.3.5a. Hence, these boundary values are not updated, only their contributions enter into the solution domain via the L surface. Neither the physical velocity component nor the contravariant component U needs to be updated.

3.6.2.2 Outlet Boundary

There is no unique definition of an outflow boundary. If the dependent variables are known (which is usually rare) at exit, then they can be fixed. The most commonly employed procedure is to set to zero the gradients of all the dependent variables in the outflow direction. The rationale behind this boundary condition is that the flow field of interest is 'far' upstream from the exit and hence any inaccuracy in estimating the outlet will not propagate further into the solution domain of interest.

This boundary condition has been employed for most of the calculations performed in this research programme. For example, in Fig.3.5b, the zero-gradient boundary condition can be prescribed by setting $\psi_P = \psi_R$. For the velocity components such as u (in the x-direction) the same treatment can be adopted. Additionally at the end of each iteration, the contravariant components, U (Eq.2.35) are updated in a way such that the overall continuity constraint is maintained. This is done in the usual way by calculating a factor f and multiplying U values at exit by f.

$$f = \dot{m}_{in} / \dot{m}_{out} \qquad (3.30)$$

where, $\dot{m}_{in}$ is the total mass flux into the solution domain and $\dot{m}_{out}$ is the total mass flux out of the solution domain. One particular problem may arise if the exit boundary falls in a region where there is a recirculation (shown in Fig.3.5b). In these cases, special treatments are to be adopted (for example, Pressure boundary condition, Manners,1988).

3.6.2.3 Symmetry Boundary

If a symmetry plane exists in a flow domain, then it is usually unnecessary to solve the transport equations for the whole flow field; because the solution domain can be conveniently truncated along this plane. A plane of symmetry in the flow domain is characterized by two physical phenomena viz.,

i) No cross-flow (zero convective flux) and
ii) No diffusion of dependent variables in the direction normal to the plane or axis.

A two-dimensional illustration of a flow domain (flow through a curved duct of square cross-section) having a symmetry plane is shown in Fig.3.5c. With the coordinates η and ζ in the plane of symmetry and the coordinate ξ normal to this plane, the above two conditions give :

$$\partial\psi/\partial\xi=0; \; \partial u/\partial\xi=0; \; \partial v/\partial\xi=0; \; w=0 \qquad (3.31)$$

If the grid lines are not orthogonal near the symmetry plane (in the present study, the grid lines near the symmetry plane were almost orthogonal for all the cases), then some geometric manipulations are necessary for applying the above conditions as can be found in Peric (1985).

3.6.2.4 Impermeable Walls

The boundary conditions for rigid impermeable walls are obvious i.e., the velocity components and hence the mass fluxes are zero there. For laminar flows, these conditions are sufficient and very easy to implement. On the other hand, for turbulent flows this boundary condition would require a large number of grid lines to be placed next to the wall in order to resolve the steep gradient of the dependent variables. Additionally, a low Reynolds number turbulence model should be used for the viscous sub-layer. The alternative is to use the formulae known as 'Wall Functions' (Launder and Spalding, 1974) which avoid these problems by assuming the flow next to the wall varies in a known way (i.e., the log-law).

The objective of such wall treatment is to incorporate the wall diffusion into the solution domain without resolving the steep gradients near the viscous sub-layer. The procedure for implementing this boundary condition is essentially the same as that of Gosman and Ideriah (1976) and is discussed in detail in Peric (1985); but for completeness an outline of the technique is given here for a two-dimensional flow configuration.

In Fig.3.5d, a scalar cell is shown next to a rigid impermeable wall. For the first grid node P which is sufficiently close to the wall, a one-dimensional Couette-flow assumption is believed to be valid for many situations. However, this assumption may be significantly in error in case of recirculating flows, and when the flow is not parallel to the wall. More will be discussed in Chapter 5.

The wall shear force $\overline{T}_w$ can be expressed as :

$$\overline{T}_w = \overline{\tau}_w A_w \tag{3.32}$$

where, $$\overline{\tau}_w = - \lambda_w (\overline{V}_P)_P$$

In the above expressions, $\overline{\tau}_w$ is the shear stress, A_w is the cell-surface area on the wall and $\overline{V}_P$ is the velocity component parallel to the wall. $\overline{\tau}_w$ is determined from a two-part 'universal' velocity profile expression (Gosman and Ideriah, 1976), that is :

a) Laminar sub-layer

$$\lambda_w = \mu/\Delta n \qquad \text{if } y_P^+ < 11.6 \tag{3.33}$$

b) Fully turbulent layer

$$\lambda_w = \frac{\rho\, C_\mu^{1/4}\, k_P^{1/2}\, \kappa}{\ln (E\, y_P^+)} \qquad \text{if } y_P^+ > 11.6 \tag{3.34}$$

where,

$$y_P^+ = \frac{\rho\, C_\mu^{1/4}\, k_P^{1/2}\, \Delta n}{\mu} \tag{3.35}$$

In the above equations Δn represents the normal distance of P from the wall, κ is the von Karman's constant (κ=0.4187) and E is an integration constant which depends on the wall roughness, and through which other effects such as pressure gradients and mass transfer can be accounted for. For smooth rigid wall E is assigned a value of 9.0.

The velocity component $\overline{V_P}$, parallel to the wall at node P can be obtained as follows :

$$\overline{V}_P=\overline{V} - \overline{V}_n=\overline{V}- (\overline{V}. \overline{n})\overline{n} \tag{3.36}$$

where $\overline{n}$ is the unit normal vector, which can be calculated as follows (Fig.3.5d) :

$$\overline{n}= - (\Delta z/\Delta l)\overline{i}_1 + (\Delta r/\Delta l)\overline{i}_2 \tag{3.37}$$

Δl in Eq.(3.37) is the length of the boundary cell face projection, and easily calculated as:

$$\Delta l=\sqrt{\{(\Delta z)^2+(\Delta r)^2\}} \tag{3.38}$$

Δz and Δr can be obtained from the location of the grid nodes :

$$\Delta z=0.5(z_{SW} - z_{NW}) \quad \text{and} \quad \Delta r=0.5(r_{SW} - r_{NW}) \tag{3.39}$$

The normal distance Δn of node P from the wall can be determined by taking the dot-product of the two vectors as :

$$\Delta n= \overline{WP}.\overline{n} \tag{3.40}$$

Hence, all the quantities featuring in Eq.(3.32) can be determined from the locations of the grid nodes only.

So, when the w boundary (Fig.3.5d) is considered as the wall, the a_W coefficient (Eq.3.16) of the discretised Eq.(3.15) is suppressed and the wall shear stress is incorporated into the computer programme through the source terms (Eq.3.15).

As mentioned earlier in the chapter, four different computational cells are involved because of the staggered arrangement of the variables and hence the programming is also significantly more complex. However, the technique is exactly the same and straightforward.

Following the standard practice (Gibson et al, 1988; Launder and Spalding, 1974 etc.), the dissipation rate ε is explicitly specified at the near-wall node as:

$$\varepsilon_P = \frac{C_\mu^{3/4} k_P^{3/2}}{\kappa \Delta n} \tag{3.41}$$

This is fixed by means of linearised source terms (Eq.3.14) as follows:

$$S'_\varepsilon = G \frac{C_\mu^{3/4} k_P^{3/2}}{\kappa \Delta n} \quad \text{and} \quad S''_\varepsilon = G \tag{3.42}$$

where, G is a large number, typically 10^{30}.

Further, the generation component of the turbulence energy source term S_k is calculated from a Couette flow formula which involves the assumption of a constant stress region and velocity gradient as given by the log-law (For details, see Gibson et al, 1988 and Peric, 1985). This again is introduced through the linearised source terms.

3.6.2.5 Special Boundaries

Depending on the particular flow configuration, there may be various other types of boundary conditions such as cyclic boundary, porous wall, fixed static pressure, free-stream boundary etc. All of these need special treatments and can be found in the relevant literature (such as Manners,1988; Koutmos and McGuirk,1983; Demirdzic,1982; Chen et al, 1986 etc.).

3.7 Solution Technique and Summary of the Algorithm

The discretised algebraic equations resulting from the exact governing equations are coupled. If they are solved simultaneously along with proper boundary conditions, a flow field is established or in other words a solution is obtained. In this section the solution technique is briefly described and a summary of the algorithm is presented.

3.7.1 Solution Technique

The algebraic Eq.(3.15) exists for every computational node in the solution domain. If N is the total number of nodes, then the problem can be considered as a system of N equations with N number of unknowns. The system of equations can be written in matrix form as:

$$[A][\psi]=[T] \tag{3.43}$$

where, [A] has NxN coefficients, $[\psi]$ is a column matrix and [T] is the matrix containing N number of source terms. Such an equation can be solved by several methods which can be broadly divided into 'direct' and 'iterative' techniques. Generally speaking, the direct methods (matrix inversion) result in 'exact' solutions (to within machine accuracy) but are considerably more time consuming and need a large amount of computer storage compared with iterative techniques. Since the finite difference equations are themselves approximations of partial differential equations; it would therefore, seem in-appropriate to adopt a direct solution method. In addition, the coefficients 'a_i' (Eq.3.16) are not constants but functions of the dependent variables, and therefore an iterative approach is eventually required in which the coefficients 'a_i' are updated each time a new value of the dependent variable is obtained.This makes the direct methods more unattractive.

For the reasons stated above, an iterative solution technique in which the equations are solved to a certain level of convergence (to be described in §3.7.2) has been chosen for the present methodology. The solution technique is the well-known Tri-diagonal Matrix Algorithm (TDMA) (Patankar,1980). In this method, the equations are solved along a particular coordinate line (say, η) assuming that the variables along the neighbour lines (i.e., the ζ and ξ-direction) are known from their 'latest' values. The same procedure is repeated, if desired, for the lines in other directions. At the end of each iteration a new set of field values of the dependent variables are obtained which, in principle, should be 'a better approximation' to the 'exact' values compared to the values obtained in the previous iteration.

In an iterative scheme, it is often desirable to 'speed up' or to 'slow down' the changes, from iteration to iteration, in the values of the dependent variables. This is known as over-relaxation or under-relaxation. Usually for the solution of Navier-Stokes equations which are non-linear and strongly coupled, the process of convergence need to be slowed down which means that some form of under-relaxation factors are necessary in order to avoid divergence. There are many ways of introducing under-relaxation in the solution method (Patankar, 1980). The procedure followed in this study is outlined below.

The discretised Eq.(3.15) for the general variable ψ can be rewritten as:

$$\psi_P = \frac{\sum_{i=m} a_i \psi_i + S}{a_P} \qquad (3.44)$$

If ψ_P* represents the value of the dependent variable ψ_P from the previous iteration, then the quantity $\{\psi_P - \psi_P^*\}$ is the difference between the two consecutive iterations and should be added to ψ_P^* in order to obtain a better solution. Instead of adding the full difference of $\{\psi_P - \psi_P^*\}$, a fraction of the difference is considered as follows:

$$\psi_P = \psi_P^* + \alpha_\psi \{ \frac{\sum_{i=m} a_i \psi_i + S}{a_P} - \psi_P^* \} \tag{3.45}$$

In the above expression, α_ψ represents the under-relaxation factor ($0 < \alpha_\psi < 1$) for the general variable ψ. It can be seen that at the end of convergence, the difference $\{\psi_P - \psi_P^*\}$ of the above equation will be zero. The optimum values of the under-relaxation factors are problem dependent and can be known by experience. However, as an example, an assessment of the solution procedure in terms of the under-relaxation factors will be shown in Chapter 5.

3.7.2 Convergence

In an iterative solution technique, 'convergence' is of vital importance. A solution is said to be converged when the field values have reached a level when further iteration will not cause any significant change of flow variables. In literature, convergence is found to have been defined in several ways, the more popular of which are :

i) To monitor all the field values from one iteration to another. This, however can be a misleading approach and is not usually adopted on its own.

ii) To calculate the total mean kinetic energy of the flow domain at every iteration. When the final solution is reached, the total kinetic energy curve becomes a straight line parallel to the coordinate axis. This approach has been used by Braaten and Shyy (1986). This is, in a sense, similar to (i), but on an exaggerated scale because the squares of the velocities are used.

iii) To monitor the residual sources in the discretised equations.

The third definition is by far the most popular and has been adopted for use in the present study. The sum of the absolute residuals for the pressure-correction Eq.(3.27) at all computational nodes was used as the primary index of convergence. The residual at node P is calculated as (by using Eq.3.15) :

$$\varepsilon_P^n = \mathrm{Abs}[\sum_i a_i^n \psi_i^{n-1} + (S'_P)^{n-1} - a_P^n \psi_P^{n-1}] \tag{3.46}$$

and the sum is given by :

$$\varepsilon_\psi = \sum_m \varepsilon_m^n \quad , \ m=1,2, \ldots., N. \tag{3.47}$$

where, N is the total number of grid nodes and n is the iteration number. At the end of an iteration, such residual sums are calculated and non-dimensionalized by the total inlet mass flow. Convergence is declared when the sum of the residuals reach a value less than the maximum allowable value, that is :

$$\max(\varepsilon_\psi) \leq \lambda \tag{3.48}$$

where, λ is the maximum allowable value which was taken to be 1×10^{-3} for this study. For all other equations (momentum, k, ε) the maximum value of the residual was calculated by the same procedure and instead of mass flow they were normalized by the corresponding fluxes.

It is not irrelevant to mention here that the pressure-correction equation appeared to be the most sensitive from convergence point of view. The reason is that it is an approximate equation derived from continuity. Especially, for highly non-orthogonal grids the neglected terms of pressure-correction equation (§3.5) may become more significant and hence cause convergence problem. (More will be discussed in Ch. 5). In this work, apart from monitoring the total residuals, the cell for which the individual residual was the highest was also monitored for the pressure-correction equation, and in most cases it was found to be at the severely non-orthogonal cells.

For each dependent variable (u,v,w,k,ε) usually one 'sweep' (inner iteration i.e., the number of times the TDMA solver is called without updating the coefficients) was sufficient; but for pressure-correction equation, the number of inner sweeps varied between 5-30. Of course, after a certain number of outer iterations, the number of 'sweeps' required was less.

3.7.3 Summary of the Algorithm

The procedure for the solution of the governing differential equations described in this and the previous chapters can be summarized as follows:

i) Initialise all field values by an initial guess;
ii) Calculate the contravariant variables U, V, W from Eq.(2.35) using the 'latest' u,v,w;
iii) Solve the momentum Eqs.(3.20), to obtain u*, v*, w*, using the pressure as p*;
iv) Solve the pressure-correction Eq. (3.27);
v) Calculate p from Eq.(3.18);
vi) Correct u, v, w from their starred values using the velocity correction Eqs.3.22;
vii) Solve the discretisation equation for scalar variables (such as k and ε) ;
viii) Treat the corrected pressure p as a new guessed p*, return to step (ii), and repeat the whole procedure until a converged solution is obtained.

3.8 Grid Generation

The present solution method requires the specification of only the coordinates of the cell vertices. Other parameters which feature in the discretised equations (e.g., the metric components) can be calculated from grid-node locations. For simple systems, such as Cartesian or Cylindrical-polar coordinates the question of grid generation is trivial and it involves the specification of grid points only along each coordinate line. On the other hand, for a body-fitted coordinate system such as the one employed for the current reasearch programme, the accuracy of results as well as economy and stability of the procedure depends largely on the gridding of the domain. During the last fifteen years, significant advances have taken place in this field. For static boundaries, the commonly employed procedures can be broadly classified into two categories viz., the methods which solve differential equations (e.g., Poisson type equations) and the others are the so-called 'transfinite mappings'. The first type is usually applied for curvilinear orthogonal coordinate system where certain stringent requirements (see §2.3) such as orthogonality and continuity of grid lines are to be met. They are in general more expensive and time consuming. On the other hand, the second category of grid generation technique is relatively simple, quick and less expensive and requires very little experience to adopt. Since the solution method developed for the present work is quite general and is not sensitive to grid properties, this type of grid generation procedure was found to be reasonably adequate for this study. A collection of the most important grid generation procedures can be found in Ghia et al (1983).

3.8.1 Desired Properties of Grids

The computational grids should be generated in such a way that the following criteria are met as closely as possible.

Orthogonality

Although the developed computer code is capable of handling non-orthogonal grid lines, it is desirable to minimize the deviation from orthogonality. As will be shown in Ch. 5, the more is this deviation, (usually) the less economical the solution will be. However, for moderate non-orthogonality, apart from requiring a larger computational time, no other adverse effect will take place. In some extreme cases, if the non-orthogonality becomes too severe, especially in the boundary region, the solution method may be unstable. Braaten and Shyy (1986) have also observed this situation. The reason is that the cross-diffusion terms of Eqs.(2.29-2.32) which are treated explicitly via the source terms 'S' will outweigh the main coefficients (Eq.3.16) if the non-orthogonality is very high (Peric, 1985) and can affect the solution in two ways. Firstly, the desirable 'diagonal dominance' of the coefficient matrix (Eq.3.43) is degraded and secondly, it may cause unboundedness (Patankar, 1980).

Smoothness

Smoothness of grid lines refers to the continuity of grid lines and their first derivatives. The methods which employ grid oriented velocity components are very sensitive to this constraint because of the presence of the so-called 'curvature terms' (Demirdzic, 1982). In this study, the effect of non-smoothness may cause inaccuracy by way of interpolation errors. The continuity of grid lines can be improved by refining the grids locally. It is to be noted here that the errors appearing as a result of non-smoothness will diminish with finer mesh.

Alignment of Grid Lines and Streamlines

As shown by Patankar (1980), the so-called 'numerical diffusion' which affects the accuracy of results depends on the skewness of grid lines and streamlines and is reduced if one of the grid lines aligns itself with streamlines.* In this study, this is particularly important in a sense that the 'hybrid differencing scheme' (Spalding, 1972) has been followed throughout. Although it is difficult to know the streamlines beforehand, especially for the type of complex geometries studied here, the predominant flow direction and the grid lines in the streamwise direction are always aligned. However, this aspect needs special attention as will be mentioned in Chapters 5 and 7.

Uniformity of Cells

For a Cartesian frame of reference, the most desirable computational cell would be the square one for a two-dimensional flow domain. However, it is usually very difficult (and often uneconomical) to generate such a grid system. What should be done in practice is to generate the cells in such a way that the cell 'aspect ratio' and the 'expansion ratio' can be kept under control. With reference to Fig.3.3a, these two geometrical quantities can be defined as :

$$\text{Aspect Ratio} = \max(\Delta\eta_1, \Delta\xi_1) / \min(\Delta\eta_1, \Delta\xi_1) \tag{3.49}$$
$$\text{Expansion Ratio} = \max(\Delta\eta_1, \Delta\eta_2) / \min(\Delta\eta_1, \Delta\eta_2)$$

As mentioned by Roache (1976), these two parameters affect both the stability and accuracy of the solution procedure. The most desirable values for these two factors are 'unity' and experience suggests that their maximum values should be around 10 for aspect ratio and 1.4 for the expansion ratio.

---

* Note, numerical diffusion is only reduced to negligible levels for a strictly conserved variable, in other cases it is still present even with aligned grids.

3.8.2 The Grid Generation Technique

The geometries which are of interest in the present study are three-dimensional. However, the main flow direction (for the case of curved ducts and volute casings) is usually straightforward and by specifying the angular positions (θ-direction in Fig.1.1), these planes can be determined. So, the grid generation was necessary for two dimensional situations only. The method followed in this study is described below.

Fig.3.6 shows a two-dimensional flow domain (cross-section of circular duct truncated along the symmetry plane) enclosed within four boundaries AB, AC, CD, DB. First, the Cartesian coordinates of the grid nodes on all four boundaries (η_{min}, η_{max}, ξ_{min}, ξ_{max}) of the solution domain are specified with reference to the y-z frame of reference.

Then the distribution functions for boundary grid nodes are calculated as :

$$f^i_{AB} = \frac{y_{i,1} - y_{1,1}}{y_{LP1,1} - y_{1,1}} \qquad f^i_{CD} = \frac{y_{i,MP1} - y_{1,MP1}}{y_{LP1,MP1} - y_{1,MP1}}$$

$$f^j_{AC} = \frac{z_{1,j} - z_{1,1}}{z_{1,MP1} - z_{1,1}} \qquad f^j_{BD} = \frac{z_{LP1,j} - z_{LP1,1}}{z_{LP1,MP1} - z_{LP1,1}} \qquad (3.50)$$

The coordinates of the interior grid points (i,j) can then be calculated by using coordinates of grid nodes along the boundaries and the distribution functions (Eqs.3.50). The distribution function for any interior grid node is :

$$f^y_{i,j} = \frac{(MP1 - j)\, f^i_{AB} + (j-1)\, f^i_{CD}}{MP1 - 1}$$

$$f^z_{i,j} = \frac{(LP1 - i)\, f^j_{AC} + (i-1)\, f^i_{BD}}{LP1 - 1} \qquad (3.51)$$

Finally, the coordinates of the internal nodes are calculated as :

$$y_{i,j} = y_{1,j} + f^y_{i,j}\,(y_{LP1,j} - y_{1,j})$$

$$z_{i,j} = z_{i,1} + f^z_{i,j}\,(z_{i,MP1} - z_{i,1}) \qquad (3.52)$$

This method of grid generation was found to produce quite reasonable grid layout of the solution domain (on the basis of grid properties mentioned in §3.8.1) for most of the test cases presented in this study. However, these aspects need further attention as will be mentioned in Chapter 7.

3.9 Closure

The methodology for obtaining numerical solution of the transport equations (presented in Chapter 2) was described in this chapter. Choices regarding the computational cell, solution algorithm etc., are made and a brief description of the chosen method is included along with sufficient references for more detailed information.

The common boundary conditions as encountered in practical flow configurations are described. As has been mentioned before, for curvilinear coordinate system, the success of a solution depends significantly on the type of grid employed. Hence, the desired properties of grid lines were first discussed and then the grid generation technique used in this study is presented.

The methodology has been incorporated into two computer programmes: one for two-dimensional laminar flows and the other for three-dimensional turbulent flows. Both of these computer codes have been subjected to rigorous testing by applying them to several test cases, some of which will be presented in Chapter 5, in conjunction with the study of flow through constant curvature and constant/variable cross-section ducts. In the next chapter, a study of laminar flow through toroidally curved ducts is presented.

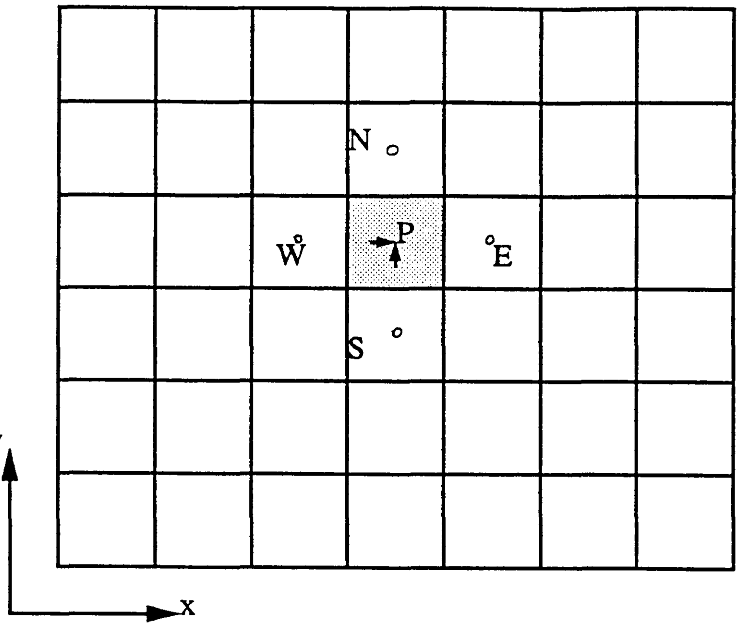

(a) Non-staggered arrangement; both the velocity components and pressure stored at the centre P of the control volume.

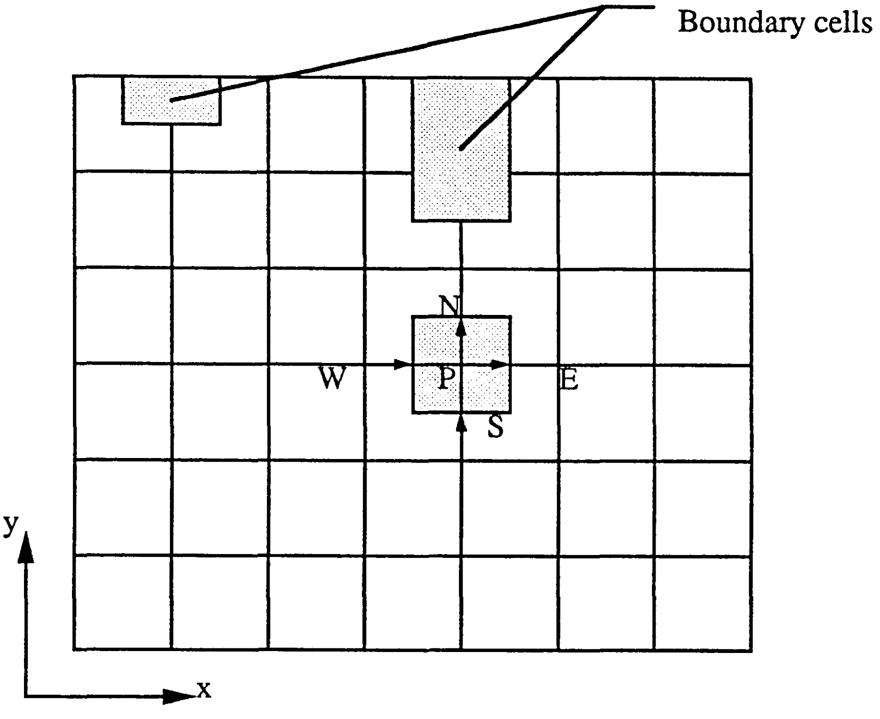

(b) Staggered arrangement; pressure stored at the centre P of the control volume but the velocity components located on the cell faces.

Fig. 3.1 Grid and variable arrangement for a plane two-dimensional geometry.

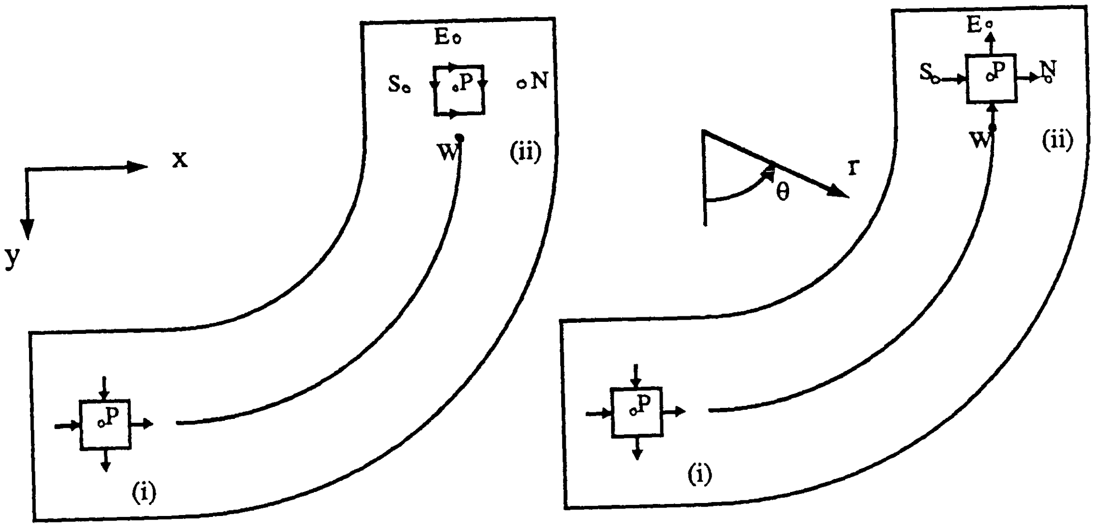

(a) Cartesian frame

(b) Cylindrical-polar frame

Fig. 3.2 Pressure-velocity decoupling with staggered arrangement

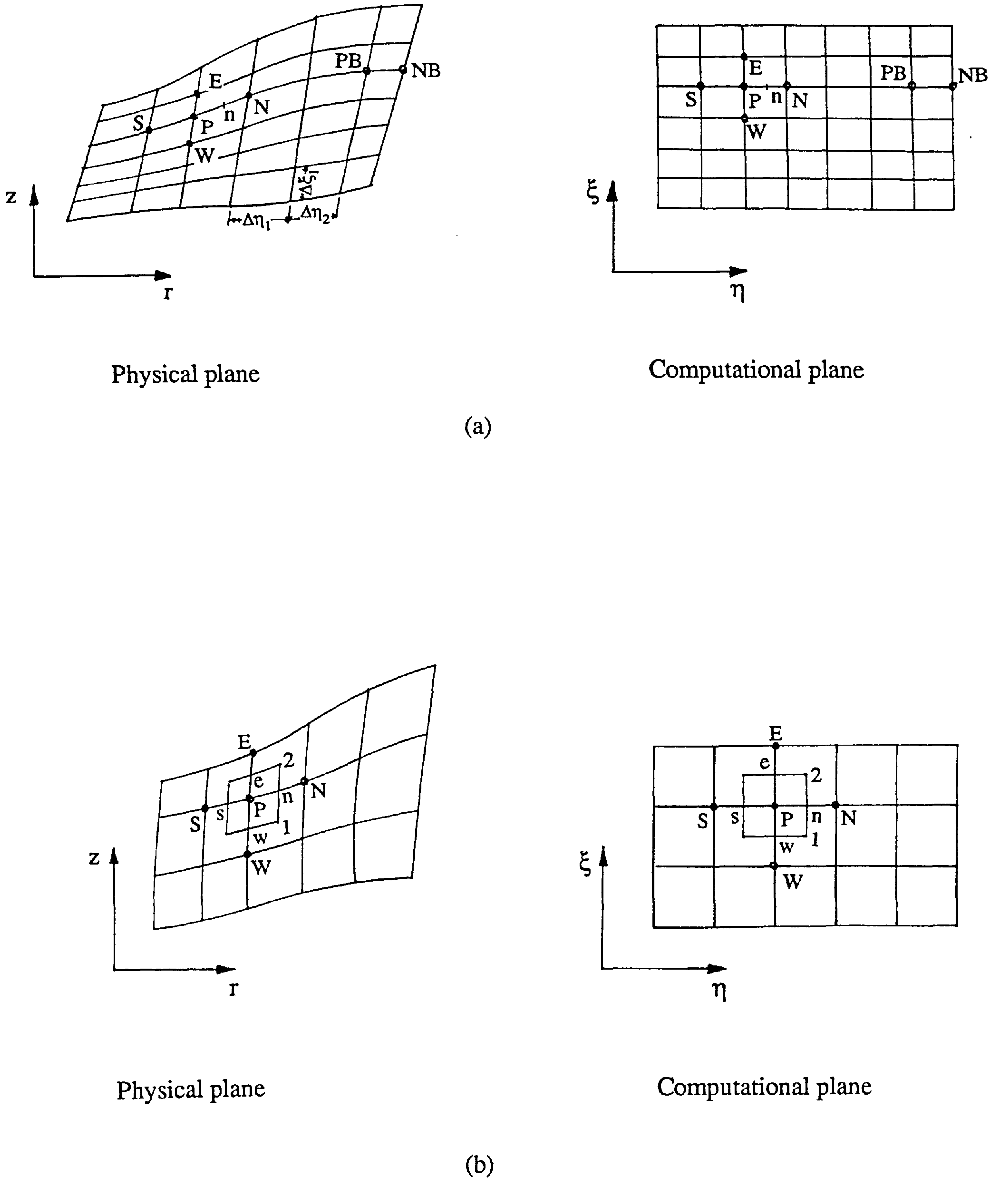

Physical plane

Computational plane

(a)

Physical plane

Computational plane

(b)

Fig. 3.3 Schematic representation of transformation (Eq. 2.24) in two dimensions

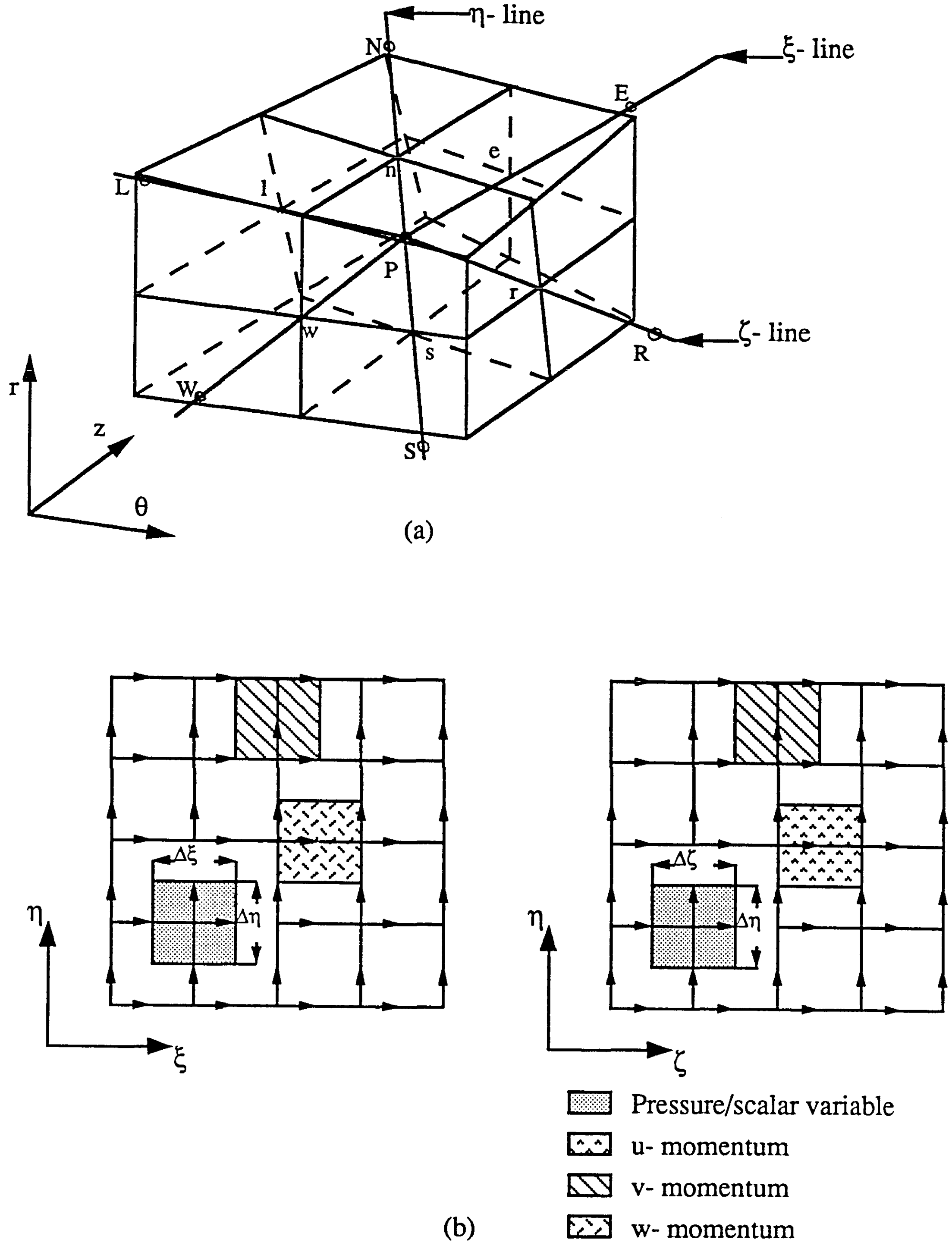

Fig. 3.4 Schematic representation of computational cells.
(a) A three-dimensional scalar cell in physical space.
(b) Momentum and scalar control volumes in two-dimensional computational space.

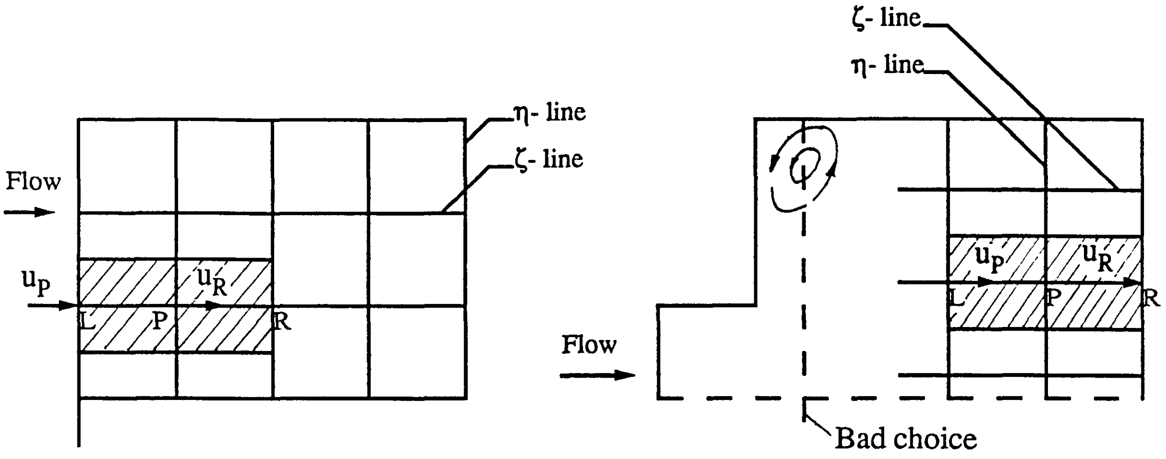

(a) Inlet boundary (b) Outlet boundary

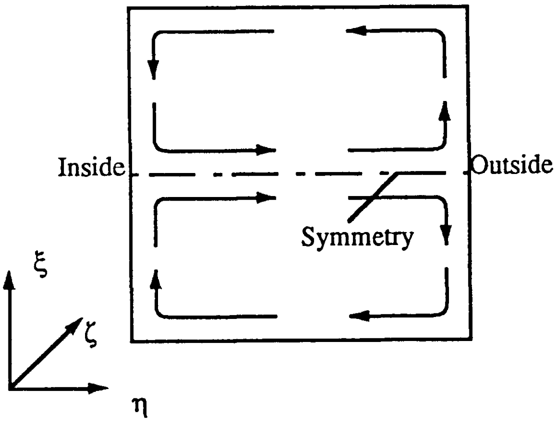

(c) Symmetry

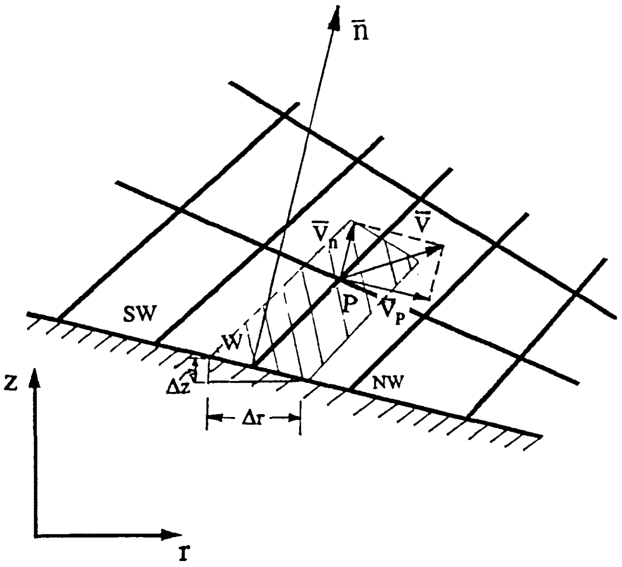

(d) Impermeable Wall

Fig. 3.5 Schematic representation of common boundaries

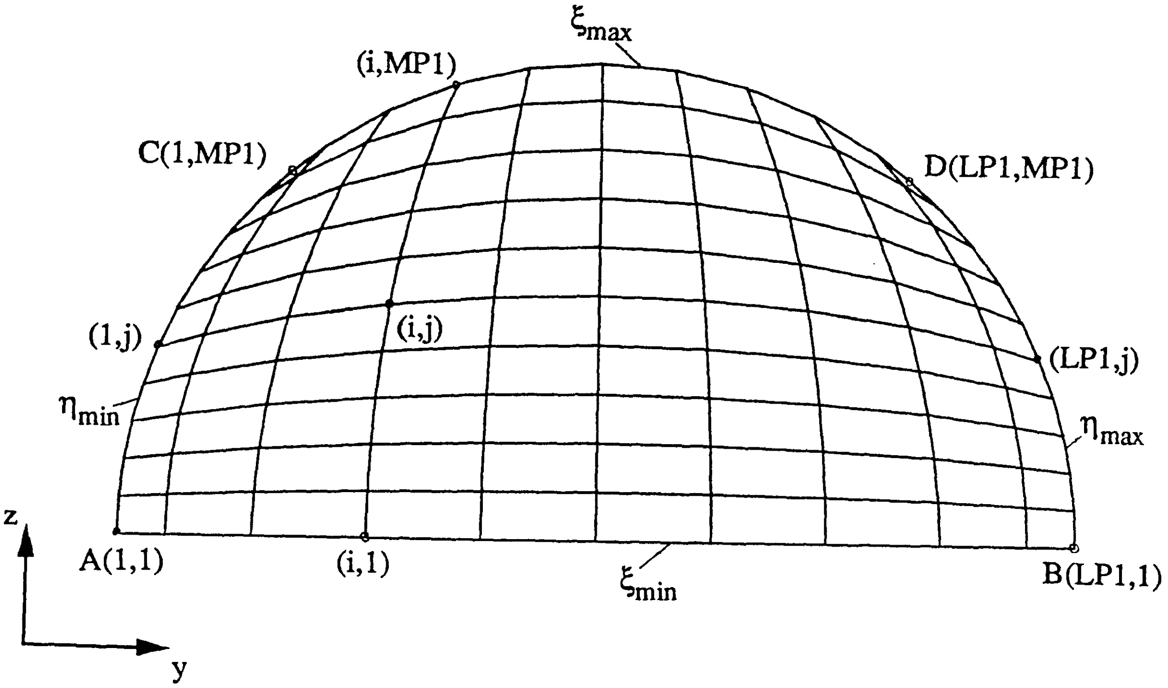

Fig. 3.6 Illustration of the grid generation technique

CHAPTER 4

LAMINAR FLOW THROUGH DUCTS WITH CONSTANT CURVATURE AND CONSTANT CROSS-SECTION

4.1 Introduction

This chapter presents a study of laminar flow in constant cross-section and constant curvature ducts without upstream and downstream tangents. A computer code employing a toroidal coordinate system was developed by modifying an existing programme (McGuirk, 1988). With this new code, calculations were carried out for different cross-sectional shapes (circular and square) and curvatures of the ducts. The objectives of these initial investigations were to identify the basic characteristics of viscous turning flows under circumstances where no doubts existed about the physical models or numerical methods used in the calculations. These then provided relevant guidelines and bench-mark predictions for subsequent analysis of similar and more complicated flows, using the general computational methodology described in Chapter 3, to be presented later in the thesis. It may be recalled that this category of curved ducts represents the simplest of the once-curved ducts mentioned in §1.1.

In the next section, a brief review of previous related investigations is made in an effort to highlight the trend of research in this area.

The methodology of numerical solution for this study is essentially the same as that described in the previous chapter. However, to minimize the modifications required to the existing code (McGuirk, 1988), orthogonal coordinates were used, and therefore grid-oriented velocity vectors were retained (rather than fixed components); the form of governing equations is thus different. These aspects along with the special boundary condition needed for the study of circular ducts are described in section 3.

Results and discussion are given in section 4. For convenience of presentation, the results obtained are discussed under two different headings viz., fully-developed and developing flows.

Finally, conclusions are summarized in section 5.

4.2 Literature Review

The general features of the flow through turning channels has been known for a long time. The most important characteristic of such flows is the presence of a strong secondary velocity which originates from the centripetal acceleration experienced by the streamwise velocity in the core region. In order to counter the 'excess' force it experiences, the slower moving fluid in the boundary layers moves from the outside of the bend towards the inside along the wall and, by continuity, induces motion in the core from inside to outside along the centre-line. These curvature induced secondary flows, when superimposed on the general axial through-flow, result in counter-rotating helical vortices as shown schematically in Fig.4.1. The other characteristic feature of the flow in a curved duct is the displacement of the maximum streamwise velocity from the centre-line (unlike that of a straight pipe) towards the outside. The amount of displacement and the strength of the secondary velocities are all coupled and depend strongly on the two most important geometrical characteristics of duct bends viz., curvature and cross-section.

It was probably Thompson (1876) who first observed the secondary motion of fluid in a winding course of a river. Since then, numerous works have been reported on the flow in ducts with different cross-sectional shapes and mean radii of curvature. These works can be broadly divided into two categories as far as the flow is concerned viz., fully-developed, in which the pattern of flow remains unchanged from one streamwise station to the next, and the developing or 'entry flow'. The cross-sectional shapes of ducts studied are found to be mostly circular because of its relevance to engineering applications; however, other shapes are also quite common. In the following, the first two sub-sections review the literature on circular ducts and the third presents a short account of past work on rectangular ducts.

4.2.1 Fully-developed Flow

The pioneering theoretical study on the fully-developed flow through a curved pipe was done by Dean (1927). He showed that for a slightly curved pipe, the flow pattern depends primarily on a single parameter defined as :

$$k=(D/R_c)(0.5D\rho W_o/\mu)^2 \qquad (4.1)$$

where D is the hydraulic diameter of the duct cross section (for circular pipe, D=2a=pipe diameter, see Fig.4.1a), R_c is the mean radius of curvature of the pipe and ρ and μ are the fluid density and viscosity respectively. W_o is a constant having the dimensions of velocity. This parameter (now called the Dean number) is more commonly defined as:

$$De=Re\delta^{1/2} \tag{4.2}$$

where, δ is the radius-ratio defined as:

$$\delta=D/2R_c \tag{4.3}$$

Re is the Reynolds number defined as $Re=\rho u_0 D/\mu$, u_0 being the flow bulk velocity. (Unless otherwise specified, this definition of Dean number will be used throughout this thesis). By applying a perturbation technique, Dean calculated the friction factor ratio λ_c/λ_s, the ratio of (fully-developed) resistance in a curved pipe to that in a straight pipe for the same flow rate ($\lambda_c/\lambda_s>1$). After Dean's work, many experimental and theoretical studies have been carried out on the fully-developed laminar flow through curved pipes and a thorough review has been made by Berger, Talbot and Yao (1983) on this subject. However, for the purpose of continuity, a few of the important works are mentioned below whose results will be used to check the present predictions.

Among others, McConalogue and Srivastava (1968), Greenspan (1973) and Collins and Dennis (1975) have reported the fully-developed flow for a range of Dean numbers $96<Dp<5000$, where Dp is equal to:

$$Dp=(Ga^2/\mu)(2a^3\rho^2/\mu^2R_c)^{1/2} \tag{4.4}$$

In the above expression for Dean number, G is the constant pressure gradient along the bend. Since in the fully-developed situation, the axial pressure gradient along a duct becomes constant, the above definition which includes the G term is convenient for theoretical study. Dp=5000 corresponds to De=363.6; other relations between De and Dp can be found in Ward-Smith (1980). By using a simplified version of the governing differential equations in terms of stream-function and non-dimensional velocity and representing these two quantities by Fourier series, McConalogue and Srivastava obtained numerical solutions in the range of $96<Dp<600$. On the other hand, Collins and Dennis and Greenspan followed finite-difference techniques. All have shown that the friction factor ratio is a function of $De^{1/2}$ and that the radius at which the maximum velocity occurs 'r_{max}' increases asymptotically with Dean number.

On the analytical side, for higher Dean number, Barua (1963) proposed a secondary flow model which assumed (i) the flow domain to be divided into two distinct regions, one the viscous region near the wall and the other an inviscid core (see Fig.4.2a), and (ii) that the secondary flow was parallel to the plane of symmetry outside the boundary layer. Barua found that a separation of secondary flow (evidenced by the appearance of an extra vortex at the inner wall) occurs at about 27^{o} from the inner bend (i.e., lying between $180<\phi<153$ deg). However, the works of Ito (1969) and Collins and Dennis (1975) did not predict any such separation.

Van Dyke (1978) has extended Dean's analysis for all values of Dean numbers and showed that the friction factor ratio λ_c/λ_s increases asymptotically as $De^{1/4}$. For lower values of Dean number ($De \cong 100$) the analytically calculated friction factor ratios agree very closely with existing experimental (such as Adler, 1934) and numerical data (such as Barua, 1963), but for higher values of De the predictions are found to progressively under-predict all other data (which suggest that it increases as the square root of De). Van Dyke also comments that the Barua-like flow models (Fig.4.2a) are only of limited validity as the Dean numbers are raised and suggests that instead of one core flow and one boundary layer, a better approach would be to use multiple regions scaled according to various powers of De; although no specific strategy has been proposed.

4.2.2 Developing Flow

The entry flow in a curved pipe has been studied far less compared with the amount of work on fully-developed flow situations. Theoretical attempts to solve such flows were seriously hindered by the difficulty of making the simplifying assumptions which underly analytical approaches.

By using a perturbation of the developing flow in a straight pipe, Singh (1974) was able to obtain analytical solution in the very entrance region of a curved pipe upto a distance $0(a\delta^{1/2})$. Typical secondary velocity streamlines as obtained from his solution (see Fig.4.2b) shows that at the very inlet an inward flow from the entire pipe cross-section is induced as a result of the displacement of boundary layer. Two singularities were observed, one at the origin (point O) and the other slightly to the right (point P). As the flow moves downstream, the second singularity gradually moves towards the outside and eventually vanishes at the outer bend, which of course may be considered as a stagnation point once the cross-flow is established. He also showed that initially the wall shear stress in the outer bend is smaller than the inner because of flow acceleration and after some distance, a cross-over takes place and the shear on the outer wall becomes larger. The location of this cross-over was found to be dependent on the inlet boundary condition, for example, as was shown by Singh (1974), the cross-over takes place at $\theta=1.9\delta$ for an inviscid-vortex inlet and at $\theta=0.95\delta$ for uniform entry.

Yao and Berger (1975) have presented a model for the developing flow in a curved pipe for large Dean number. They derived two sets of equations; one for the inviscid-core flow and the other for the three-dimensional boundary layer following Barua's flow model.They found a separation of the cross-flow near the inner bend, the width (see the separation length in Fig.4.2a) of which was found to increase asymptotically as the flow moves downstream.

Soh and Berger (1984) have solved the entry flow into a curved pipe for Dean numbers of 108.2 to 680.3 for different curvature ratios. The full elliptic Navier-Stokes equations were solved using the artificial compressibility technique as developed by Chorin (1967). They have observed the separation of secondary flow in the developing region of the curved pipe. Similar to the experimental findings of Agrawal et al (1978), they have reported a two-step plateau like streamwise velocity profile and double peaked streamwise velocity contours along lines parallel to the plane of symmetry; these features will be illustrated more clearly in the predictions which follow.

Humphrey et al (1985) conducted numerical calculations on similar types of flows. By using a partially-parabolic version of the governing equations and adopting a parabolic sub-layer treatment near the walls, they have shown the behaviour of streamwise shear stress ($\partial u/u_0)/(\partial r/a)$ along the inner bend of the pipe and concluded that with increase of Dean number the longitudinal shear stress exhibits a progressive shift towards the analytical results of Stewartson, Cebeci and Chang (1980) which says that shear stress vanishes (i.e., separation takes place) at $Z=\theta(R_c/a)^{1/2}=0.943$ for $De=\infty$. Humphrey's prediction of a tendency towards longitudinal flow separation is associated with a smaller magnitude of circumferential shear stress near the inner bend (which may cause secondary flow separation as observed by Agrawal et al, 1978) at the same streamwise location; and hence are found to be consistent. The smaller value of the circumferential shear stress contradicts Stewartson's prediction but are in agreement with the experimental findings of Talbot and Wong (1982). However, even by using a higher order differencing scheme for the approximation of convection terms and special treatments near the walls, significant discrepancies can be observed between experimental data and numerical predictions of Humphrey et al (1985). The reasons are believed to be associated with uncertainty about the inlet boundary layer thickness, which is of critical importance for flow development in the entrance region.

In a recent Laser Doppler experiment on the entry flow into a 90^o bend of circular cross-section with a radius-ratio of $\delta=1/6$ and $De=286$, Bovendeerd et al (1987) have shown that the development of the streamwise velocity can be quite well explained from the secondary velocity field. The maximum secondary velocity was found to occur near the entrance to the pipe at an axial location of $\theta=39.8^o$. A weak separation of the secondary boundary layer near the inner bend at a downstream station of $\theta=58.5^o$ and $\theta=81.9^o$ was suspected which is in accordance with the numerical findings of Soh and

Berger (1984). In an attempt to quantify the overall acceleration-deceleration taking place near the entrance due to the sudden pressure gradient, the first moment of the streamwise velocity was calculated. This shows that the flow is directed towards the inner bend upto an axial distance of $\theta=11.7^o$. Similar analysis was made by Olson and Snyder (1985). However, the two sets of data are found to differ significantly in the entrance region which may be attributed to the differences in the inlet profiles.

4.2.3 Flow Through Rectangular Ducts

The study of flow through toroidally curved ducts having rectangular cross-section has also drawn much attention during the past few decades. Among others Mori, Uchida and Ukon (1971) have reported analytical and experimental results for a fully-developed laminar flow in a curved duct with square cross-section for a range of Dean numbers $19.8<De<389$.The hydraulic diameter used in the definition of De (Eq.4.2) is $D=4ml/(m+l)$ (see Fig.4.1b). Numerical calculations have been performed by Cheng, Lin and Ou (1976) on fully-developed laminar flow and they showed that for an intermediate range of Dean numbers $106<De<367.7$, an additional pair of counter rotating vortices appear near the central region of the outer wall of the bend. Khalil and Weber (1984) have also obtained numerical results for a developing flow in a square duct for low Dean number.

4.2.4 Conclusions Drawn from the Survey

The first point which appears from the brief literature review is the definition of Dean number. Various authors have proposed various definitions (Eqs.4.1, 4.2 and 4.4). However, the relation given by Eq.(4.2) is found to be the most popular because it employs the quantities which can be readily determined as well as it rests on a sound theoretical basis (Berger et al, 1983). In this thesis, this definition of Dean number has been followed throughout. Physically, the Dean number is equal to the ratio of the square root of the product of the inertia and centrifugal forces to the viscous force, and hence it provides a measure of the intensity of the secondary flow. In the case of fully-developed flow, there is still some controversy about the growth of λ_c/λ_s.

For developing flows, there is now enough evidence to believe that a secondary flow separation near the inner bend is a very likely phenomenon at higher Dean numbers, as this has been predicted by different numerical procedures and also has been verified experimentally (often qualitatively, because of very small magnitude of velocity). On the other hand, the behaviour of the longitudinal shear stress along the length of the duct is not well resolved. The experimental methods suffer from large uncertainties for such delicate phenomena while the numerical methods may over-predict or under-predict this type of flow characteristic due to various simplifying assumptions as well as due to inherent numerical errors.

Prescription of the correct inlet data is of utmost importance for a successful prediction of such flows. It has been shown by experimental measurements as well as by analytical solutions that the flow development in the downstream region is greatly influenced by the flow pattern in the very beginning of the flow.

The results which will be presented in this chapter put emphasis on the predictive ability of the adopted numerical method both for the fully-developed and the developing flow situations. Qualitative and quantitative comparisons are made with other works mentioned in this section and the reasons for the differences are discussed. However, before presenting the results, the numerical methodology for this particular study forms the topic of the next section.

4.3 Numerical Procedure

The geometry of a constant curvature and constant cross-section pipe is relatively simple and can be defined with respect to a toroidal coordinate system (r,θ,ϕ) as shown in Fig.4.1a. R_C in this figure represents the (constant) 'radius of curvature' of the curved duct which does not vary with streamwise direction θ. 'r' is the radius measured from the centre of the pipe cross-section and 'ϕ' is the angular position measured from the outside bend RO. For the rectangular duct (Fig.4.1b), 'y' and 'z' are the two coordinate directions over the cross-section. Both of these coordinate systems are orthogonal ; and hence, in order to derive the transport equations in these systems, the grid-oriented velocity vectors were chosen because of the advantages mentioned in Chapter 2. In the next sub-section the transport equations for laminar flow situations are presented.

4.3.1 The Governing Equations

The general transport equations for momentum conservation employing contravariant velocity components were given in Chapter 2 (Eq. 2.13). In an orthogonal coordinate system, this set of equations can be rewritten for steady incompressible fluid flow as:

$$\frac{1}{\sqrt{g}}\frac{\partial}{\partial \eta^j}[\sqrt{g}\,\rho g_{ii}^{1/2} V^i V^j] - \frac{1}{\sqrt{g}}\frac{\partial}{\partial \eta^j}[\mu\sqrt{g}\; g_{ii}^{1/2} g^{ij}\frac{\partial V^i}{\partial \eta^j}]$$
$$= S_F(i) + S_P(i) + S_D(i) - S_C(i) \qquad (4.5)$$

where, $S_F(i)$ = Body Force = $\rho f(i)$

$S_P(i)$ = Pressure Force = $- g_{ii}^{-1/2}\, p_{,i}$

$S_C(i)$ = Convection Source Terms=

$$\rho\, g_{ii}^{1/2} V^j \{{}_m{}^i{}_j\}\, V^m - \rho\, V^i V^j \frac{\partial g_{ii}^{1/2}}{\partial \eta^j}$$

$S_D(i)$ = Diffusion Source Terms=

$$\mu\, g_{ii}^{1/2}\; \{ \frac{1}{\sqrt{g}}\frac{\partial}{\partial \eta^j}[\sqrt{g}\; g^{jj}\{{}_k{}^i{}_j\}\, V^k]$$
$$+ g^{kk}\{{}_k{}^i{}_j\}\,[\frac{\partial V^j}{\partial \eta^k} + \{{}_m{}^j{}_k\}\, V^m]\} - \mu\, g^{jj}\frac{\partial V^i}{\partial \eta^j}\;\frac{\partial g_{ii}^{1/2}}{\partial \eta^j}$$

The continuity equation is:

$$\frac{1}{\sqrt{g}}(\sqrt{g}\;\rho\, V^i)_{,i} = 0 \qquad (4.6)$$

By making use of the relation between the contravariant and physical components (Eq.2.18) and expanding the nonvanishing Christoffel symbols (Eq. 2.10), the transport equations can be derived in the toroidal coordinate systems.

For the circular pipe, the equation of motion for a general variable ψ can be written as:

$$\frac{1}{r\, r_c}[\frac{\partial}{\partial r}(\rho r\, r_c\, v\, \psi) + \frac{\partial}{\partial \phi}(\rho r_c\; w\, \psi) + \frac{\partial}{\partial \theta}(\rho r\, u\, \psi)] + S_C(\psi)$$
$$= S_P(\psi) + \frac{1}{r\, r_c}[\frac{\partial}{\partial r}\{\mu r\, r_c \frac{\partial \psi}{\partial r}\} + \frac{\partial}{\partial \phi}\{\mu \frac{r_c}{r}\frac{\partial \psi}{\partial \phi}\} + \frac{\partial}{\partial \theta}\{\mu \frac{r}{r_c}\frac{\partial \psi}{\partial \theta}\}] + S_D(\psi) \quad (4.7)$$

where, $r_c = R_c + r\cos\phi$ and v,u,w are the velocity components in the r,θ,ϕ directions respectively (see Fig.4.1a). The expressions for the source terms are given in Table 4.1.

Table 4.1

Equation	Value of ψ	$S_P(\psi)$	$S_C(\psi)$	$S_D(\psi)$
Continuity Equation	1	0	0	0
u- momentum Equation	u	$-\frac{1}{r_c}\frac{\partial p}{\partial \theta}$	$\frac{1}{r}\rho vu\cos\phi$ $-\frac{1}{r_c}\rho wu\sin\phi$	$\frac{2\mu}{r_c^2}(\frac{\partial v}{\partial \theta}\cos\phi-\frac{\partial w}{\partial \theta}\sin\phi-\frac{u}{2})$
v- momentum Equation	v	$-\frac{\partial p}{\partial r}$	$-\frac{\rho w^2}{r}-\frac{\rho u^2\cos\phi}{r}$	$-\frac{\mu}{r^2}(2\frac{\partial w}{\partial \phi}+v)+\frac{\mu w}{rr_c}\sin\phi$ $+\frac{\mu\cos\phi}{r_c^2}(w\sin\phi-v\cos\phi-2\frac{\partial u}{\partial \theta})$
w- momentum Equation	w	$-\frac{1}{r}\frac{\partial p}{\partial \phi}$	$\frac{1}{r}\rho vw$ $+\frac{1}{r_c}\rho u^2\sin\phi$	$\frac{\mu}{r^2}(2\frac{\partial v}{\partial \phi}-w)-\frac{\mu}{rr_c}v\sin\phi$ $-\frac{\mu}{r_c^2}\sin\phi(w\sin\phi-v\cos\phi-2\frac{\partial u}{\partial \theta})$

For the rectangular duct (see Fig. 4.1b), the equations of motion for a general variable ψ can be written as:

$$\frac{1}{r_c}[\frac{\partial}{\partial y}(\rho r_c v\,\psi)+\frac{\partial}{\partial z}(\rho r_c w\,\psi)+\frac{\partial}{\partial \theta}(\rho u\,\psi)]+S_C(\psi)$$
$$=S_P(\psi)+\frac{1}{r_c}[\frac{\partial}{\partial y}\{\mu r_c\frac{\partial \psi}{\partial y}\}+\frac{\partial}{\partial z}\{\mu r_c\frac{\partial \psi}{\partial z}\}+\frac{\partial}{\partial \theta}\{\frac{\mu}{r_c}\frac{\partial \psi}{\partial \theta}\}]+S_D(\psi) \quad (4.8)$$

where, $r_c= R_c+y$ and v,u,w are the velocity components in the directions of y,θ,z respectively. The source terms are shown in Table 4.2.

Table 4.2

Equation	Value of ψ	$S_P(\psi)$	$S_C(\psi)$	$S_D(\psi)$
Continuity Equation	1	0	0	0
u-momentum Equation	u	$-\frac{1}{r_c}\frac{\partial p}{\partial \theta}$	$\frac{\rho u v}{r_c}$	$\frac{2\mu}{r_c^2}\frac{\partial v}{\partial \theta}-\frac{\mu u}{r_c^2}$
v-momentum Equation	v	$-\frac{\partial p}{\partial y}$	$-\frac{\rho u^2}{r_c}$	$-\frac{2\mu}{r_c^2}\frac{\partial u}{\partial \theta}-\frac{\mu v}{r_c^2}$
w-momentum Equation	w	$-\frac{\partial p}{\partial z}$	0	0

It should be mentioned that the above equations are identical to those given in Berger, Talbot and Yao (1983), although their forms are slightly different to these.

4.3.2 Boundary Conditions

A. Circular Pipe

i) Inlet plane: Strictly speaking, the inlet conditions can only be determined by solving the developing flow simultaneously with the flow development before fluid enters into the curved portion of the pipe. Hence, setting an inlet profile is an approximate one. The experimental results of Agrawal et al (1978) show that when a fluid moves from a stagnant condition (usually called a reservoir) to a curved duct, the velocity profile immediately after the reservoir (i.e.,$\theta=0^o$) develops to an inviscid free vortex with its centre at the centre of curvature of the pipe. Following this observation , an inviscid vortex profile $u=R_c u_o/(R_c+r\cos\phi)$, was chosen for the streamwise velocity at inlet. The radial and circumferential velocities were assumed to be equal to zero i.e., v=w=0. The implication of the wall boundary condition implies that the inlet boundary layer thickness is determined by the position of the grid-node nearest to the wall.

ii) Wall: No-slip boundary conditions were imposed for all the velocity components on the walls. That is $u=v=w=0$.

iii) Outlet plane: The outlet plane was assumed to be at such a far removed distance that the flow variables do not vary strongly along the streamwise coordinate. For the Dean number range considered in this chapter it was found from other works that $\theta=180^{o}$ can be chosen safely as the outlet plane. A zero gradient boundary condition was therefore assumed for all the velocity components. That is:

$$\partial u/\partial\theta=\partial v/\partial\theta=\partial w/\partial\theta=0.$$

iv) Plane of symmetry: Since there is a plane of symmetry (see Fig. 4.1a) for the flow configuration investigated, the present calculations in the circumferential direction fall within the range of $0\leq\phi\leq\pi$. The boundary conditions on the plane of symmetry were:

$$\partial u/\partial\phi=\partial v/\partial\phi=0 \text{ and } w=0.$$

v) Boundary conditions at the centre: Since the calculations started from the centre i.e., $r=0$ or $I=1$ (see Fig.4.3a), one needs to specify the boundary conditions at that point. For an axi-symmetric pipe flow the obvious choice is to put the radial gradients of all dependent variables to zero. But in this case the situation is different. The main difficulty is that at $r=0$, there are many coincident nodes each corresponding to a different circumferential angle $\phi(J)$. For this investigation, streamwise velocity u at $I=1$ was taken to be the average of the u's at the neighbouring nodes i.e.,

$$u(1,J,K)=\sum_{J=1}^{J=MP1} u(2,J,K)/MP1$$

where $J=1$ and $J=MP1$ corresponds to $\phi=0$ and $\phi=\pi$ radians respectively. A problem arises with the v and w components at the centre. At $r=0$ there is a component of velocity v_{res} which acts along the symmetry plane. The resultant of v and w at the centre should be the same for all circumferential angles and should be equal to v_{res}, which is calculated as:

$$v_{res}=0.5(v(3,1,K)+v(3,MP1,K))$$

It should mentioned that the radial grid location ($I=3$) arises as a result of grid staggering.

The v and w components are taken to be:

$$v(1,J,K)=v_{res}\sin\phi$$
$$w(1,J,K)=v_{res}\cos\phi$$

Humphrey et al (1985) have adopted the same approach for finding the radial and circumferential components at the centre.

B. Rectangular Duct

i) Inlet plane: A uniform streamwise velocity was assumed in the θ direction following Khalil and Weber (1984). The other two components, v and w were set to be zero.

ii) Walls: No-slip boundary conditions were employed for all the velocity components.

iii) Plane of symmetry: It can be seen from Fig.4.1b that for this flow domain, $z=0$ is a plane of symmetry. So the calculations were performed for only one-half of the cross-section. The boundary conditions employed for this plane were:

$$\partial u/\partial z=\partial v/\partial z=0 \text{ and } w=0.$$

iv) Outlet plane: A zero gradient boundary condition was employed at $\theta=110^{o}$. Since the Dean number of this flow was taken to be smaller than those considered for the circular pipe (to be descrbed in §4.4), a smaller value of θ was sufficient for this study.

4.3.3 Summary of the Solution Method

The partial differential Eqs.(4.7-4.8) were discretised in a finite volume fashion as described in Chapter 3. A non-uniform staggered grid system was chosen for the velocity components (see Fig.4.3). Pressure was stored at the main grid nodes while the velocity components were stored midway between the nodes. As a result of the discretisation, the exact transport equations were cast into an algebraic form (Eq. 3.15) suitable for an iterative solution. For the calculation of pressure, the pressure-correction equation was derived following Patankar (1980). The SIMPLE algorithm has been followed as usual. In order to approximate the convection terms the Hybrid differencing scheme (Spalding, 1972) has been adopted.

4.4 Results and Discussion

Numerical calculations were performed for circular and rectangular ducts with different curvature and flow rates. For a circular sectioned pipe, computations were carried out for δ=1/7, De=183; δ=1/20,De=370.6 and δ=1/20, De=566; and for the square sectioned duct δ=1/27.8, De=38.9. These particular values have been chosen because of the availability of experimental and numerical data for these flow situations.

4.4.1 Convergence and Grid Dependence

The convergence criterion was chosen to be the sum of the individual mass source errors of the cells normalized by the total flow rate. The solution was assumed to be converged when the normalized mass source residual was less than 0.5%. The computations were done on the Amdahl V8 computer at the University of London Computer Centre. CPU time varied between 1600 and 4000 seconds increasing with Dean number. For a Dean number of 183, δ=1/7 (Re=484), CPU required was about 1600 seconds and for the same Reynolds number for a straight pipe it was about 1200 seconds.

A typical convergence pattern (De=183) is shown in Figs.4.4a and 4.4b. ICYCL is the computer programme variable which controls the number of solution sweeps (see section 3.7) through different equations; the first value corresponds to the momentum equations and the second that for the pressure-correction equation. It may observed that with ICYCL/3,30/ the solution converges with fewer iterations than with ICYCL/1,3/. However, the total CPU required is significantly less for ICYCL/1,3/. So, for all the calculations the number of sweeps were taken to be one and three for the momentum and pressure-correction equations respectively.

Usually a non-uniform 20x20x30 (in the r, ϕ and θ directions respectively) staggered grid system (see Fig.4.3) has been employed for the present numerical computations. The dependence of streamwise velocity on grid density for De=566, δ=1/20 (this was found to be the most sensitive to grid refinement) is shown in Figs.4.5a-b. Even when the grid density was increased to 36x36x54 the variations were found to be very small (less than 4%). Hence, all the results presented here were obtained with the other grid arrangement. For convenience, the results obtained are discussed under two different headings viz., fully-developed and developing flows.

4.4.2 Fully-developed Flows

The flow was considered to be fully-developed when there was no appreciable change of flow field with increasing streamwise distance along the duct. The zero-gradient boundary condition at exit is justified only for such a situation and, fortunately, for all the range of Dean numbers considered in this study it was possible to attain a situation where the flow can be called 'fully-developed'. (It may be mentioned here that, at the exit there were very slight oscillations in the v and w components, which was considered to have no significant influence on the overall flow field).

In Fig.4.6a, the fully-developed streamwise velocity,u on the plane of symmetry for $\delta=1/20$, De=370.6 is compared with experimental data of Adler (1934) and computational results by Collins and Dennis (1975). The isovelocity contours of the normalized streamwise velocity (equal to $(2a^3\rho^2/\mu^2R_c)^{1/2}u$) are shown in Fig.4.6b. For both cases excellent agreement can be seen. The maximum velocity is found to occur on the plane of symmetry. It can be observed from Fig.4.7 that the position of maximum axial velocity, r_{max}/a varies asymptotically with Dp and the present results are in close agreement with those obtained by Collins and Dennis. The magnitude of the maximum axial velocities (normalized by u_0) were found to be 1.66, 1.65 and 1.61 for Dean numbers of 183, 370.6 and 566 respectively. It is observed that with increase of Dean number the value of maximum velocity decreases which is in accordance with the findings of Soh and Berger (1984).

Fully-developed streamwise velocities for the square duct ($\delta=1/27.8$, De=38.9) are presented in Fig.4.8. The results in Fig.4.8a are very close to the computations by Khalil and Weber (1984). Both results are found to over-predict the peak experimental values of Mori et al (1971) by about 10-15%. The reason for the discrepancy between the measurements and both the predictions has not been fully understood, although some doubt has been cast regarding the accuracy of measurements. The magnitude of the normalized maximum velocity is found to be 1.9 and it occurs on the plane of symmetry at a point (0.261,0) (see Fig.4.1b). The isovelocity contours plotted in Fig.4.8b show a steeper gradient near the outer wall of the duct cross section. This configuration of isovels can be observed also for circular pipes (Fig.4.6b), and is a consequence of centrifugal forces linked to the secondary flow.

The variation of pressure at several selected positions along the whole length of pipe are shown in Fig.4.9a-d. The pressures are normalized as $Cp=(p-p_{ref})/0.5\rho u_0^2$, where p_{ref} is taken on the centre-lines of the ducts at locations corresponding to Cp=0. From these plots λ_c/λ_s, the ratio of fully-developed friction factor for a curved pipe to that for a straight pipe for the same Reynolds number can be found as follows:

$$\lambda_c/\lambda_s = (\partial p/\partial \theta)_c/(\partial p/\partial \theta)_s = (1/16)\ \mathrm{Re}\delta\ (\partial p/\partial \theta)_c$$

The results are shown in Fig.4.10. The present calculations are compared with other authors and it can be seen that the computed results show closer agreement with those of Collins and Dennis and suggests that the friction factor ratio grows as $De^{1/2}$ and not $De^{1/4}$ as obtained by Van Dyke (1978).

The ratio of friction factors for the square duct has been calculated as:

$$\lambda_c/\lambda_s = (\partial p/\partial \theta)_c/(\partial p/\partial \theta)_s = (1/28.45)\ \mathrm{Re}\delta\ (\partial p/\partial \theta)_s$$

and from the single computation carried out at De=38.9, it was found to be 1.216. Cheng et al (1976) have proposed an empirical correlation for friction factor ratio for different aspect ratios (m/l , see Fig. 4.1b) of the cross-section as:

$$\lambda_c/\lambda_s = K_0 E^{1/2}[1+K_1 E^{-1/2}+K_2 E^{-1}+K_3 E^{-3/2}+K_4 E^{-2}]$$

where $E=\sqrt{2}De$. For m/l=1; the values of K_0, K_1, K_2, K_3, K_4 are 0.1278, -0.257, 0.669, 187.7 and -512.2 respectively. Using this correlation for De=38.9, $\lambda_c/\lambda_s=1.202$ which is very close to the computed value.

The longitudinal shear stresses are shown in Fig.4.19a-c. For the fully-developed situations it is found that the ratio of shear stress at the outer bend to that at the inner bend increases with Dean number, the ratios being 2.38, 4.04 and 5.5 for De=183, 370.6 and 566 respectively.

4.4.3 Developing Flows

4.4.3.1 Streamwise Velocity

The development of streamwise velocity u on the plane of symmetry of the ducts is shown in Figs.4.11 and 4.12. As the flow enters the curved duct it experiences an adverse pressure gradient at the outer bend and a favourable pressure gradient at the inner bend. The obvious effect is that the main flow is accelerated on the inside and decelerated on the outside. This phenomenon can be clearly observed from Fig.4.11a (De=183) upto $\theta=12.75^{\circ}$. After this initial zone, the boundary layers start developing both on the inside as well as on the outside of the bend. The rate of growth of the boundary layer near the inner bend is much faster than that near the outer bend. Initially, there are two distinct regions in the streamwise velocity profiles viz., a) the boundary layers near the walls and b) the potential core (represented by the flat zone of streamwise velocity). As the flow moves downstream the boundary layers occupy more space with gradual diminution of the potential core. The position of maximum velocity is found to be shifted towards the outer wall and in the fully-developed state it represents the border where both the layers collide. For the higher Dean number plots (Fig.4.11b and 4.11c), two-step plateau like profiles can be observed for streamwise locations of θ=48.5 and 62.2 degree. Such a profile is supported by the experimental results of Agrawal et al (1978). On the other hand, for lower Dean numbers a smooth development of the boundary layers is found to occur both for the circular and square ducts (see Fig.4.11a and 4.12a-b).

The development of flow in a curved pipe is much faster than that in a straight pipe. The main reason being that in the latter case it is mainly controlled by the molecular viscous effect because the secondary flow is very small. Whereas for curved pipes secondary flows are very significant , this is illustrated for the current predictions in Figs.4.14,4.15 and 4.18. The secondary streams carry fluid from the inside of the bend to the outside along the plane of symmetry, and towards the inside along the circumference. This explains why the thickness of the boundary layer near the outer bend is so small compared to that at the inner bend. The secondary flow acts on the outer bend in a way as if 'squeezing' the boundary layer there.

An important feature of the streamwise isovelocity contours is the appearance of double peaks with increased Dean number (De=566) as shown in Fig.4.13a -b. In Fig.4.13a and 4.13a' the isovelocity contours are plotted at an axial location of $\theta=83^{\circ}$. Although there are some discrepancies with the experimental results of Agrawal et al (1978), the qualitative behaviour of the contours are very close to each other. The double peak nature is found to persist even in the fully-developed situation (Fig.4.13b). The experimental results by Bovendeerd et al (1987) also confirm this double-peak nature of the axial isovelocity contours. For lower Dean number flows no such pattern can be observed for the isovelocity contours (Fig.4.6b).

The streamwise velocity attains fully-developed state at about θ=140,120 and 140 degrees for De=183, 370.6 and 566 respectively for the circular sectioned pipe. Whereas for the square duct the flow develops at about θ=80 deg. For circular pipe, Austin et al (1973) proposed a correlation for the length required for the attainment of fully-developed state, given by $\theta=49(De\delta^{1/2})$ degrees. It is found that this correlation over-predicts the required length by about 6-10%.

4.4.3.2 Development of Secondary Velocity

A secondary velocity is set up immediately after the flow enters the curved duct. In Figs.4.14a-h and 4.15a-h, the secondary flow streaklines (analogous to a flow visualization; obtained by tracking weightless particles through the respective planes for a time of 0.3 sec) are presented for two circular duct cases (δ=1/7, De=183 and δ=1/20, De=566). For the square duct, velocity vectors were plotted at different streamwise locations along the bend and are given in Fig.4.18a-h.

It can be seen from Figs.4.14a and 4.15a that just after the inlet (θ= 3 deg), a secondary velocity of considerable magnitude acts radially inward. This is due to the displacement effect of the boundary layers as the flow enters into the bend. The analytical results of Singh (1974) also produces similar secondary flow pattern (see Fig.4.2b). After this zone the secondary velocities near the wall become parallel to the curved surface with a gradual development of the circumferential shear layer. The velocities near the outer wall change direction and give rise to a vortex structure. The location of the vortex centre changes position fron near the outer bend towards the inner as the flow moves downstream. For δ=1/7, De=183, the vortex centre is found to be at r/a=0.73,$\phi=61^o$ at $\theta=15^o$ (Fig.4.14c) whereas at $\theta=167.5^o$ (Fig.4.14h) it is at r/a=0.66,$\phi=95^o$. For δ=1/20, De=566 the vortex centre is found to occur at r/a=0.78,$\phi=33^o$; r/a=0.75,$\phi=115^o$ and r/a=0.75,$\phi=121^o$ for θ=8, 20 and 140 degrees respectively (see Figs.4.15b,c,g). With increase of Dean number the vortex develops a tail which extends towards the outer wall. The experimental work of Bovendeerd et al (1987) also reported such a tailed-vortex. This elongated vortex is probably the reason for the existence of double peaks in the streamwise isovelocity contours mentioned previously. For lower Dean number flow, no distortion of the vortex takes place.

The development of the circumferential velocity w, along the meridional plane ($\phi=90^o$) is shown in Fig.4.16a-c. For each of the three cases, the secondary velocity reaches its maximum in the early stages of flow development and then decreases slightly in the downstream direction. The magnitudes and locations of the maximum circumferential velocities (normalized by u_0) are 0.264 at $\phi=94.5^o$ and at $\theta=69.9^o$ for De=183 (δ=1/7); 0.177 at $\phi=106^o$ and at $\theta=34.75^o$ for De=370.6 (δ=1/20); 0.179 at $\phi=116^o$ and at $\theta=31.5^o$ for De=566 (δ=1/20). It is found that for the same δ, the maximum circumferential velocity is rather insensitive to Dean number (a 50% increase in Dean number causes an increase of only 1% for the maximum w). On the other hand, it is strongly dependent on the radius-ratio δ.

As the Dean number increases, the cross-sectional location, ϕ of the maximum circumferential velocity w, shifts more towards the inner bend i.e., $\phi=180^o$ (For an increase of De from 370.6 to 566, the circumferential location shifts from 106° to 116°). Hence, the length between the inner bend and the point of maximum w, decreases with increasing Dean number; and in order to satisfy the boundary condition constraint of $w=0$ at $\phi=180°$, the deceleration of secondary velocity also increases with De. As a result, at higher Dean numbers the inflowing secondary fluid may not turn smoothly around the curved wall near the inner bend and this may give rise to separation of the secondary boundary layer. In the present calculations, a weak separation of this nature has been observed for De=566 case and it occurred between $\theta=38°$ and 52°. The profiles of w at a streamwise section of $\theta=45°$ are shown in Fig.4.17a. The existence of this separation can be better seen from the circumferential shear stress $(\partial w/u_0)/(\partial r/a)$ plots (Fig.4.17b). A magnified (x20, only along the ordinate) view of the separation region is shown in the inset. It can be seen that the separation bubble was within the last 10° ($170<\phi<180$ deg) of the cross-section. The shear stress for the fully-developed state ($\theta=167.5$ deg) is shown for comparison.

Figure 4.18 shows vector plots of secondary velocity for the square duct. Similar to the circular ducts, a radially inward nature of the secondary flow can be seen just after the inlet ($\theta=2$ deg). The effects due to the pressure gradient and boundary layer displacement can be observed very clearly from the shifting of the directions of secondary velocities in the downstream locations (Fig.4.18b and 4.18c). The pattern of development in this initial region resembles Singh's (1974) solution, shown in Fig.4.2b. Movement of the off-centred singularity towards the outer bend is confirmed, while the singularity at the origin appears to be unrealistic and is probably an outcome of the analytical solution. Finally the vortex takes a regular structure with its centre pushed nearer the outer wall. As the vortical flow carries fluid from the outer to the inner bend along the wall, a secondary boundary layer is developed, which 'pushes' the fluid particles towards the plane of symmetry. This explains why the flat zone of the isovelocity contours is found to be inclined towards the symmetry plane as shown in Fig.4.8b.

The maximum value of the secondary velocity v, was found to be $0.131u_0$ and it occurred on the plane of symmetry at a streamwise location of $\theta=36°$. In the fully-developed state, the maximum v decreases to a value of $0.113u_0$ and again it occurs on the symmetry plane. It can be seen that the intensity of the secondary flow (when normalized by the corresponding bulk velocities) is much less in comparison to the circular ducts, which is due to the combined effect of smaller values of δ and De. However, in this case the maximum secondary velocity occurs on the plane of symmetry rather than near the wall for the circular ducts.

4.4.3.3 Longitudinal Shear stress

The variations of longitudinal wall shear stress (equal to $(\partial u/u_0)/(\partial r/a)$) with axial distance ($Z=\theta(R_c/a)^{1/2}$) at $\phi=0$ deg (outer bend) and $\phi=180$ deg (inner bend) are shown in Fig.4.19a-d. It can be observed from Fig.4.19a-c that the stress at the outer bend takes much longer to attain its maximum value. The magnitude of the stress at the outer bend is largely dependent on the Dean number and with increase of Dean number this value increases. But the magnitude of the shear stress at the inner bend gradually goes down but this is not found to be very dependent on the Dean number. Comparison is also made with numerical results of Humphrey et al (1985) and experimental measurements of Talbot and Wong (1982).

The two shear stresses at the outer and inner bends are found to cross-over near the entrance region. With smaller values of δ the cross-over takes place at a much earlier streamwise section. For $\delta=1/7$, De=183, cross-over occurs at $\theta=19$ deg. Whereas for $\delta=1/20$, cross-over takes place at $\theta=9^o$ and 8.3^o for Dean numbers of 370.6 and 566 respectively. Singh's (1974) analytical solution suggests that this cross-over point (for the inviscid vortex inlet profile) should be at $\theta\cong180\delta/\pi$ degrees, and the locations calculated are 15.6 deg (for $\delta=1/7$) and 5.5 deg (for $\delta=1/20$) respectively. The agreement for both the ducts can be taken to be reasonably good given the present streamwise resolution in this very entrance region.

In Fig.4.19d, comparison of shear stress at the inner bend is made with other authors for a large Dean number of De=1356, $\delta=1/7$. The experimental data seem to imply a local maximum in shear stress, although this relies heavily on one data point at Z=2.6. The present calculations show a very slight maximum, and the calculations of Humphrey et al (1985) indicate a much larger oscillation. The discrepancy between the calculations may be due to differences between the two numerical techniques (partially-parabolic by Humphrey's and fully elliptic in the present study) and prescription of inlet conditions; although the present mesh density (20x20x30 as against 28x20x150 grid nodes by Humphrey's) may be too coarse to pick up such variations accurately.

4.5 Conclusions

The characteristics of laminar flow through toroidally curved circular and square cross-sectional ducts have been presented in this chapter. Both the fully-developed and the developing flows were studied and the results compared with available numerical and experimental data for their validation. The important observations of this study are summarized as follows.

The flow pattern in a curved duct depends primarily on two parameters viz., the radius ratio, δ and the Dean number, De.The flow structure becomes more complicated as the Dean number is raised. This is evidenced by the appearance of a two-step plateau like streamwise velocity profile, distorted vortex structure for the seconday velocities and a separation of the secondary boundary layer near the inner bend.

For the range of Dean numbers considered in this study, the flow domain shows two distinct regions, one the potential core and the other the slower moving viscous layer close to the wall. The flow development is an outcome of the interaction of the viscous, inertia and centrifugal forces.

The longitudinal shear stress at the inner bend develops much faster than that at the outer bend. The magnitudes of the shear stress at the outer bend is found to increase significantly with Dean number.

In the fully-developed state, the ratio of friction factors is found to grow as $De^{1/2}$ for circular pipe.

The results of this chapter have, most importantly, established a background for subsequent numerical analyses of similar but more complicated turning flows. The ability of the CFD approach to simulate all important physical phenomena in viscous turning flows has been demonstrated and, for example, the density of numerical mesh which can adequately resolve these features has been established, without introducing the added complexity of non-orthogonal mesh. In the next chapter, an assessment of the general non-orthogonal computer code is first made, and then the 'proven code' is applied to the prediction of flow through other types of curved ducts similar to these in this chapter, but with upstream and downstream tangents and with the added complications of turbulence and area variation.

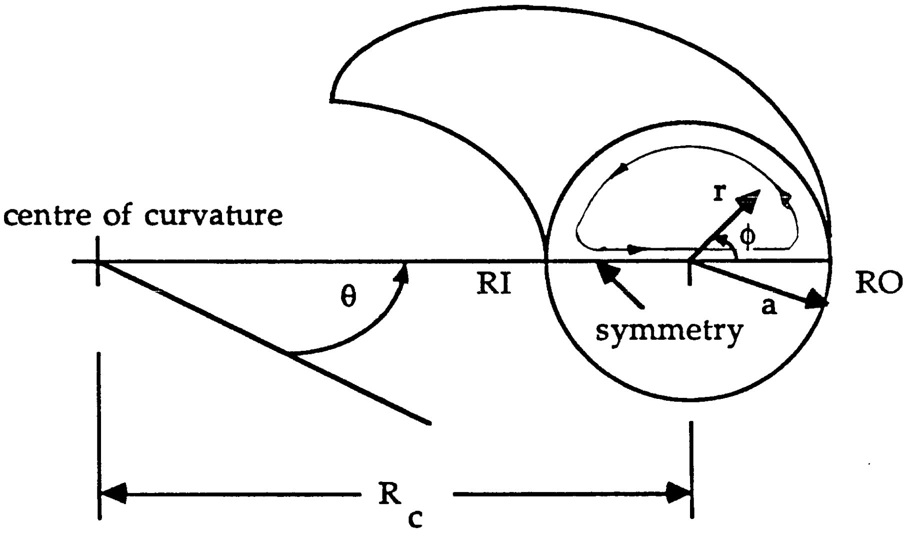

(a)

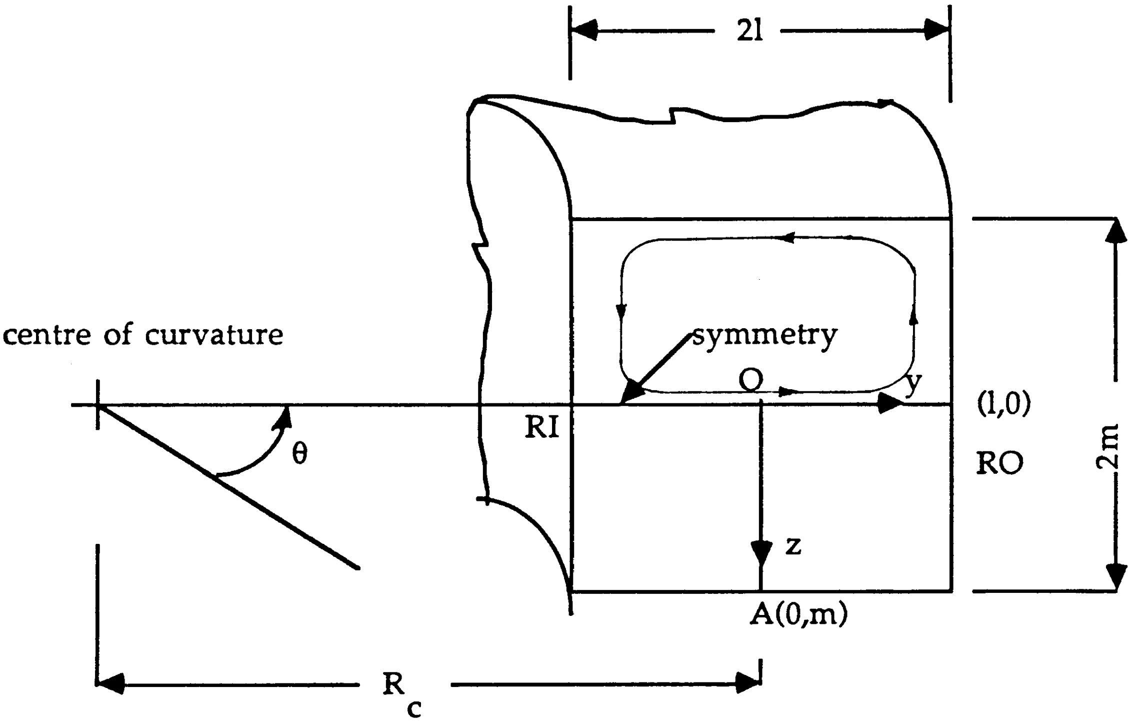

(b)

Fig. 4.1 Coordinate systems for (a) Circular pipes and (b) Rectangular duct

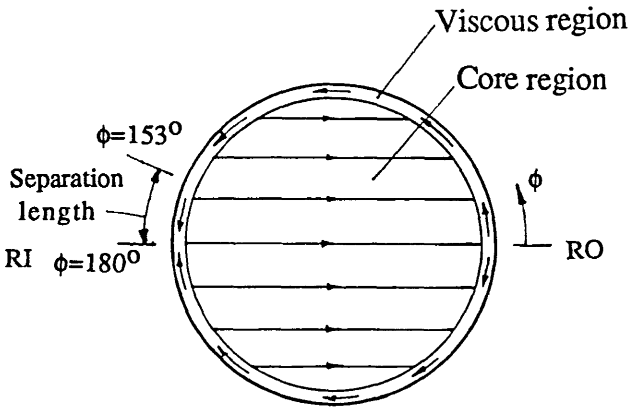

Fig. 4.2a Idealized flow model of Barua (1963)

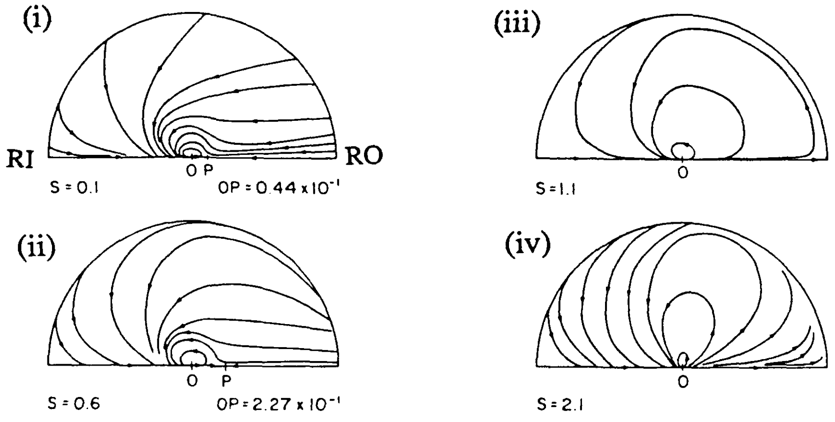

Fig. 4.2b Predicted streamlines of flow in the entrance region in a curved pipe (Singh, 1974). 's' denotes the non-dimensional curved length along the streamwise direction given by $s=\theta/\delta$.

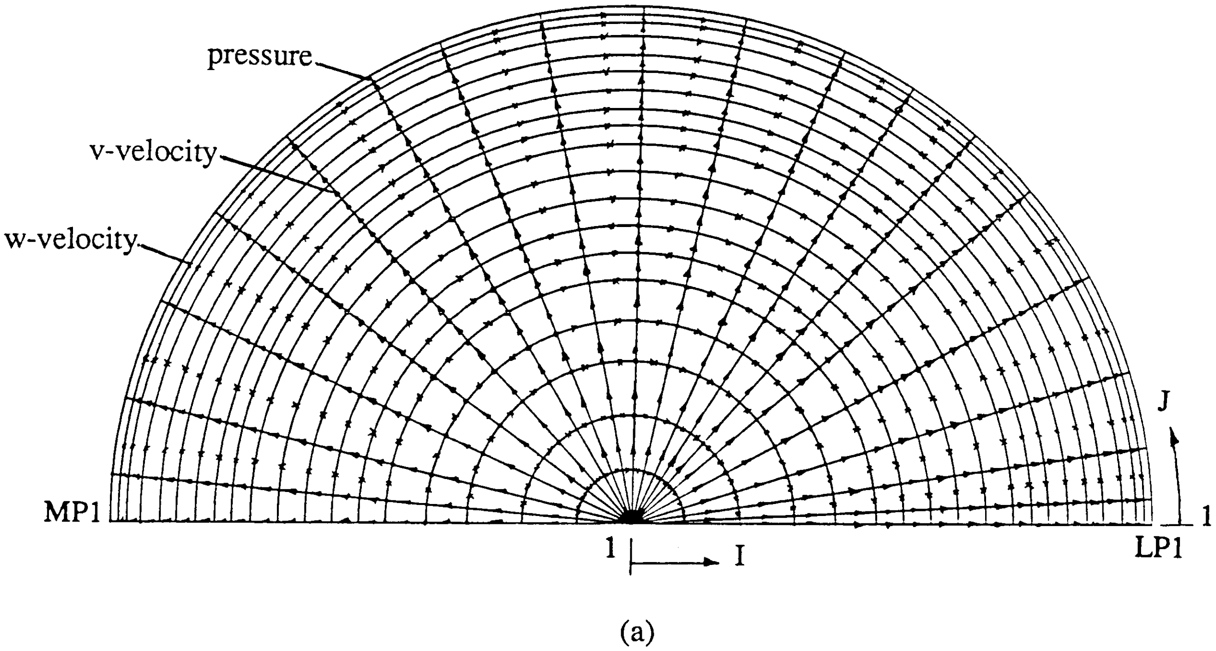

(a)

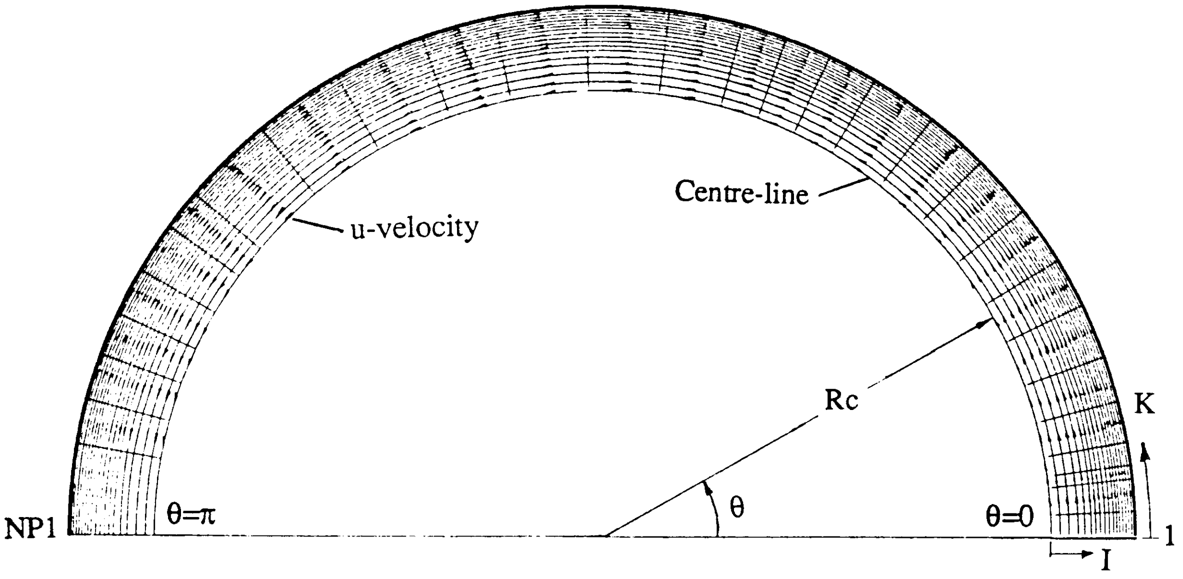

(b)

Fig. 4.3 (a) Grid arrangement in the cross-section of circular pipe (Plane I-J)
(b) Grid arrangement on the plane of symmetry (Plane I-K)

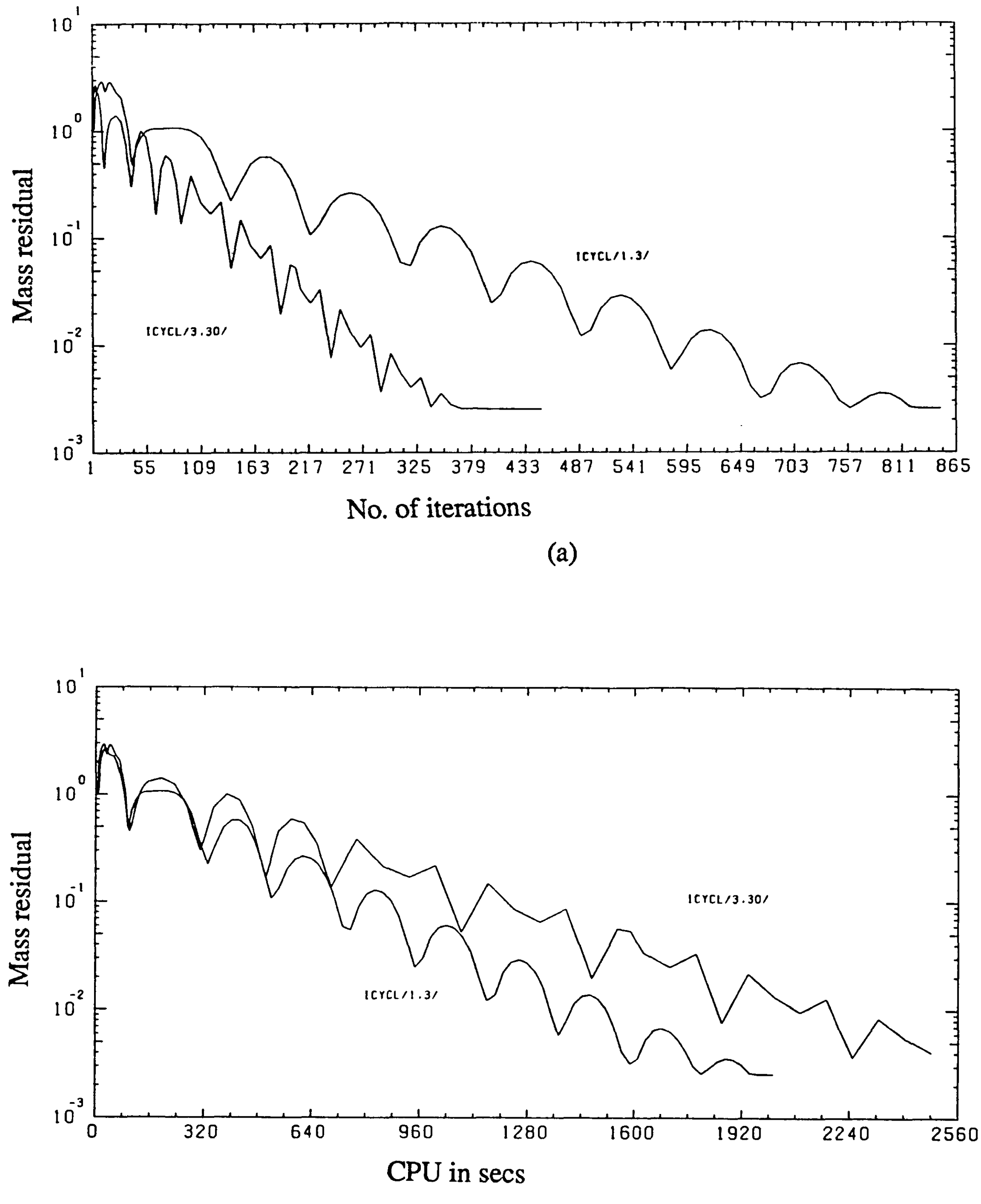

(a)

(b)

Fig. 4.4 Convergence pattern for circular pipe; δ=1/7, De=183

(a) Mass residual vs. No. of iterations

(b) Mass residual vs. CPU

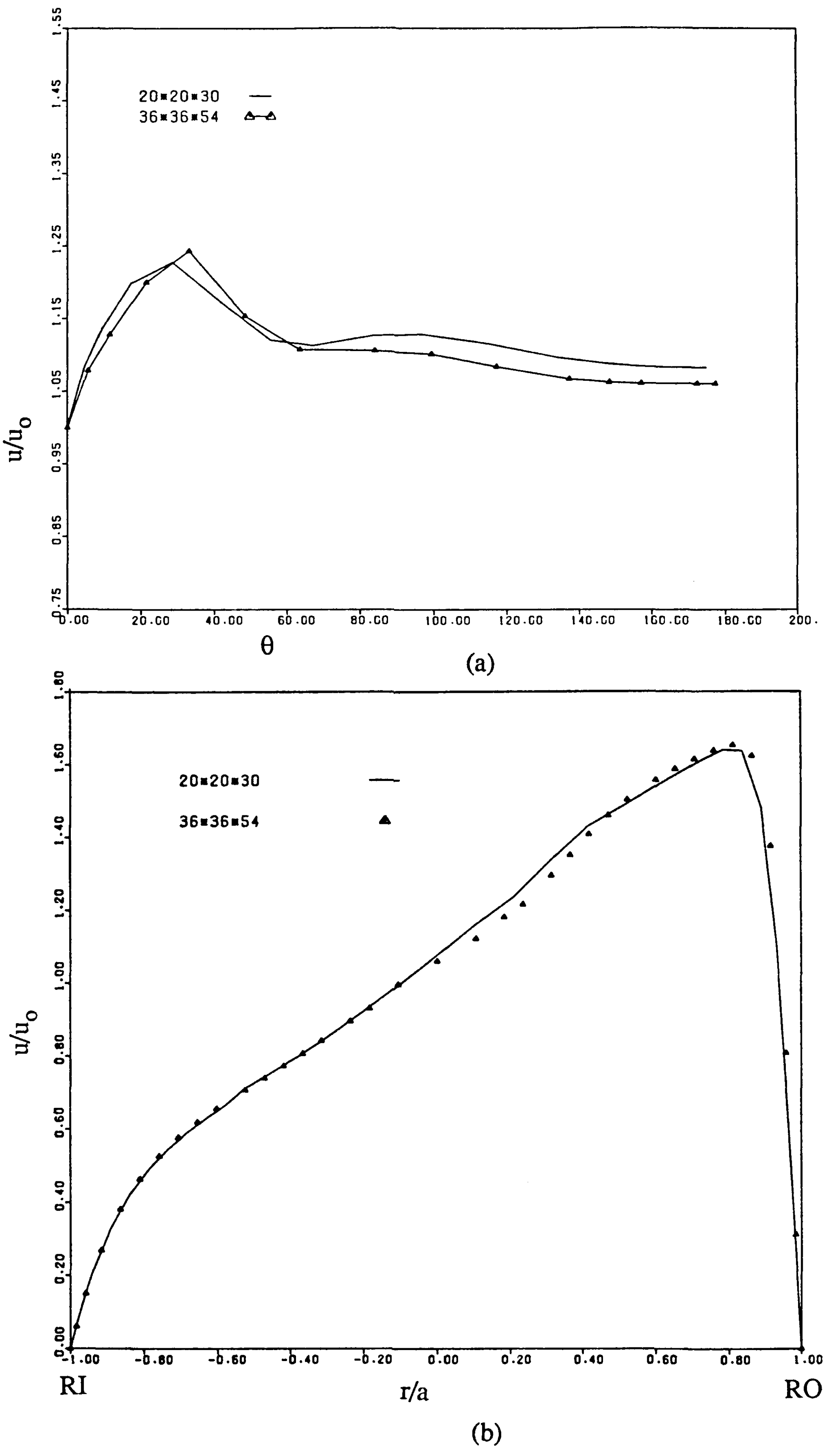

Fig. 4.5 Effect of grid density on streamwise velocity; δ=1/20, De=566

(a) Centre-line velocity vs. θ

(b) Fully-developed velocity on the symmetry plane at θ=167.5 deg

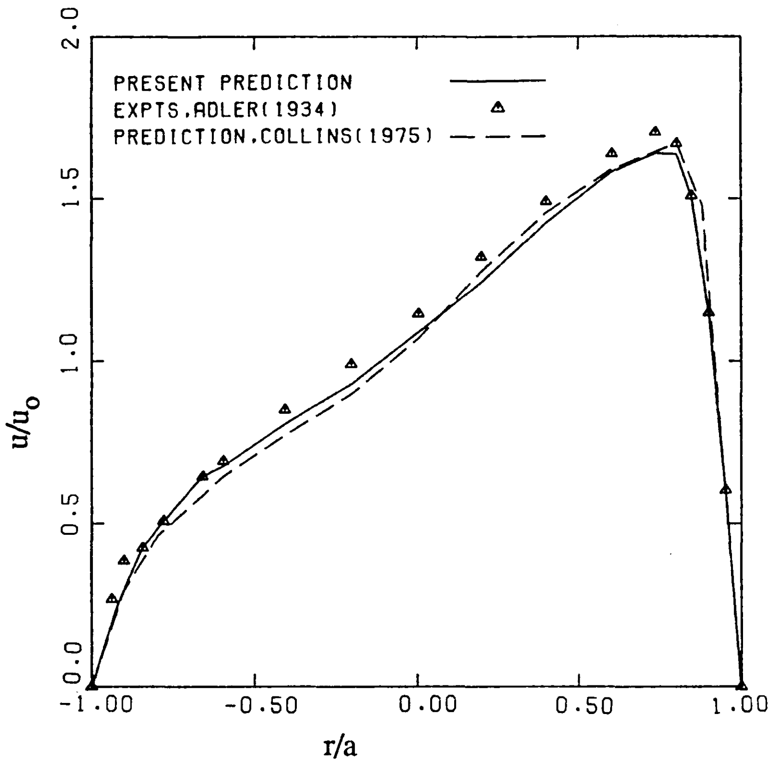

(a)

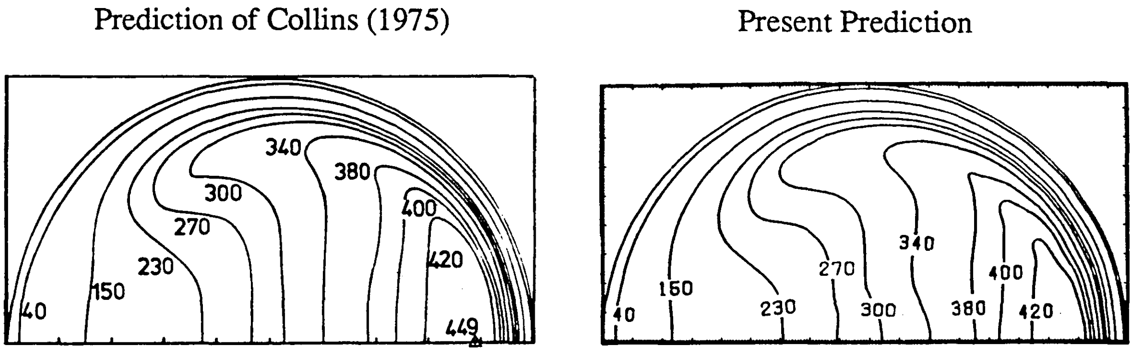

(b)

Fig. 4.6 (a) Fully-developed streamwise velocity on the symmetry plane; De=370.6
(b) Fully-developed streamwise velocity (normalized) contours; De=370.6

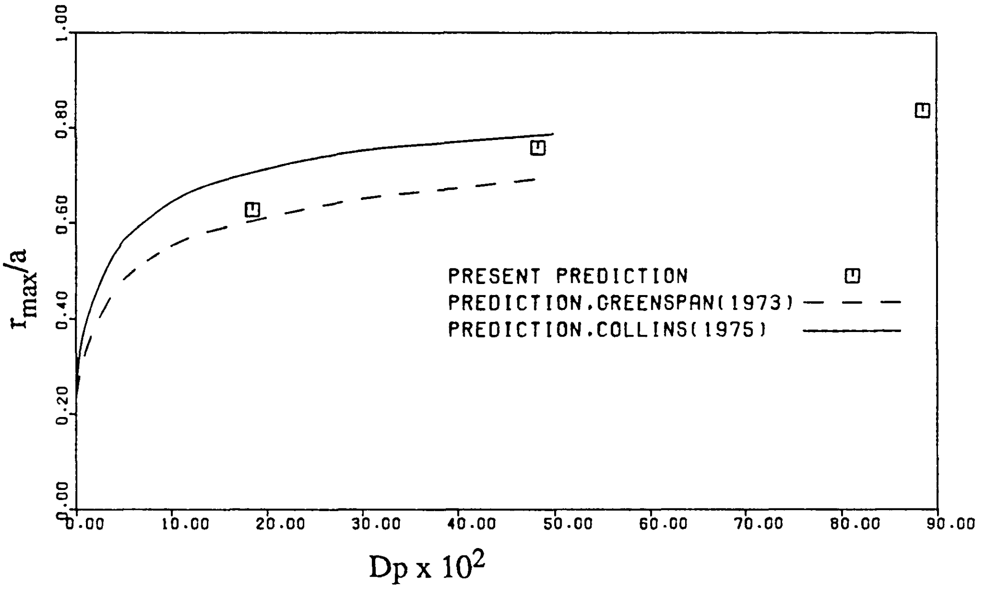

Fig. 4.7 Variation of position of maximum streamwise velocity, r_{max}/a vs. Dp for circular pipes

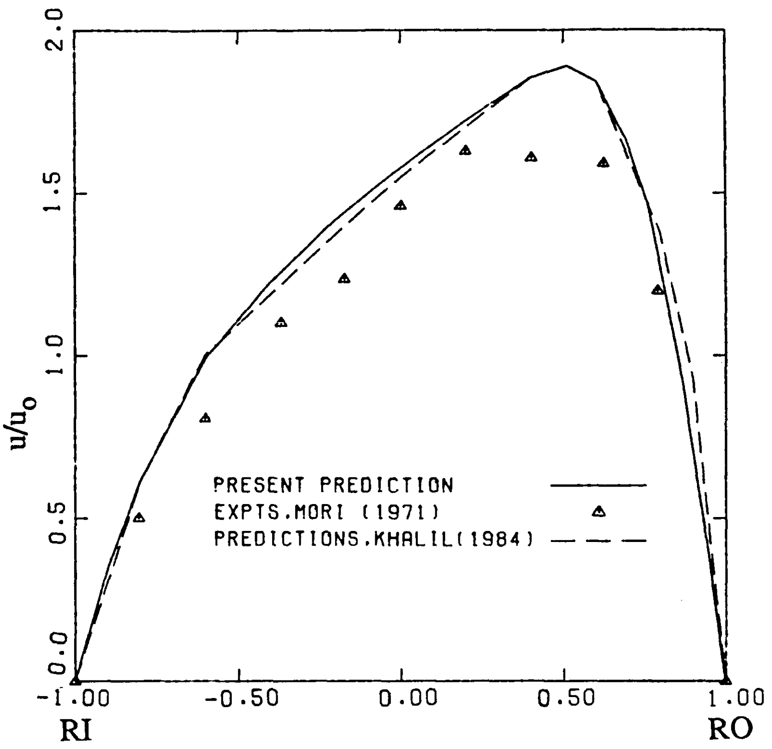

(a)

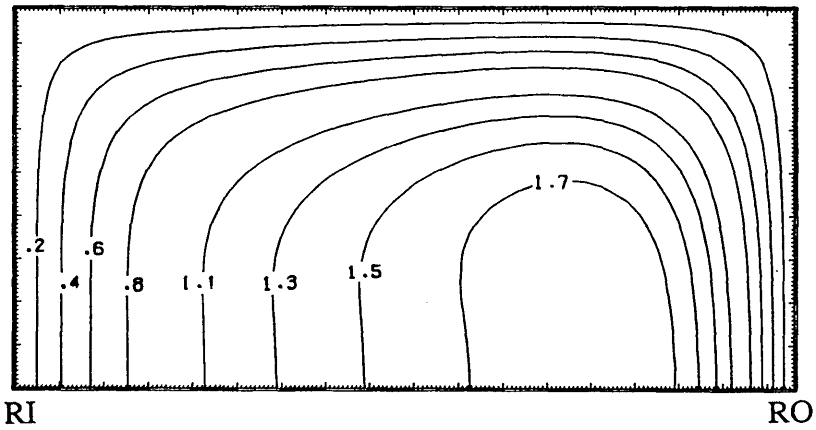

(b)

Fig. 4.8 Fully-developed streamwise velocity for the square duct

(a) Comparison of velocity profile on symmetry plane

(b) Isovelocity contours on the cross-section (u/u$_0$)

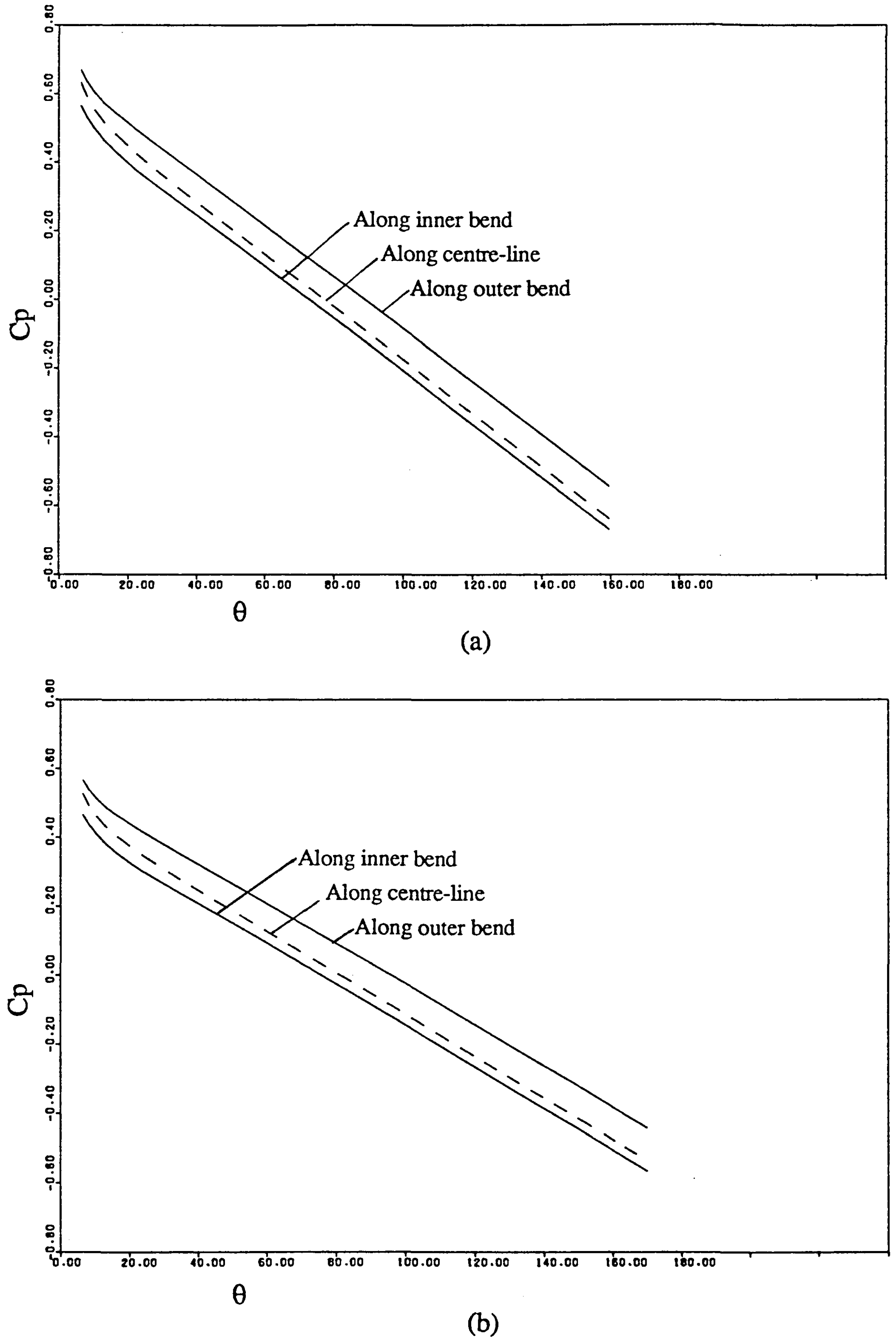

(a)

(b)

Fig. 4.9 Variations of static pressure along the ducts
(a) δ=1/7, De=183 (b) δ=1/20, De=370.6
-- cont'd

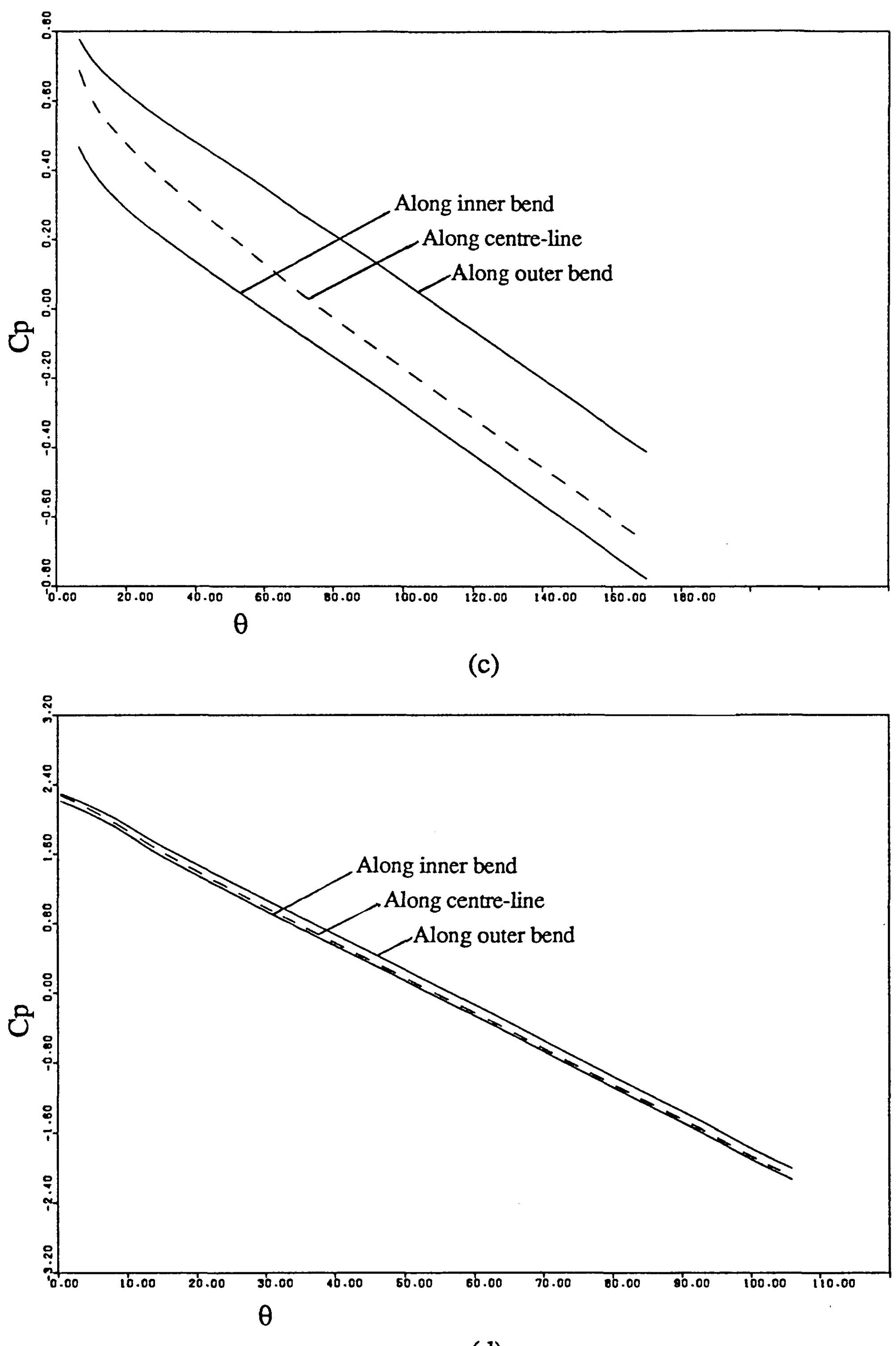

Fig. 4.9 (cont'd) Variations of static pressure along the ducts
(c) δ=1/20, De=566 (d) Square duct

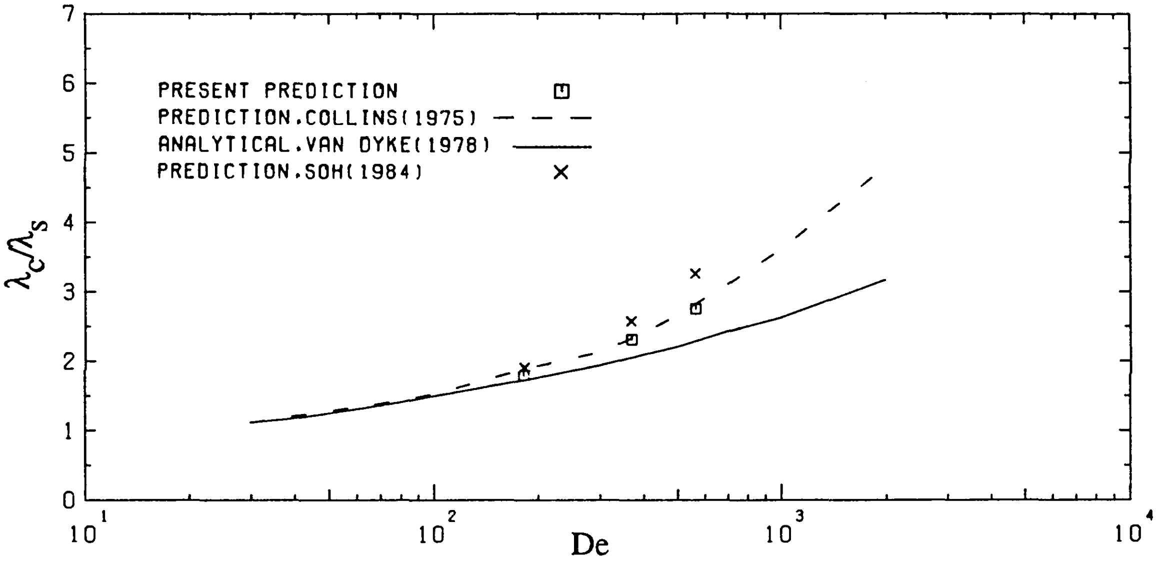

Fig. 4.10 Ratio of fully-developed friction factors for circular pipes

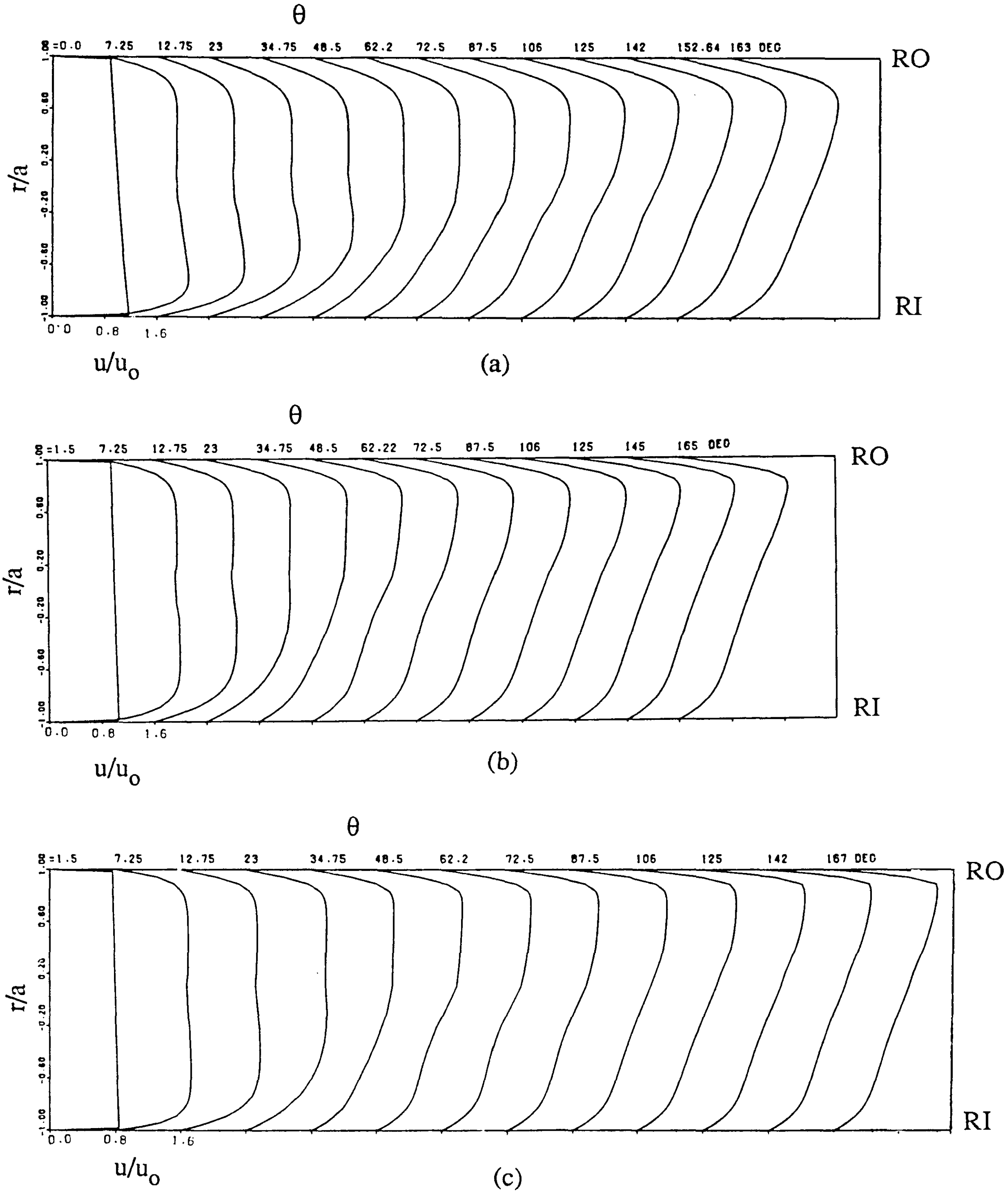

(a)

(b)

(c)

Fig. 4.11 Development of streamwise velocity on the symmetry plane for circular pipes (a) $\delta=1/7$, De=183 (b) $\delta=1/20$, De=370.6 (c) $\delta=1/20$, De=566

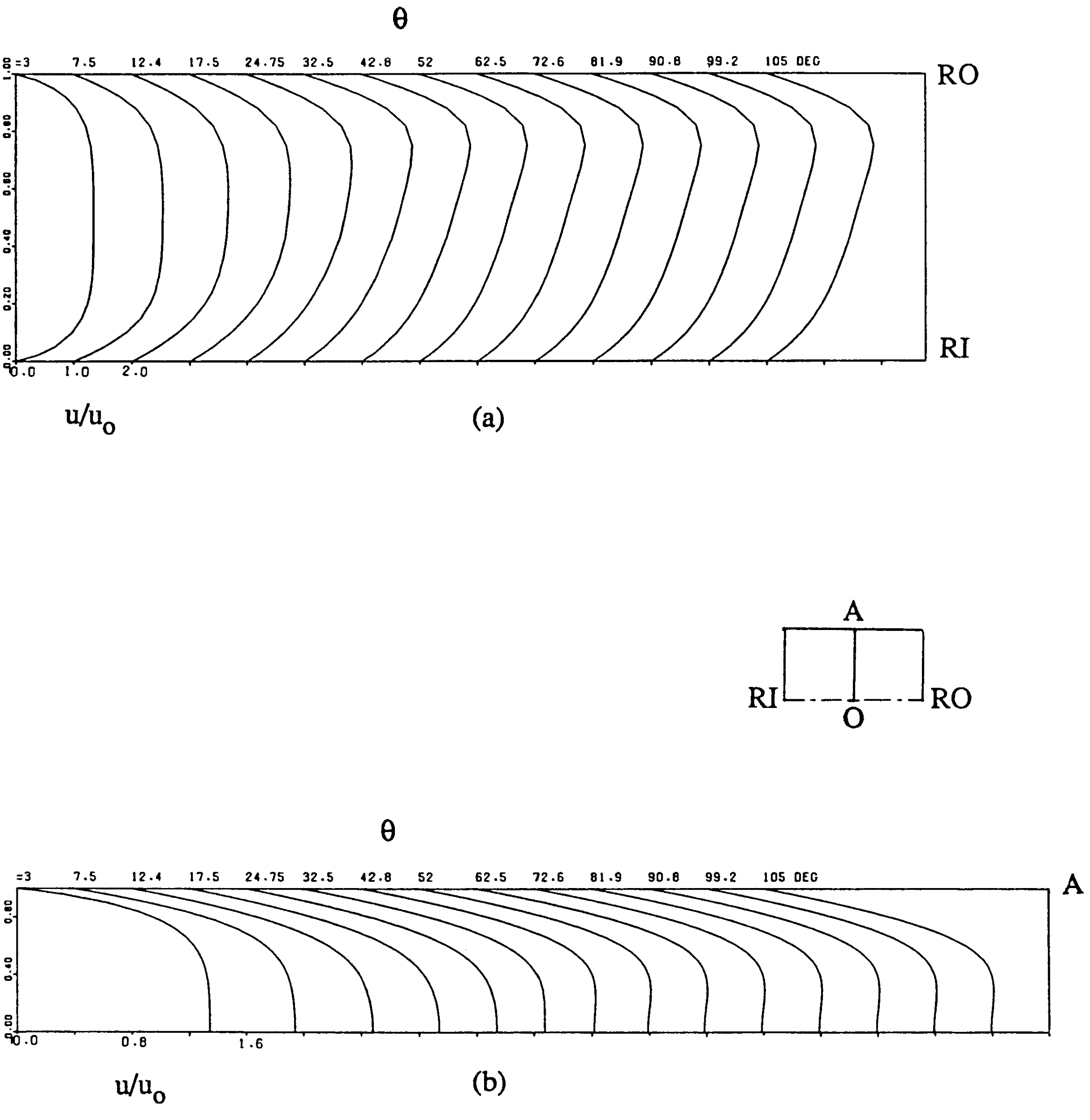

Fig. 4.12 Development of streamwise velocity of the square duct
(a) along RI-RO (b) along meridional plane O-A

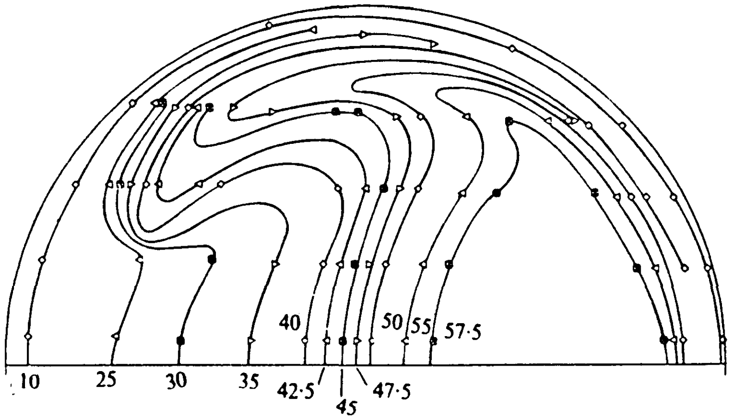

(a)

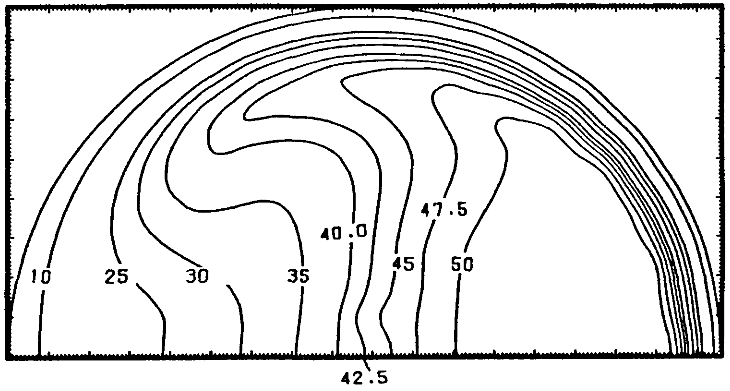

(b)

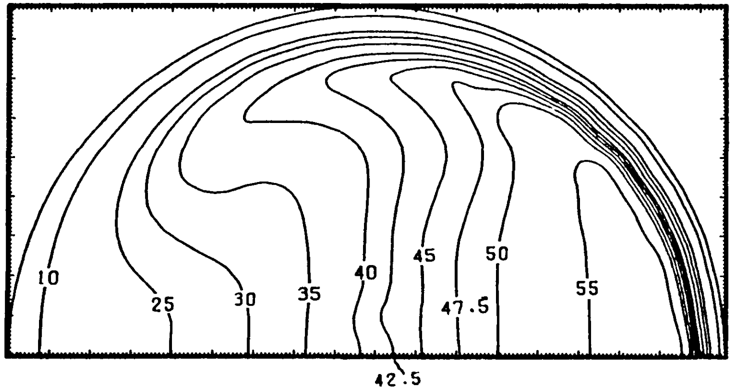

(a')

Fig. 4.13 Isovelocity contours (u/u_0) for circular pipe; δ=1/20, De=566

(a) Experimental results by Agrawal et al (1978) at θ=83 deg

(a') Present prediction at θ=83 deg

(b) Present prediction at fully-developed state

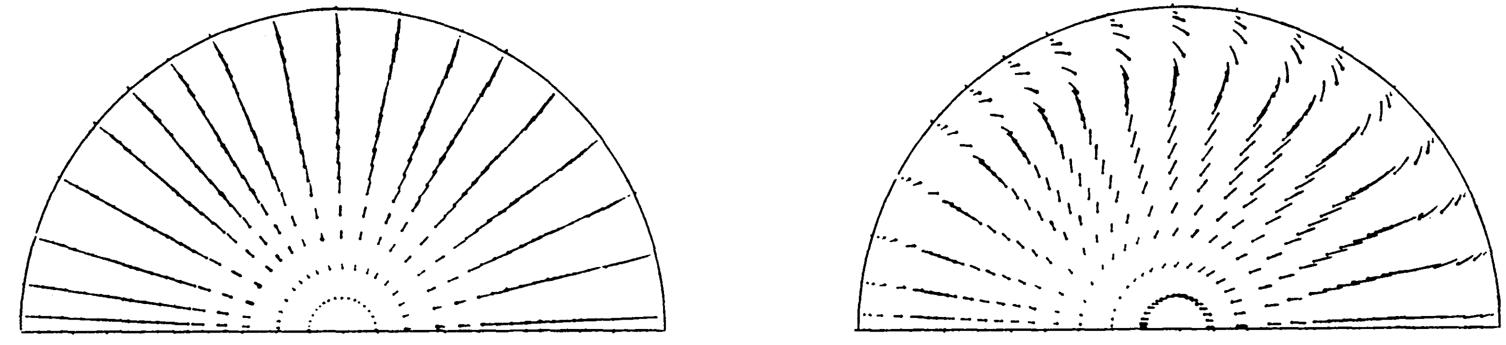

(a) θ =3 deg

(b) θ =8 deg

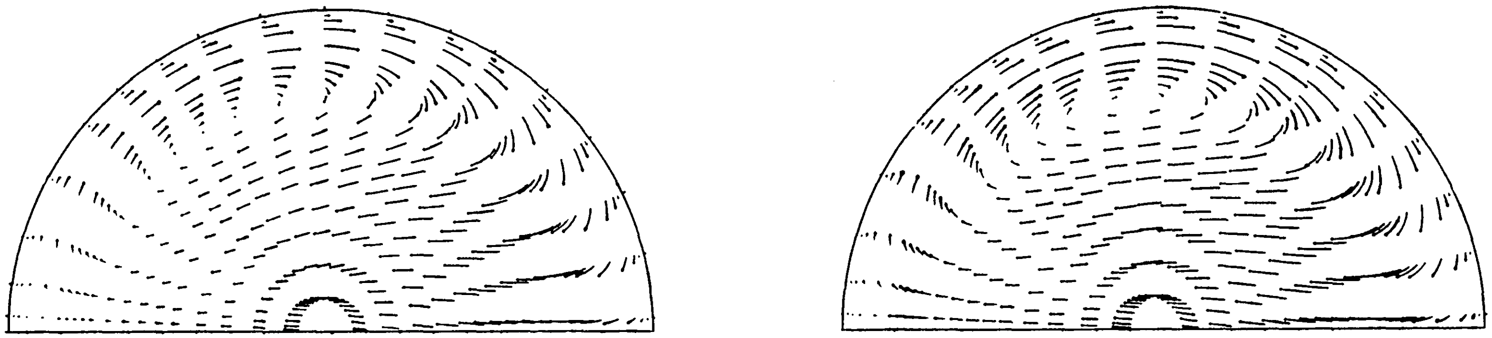

(c) θ =15 deg

(d) θ =20 deg

Fig. 4.14 Secondary flow streaklines at different cross-sectional locations of circular pipe; $\delta=1/7$, De=183

-- cont'd

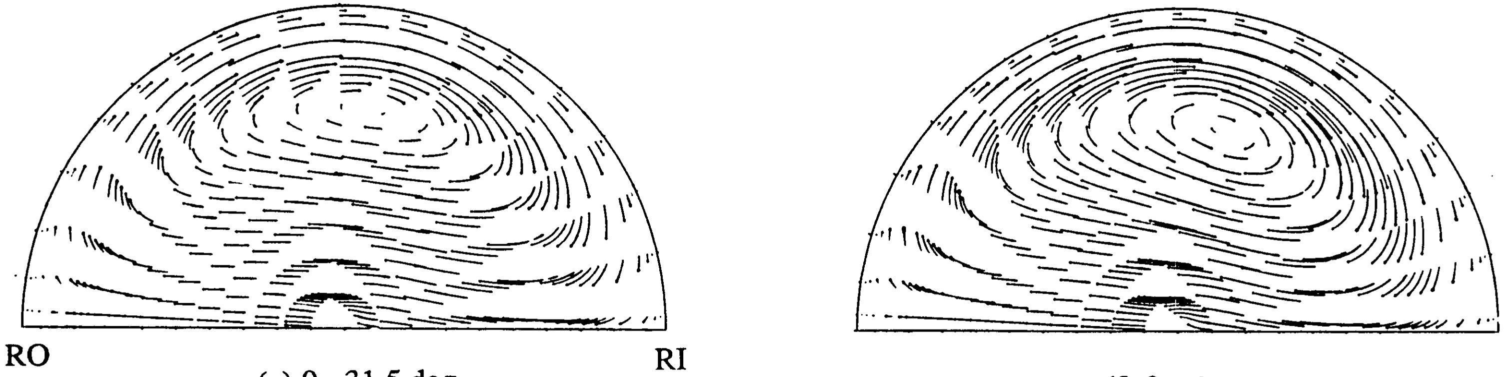

(e) θ =31.5 deg

(f) θ =65 deg

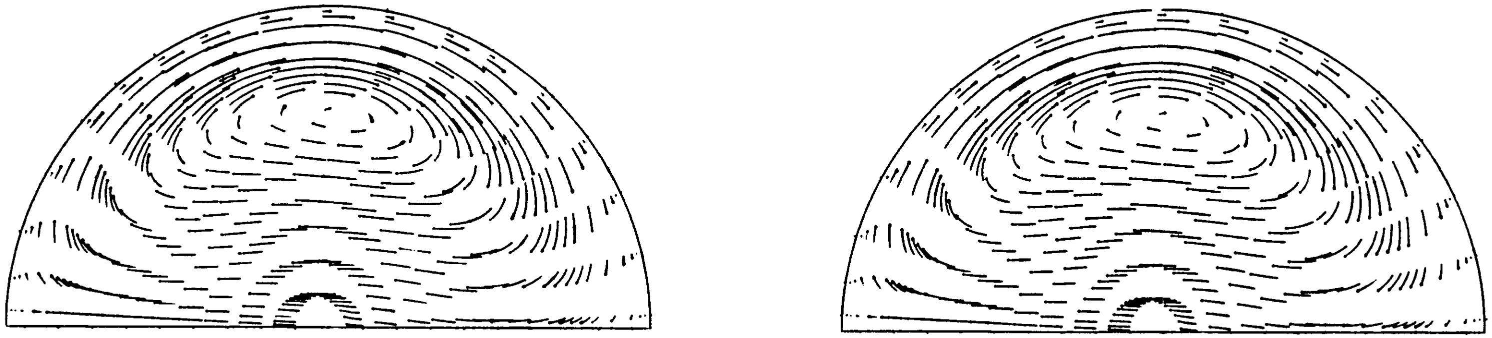

(g) θ =140 deg

(h) θ =167.5 deg

Fig. 4.14 (cont'd) Secondary flow streaklines at different cross-sectional locations of circular pipe; δ=1/7, De=183

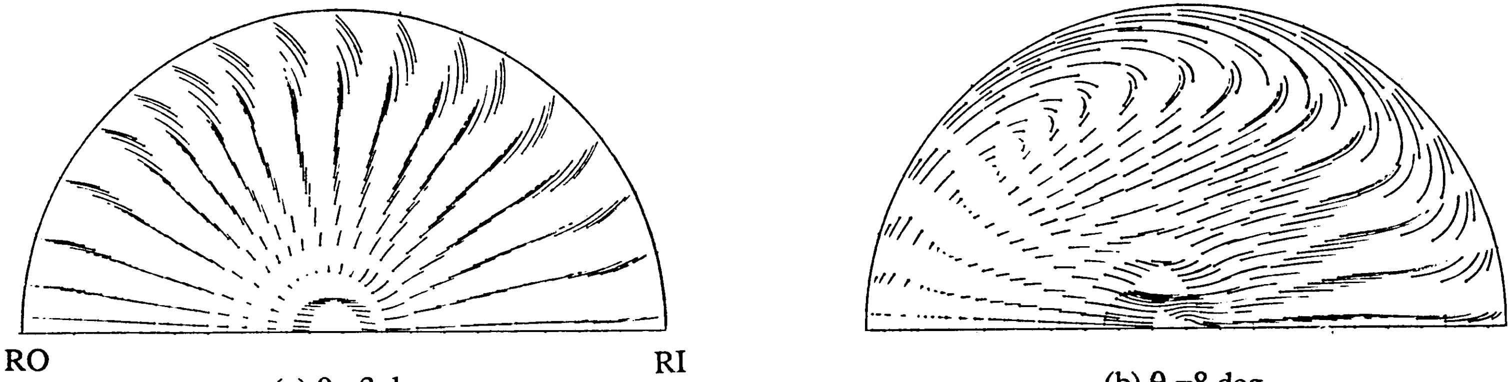

(a) θ =3 deg

(b) θ =8 deg

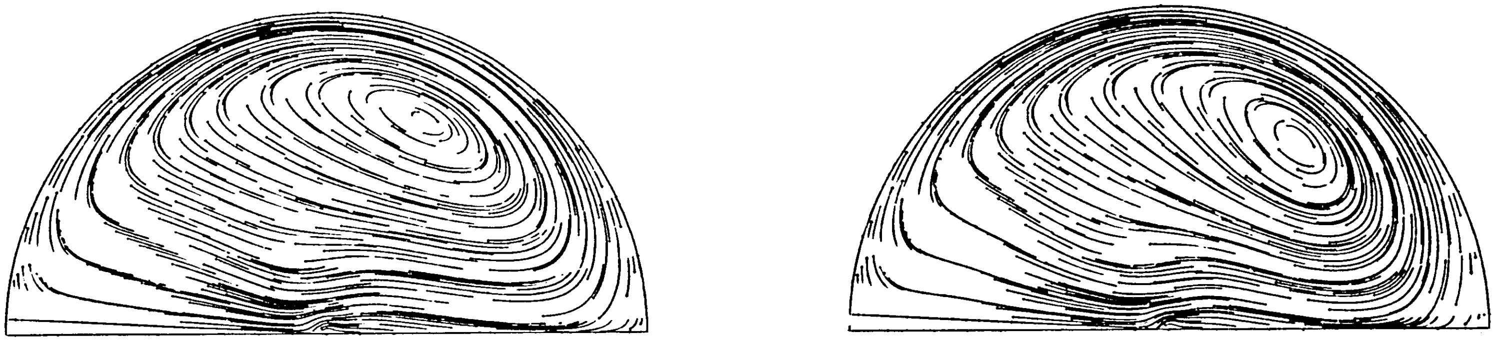

(c) θ =20 deg

(d) θ =38 deg

Fig. 4.15 Secondary flow streaklines at different cross-sectional locations of circular pipe; δ=1/20, De=566

-- cont'd

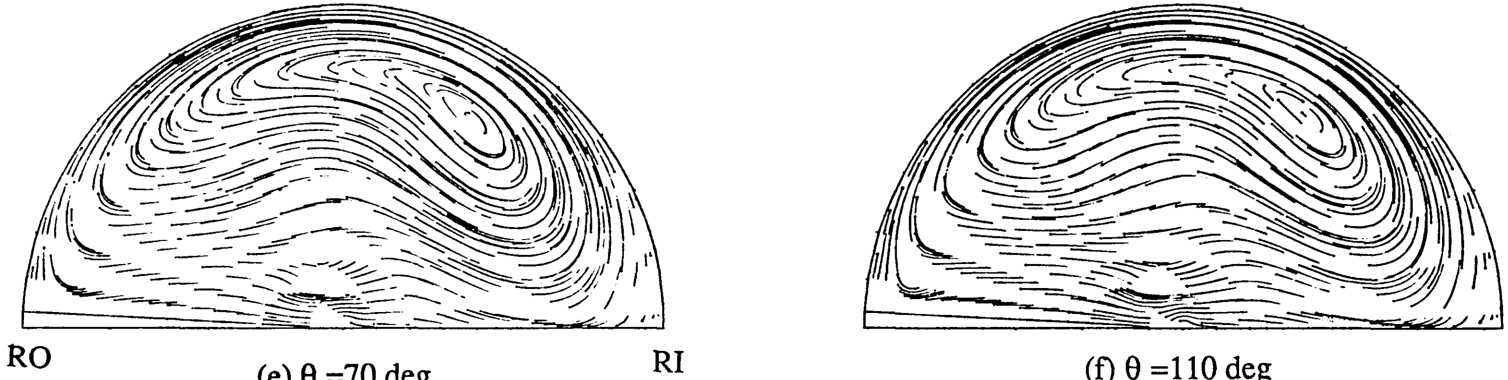

(e) θ =70 deg

(f) θ =110 deg

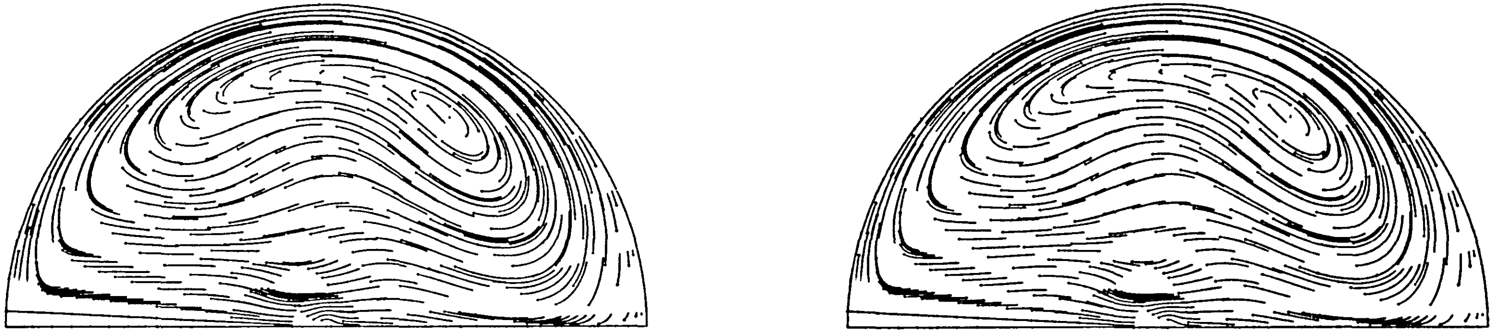

(g) θ =140 deg

(h) θ =167.5 deg

Fig. 4.15 (cont'd) Secondary flow streaklines at different cross-sectional locations of circular pipe; $\delta=1/20$, De=566

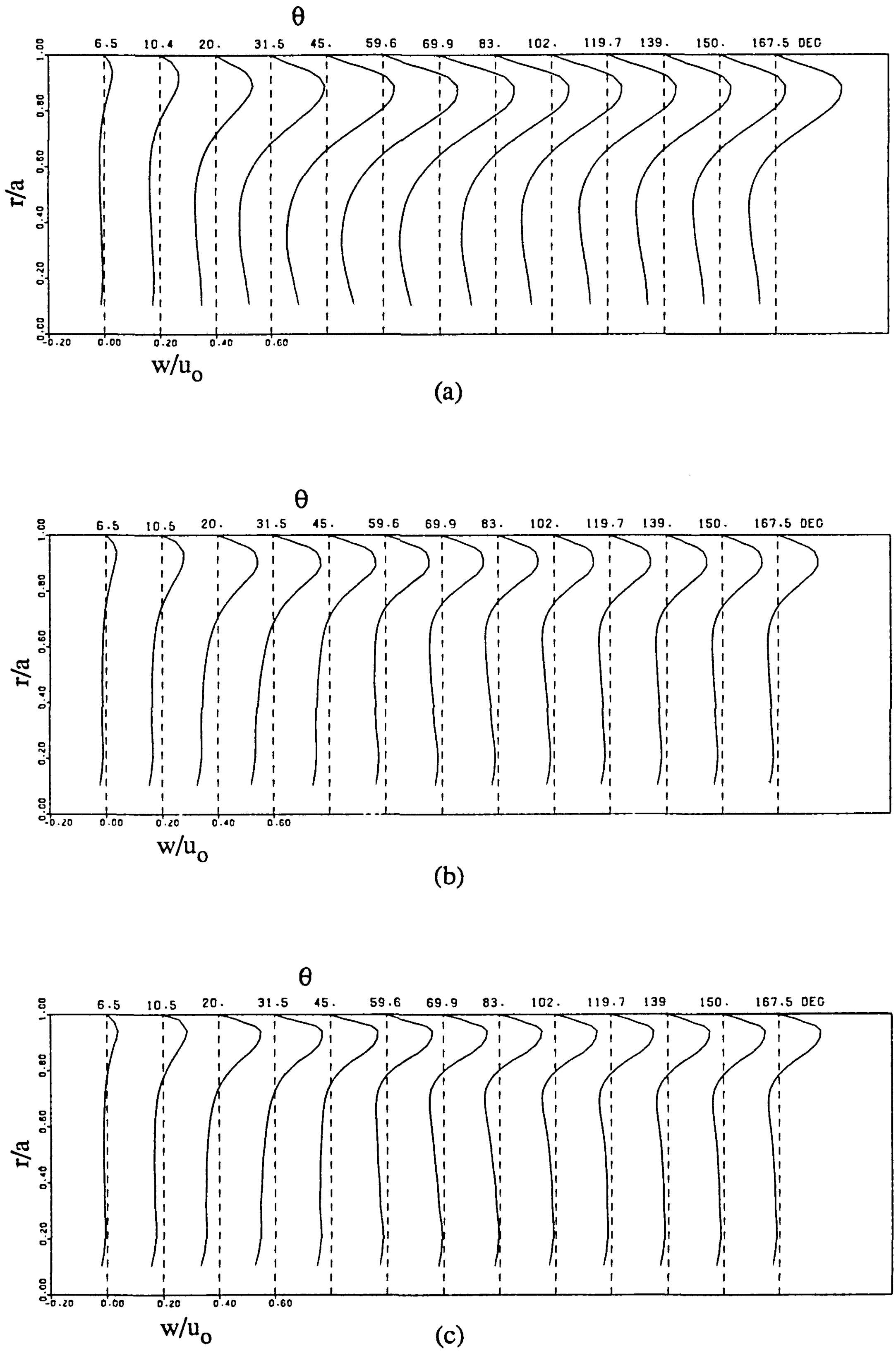

Fig. 4.16 Development of circumferential velocity (w/u_o) on the meridional plane (ϕ=90 deg) of circular pipes
(a) δ=1/7, De=183 (b) δ=1/20, De=370.6 (c) δ=1/20, De=566

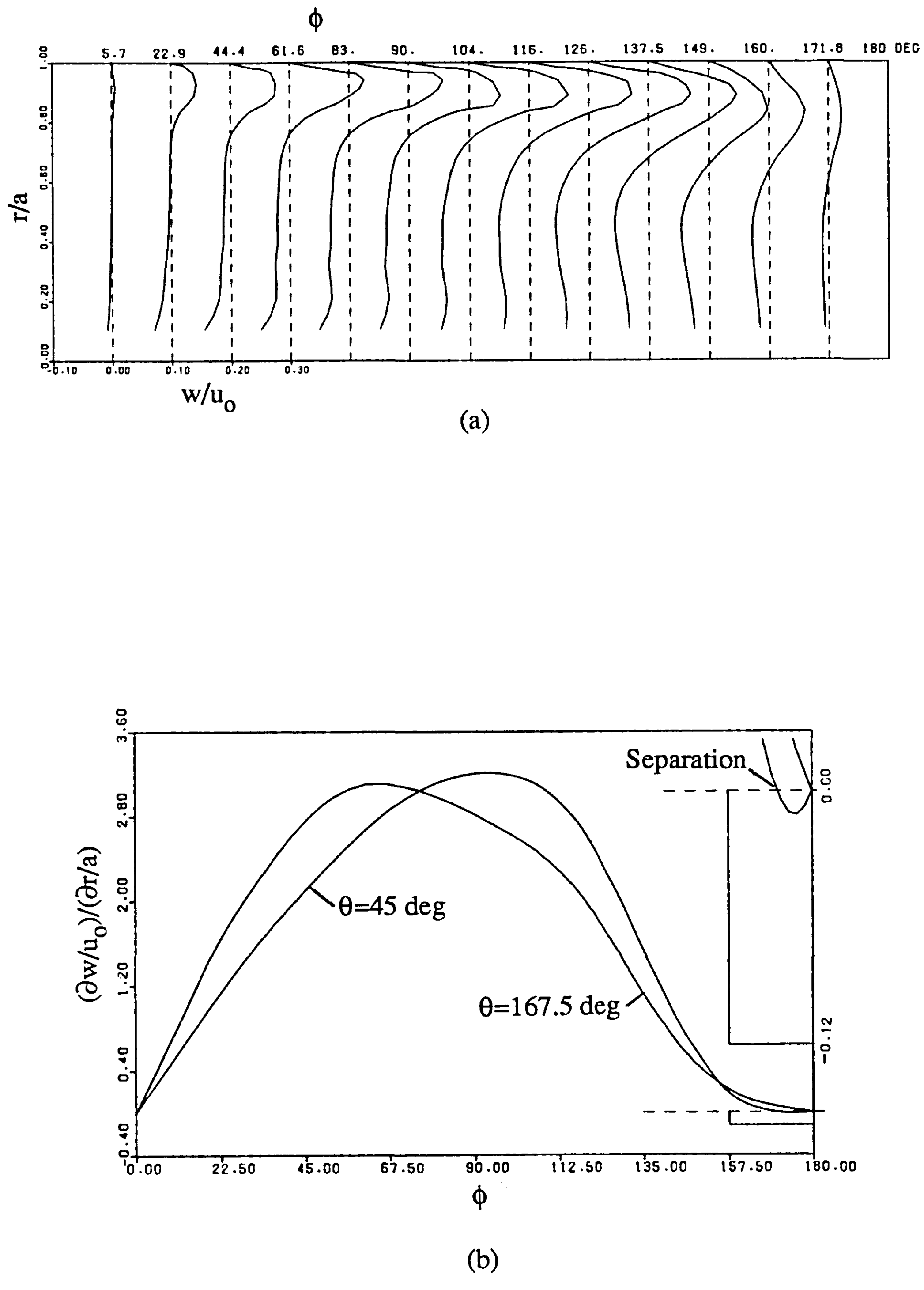

Fig. 4.17 (a) Circumferential velocity profiles in ϕ-direction at θ=45 deg for De=566
(b) Circumferential wall shear in ϕ-direction for De=566. The inset shows the separation region magnified 20 times only in the ordinate.

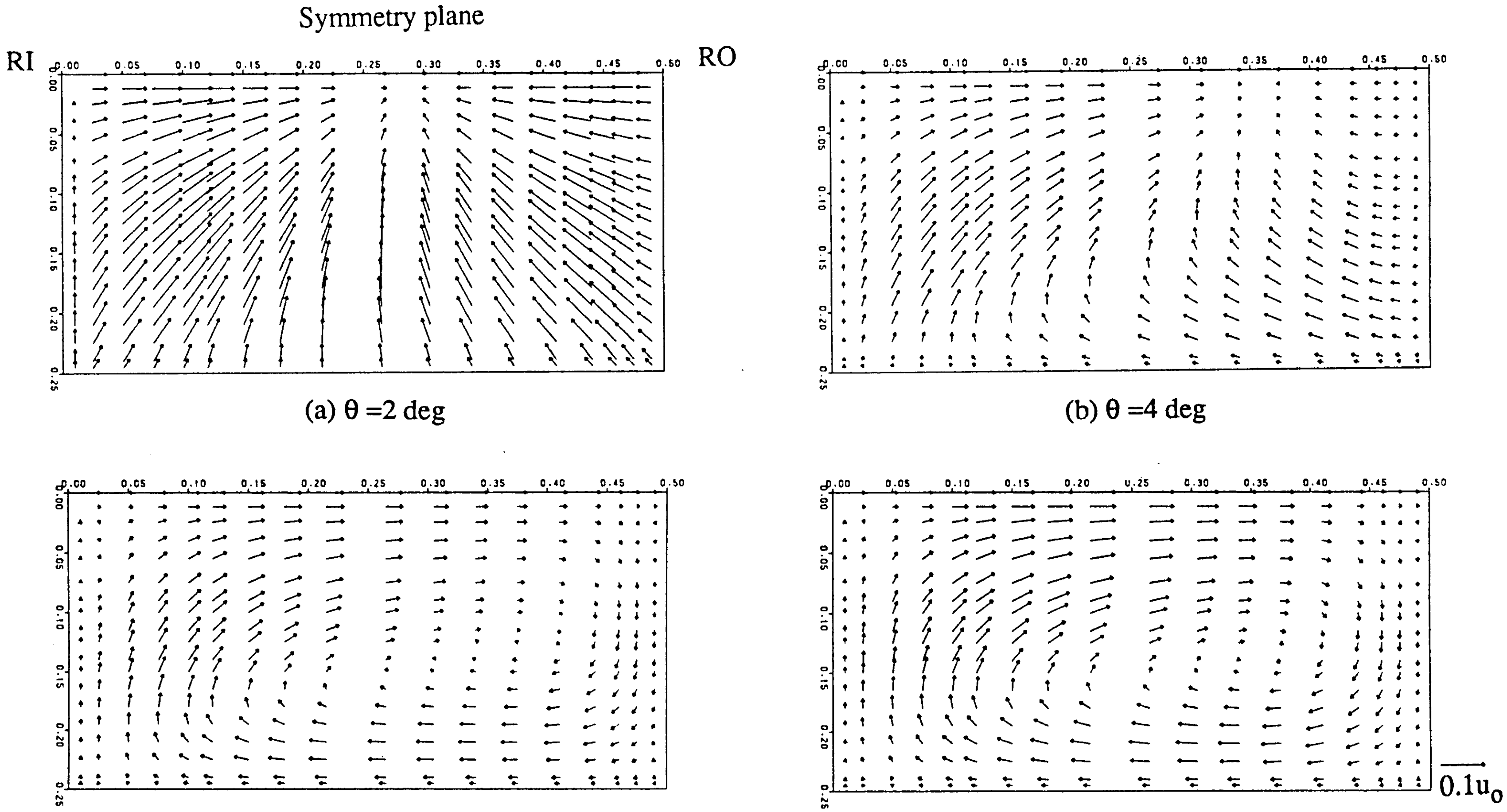

(a) θ =2 deg

(b) θ =4 deg

(c) θ =6 deg

(d) θ =8 deg

Fig. 4.18 Secondary velocity vectors at different cross-sections of the square duct

-- cont'd

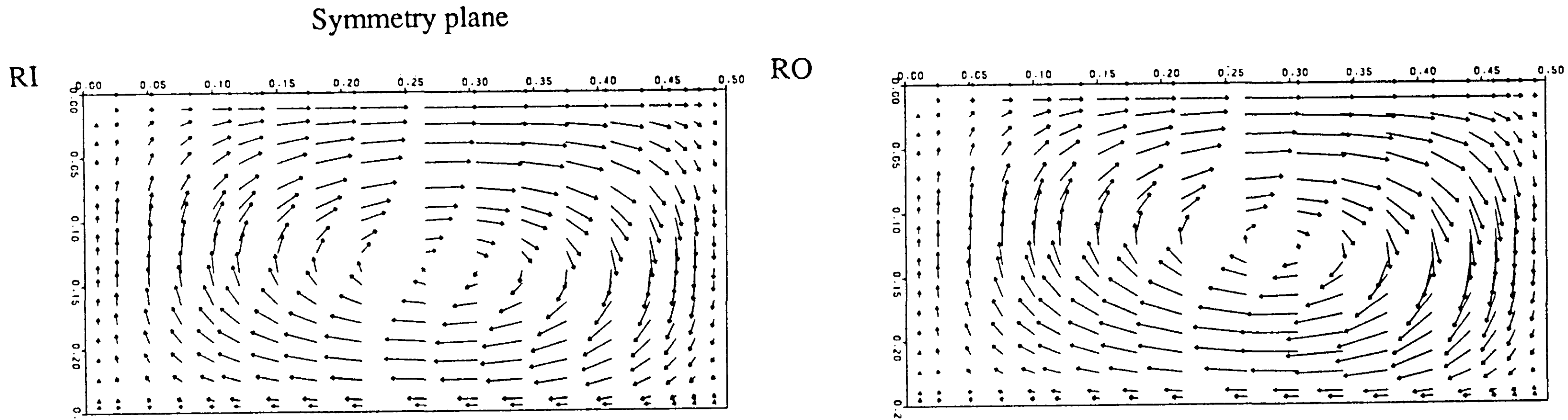

(e) θ =19 deg

(f) θ =36 deg

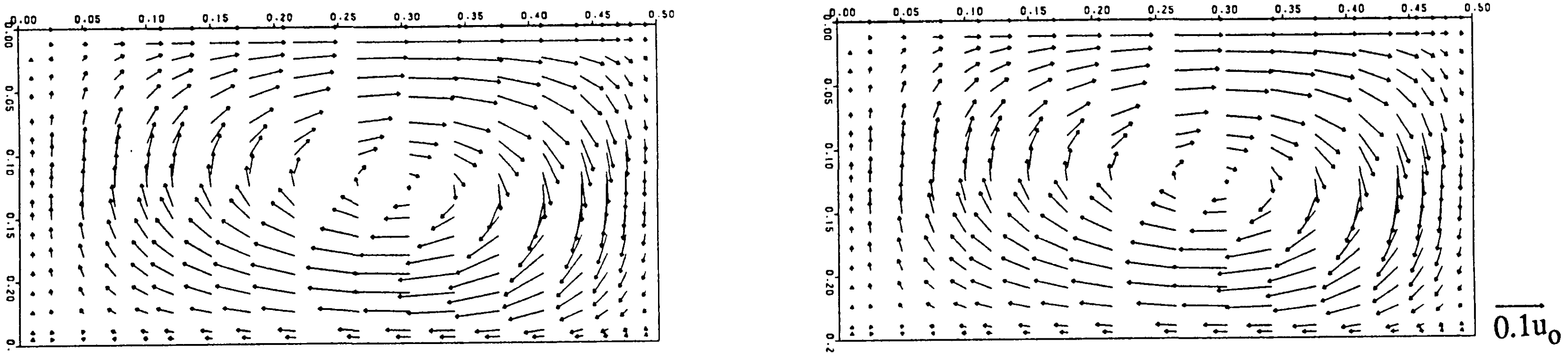

(g) θ =50 deg

(h) θ =105 deg

Fig. 4.18 (cont'd) Secondary velocity vectors at different cross-sections of the square duct

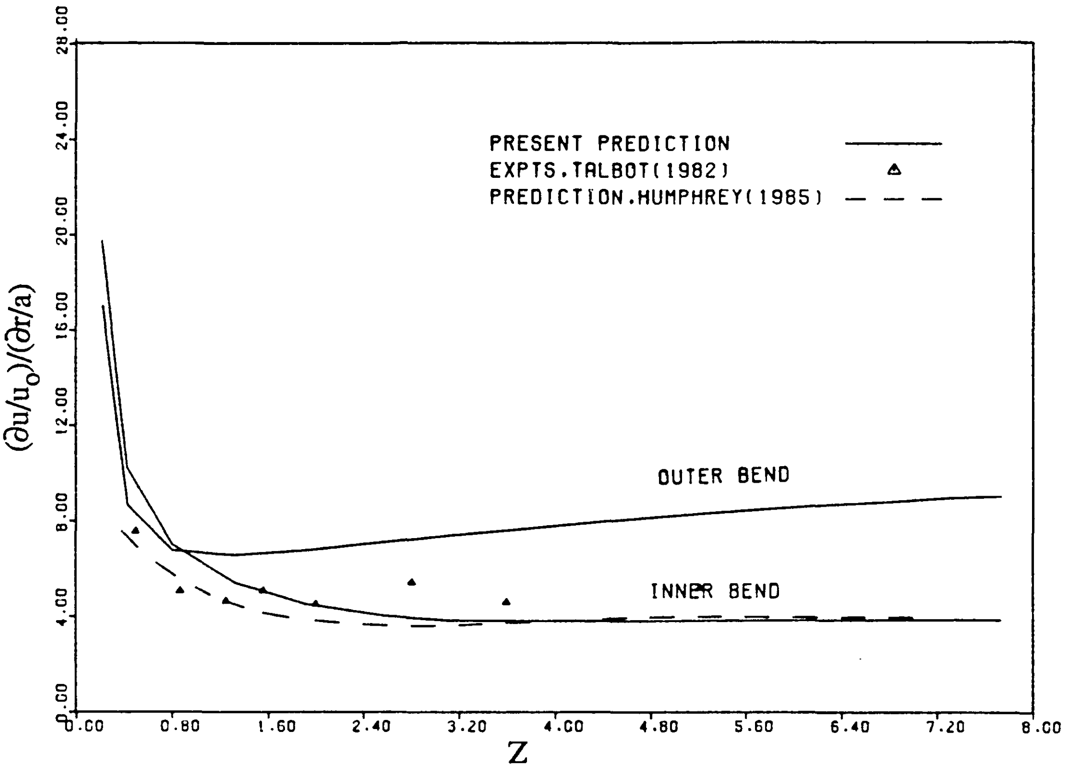

(a)

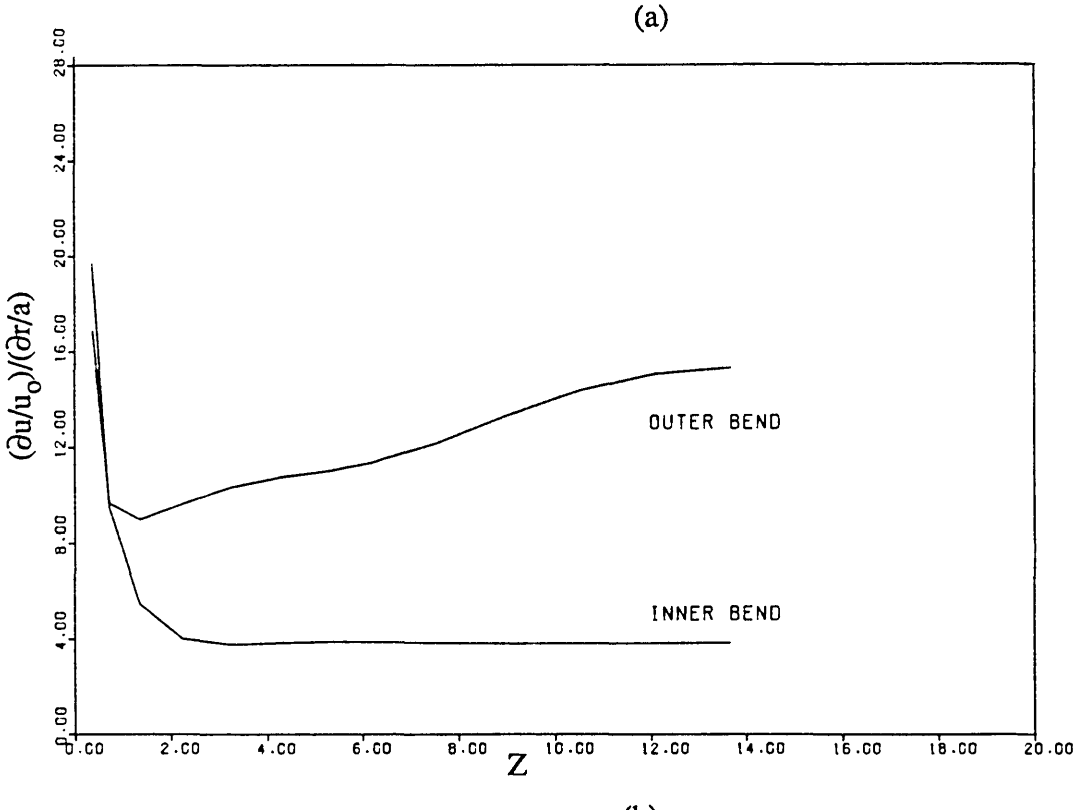

(b)

Fig. 4.19 Variations of longitudinal shear stress along the bends for circular pipes
(a) δ=1/7, De=183 (b) δ=1/20, De=370.6

-- cont'd

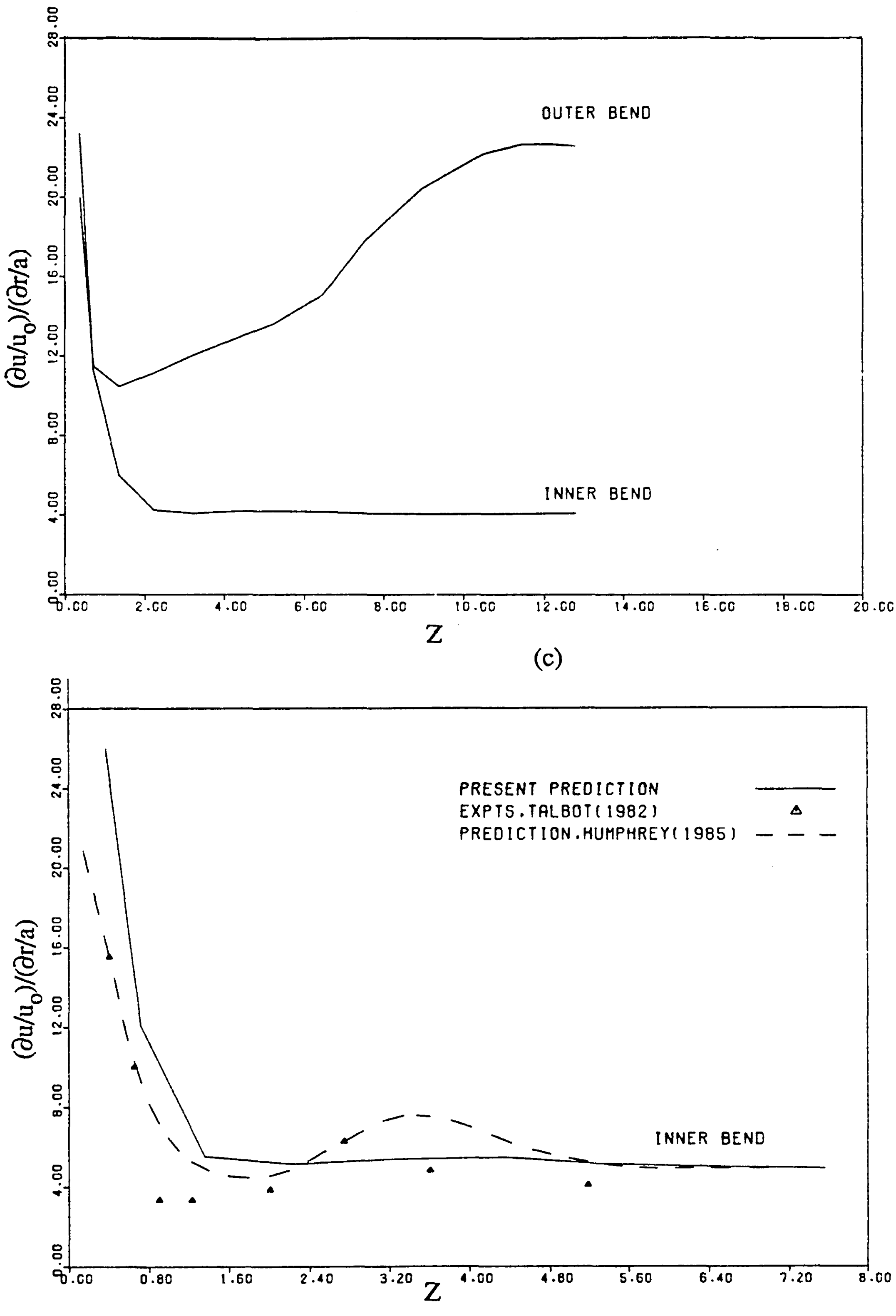

(c)

(d)

Fig. 4.19 (cont'd) Variations of longitudinal shear stress along the bends for circular pipes (c) $\delta=1/20$, De=566 (d) $\delta=1/20$, De=1356

CHAPTER 5

ASSESSMENT OF THE GENERAL CODE AND STUDY OF FLOW IN CONSTANT CURVATURE DUCTS WITH TANGENTS

5.1 Introduction

The general methodology presented in Chapter 3 has been incorporated into two computer programmes: one for two-dimensional laminar flows (as a preliminary test vehicle for the methodology) and the other for fully three-dimensional flows, both laminar and turbulent. Before applying the developed codes to the study of curved ducts and volute casings, extensive testing was carried out by considering a variety of flow configurations ranging from simple to complex in which code performance could be assessed. The test cases considered allowed the capabilities and limitations of the codes in terms of accuracy, reliability and cost to be ascertained. Emphasis was placed on laminar flows, to avoid complications due to uncertainties of turbulence model performance, but one turbulent flow case was included to allow comparison with previous calculations and ensure that the model had been coded properly.

First, in section 2, a few laminar flows through plane two-dimensional curved geometries are considered in order to determine the effects of grid non-orthogonality on the accuracy, stability and convergence rate of the solution procedure. The importance of proper choice of under-relaxation factors is also highlighted. A recirculating flow has also been predicted in order to show the capability of the code in such situations.

In section 3, the fully three-dimensional version of the computer code is first applied to the inviscid, laminar and turbulent flow developing in a straight circular pipe. The flow here is, of course, axi-symmetric and does not require a three-dimensional code, but by choosing a three-dimensional non-orthogonal grid and examining the axi-symmetry of the solution, much of the coding of the three-dimensional code can be critically assessed. The programme is then applied to the prediction of laminar flow through a toroidally curved square duct; the previous chapter has defined an ability to calculate the important features of such flows using a different code based on an orthogonal coordinate system. By using the same system, but the fully programmed non-orthogonal code, it is possible to check at least partially, the coding of the general method.

Section 4 presents the results for laminar and turbulent flow through a constant curvature and constant (circular) cross-sectional 90-deg bend with upstream and downstream tangents. The results of the previous chapter will again help in assessing the code performance in the case of laminar flow. For turbulent flow, experimental data and previous calculations using the same turbulence model but different numerical strategies are used for assessment purposes. Fortunately, a bench-mark experimental data (Enayet et al, 1982) is available and both laminar and turbulent flow were examined in the same geometry.

In section 5, laminar flow through a constant curvature, 45-deg C-diffuser with upstream and downstream tangents was solved in order to ascertain the effects of area variation through curved ducts. This test case requires the full three-dimensional non-orthogonal code and therefore serves to prove the coding of all extra terms.

Finally, closing remarks in terms of code evaluation and flow characteristics through curved ducts are made in section 6.

5.2 Two-dimensional Test Cases

5.2.1 Flow Through Plane 2D Curved Ducts

Laminar flow through three test geometries as shown in Figs.5.1a-c was first considered. The first two model problems were 90-deg bends having cross-sectional areas reducing linearly with the streamwise coordinate θ. The inside bends were assumed to be arcs of a circle whereas the contour of the outside bend had a reducing radius of curvature. The radius-ratio at the inlet $\delta= r_o/R_c$ was 1/12 for the first case (moderate curvature) and for the second case (Fig.5.1b) was 1/3 (strong curvature). The third problem was a constant area curved duct with $\delta=1/3$ but the streamwise coordinate extends to $\theta=340^o$ (Fig.5.1c). The reason for this particular test case was to demonstrate that the accuracy of solution is not jeopardized by non-orthogonality of grid lines because as will be shown later that the predicted results are in excellent agreement with analytical results.

A uniform velocity u_o was assumed at the inlet and the Reynolds number of the flow, ($Re=2\rho u_o r_o/\mu$) was taken to be 100 for all the cases. No-slip boundary conditions on the walls and a zero-gradient boundary condition at the outlet plane were employed.

Effect of Non-orthogonality

For the first two test geometries, in order to study the effect of grid non-orthogonality, the transverse grid lines in the interior of the flow domain (see Fig.5.1a) were systematically inclined to the radial direction by changing the angle of inclination ϕ ($\phi=0^o$,$\phi=20^o$, $\phi=45^o$). This was done for all the grid lines except two (Fig.5.1a), so that the staggered velocity locations between these lines remained identical for all values of ϕ. Initially an 11x11 grid nodes was employed for the 90-deg bends. The convergence pattern and the streamwise velocity profiles at $\theta=50.4^o$ (the non-inclined velocity location) are shown in Figs.5.2-5.4. It can be observed that the grid non-orthogonality does not have any significant effect on the accuracy of results. The discrepancies for the strongly curved duct are probably due to coarseness of mesh and exit boundary condition; doubling the grids (21x21), significantly improves the predictions as can be seen from Fig.5.4b. It can also be seen that the velocity profile of the moderate curvature duct (Fig.5.2b) shows an almost axi-symmetry and propagation of wall boundary layers up to the middle of the core region, while that of the strongly curved duct (Fig.5.4b) exhibits curvature effects more clearly and that the boundary layers have not yet propagated up to the centre. The differences are due to curvature variations (1/12 and 1/3) and different lengths covered by the flow (shorter length for the strongly curved duct). For both the cases, the number of iterations required to reach a particular level of convergence increases significantly with increase of non-orthogonality (i.e., higher values of ϕ). The reason is that, with increase of ϕ, the cross-derivative terms become more significant. These slow down convergence for two reasons: firstly, in the derivation of the pressure-correction equation (3.27) these cross-derivatives were omitted and hence the mass flux error calculated at the end of an iteration is likely to be larger compared with a less non-orthogonal mesh; as a result, more iterations would be required. Secondly, cross-derivative terms in the momentum equations are treated in an explicit manner via the source terms (Eq.3.14), larger values of these will again slow convergence rate.

Fig.5.5 shows the developing flow through the constant area strongly curved bend of Fig.5.1c. This is one of the very few two-dimensional curved ducts for which an analytic solution can be obtained for the fully-developed situation (Ward-Smith, 1980). The streamwise velocities at different azimuthal (θ- direction) stations ($\theta=0^o$, 24.75^o, 85.5^o and 266^o) presented in Fig.5.5a were obtained by employing a toroidal orthogonal mesh as described in Chapter 4 with a non-uniform 37 (radial)x50 (streamwise) grid nodes (although of course the full non-orthogonal equations were programmed). For this orthogonal grid arrangement, the non-orthogonal computer code provided identical results to the orthogonal code in the previous chapter (both are plotted in Fig.5.5a). The radial lines were then inclined in a similar fashion as was done for the previous cases (see Fig.5.1a); and Fig.5.5b shows the velocity profiles at corresponding azimuthal locations for an inclination angle of $\phi=20^o$. Virtually no difference in the predicted velocities are noticeable. The predicted pressures were also in excellent agreement for the different runs. The fully-developed analytical solution is obtained accurately by the programme for both $\phi=0^o$ and $\phi=20^o$.

Effect of Under-relaxation Factors

Since the Navier-Stokes equations are non-linear and strongly coupled, the momentum equations need to be under-relaxed to ensure iterative convergence (Patankar, 1980). The pressure-correction equation, which has been derived (Ch.3) from a combination of approximate momentum and continuity equations, provides pressure changes from one iteration to another which must also be slowed down by making use of under-relaxation factors (see Eqs.3.44 and 3.45). The popular values of these factors for optimum convergence as suggested by Patankar (1980) (for momentum, $\alpha_u=0.8$ and for pressure, $\alpha_p=0.5$) were found to be inadequate for the current solution method and these particular values may even lead to divergence if the grid non-orthogonality becomes too severe.

As an example, the flow through the moderate curvature duct of Fig.5.1a was solved using various combinations of α_u and α_p and the results are presented in Fig.5.6. In Fig.5.6a the radial lines were kept non-inclined ($\phi=0$ deg) and for Fig.5.6b, they were inclined at an angle of $\phi=45$ deg. These two figures reveal the following features of the solution method in terms of under-relaxation factors.

i) The non-orthogonality of grid lines in general make the method more expensive and in this particular case, the minimum number of iterations increases by an order of 100% (for all combinations of α_u and α_p) for the severe non-orthogonality of about 45 deg.

ii) For a particular value of α_u, the range of α_p over which a stable and economic solution can be obtained decreases with increase of non-orthogonality. That is, the region of stable operation becomes narrower.

iii) The presence of non-orthogonality reduces the levels of the optimum combination of under-relaxation factors from ($\alpha_u=0.8$, $\alpha_p=0.85$) for $\phi=0^o$ to ($\alpha_u=0.7$, $\alpha_p=0.4$) for $\phi=45^o$. The relative change of the under-relaxation factors for optimum convergence is more prominent for pressure than for momentum.

iv) Too small or too high values of α_u and α_p make the solution more expensive and in severe cases the solution may be impossible to obtain.

As has been stated earlier, the optimum values of the under-relaxation factors are problem dependent. Peric (1985) has shown that the values of α_u and α_p tend to be such that their summation is unity or less. It has been found from later studies in the present work that under-relaxation factors of α_u=0.5-0.8 and α_p=0.1-0.3 may be taken as a safe guideline. These values are very close to the ones proposed by Braaten and Shyy (1986).

5.2.2 Flow Through a Plane 2D Curved Diffuser

This test case has been considered in order to test the correctness of the present code for recirculating flows. Among others, Demirdzic (1982) has also solved this flow configuration for the evaluation of his code employing grid-oriented velocity vectors and non-orthogonal curvilinear grids. The geometry (shown in Fig.5.7a) consists of a lower symmetry plane, an inlet, an outlet and an upper wall which is given by a hyperbolic tangent function in Cartesian (x,y) coordinates as:

$$y=[1+0.5\tanh 2 - 0.5\tanh\{2-(30/L)x\}]B \qquad (5.1)$$

where, L=10, x_{max}=L/3 and 2B is the duct height at inlet plane.

A parabolic velocity profile is assumed at the inlet and a zero-gradient boundary condition applied at the exit. A non-uniform 20x20 computational grid was employed as shown in Fig.5.7b. This grid was generated by a simple algebraic transformation. The Reynolds number, $Re=\rho u_0 B/\mu$ was taken to be equal to 10, where u_0 is the bulk velocity.

Flow recirculation takes place near the diverging neck of the solution domain; this can be clearly seen from the velocity vectors and streamline plots in Figs.5.8a-b. The wall vorticity (equivalent to the wall shear stress in this flow) is compared with the computational results of Demirdzic (1982) (who has employed 20x21 grids of similar distribution) and the agreement is reasonably good except in the first two grid nodes in the axial direction. The reason may be attributed to the fact that due to double-staggering of the u-velocity (Ch.3) at the inlet, the effective grid density there is too coarse to pick up such variations accurately. The length of the recirculation region in the present prediction is between x/x_{max}=0.18 - 0.54 as against Demirdzic's prediction of x/x_{max}=0.192 - 0.52; the present calculations over-predict this length by about 8%. Nevertheless, the current non-orthogonal code does reproduce the recirculation region in this flow to acceptable accuracy.

5.3 Three-dimensional Test Cases

In order to establish the correctness of the three-dimensional computer code, two simple flows were first studied: i) Inviscid, laminar and turbulent flows through a straight circular pipe and ii) Laminar flow through a toroidal square duct of moderate curvature.

5.3.1 Flow Through a Straight Pipe

This flow has been studied in details for inviscid, laminar and turbulent cases. Instead of using an orthogonal cylindrical-polar grid (which renders the flow to be axi-symmetric two-dimensional), a three-dimensional 21x11 body-fitted grid has been generated over half of the cross-section, as shown in Fig.5.9a. Rhie (1985) has also reported such a grid arrangement for code evaluation. The main flow direction was divided equally into 21 sections covering a total length of 120 pipe diameters.

First, the orientation of the pipe axis was taken to be such that u was in the main flow direction (x-direction) and v and w were the secondary velocity components over the cross-section (in the y- and z-directions respectively; this arrangement is shown in Fig.5.9a). Next, the orientation of the pipe axis was rotated through 90^o and a solution obtained with v as the main flow component ; finally the component w was taken as the predominant velocity. This procedure was followed for all the three flow types discussed in this section and provided a complete check of the coding of the cross-derivatives in all the momentum equations (2.30-2.32). Thus, for each of the three flow situations (inviscid, laminar and turbulent), three calculations were carried out i.e., a total of nine sets of results were obtained for this test case. It should be noted here that instead of using a cylindrical-polar coordinate, the frame of reference was taken to be Cartesian. Hence, these test cases do not take into account the explicit source terms (Eq.2.30 and 2.31) of the momentum equations.

Inviscid Flow

The flow was set to be inviscid ($\mu=0$) and slip conditions prescribed on the solid boundary. In this case both the pressure and velocity fields should remain uniform at their inlet values. Various initial field values were used. In addition, the initial guesses of field values were perturbed at random locations within the solution domain. For all the cases, the solution was found to be stable and the uniform field values restored within machine accuracy. In this test case, since the viscosity is set to be zero, all cross-derivative diffusion terms are zero. However, the pressure gradient terms are non-zero (in every run, two non-zero gradients out of three) and hence the programming of these terms are checked by this set of calculations.

Laminar Flow

Next, laminar flow through the straight pipe was studied in which case, similar to the inviscid calculations, three momentum and one pressure-correction equations were solved. A plug inlet velocity, u_0 corresponding to a Reynolds number of $Re=\rho u_0 D/\mu=100$ (where, D is the diameter of the pipe) was applied. At the exit, a zero-gradient boundary condition, and on the symmetry plane, symmetry boundary conditions were employed. The flow attained a fully-developed state which was in very good agreement with analytical results (Schlichting, 1979) as shown in Fig.5.9b-c. No adverse effect due to the severe non-orthogonality (about 30 deg) of grid lines near the corner cells (Points A,B in Fig.5.9a) took place as can be seen from the circular shape of the u/u_0 contours shown in Fig.5.9b. The pressure drop in the fully-developed region was also in excellent agreement with analytical results. By this test case (three runs), it was confirmed that the coding of the cross-derivative diffusion terms were performed properly.

Turbulent Flow

Finally, developing turbulent flow was predicted for this flow configuration to act as a check on the coding of the turbulence (k, ε) equations. The Reynolds number was taken to be 5×10^5, based on the uniform inlet velocity, u_0. For turbulence energy k and dissipation rate ε, uniform values were assumed at the inlet. The values were taken to be:

$$k_{in}=0.05\ u_0^2 \qquad \varepsilon_{in}=k_{in}^{3/2}/0.1D \qquad (5.2)$$

As usual the flow attained a fully-developed state within the solution domain. The main stream velocity u/u_{max} , turbulence energy k/u^2_{max} and length scale $C_\mu k^{3/2}/(\varepsilon D)$ contours plotted in Fig.5.10a-c reveal no adverse effect due to the non-orthogonality of the mesh, the solution was axi-symmetric to an excellent degree. The profiles of the main velocity and turbulence energy are compared in Figs.5.10d-e with experimental data of Laufer (1954). The comparisons can be taken as quite satisfactory given the coarse mesh over the cross-section and are at a level of agreement expected with an eddy-viscosity model of turbulence (e.g., Demirdzic, 1982). Finally, the pressure drop coefficient obtained from a Moody diagram for this Re and a smooth pipe is 0.0032; the value calculated from the numerical calculations was 0.00325. Hence, the coding of the turbulence quantities are checked.

5.3.2 Laminar Flow Through a Toroidally Curved Square Duct

Calculations were next carried out for a 110-deg curved duct of square cross-section as described in Ch.4. The radius-ratio was taken to be δ=1/27.8 and the Dean number of the flow defined by Eq.(4.2) was De=38.9. The solution domain is confined between walls, a symmetry plane, an inlet and an exit. At the inlet, a plug velocity profile was set and at exit, a zero-gradient boundary condition was employed. This flow has of course been studied earlier using another computer code employing governing equations based on toroidal coordinates (Ch.4); this now serves as a basis for comparison of the performance of the general non-orthogonal code in this problem. The flow attained a fully-developed situation within the curved length and the streamwise velocity is shown in Fig.5.11b, which is exactly the same as that presented in Fig.4.8b. The developing streamwise velocities for the whole length of the duct at five locations on the cross-section (A-E as shown in Fig.5.11a) are compared (Fig.5.11c) and, in confirmation that the current code is performing accurately, no noticeable differences are present. The maximum difference in pressures between the two codes was found to be less than 0.5% of the inlet dynamic pressure.

It can be seen by examining Fig.5.11a that the grid employed for this study is in fact orthogonal and hence there is no difference between the physical and computational space. In the expression for the Jacobian (Eq.2.26), only three (diagonal) terms out of nine are non-vanishing. Hence, the contravariant velocity components (such as U, given by Eq.2.35) and physical velocity components (such as u) are related to each other via only one metric quantity (such as θ_ζ). The large number of cross-derivative terms arising out of the coordinate transformation should become zero for this particular case. Also, out of three pressure gradients in each momentum equation, only one is non-zero. It should be emphasized however that all metric components and all cross-derivative terms have been programmed in their entirety. Thus, this test case checks that the coding of the main coefficients and the normal diffusion quantities have been carried out properly, and that all terms which should reduce to zero, if a completely orthogonal mesh is specified, do so. The other important quantity which is checked, is the programming of the explicit source terms of Eqs.2.30 and 2.31. It may be mentioned that these terms were totally absent for the flow through straight pipes presented in previous section. However, further assessment of these terms in conjunction with a non-orthogonal mesh will be highlighted in the following sections where flow through curved ducts with upstream and downstream tangents will be presented.

5.4 Flow Through a Constant Curvature and Constant Cross-section 90-deg Bend With Upstream and Downstream Tangents

The previous section described a calculation of a turning flow using a toroidal mesh, the full programme of the non-orthogonal code is tested in this section by applying it to a flow which could not be calculated using equations based on a toroidal system, namely a bend flow with attached straight sections.

5.4.1 Laminar Flow

Description of the Problem

In this section, the laminar developing flow in a circular cross-section 90-deg bend with upstream and downstream tangents is predicted and compared with experimental data of Enayet et al (1982). This is selected because both laminar and turbulent flow data were available in the same geometry. A diagram of the duct is given in Fig.5.12. The radius-ratio defined as δ=0.5(RO - RI)/R_c is equal to 1/5.6. The Reynolds number of the flow, based on the diameter D and bulk velocity of the fluid (water) u_0 was 500. The corresponding Dean number defined as $De=Re\delta^{1/2}$ is equal to 211. The study in Ch.4 has established the behaviour to be expected of the main governing flow parameters for these values of De.

The flow domain used in the calculations consisted of an upstream straight section of 2.6D and a downstream section of 4.0D. Due to the existence of symmetry, only one half of the circular cross-section was considered. Two grids were employed for the present study : one is 21x23x11 (in the η, ζ and ξ directions respectively) and the other is 37x46x19. The finer grid is shown in Fig.5.13 and the grid distribution over the cross-section indicates the level of non-orthogonality. The inlet velocity profile at 2.6D upstream of the bend was obtained in a similar manner to that followed by Iacovides and Launder (1984). A preliminary run was made (using precisely the same 37x19 grids in the pipe half cross-section) of developing flow in a straight pipe, the flow being allowed to develop until best agreement was obtained with the experimental data specified by Enayet et al (1982) at a station 0.6D upstream of the bend. The calculated values obtained in that solution 2 diameters upstream of that position were then used as the starting profile in the actual calculation (i.e., at a position 2.6D upstream of the bend). The two other velocity components v and w are believed to be insignificant and were set to be equal to zero at inlet. Essentially this procedure makes sure that the boundary layer thickness is correct at the inlet to the straight upstream tangent (which is of vital importance for this type of flow as discussed in Ch.4). For other boundaries such as wall, symmetry plane and exit, the usual boundary conditions as described in Chapter 3 were used. Calculations were performed on the ULCC AMDAHL 5890 computer. About 1000 iterations were necessary for complete convergence, and this took about 6 hours of CPU time for the highest grid resolution (37x46x19). The under-relaxation factors were taken to be α_u=0.8 and α_p=0.1 with 1 and 20 inner sweeps (Ch.3) through momentum and pressure-correction equations respectively.

Results and Comparisons with Experiment

The velocity vectors and isobars, $(p-p_{ref})/0.5\rho\, u_o^2$ (where, p_{ref} is taken in the centre of the upstream tangent at 0.6d upstream of the bend) in the symmetry plane are shown in Figs.5.14a-b. The vectors show that as the flow enters from the upstream tangent into the curved section, it accelerates near the inner wall and decelerates on the outer due to the pressure gradient induced by curvature. The maximum pressure occurs on the outer bend in the region $15<\theta<30$ degrees. Again the maximum velocity is shifted to the outside bend, as observed in Ch.4. The location of the maximum streamwise velocity at θ=75 deg occurs at r^*=0.7, the value of r^* is defined as :

$$r^*=(r - R_c)/0.5(RO - RI) \qquad (5.3)$$

This location is comparable to the 'r_{max}/a' for the fully-developed situation shown in the last chapter (Fig.4.7) at this particular Dean number (i.e., Dp=2400 for De=211). Although the flow is not fully-developed in this case due to shorter duct length, it appears that the displacement of the streamwise velocity towards the outside takes place mostly in the entrance region.

Figure 5.15 presents a comparison between predicted and measured streamwise velocity in the symmetry plane at the measurement locations of $\theta = 30, 60, 75$ degrees in the bend and one diameter downstream in the straight section. The non-dimensional distance r^* along the symmetry plane is defined by Eq.(5.3). It can be seen that the results do differ between the two grid densities used - approaching the experimental data with the finer mesh. This is the obvious effect of numerical diffusion which is a consequence of the first order hybrid differencing scheme (Spalding, 1972) employed for approximation of convection terms (i.e., smearing of the steep gradients, reductions of the peak values). A grid independent solution could be obtained by going into a very fine mesh, but the agreement with experiments is within 10% even at the level of the fine mesh used here. The profiles show that the flow never reaches a fully-developed state within the bend, and the maximum velocity continues to increase in the downstream tangent; this is reproduced by calculations, although the maximum value is underpredicted.

Contours of streamwise velocity u/u_0 in four cross-stream planes presented in Fig.5.16a-d, show the effects of the strong secondary flow which displaces the region of maximum velocity towards the outside wall in the manner expected from results in the previous chapter. As stated earlier, the flow cannot attain the fully-developed state, unlike those of Ch.4, because of the shorter length of the duct (§4.4.3). A closer look at the contours in the curved region reveals that the core flow continues to move towards the outer bend with a gradual increase of the magnitude of the maximum velocity. At one diameter downstream of the curved section, the magnitude of the maximum velocity still continues to increase but the core flow is found to shift back towards the inside. This is believed to be due to the residual effect of the secondary velocity which cannot disappear immediately after the exit, although it must decay as the radial pressure gradient which drives it is removed. The increasing magnitude of the maximum streamwise velocity at one diameter downstream is related to the growth of the boundary layer. All these observations are in agreement with the experimental data of Enayet et al (1982). In Fig.5.17 the computed contour values are compared with the corresponding measured contours for two streamwise locations. The comparisons can be taken to be quite satisfactory, although the peak values are usually underpredicted (also shown in Fig.5.15). This comparison shows that the differencing scheme for convection terms is, as expected, significantly diffusive. More will be discussed in §5.4.3.

The secondary velocity vectors at the corresponding locations are shown in Fig.5.18.The secondary flow vortex is already well established at $\theta=30$ deg. As the flow moves downstream, the vortex centre is pushed nearer the inside of the cross-section and at around 75-deg, it develops a 'tail' as observed in similar flows in

Ch.4. Fig.5.18d shows clearly that, although the secondary flow persists in the straight tangent, its magnitude has decayed significantly. More quantitative information about the intensity of the secondary velocities can be obtained from the v and w velocity contours presented in Figs.5.19 and 5.20. Similar to the observations of the previous chapter, the secondary velocities attain maximum values in the early stages at around θ=30 deg and then weaken in magnitude. The movement of the vortex centre towards the inner bend can be clearly observed from the nature of the v velocity contours in Figs.5.19a-c. At one diameter downstream of the bend, the vortex still persists within the core region. But the intensity of the secondary flow near the walls is found to have decayed to a much smaller value (from $0.25u_0$ at 75-deg to $0.05u_0$ at one diameter downstream). In their explanation of the streamwise velocity development, Enayet et al (1982) have presumed that (since no secondary velocity measurements were taken) the strength of the secondary velocity does not decay upto one diameter downstream of the duct. This is not supported by the present computations. What really happens is that the secondary velocities are very quick to respond to the removal of the transverse pressure gradient, whereas the main stream velocities are rather sluggish and hence the residual effects of the secondary velocities can be observed in the streamwise velocities even at a downstream section.

5.4.2 Turbulent Flow

Description of the Problem

The same 90-deg bend described in the previous section was considered for turbulent flow prediction. The experimental data with which comparisons were made are again due to Enayet et al (1982). The geometrical details are identical to those in Fig.5.12 and the definitions of r^*, Re and De are also kept the same. The Reynolds number of the flow was taken to be equal to 43,000 with a corresponding Dean number of 18,170.

Three grid systems were used for the calculations viz., 21x23x11 (in the η, ζ and ξ directions respectively), 37x23x19 and 37x46x19. The first two allow conclusions to be drawn on refining the grid in the pipe cross-section, while the last two assess the streamwise grid refinement. Most results presented in this section were obtained with the finest mesh. The inlet values of the dependent variables were obtained by following the same procedure as described for the laminar flow and the usual boundary conditions (Ch.3) were applied. Computations were done on the AMDAHL 5890 computer at ULCC and it took about 2000 iterations to be absolutely sure of convergence and some 20 hours of CPU time.

Results and Comparisons with Experiment

The velocity vectors in the symmetry plane are shown in Fig.5.21. The flow acceleration in the inner wall can be seen upto about θ=30 deg. Although the maximum velocity again moves to the outer bend, the shape of the profile is very different to the laminar flow case. The isobars in the symmetry plane are shown in Fig.5.22a. The static pressure coefficient $Cp=(p - p_{ref})/0.5\rho u_o^2$ is compared with experimental data in Fig.5.22b. It can be seen that the magnitudes of Cp in the inner bend are under-predicted by as much as 15%. On the other hand, the predicted values of Cp match closely with the experimental data on the outer bend. All these observations are in accordance with findings of Manners (1988) in the case of an S-diffuser flow. The reasons for such discrepancies will be made clear from later discussions in this section.

Fig.5.23 shows a comparison of the predicted streamwise velocity on the symmetry plane at four measuring stations (θ=30, 60, 75 deg and one diameter downstream of the curved section) for the three different grids. Within the curved section, maximum improvements are obtained by refining the grids over the cross-section (from 21x11 to 37x19), suggesting that the gradients in the streamwise direction are relatively well resolved (by changing from 23 to 46). On the other hand, at one diameter downstream of the bend, opposite behaviour can be observed and hence more grids in the streamwise direction are needed for better resolution. The main discrepancies with experimental data are found in the inner half of the cross-section, for example, the double peaks at θ=60 and 75 degrees are not reproduced. In an attempt to evaluate the quality of the present prediction and to identify the reasons behind the discrepancies, the fine grid results are compared with the computations of Iacovides and Launder (1984) and Anderson (1988) (wherever available), who have also solved this particular flow configuration by employing an orthogonal meshes. The comparisons are shown in Fig.5.24.

Of the two references mentioned above, Anderson employed an algebraic mixing length turbulence model, upwind differencing scheme and a very fine mesh (50x50 on the cross-section and 86 in the streamwise direction). Iacovides and Launder, on the other hand, employed k-ε eddy-viscosity model of turbulence for the core and instead of using the log-law for bridging the gap between the wall and the first grid node, they have resolved the parabolic sub-layer by making use of very fine mesh (28 in the radial direction out of which 7 were placed in the sub-layer, 20 in the circumferential and 70 in the streamwise direction) and a one equation mixing length model. A higher order differencing scheme (QUICK, Leonard, 1979) has been used for approximation of the convection terms. Both of the above works have neglected the streamwise diffusion and hence essentially semi-elliptic equations were solved. Fig.5.24a shows that the present predictions are much closer to the experimental data than Anderson (1988). At $\theta=60$ and 75 degrees, the present predictions show a smearing of the large radial gradients near the inner half of the bend, which is also evidenced in the computations of Anderson. On the other hand, the peak velocities are relatively well predicted by Iacovides and Launder. The reason is obviously related to the difference in convection schemes. However, none of the predictions reproduces the double-peak nature at $\theta=60$ and 75 degrees. At one diameter downstream, the predictions of Iacovides and Launder and the present results show large differences and it is hard to realize which one is superior. Finally, the present computations exhibit significant discrepancy in calculating the velocity very near to the walls, which again is believed to be due to insufficient resolution of the shear layer. Also important is the validity of the log-law for the regions of very high secondary velocity (as will be shown in the next paragraph). It needs to be mentioned that, although the predictions of Iacovides and Launder can be taken to be superior in predicting the streamwise velocity near the wall within the curved section of the duct, it shows poorer agreement at one diameter downstream. The other aspect of their calculation is the streamwise velocity separation at $\theta=90$ degrees, which is neither supported by any other prediction nor by experiments. However, the application of a one equation model needs further assessment if the log-law is to be replaced. More discussion on this topic is deferred until the next section.

However, it is clearly demonstrated that reasonable predictions of velocity are possible even with a highly distorted mesh for a regular geometry. By using better grid generation technique, resolution in the near wall can be significantly improved and numerical diffusion can be substantially reduced by employing a non-diffusive higher order differencing scheme. These aspects will be addressed in Chapter 7. The turbulence intensities are defined as $(2k/3)^{1/2}$ to allow comparison with the single measured streamwise fluctuating component, u' at the corresponding locations (Fig.5.25). High values are generated near the walls and low values in the core region, but sudden peaks are not reproduced. The discrepancies are related to the computed velocity discrepancy. Other reasons will be mentioned in §5.4.3.

The streamwise velocity contours are presented at four locations in Fig.5.26. The qualitative nature of these are similar to those observed in the laminar flow cases (cf. Fig.5.16). The main difference is that the boundary layers in this case are thinner and the flow acceleration in the inside bend is found to persist even at $\theta=30$ deg. The maximum core flow is found to be shifted away from the plane of symmetry at $\theta=60$ and 75 degrees, at which locations the secondary velocity vortices (Fig.5.28) reveal a distorted structure. In Fig.5.27, the computed streamwise velocity contours are compared with the experimental results at two azimuthal stations. The comparisons clearly demonstrate that the steep gradients near the inside of the cross-section are smeared out and are in conformity with the velocity profiles.

In comparison to the laminar flow (Fig.5.18), the vortex centres in Fig.5.28 are further pushed towards the symmetry plane near the inner bend. The v and w velocity contours are presented in Figs.5.29-5.30. The magnitude of the maximum v-component is approximately the same as that for the laminar case, but its location has shifted more towards the wall and this implies that the logarithmic law of the wall which has been used for bridging the gap between the wall and the first grid node cannot be an accurate one. The rate of decay of the secondary velocity at one diameter downstream of the curved section appears to be much slower than the corresponding laminar case.

5.4.3 Discussions

The results presented in the previous two sections showed some discrepancies with experimental data. Since the developed code is intended for the calculation of complex geometry curved ducts and will be used in the next chapter for the calculation of flow in volute geometries, the reasons behind these discrepancies need to be clarified at this stage.

First the numerical error may have contributed partly (and solely for the laminar case) to these discrepancies. It is known that if the grid numbers that can be employed tend to infinity (or to a certain number after which the results do not vary), all the numerical errors tend to zero. For three-dimensional flows such as the ones studied here, one cannot increase the grid numbers very much. The alternative is to use finite grid spacing along with higher order accurate 'differncing schemes' which embody the physical behaviour of the convection-diffusion nature of fluid flow (Patankar, 1980). As has been mentioned in Ch.3, in this work, the 'hybrid' differencing scheme has been adopted for approximation of the convection terms due to its property of being unconditionally bounded. This particular scheme is only first order accurate and suffers from 'false diffusion'. This is well-known and has been confirmed by the present investigation. So, one way of improving the results would be to use higher order differencing schemes such as QUICK, LUDS (Ch.3) etc., and these are recommended as future extensions to the present numerical procedure in Ch.7.

The discrepancies for the turbulent case seem to be much higher which is believed to be due to the combined effect of numerical as well as physical limitations of the k-ε (eddy-viscosity) model of turbulence. Although the wall-function approach for bridging the gap between the first grid node and the wall is a convenient way for plane two-dimensional turbulent flows, its application here is of limited accuracy due to the strong three-dimensional nature of the flow (Iacovides and Launder, 1984). It has been shown in Figs.5.29 and 5.30 that the secondary velocities of around 30% of the bulk velocity are found to occur near the wall and hence the near-wall profile is unlikely to conform closely with the usual semi-logarithmic law. Further, the streamline curvature and the existence of turbulence anisotropy (Azzola et al, 1986) have all contributed to the observed discrepancies. The turbulence intensities in the symmetry plane given in Fig.5.25 show largest discrepancies with experiment and often failed to reproduce the qualitative behaviour. Apart from the reasons mentioned earlier there is another ambiguity about the comparison; that instead of u', v', w' only one component (u') was measured which is compared with the turbulence intensity $(2k/3)^{1/2}$, assuming that all three components of the fluctuating velocity components are equal. The other important aspect is that the predictions in general are poorer near the inner bend than on the outer bend. This is related to the rapid flow variations in the inner bend which the present calculations could not pick up accurately because of the reasons mentioned earlier. The discrepancy between the predicted static pressure and experimental data in the inner bend are also related to the poorer predictions of flow variables in the inner bend.

Nevertheless, the results of the present predictions do account for most features of the flow and suggests that the developed code can be used to reasonably predict complex three-dimensional duct flows.

5.5 Laminar Flow Through a Constant Curvature and Variable Area 45-deg Diffusing Bend

All the above flows which were used for experimental checks have been of constant area; since the volute flows have rapid area variations, this aspect of the code is also subjected to scrutiny.

Description of the Problem

Flow through a 45-deg C-diffuser of circular cross-section, studied experimentally by Rojas (1986), has been predicted and the results are presented in this section. The geometry of the duct is shown in Fig.5.31. It consists of a circular 45-deg diffusing bend having a constant mean radius of curvature, R_c. The cross-sectional shape is circular everywhere but the area increases linearly with azimuth angle θ from entrance of the curved section (A-A) to the end of the bend (B-B) giving an expansion ratio of $A_{exit}/A_{in}=1.5$. The radius ratio δ defined as $\delta=0.5(RO - RI)/R_c$ is equal to 1/14 at the upstream tangent and at exit from the bend (due to area expansion) δ is equal to 1/11.4. As for the 90-deg bend, the experimental fluid was water and the Reynolds number of the flow, based on the hydraulic diameter of the upstream tangent, D_0 and bulk velocity , u_0 was 790 with a corresponding Dean number (based on the radius ratio 1/14) of 211. The measurements of the streamwise velocity were made at three cross-stream planes at $\theta=4$, 20.5 and 41-degrees inside the curved portion.

The flow domain used in this set of calculations consisted of an upstream section and a downstream section of $2.6D_0$ and $5D_0$ long respectively. Again, due to the existence of a symmetry plane, only one half of the duct need to be considered. The grids employed are similar to those in the case of 90-deg bend (§5.4) except that due to the area expansion, the cross-sectional area increases linearly with θ. The number of grids employed were also 21x23x11 (in the η, ζ and ξ directions respectively) and 37x46x19. One of the grids in the symmetry plane is shown in Fig.5.32a.

As already mentioned, the first set of velocity measurements were reported at $\theta=4$ deg, which is well inside the curved region. This provides a difficulty in the present context, since the numerical calculations require boundary conditions upstream of the bend and the predictions are known to be sensitive to the thickness of the boundary layer specified (Ch.4). In order to get the inlet data at $2.6D_0$ upstream of the bend, a trial and error procedure was followed by setting various inlet profiles. Calculations were done on the coarse grid and the solution for which the predicted streamwise velocity profile matched closely with experimental data at $\theta=4$ deg location has been selected to be the correct one and the inlet velocity data corresponding to this run was employed also for the fine grid computation. Two other velocity components v and w were set to be equal to zero. The other boundary conditions applied were the same as those for the laminar flow through the 90-deg bend.

Results and Discussions

The flow characteristics in the symmetry plane are presented in Fig.5.32b-c. The velocity vectors clearly demonstrate the shifting of the streamwise velocity towards the outer bend and accumulation of a low velocity region (less than $0.2u_0$) in the inner half of the cross-section at and after $\theta=40$ degrees, although no separation was observed.

The isobars defined as $Cp=(p - p_{ref})/0.5\rho u_o^2$, reveal that in the curved section of the duct, the maximum pressure occurs on the outer wall between $18<\theta<35$ degrees. The steeper gradients of the isobars are directly related to the higher velocity gradients near the outer part of the bend. In Fig.5.33 comparisons of the predicted streamwise velocities are made with experimental data in the symmetry plane at the measurement stations of θ=4, 20.5 and 41 degrees. The discussion made in §5.4.1 about the comparison of laminar flow through 90-deg bend are equally valid for the present case. However, the discrepancy at the 4-deg location appears to be due to a continuity error in the experiment. Since the flow is fully three-dimensional, it was not possible to calculate the total (experimental) flow rate accurately given the very coarse resolution employed over the cross-section in the measurements (to be shown in Fig.5.35a). A conservative estimate showed a mass error of around 10%. In all the profiles of Fig.5.33, the obvious effect of area-expansion can be seen in the maximum values of the streamwise velocity. In spite of the above, the change in the shape of the profile as the flow moves through the diffuser is well represented, particularly on the finer grid. The development pattern of the streamwise velocity can be seen more clearly from the contours of u/u_0 at four azimuthal stations (Fig.5.34). In Fig.5.35 the isovelocity contours at two measuring stations are compared with the current predictions.

The secondary velocity vectors and contours of v and w components are shown in Figs.5.36-5.38. Most of the features such as location of the 'null' contours, position of maximum secondary velocity etc., are similar to the ones for the 90-deg bend (cf., Figs.5.18-5.20). However, the intensity of the secondary velocities are much lower than the 90-deg bend, although the Dean numbers (equal to 211) for these two cases are exactly the same. For the 90-deg bend the maximum v velocity was 35% of the bulk velocity (Fig.5.19b-c); but here it is only 20% (Fig.5.37b), when normalized by the 'local area-mean velocity' this increases to 25%. It has been shown in Chapter 4 that the intensity of the secondary velocity is determined mostly by the curvature i.e., the radius-ratio. With reference to Figs.4.16a-b, it can be seen that the maximum secondary velocity decreases by about 9% for a curvature variation from 1/7 to 1/20. The order of reduction of the secondary velocity for this case in comparison to the 90-deg bend of previous section is very close those shown in Fig.4.16. From this observation it can be said that the strength of the secondary velocity is not very sensitive to area variation at least for the moderate area expansion of this flow configuration.

In Fig.5.37c the F' contour near the inner bend is of particular importance because it shows a weak separation of the secondary boundary layer growing from the outside bend towards inside along the curved wall. This can be seen more clearly from the velocity vectors at corresponding location in Fig.5.36c. The w-contour in Fig.5.38c shows a second 'null' contour E in the region of separation. This secondary flow separation bubble was located in the streamwise direction between $35<\theta<45$ degrees. The reasons are believed to be the same as those described in Ch.4 which are, possibly, intensified by the area expansion. Near the exit from the bend, the streamwise velocities reach a very low value as can be seen from the isovelocity contours of Fig.5.34 as well as from the profile of Fig.5.33c. Although, the secondary boundary layer has already separated there, the streamwise velocity adheres to the curved wall and no separation took place, which is in accordance with the flow visualization study of Rojas (1986).

5.6 Closure

In this chapter, a thorough testing of the general computer code developed for handling complex geometry ducts was undertaken. The code was applied to a variety of flow configurations ranging from very simple to complex three-dimensional turbulent flows. The test cases considered were such that the various aspects of the code could be evaluated in terms of cost, reliability and accuracy. Based on the results and discussions presented in this chapter, the following conclusions can be drawn :

i) The developed computer code is capable of predicting both two- and three-dimensional laminar and turbulent flows in complex geometry ducts. The non-orthogonality of grid lines does not pose any difficulty other than slowing down the rate of convergence requiring smaller under-relaxation factors and hence making the calculations more expensive.

ii) By employing finer meshes, numerical errors can be substantially reduced and the results made more accurate. For both laminar and turbulent flows, qualitative and quantitative agreement between predictions and experiments can be obtained for highly complex three-dimensional flows given that sufficient resolution of the flow field is achieved; it was found that this could be resolved with meshes which were obtainable at the available computer resources. However, inherent limitations of the $k-\varepsilon$ (eddy-viscosity) turbulence model and the treatment of the wall boundaries adopted limits the accuracy of turbulent flow predictions in the strongly curved ducts considered. To what extent this will affect the ability to calculate even more complex curved duct flows such as found in volutes remain to be established.

iii) For the constant curvature and constant cross-section 90-deg bend, the rate of decay of the secondary velocity in the downstream tangent is much slower for the turbulent case than for the laminar. In neither flow, was any separation of the main flow observed.

iv) The obvious effect of area-variation in the case of C-diffuser is the reduction of streamwise velocity and an accumulation of low velocity region near the exit from the bend. In comparison to the 90-deg bend at the same Dean number, the magnitude of the maximum secondary velocity is at least 10% less for the C-diffuser, which is mostly due to the effect of smaller curvature and also partly due to area expansion. Although the streamwise velocity adheres to the whole length of the duct, the secondary boundary layer was found to be separated near the inner bend in the later part of the duct.

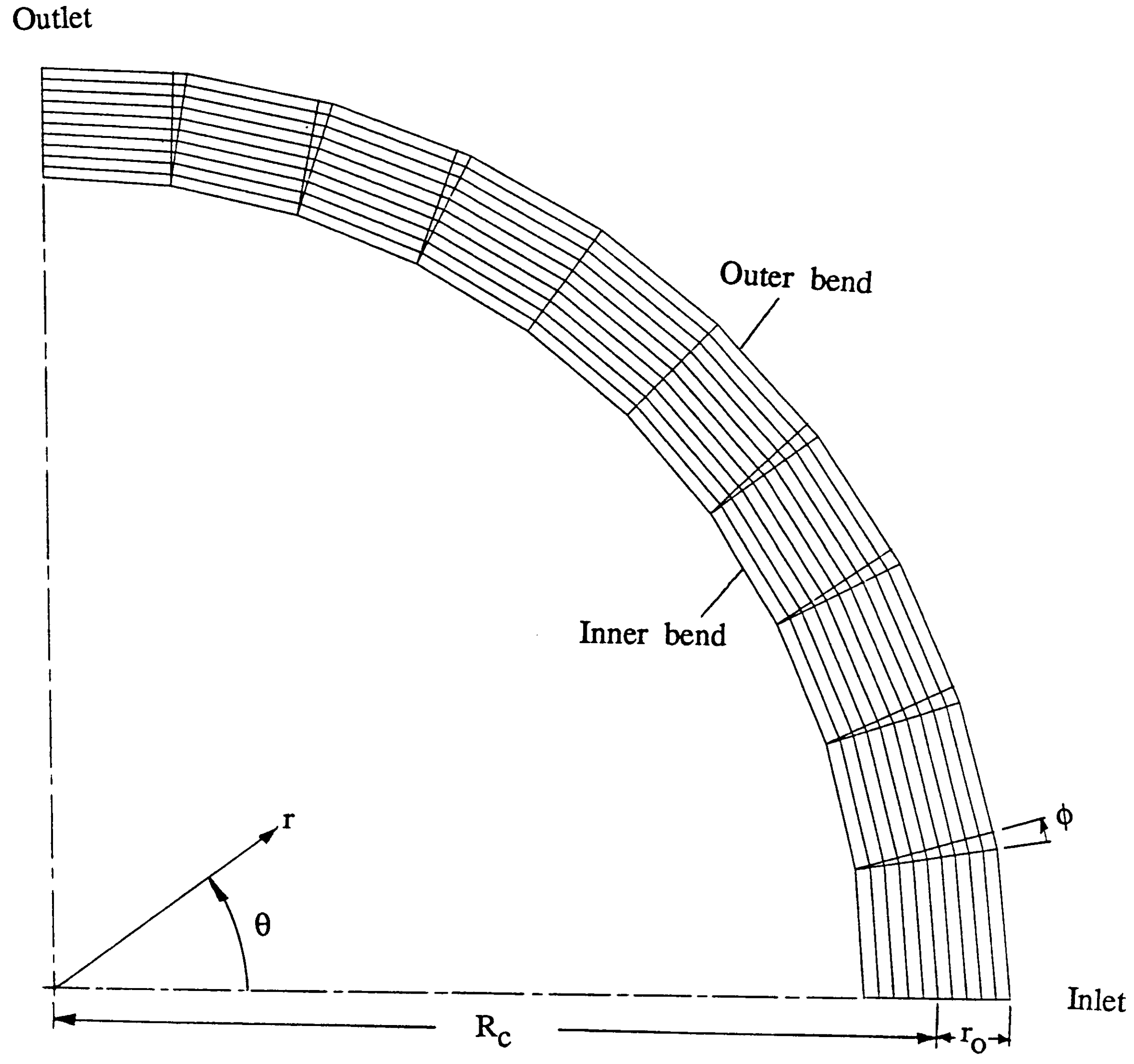

(a)

Fig. 5.1a Test geometry of the reducing-area curved duct having moderate curvature (δ=1/12, 11x11 grid nodes)

-- cont'd

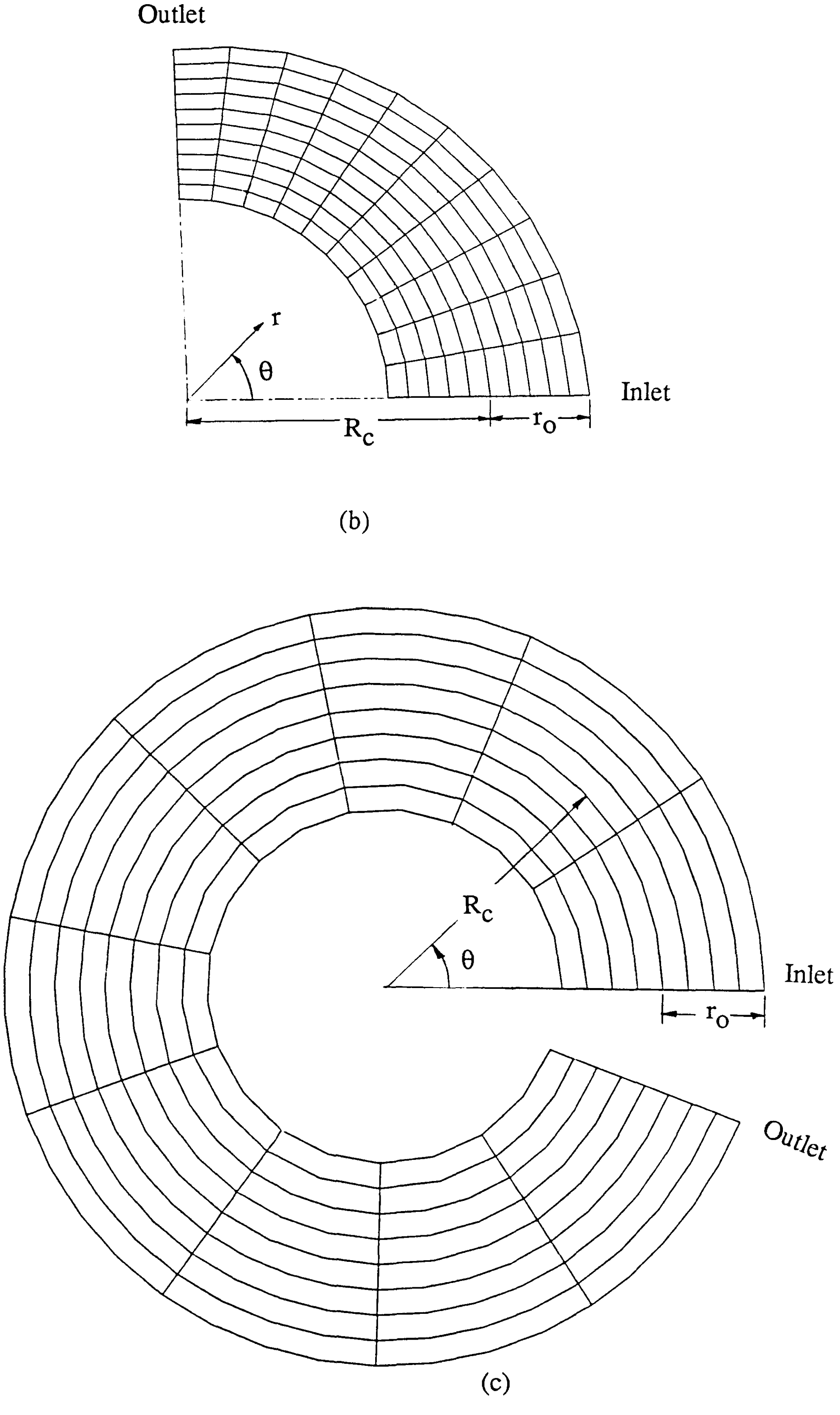

Fig. 5.1 (cont'd) Test geometries of curved ducts having strong curvature, $\delta=1/3$
(b) Reducing cross-sectional area (11x11 grid nodes)
(c) Constant cross-sectional area (not all grids are shown)

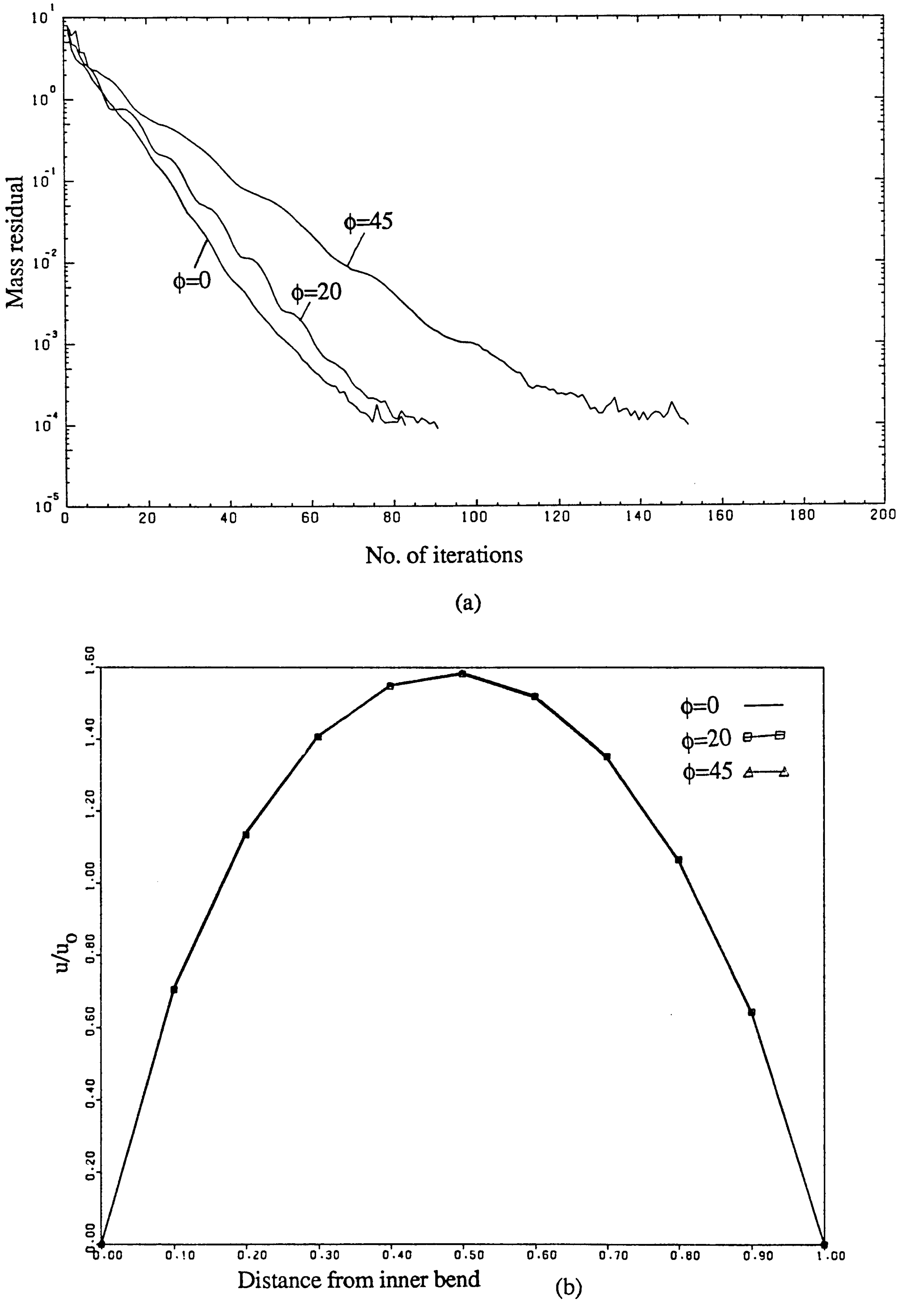

Fig. 5.2 Flow and convergence behaviour for geometry of figure 5.1a (11x11 grids)
(a) Normalized mass residual (b) Streamwise velocity at θ=50.4 deg.

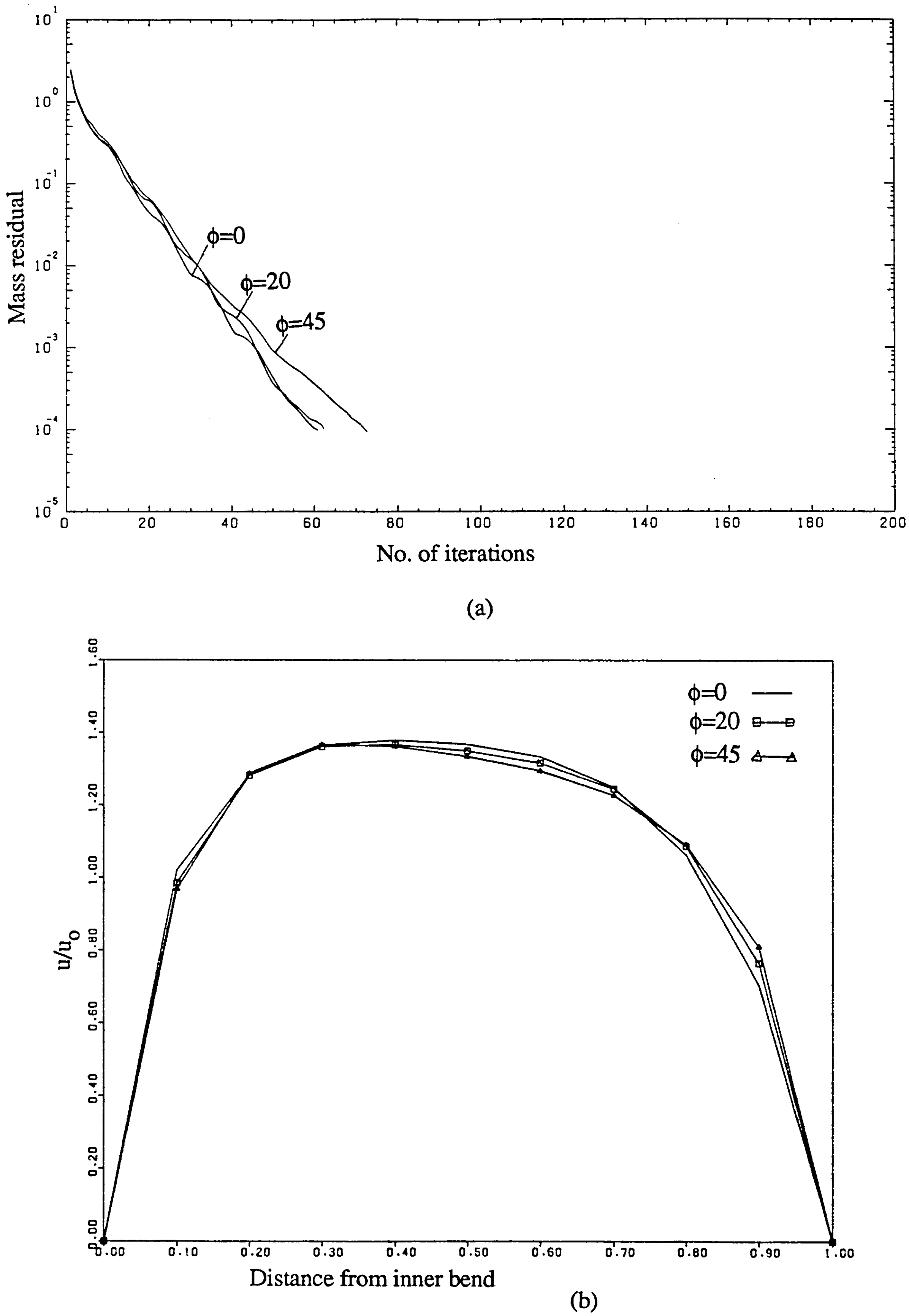

(a)

(b)

Fig. 5.3 Flow and convergence behaviour for geometry of figure 5.1b (11x11 grids) (a) Normalized mass residual (b) Streamwise velocity at θ=50.4 deg.

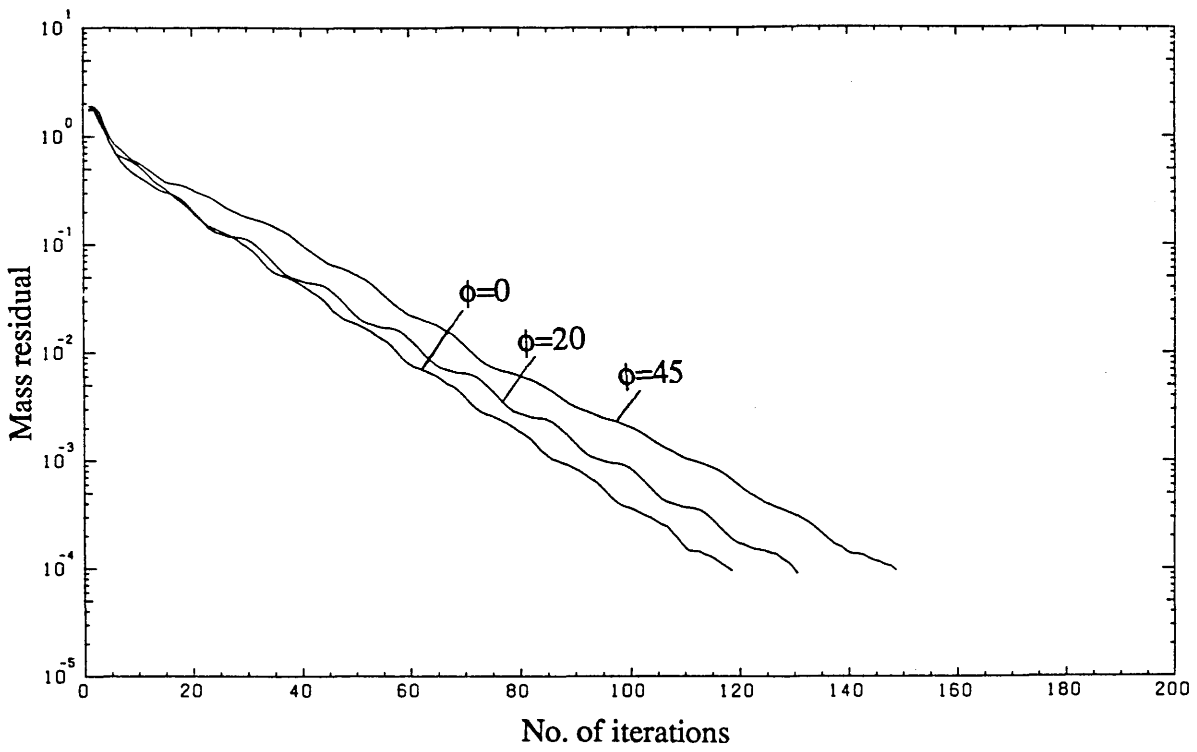

(a)

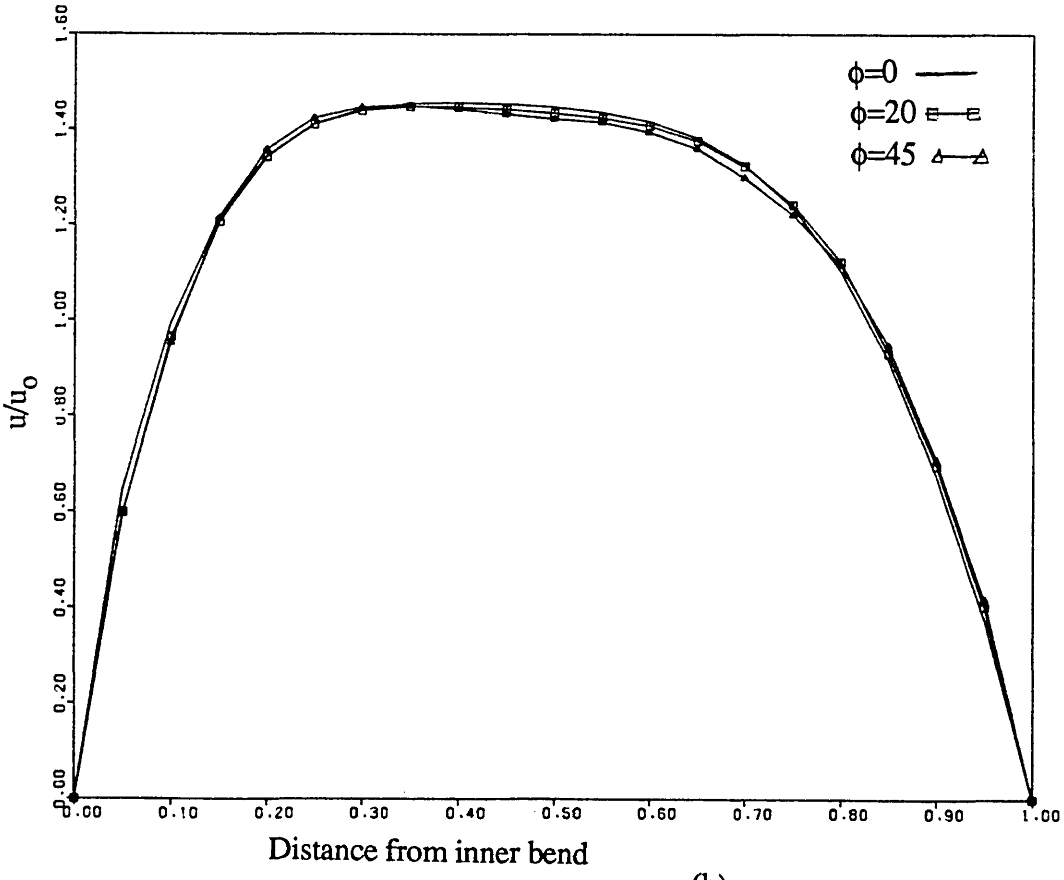

(b)

Fig. 5.4 Flow and convergence behaviour for geometry of figure 5.1b (21x21 grids)
(a) Normalized mass residual (b) Streamwise velocity at θ=50.4 deg.

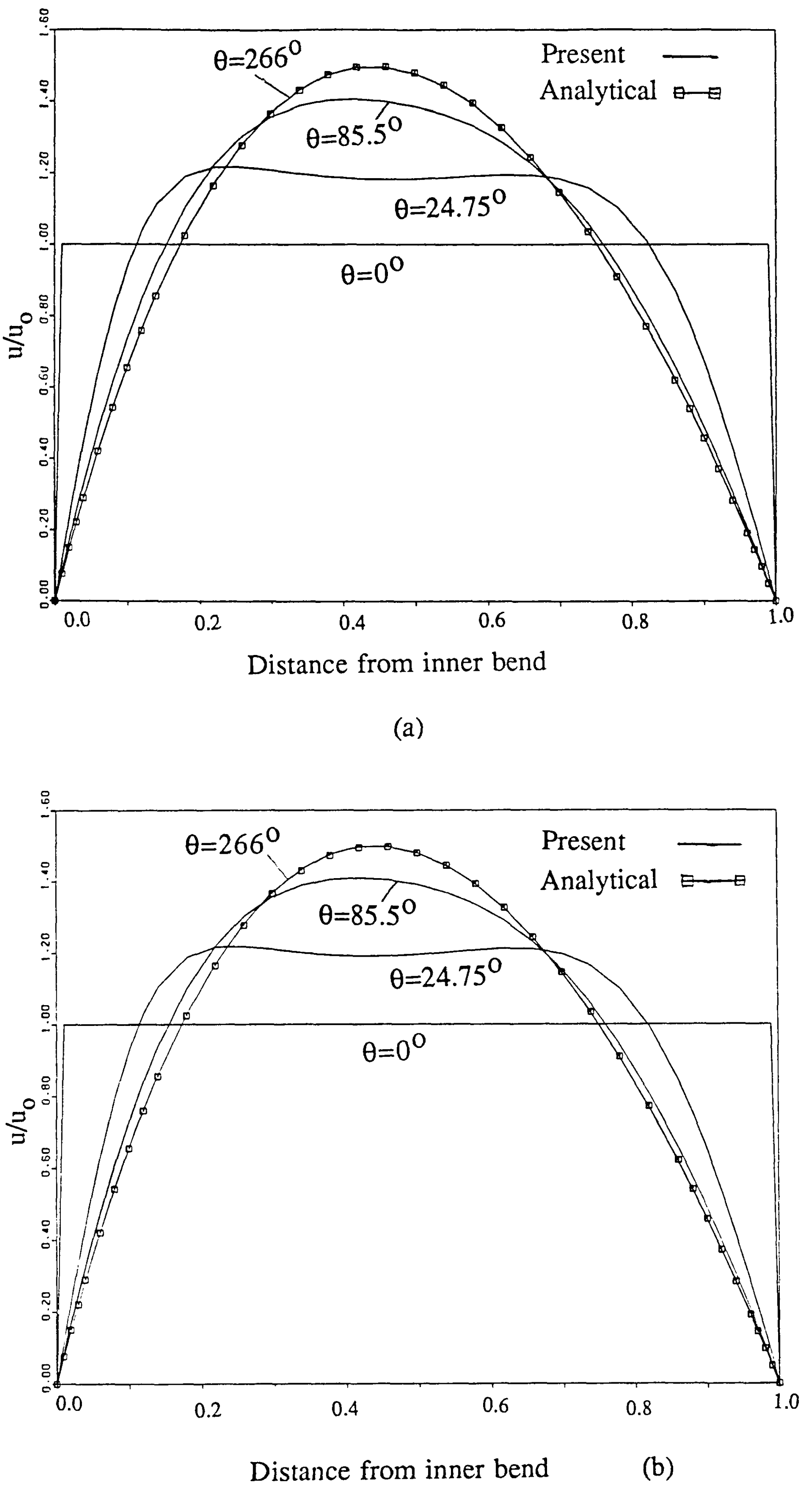

Fig. 5.5 Development of streamwise velocity through constant area duct of figure 5.1c

(a) Using toroidal coordinate system

(b) Using general code with radial lines inclined at ϕ=20 deg.

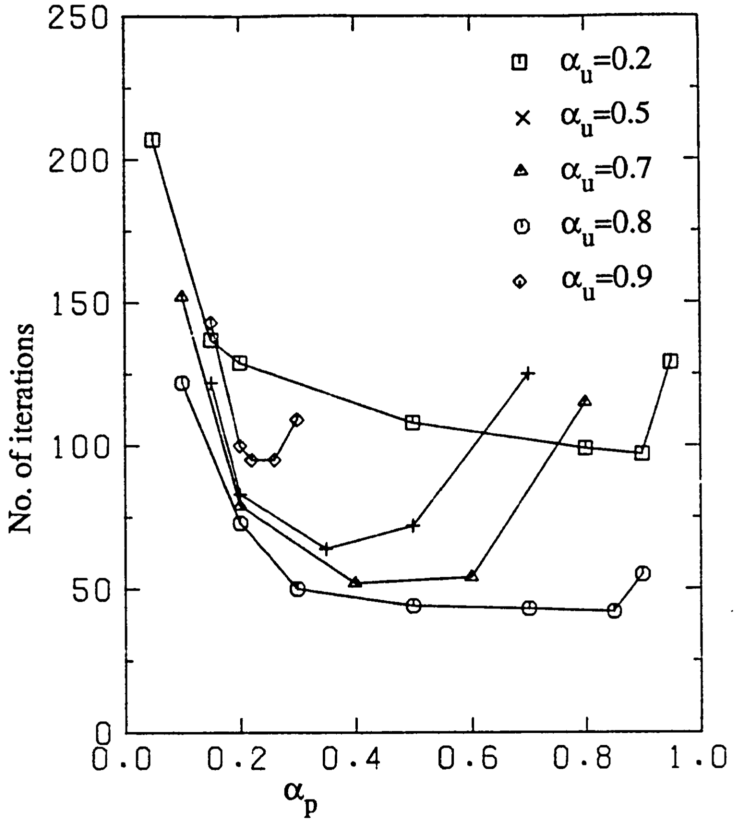

(a) Non-inclined radial lines, ϕ=0 deg.

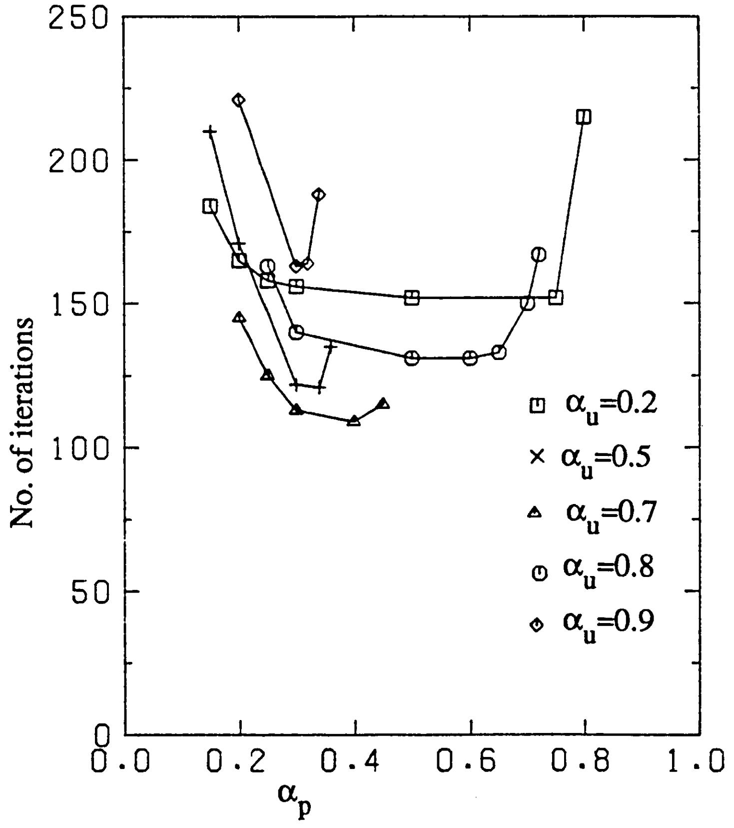

(b) Inclined radial lines, ϕ=45 deg.

Fig. 5.6 Effect of under-relaxation factors for the duct of figure 5.1a

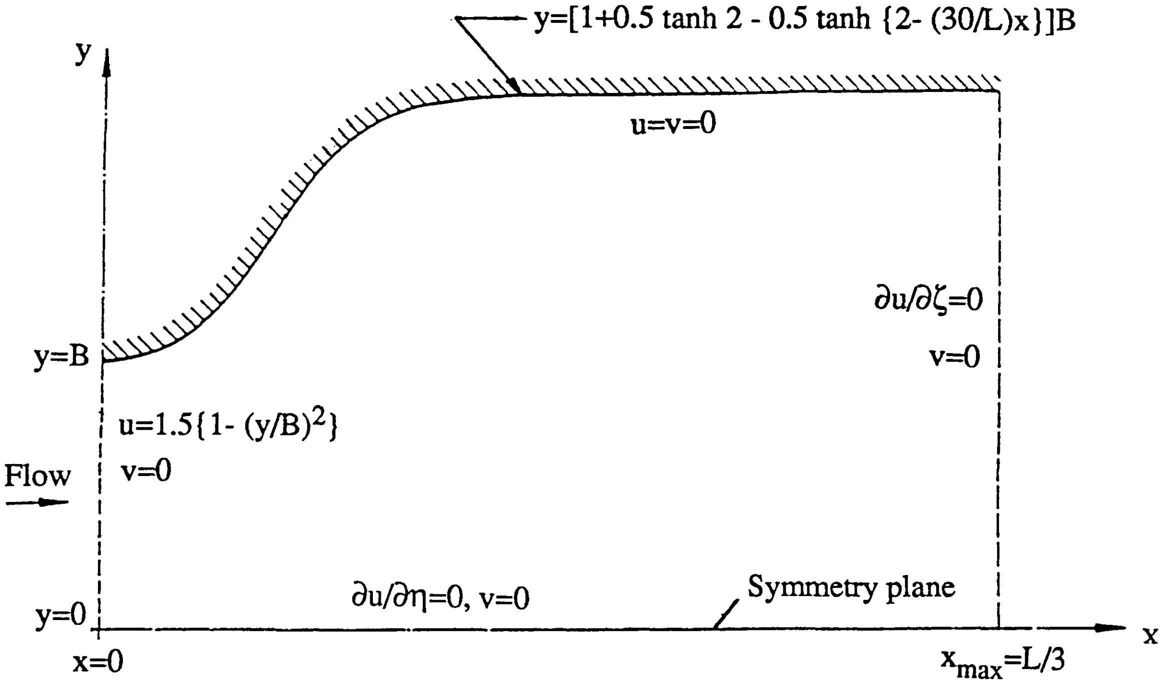

Fig. 5.7a Flow geometry and boundary conditions for 2D curved diffuser

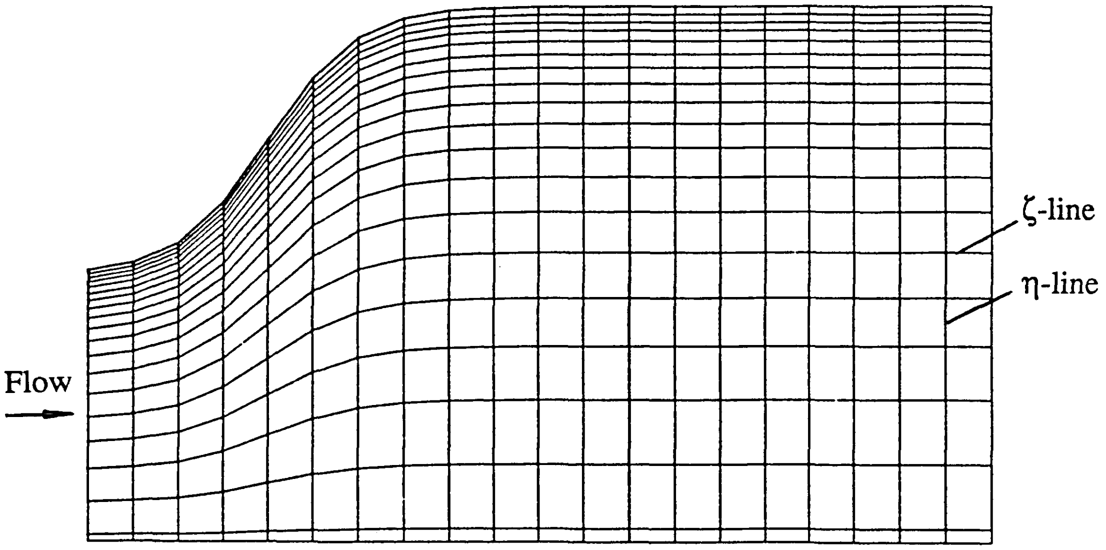

Fig. 5.7b Computational grids for curved diffuser

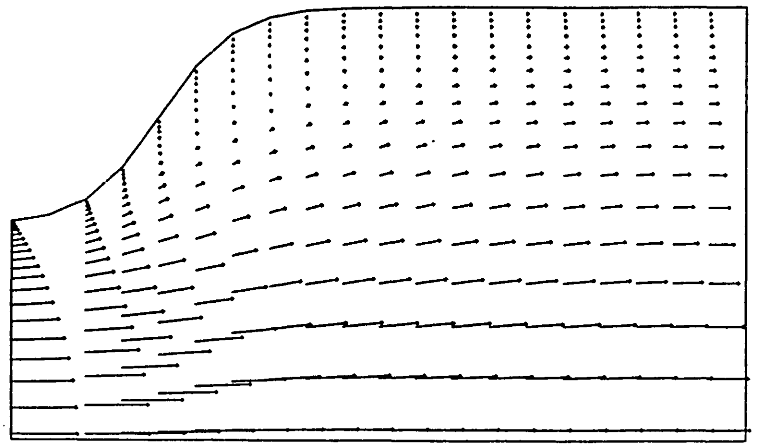

(a) Velocity vectors

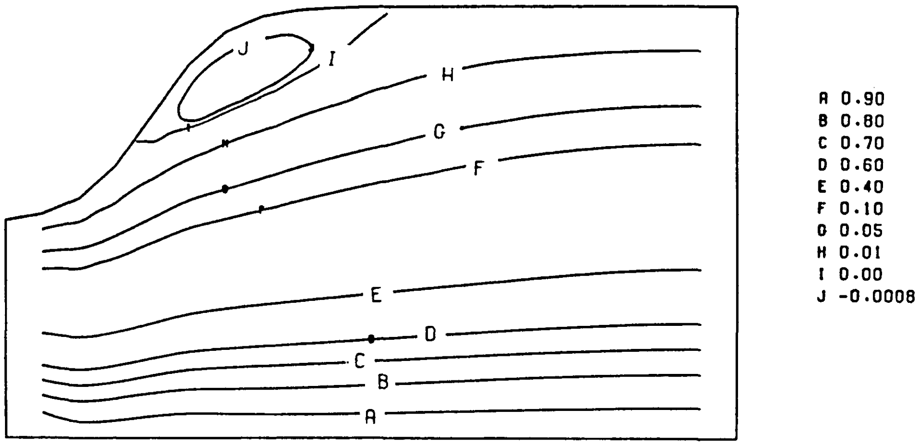

(b) Streamlines

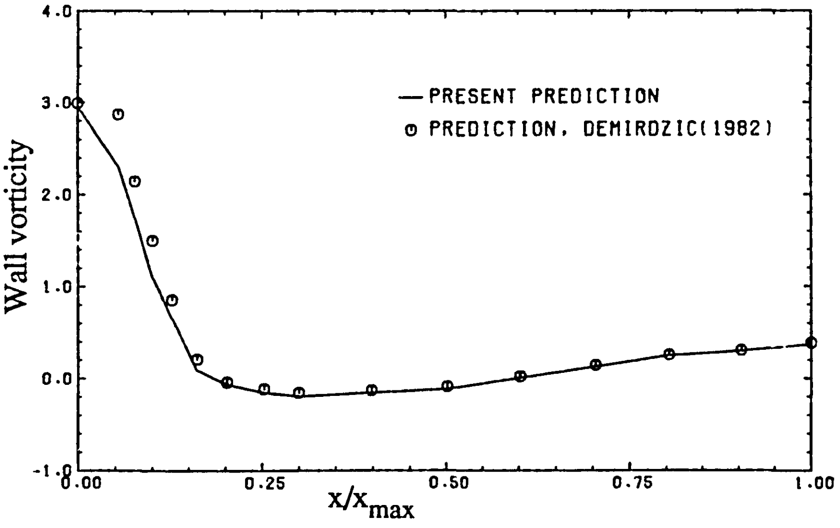

(c) Comparison with Demirdzic (1982)

Fig. 5.8 Predicted flow characteristics for 2D curved diffuser

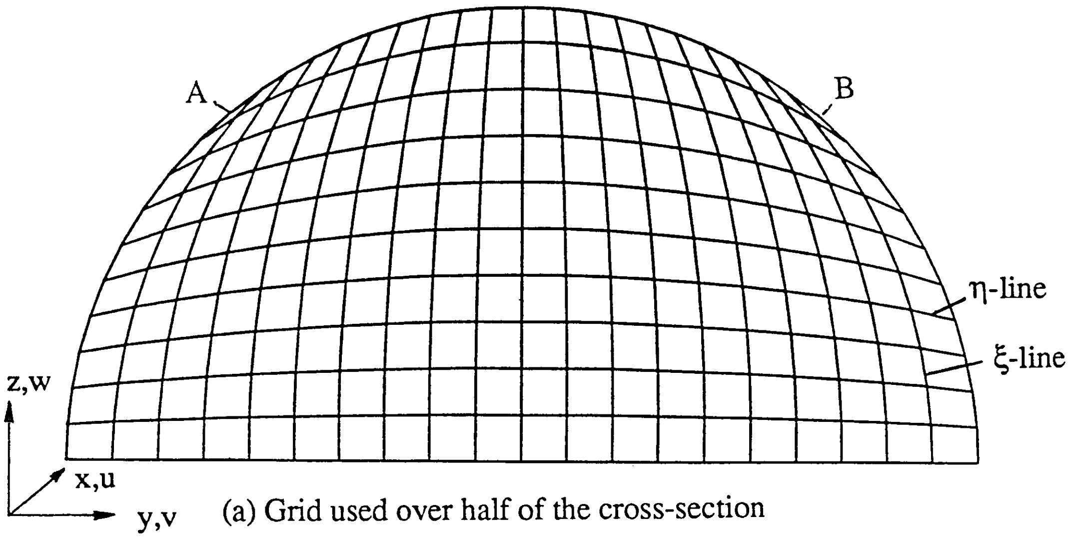

(a) Grid used over half of the cross-section

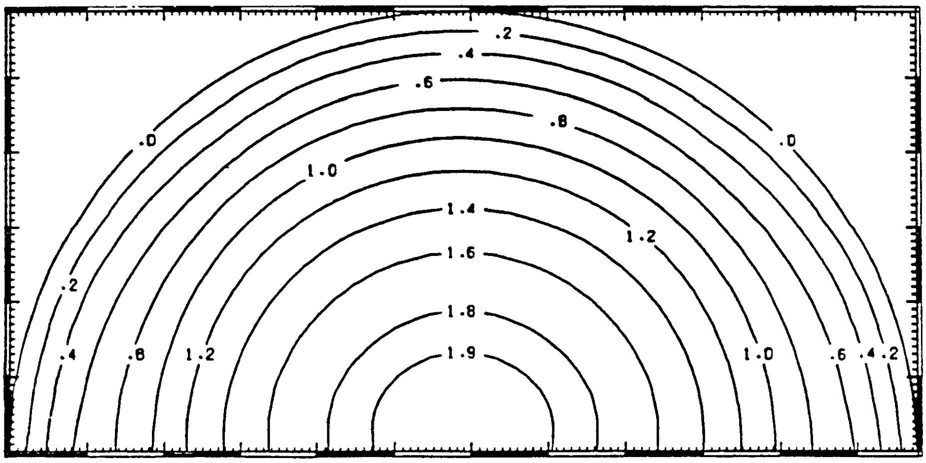

(b) Isovelocity contours, u/u_0

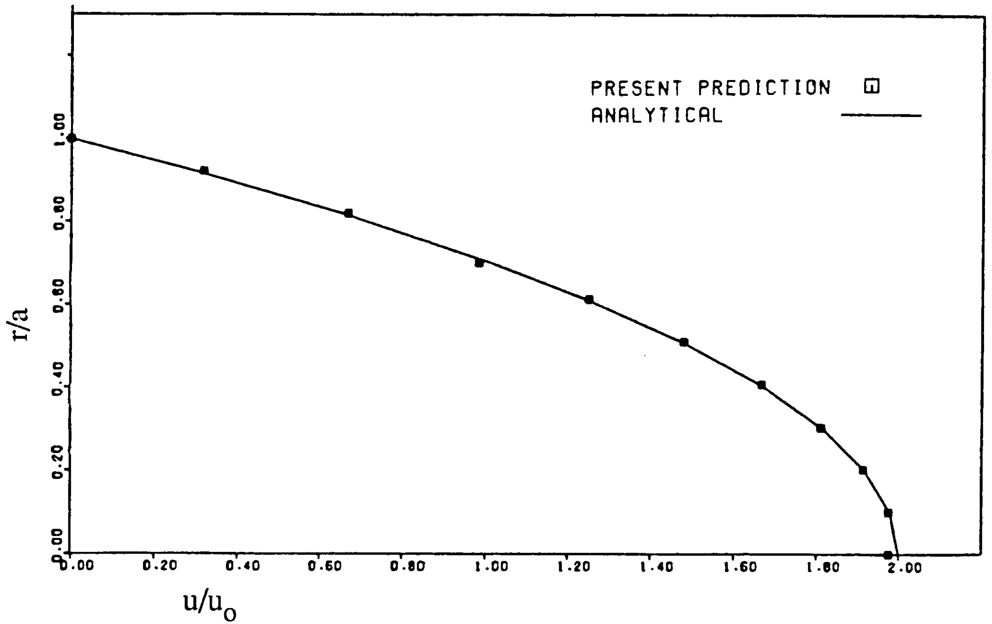

(c) Comparison of velocity

Fig. 5.9 Fully-developed laminar flow characteristics for straight circular pipe

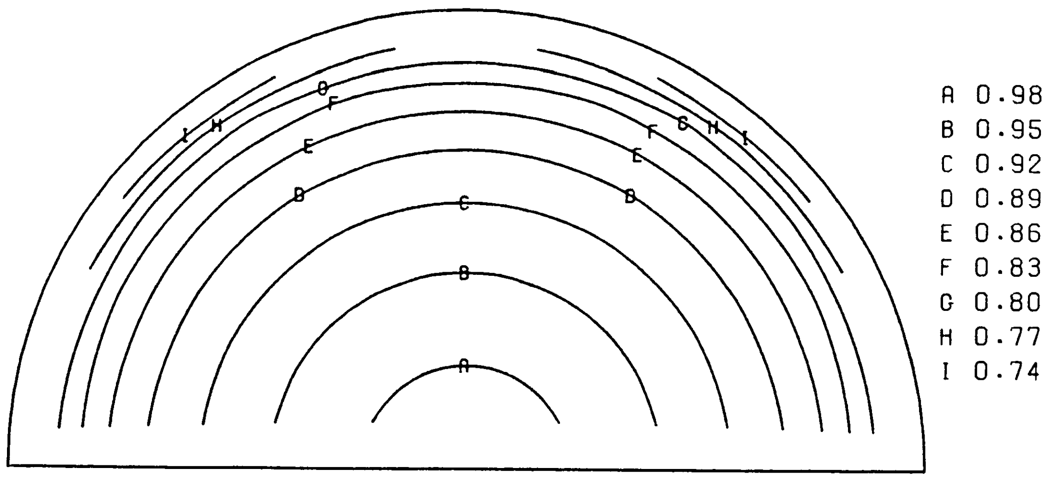

(a) Isovelocity contours, u/u_{max}

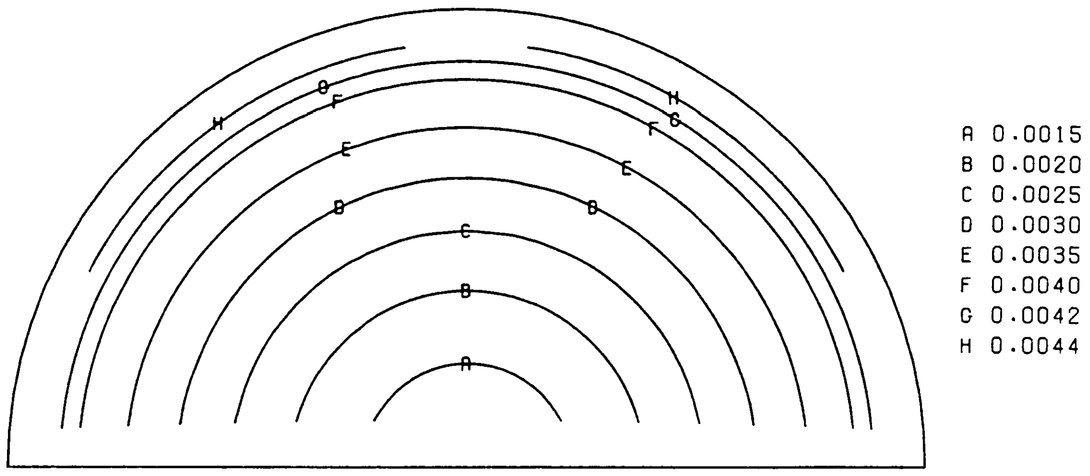

(b) Turbulence intensity, k/u^2_{max}

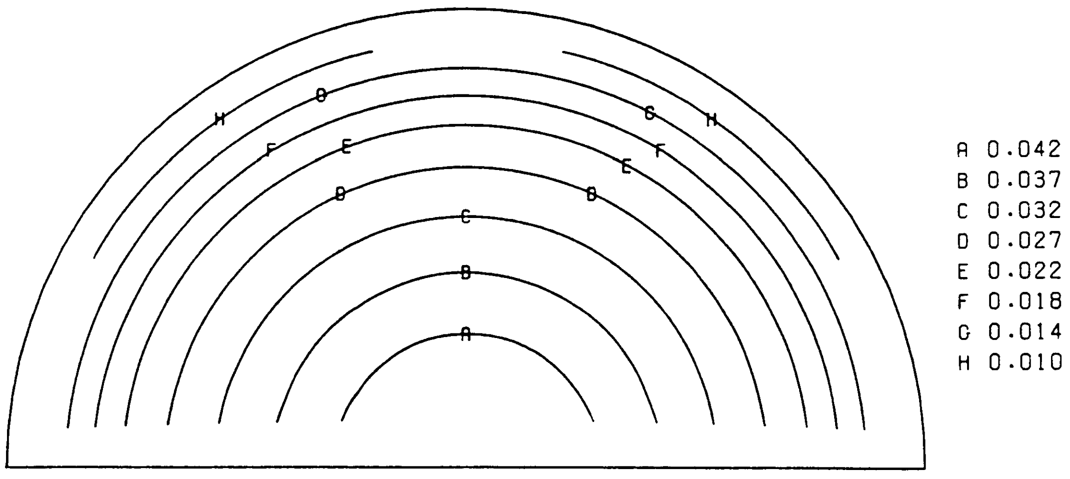

(c) Length scale, $C_\mu k^{3/2}/(\varepsilon D)$

Fig. 5.10 Fully-developed turbulent flow characteristics for straight circular pipe -- cont'd

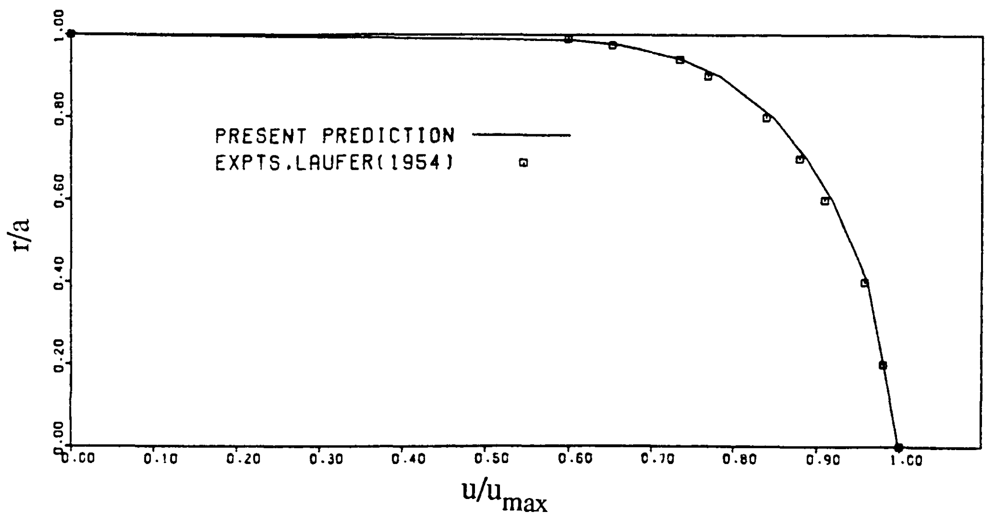

(d) Comparison of velocity

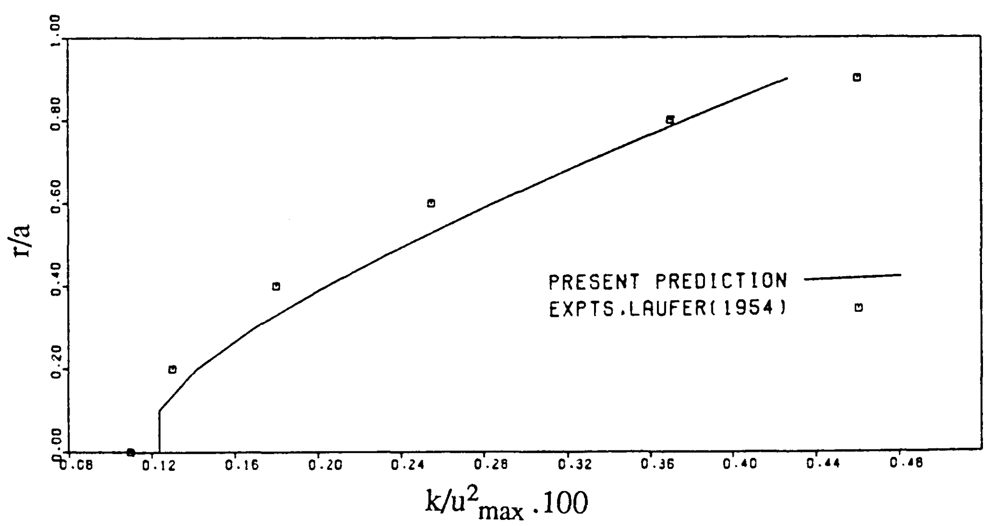

(e) Comparison of turbulence intensity

Fig. 5.10 (cont'd) Fully-developed turbulent flow characteristics for straight circular pipe

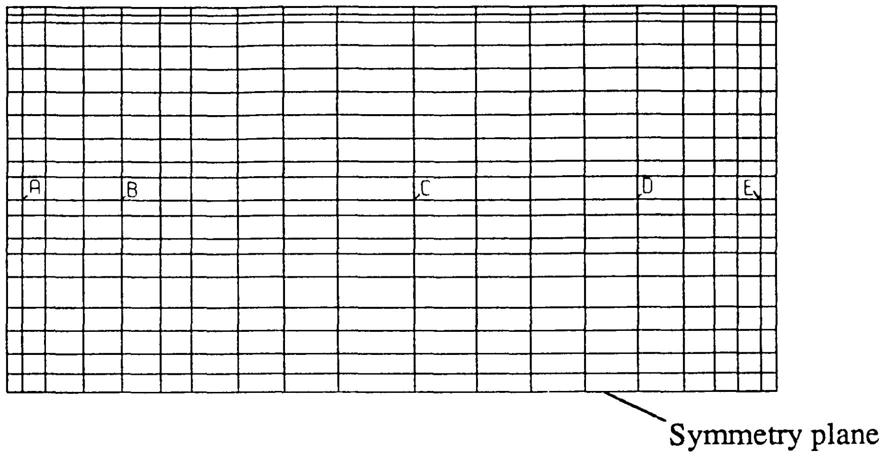

(a) Grid used over half of cross-section

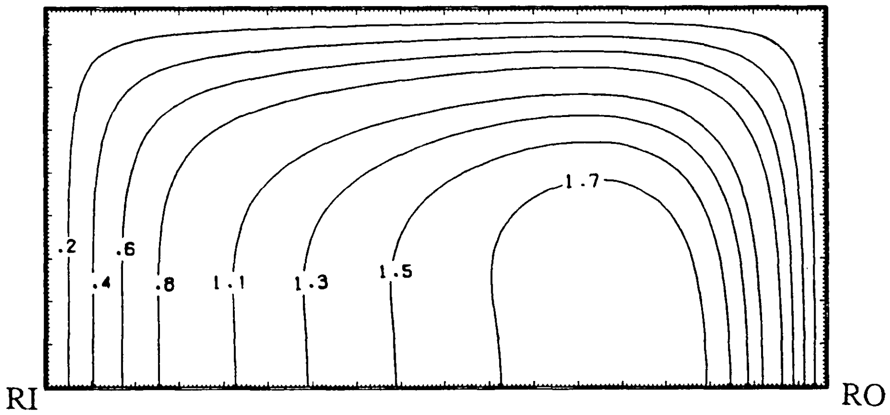

(b) Fully-developed streamwise velocity, u/u_0

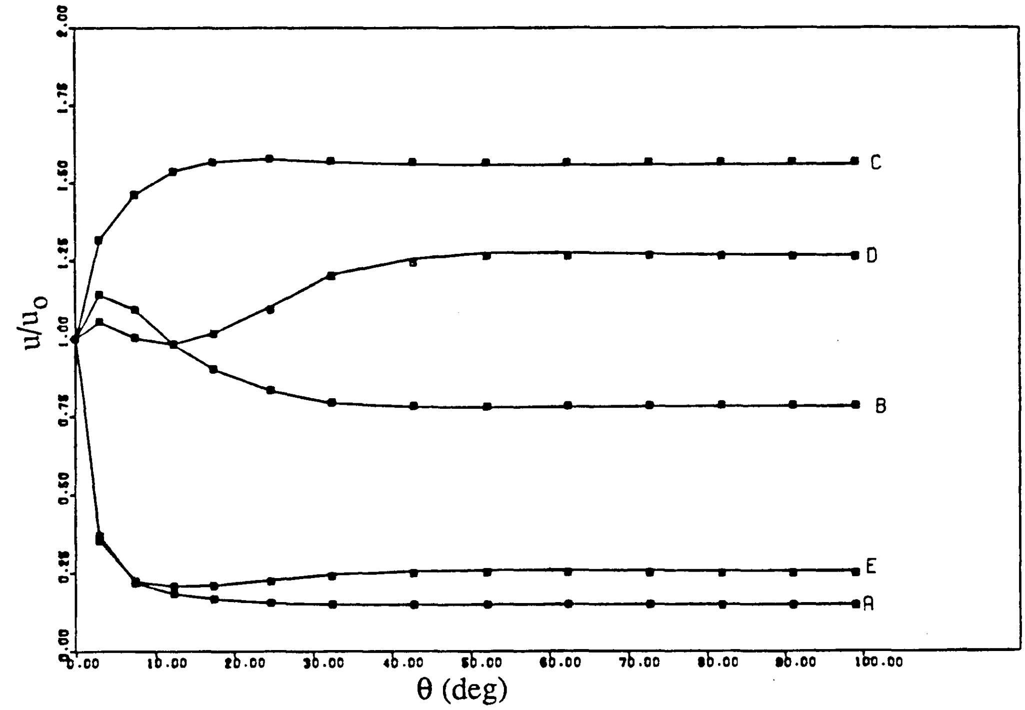

(c) Development of streamwise velocity

____ , using general code ; ▫ , using toroidal code

Fig. 5.11 Flow through a toroidal square duct

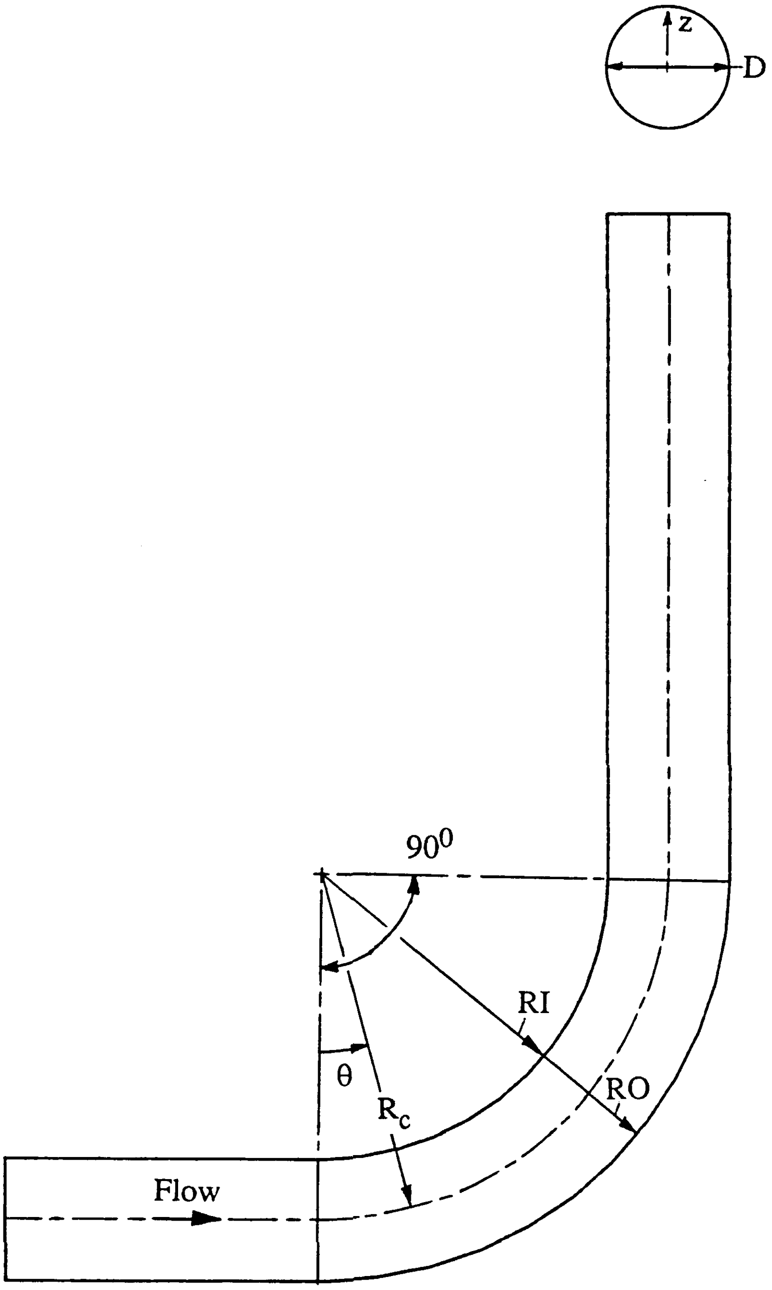

Fig. 5.12 90-deg bend: Flow configuration and definition of coordinates

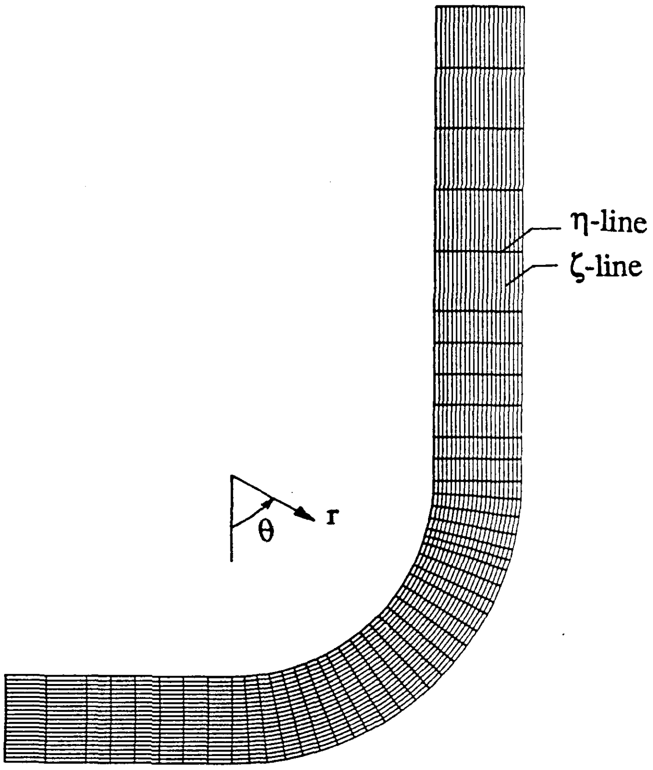

(a) Symmetry plane grids: 21x46 (η x ζ)
(21 grids shown in η-direction for clarity)

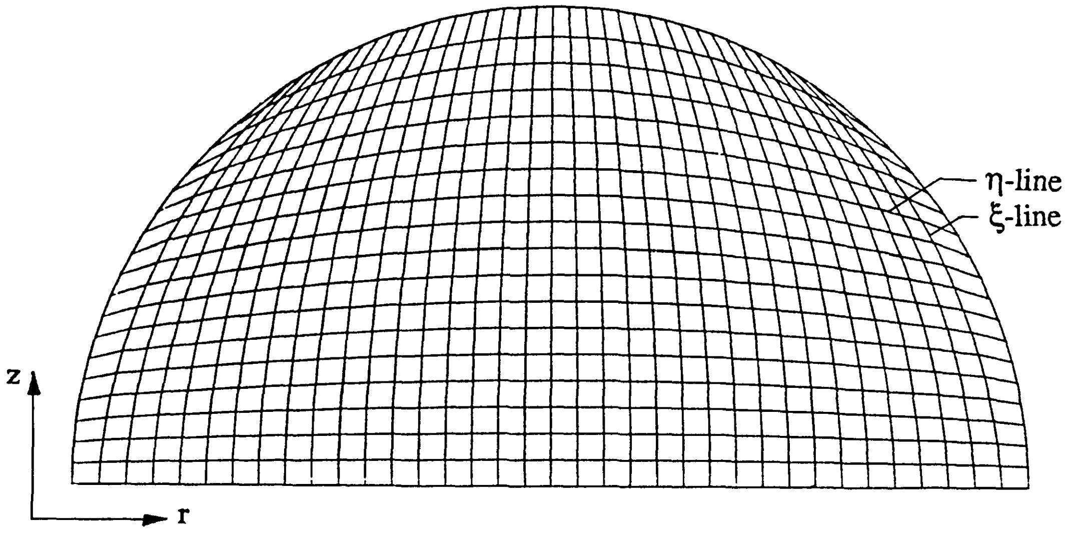

(b) Cross-sectional grids: 37x19 (η x ξ)

Fig. 5.13 90-deg bend: Computational grids

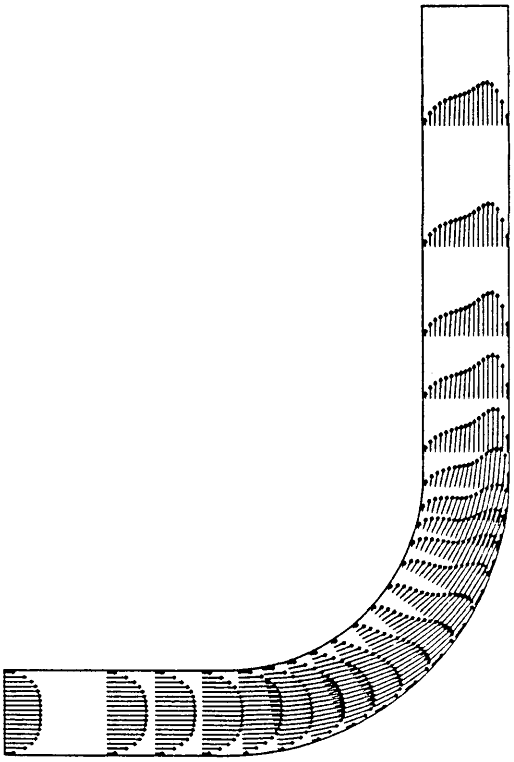

(a) Velocity vectors

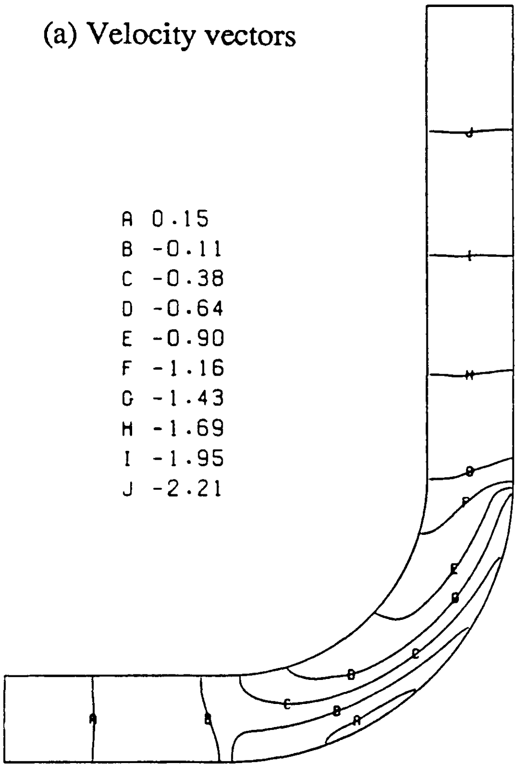

(b) Isobars, Cp

Fig. 5.14 90-deg bend: Flow characteristics in symmetry plane at Re=500

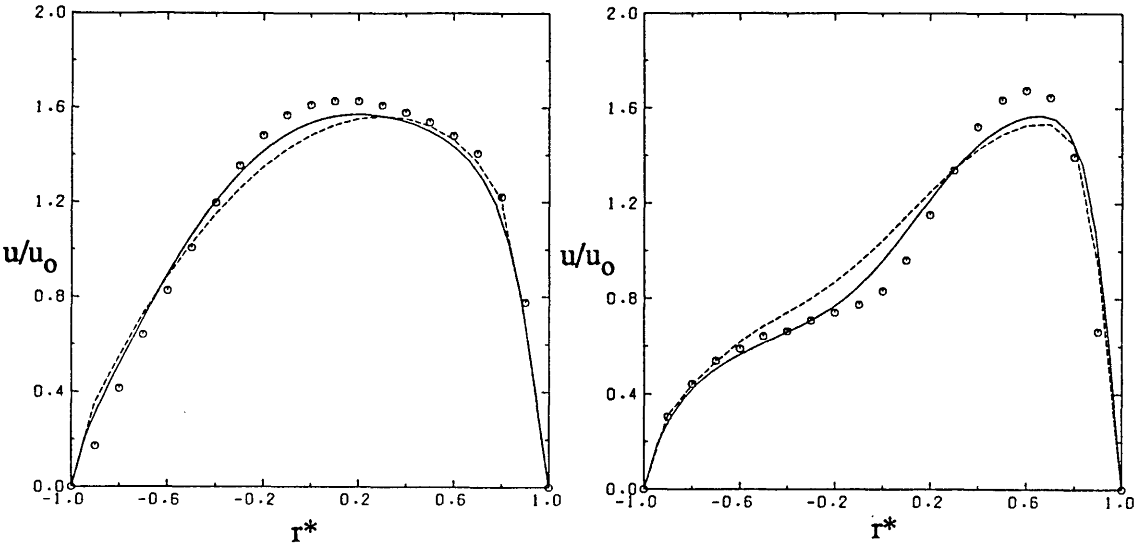

(a) θ=30 deg

(b) θ=60 deg

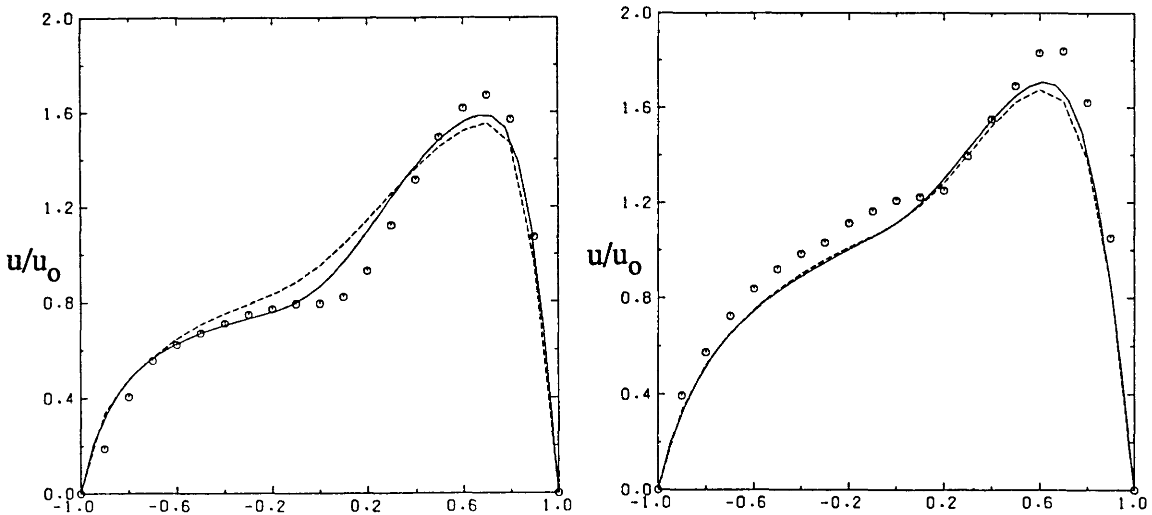

(c) θ=75 deg

(d) 1D downstream

Fig. 5.15 Streamwise velocity profiles in symmetry plane: Grid dependence and comparison with experiment. ∘ , Expts. by Enayet et al (1982); -------, Computations 21x23x11; ——, Computations 37x46x19 grids

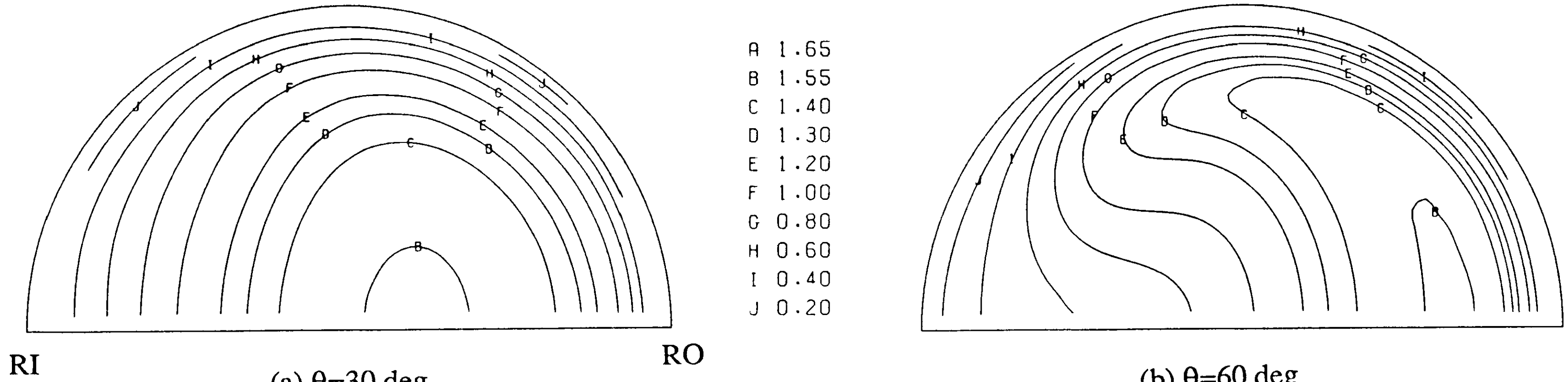

(a) θ=30 deg

(b) θ=60 deg

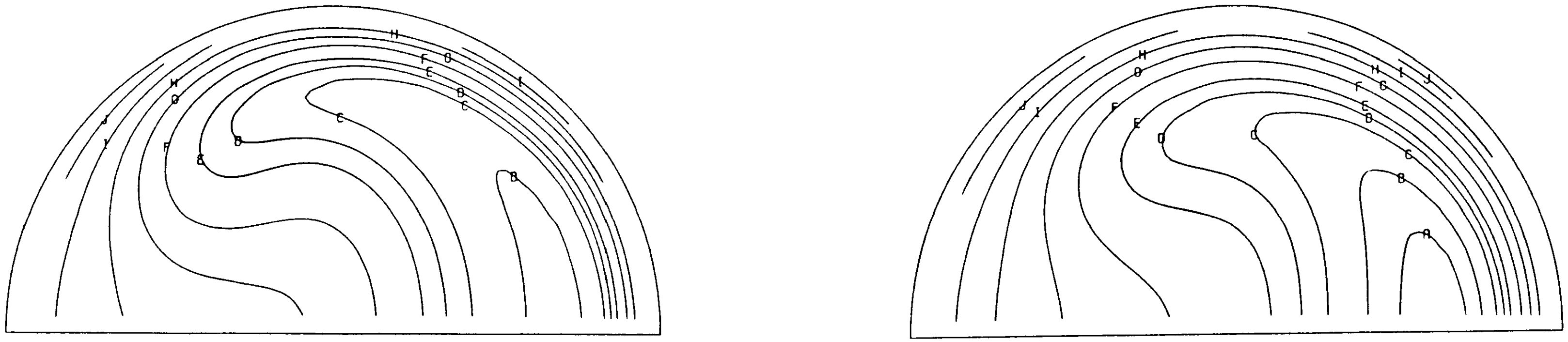

(c) θ=75 deg

(d) 1D downstream

Fig. 5.16 Contours of u/u_0 at different streamwise sections for Re=500

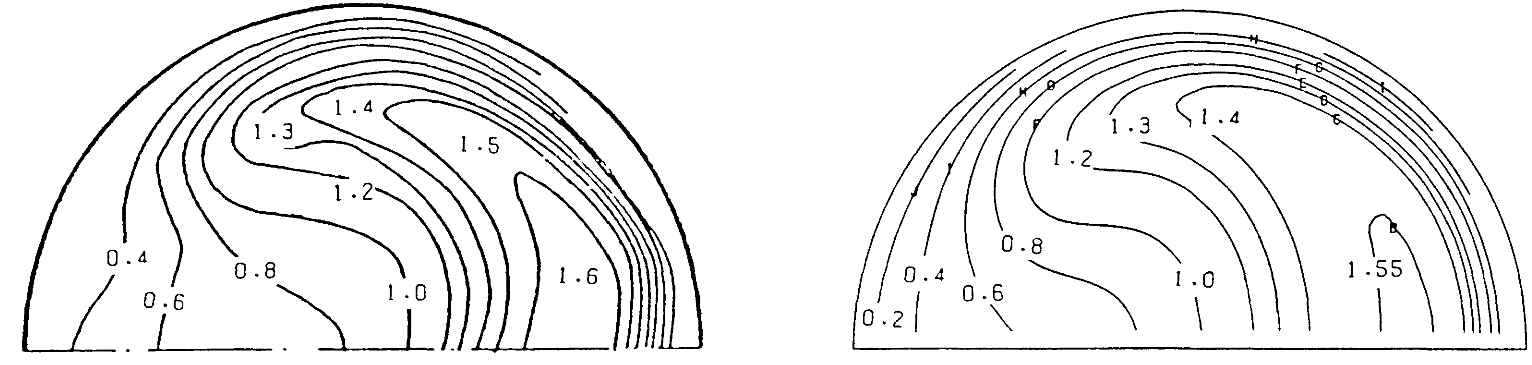

Expt. Enayet (1982)

Present Prediction

(a) θ=60 deg

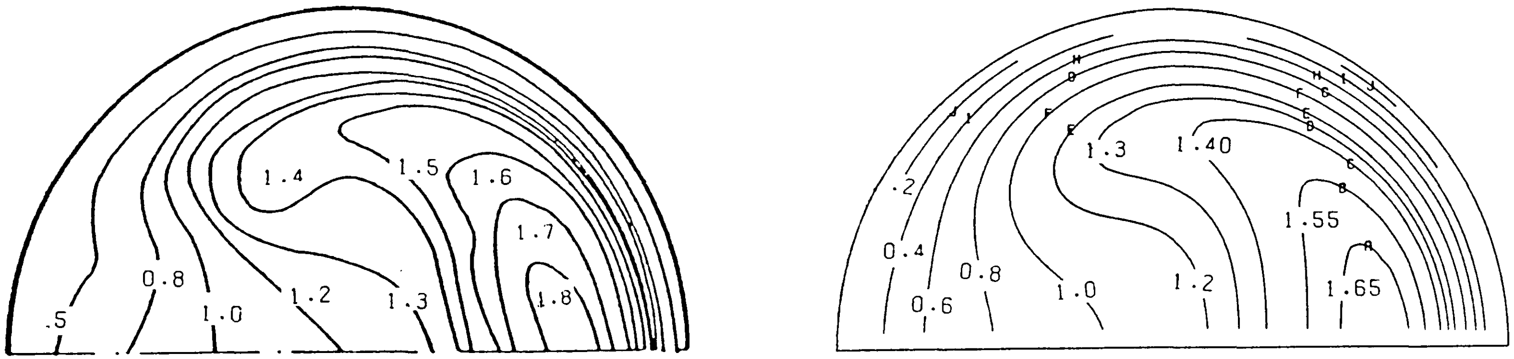

Expt. Enayet (1982)

Present Prediction

(b) 1D downstream

Fig. 5.17 Comparison of u/u_0 contour for Re=500

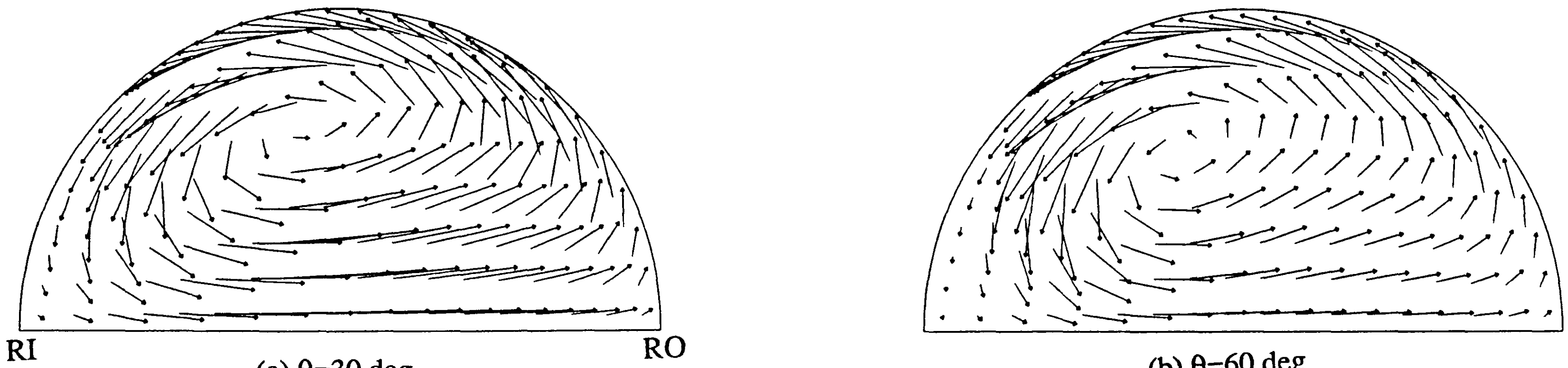

(a) θ=30 deg

(b) θ=60 deg

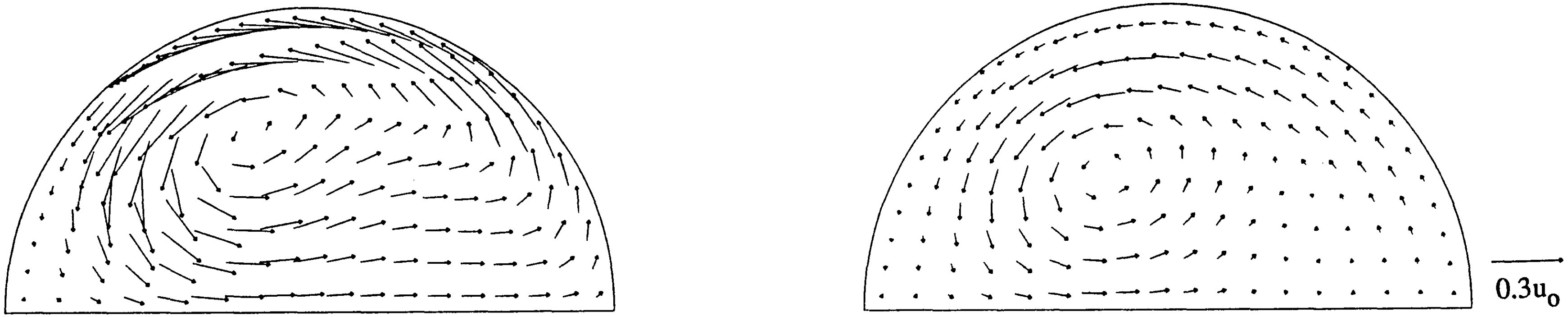

(c) θ=75 deg

(d) 1D downstream

Fig. 5.18 Secondary velocity vectors at different streamwise sections for Re=500

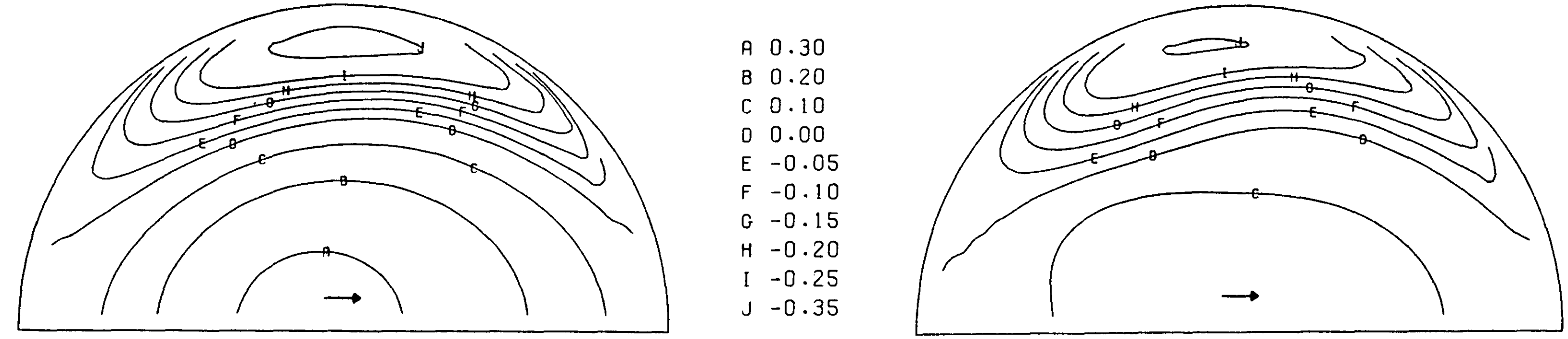

(a) θ=30 deg

(b) θ=60 deg

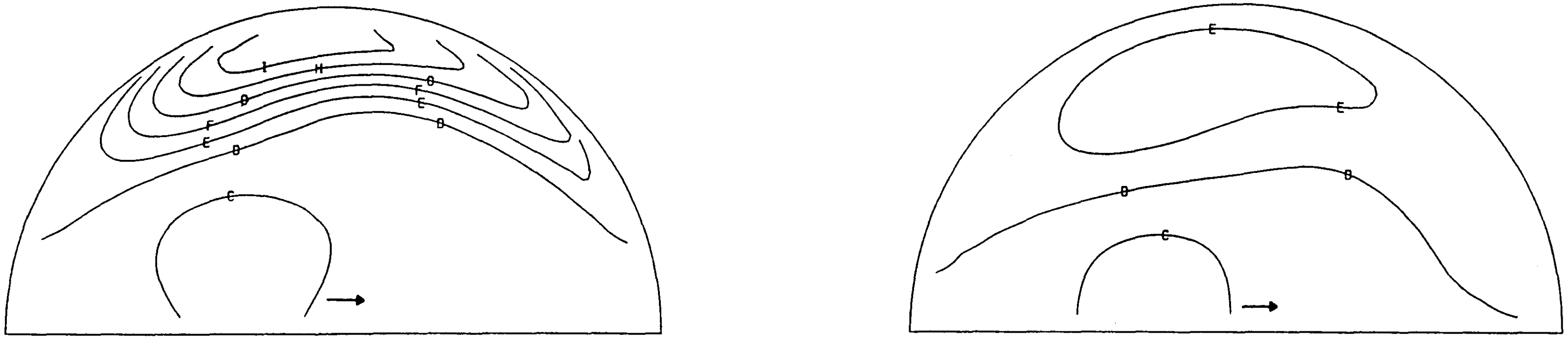

(c) θ=75 deg

(d) 1D downstream

Fig. 5.19 Contours of v/u_0 at different streamwise sections for Re=500; arrows show the positive direction of v-velocity

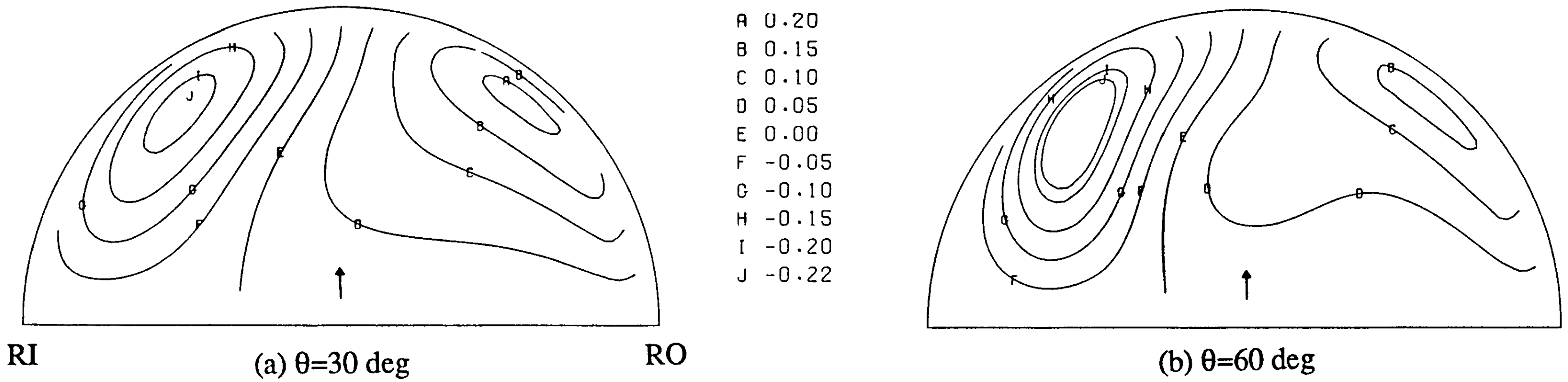

(a) θ=30 deg

(b) θ=60 deg

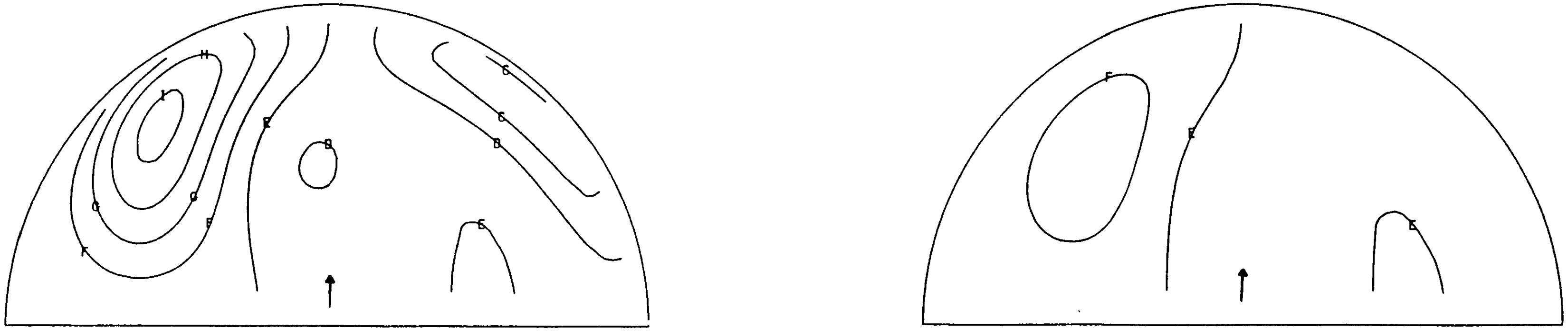

(c) θ=75 deg

(d) 1D downstream

Fig. 5.20 Contours of w/u_0 at different streamwise sections for Re=500; arrows show the positive direction of w-velocity

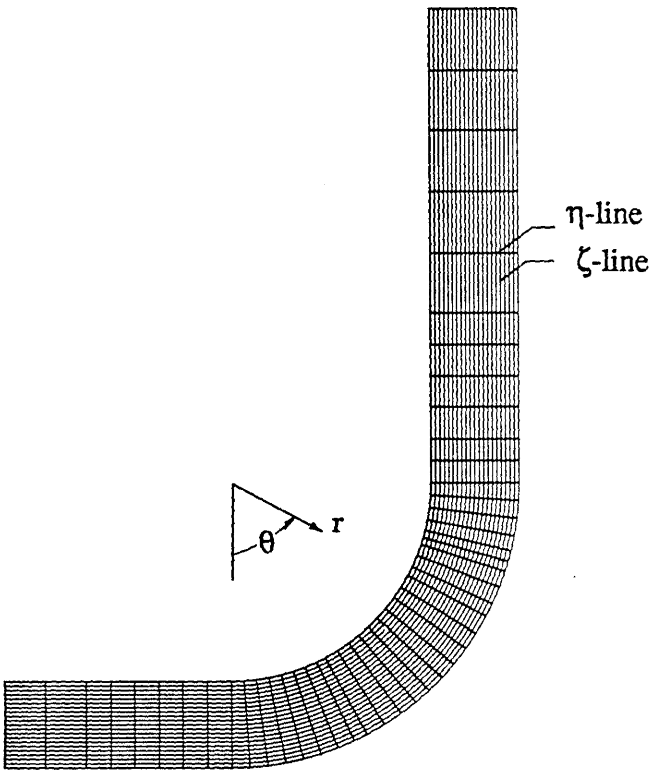

(a) Symmetry plane grids: 21x46 (η x ζ)
(21 grids shown in η-direction for clarity)

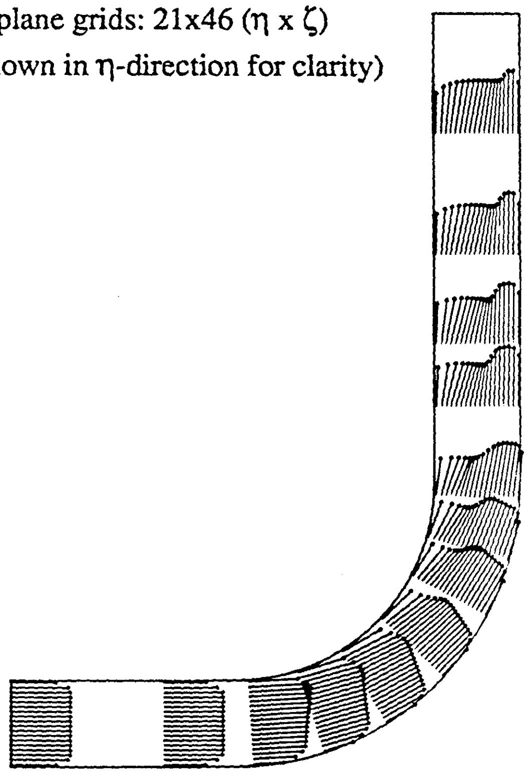

(b) Velocity vectors

Fig. 5.21 90-deg bend: Computational grid and velocity vectors in the symmetry plane for Re=43,000

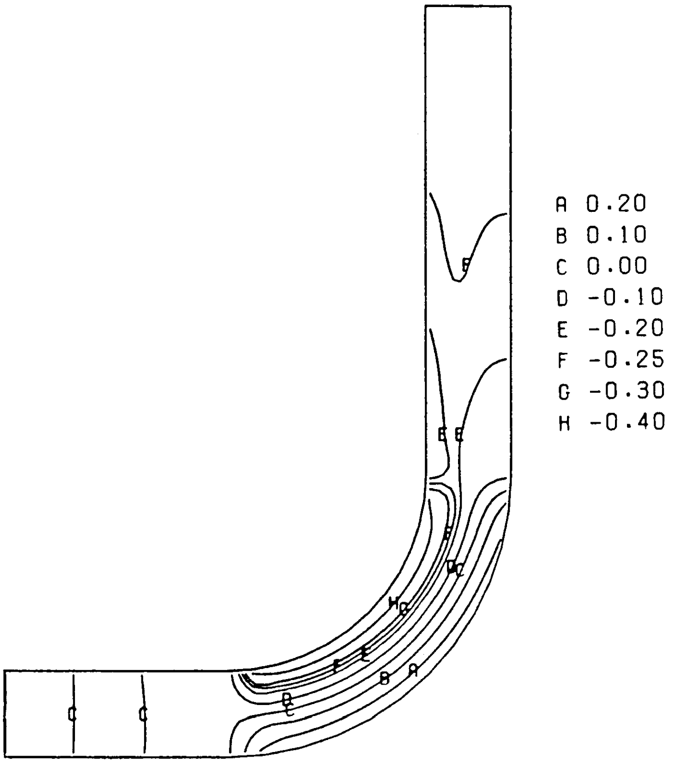

(a) Isobars, Cp on symmetry plane

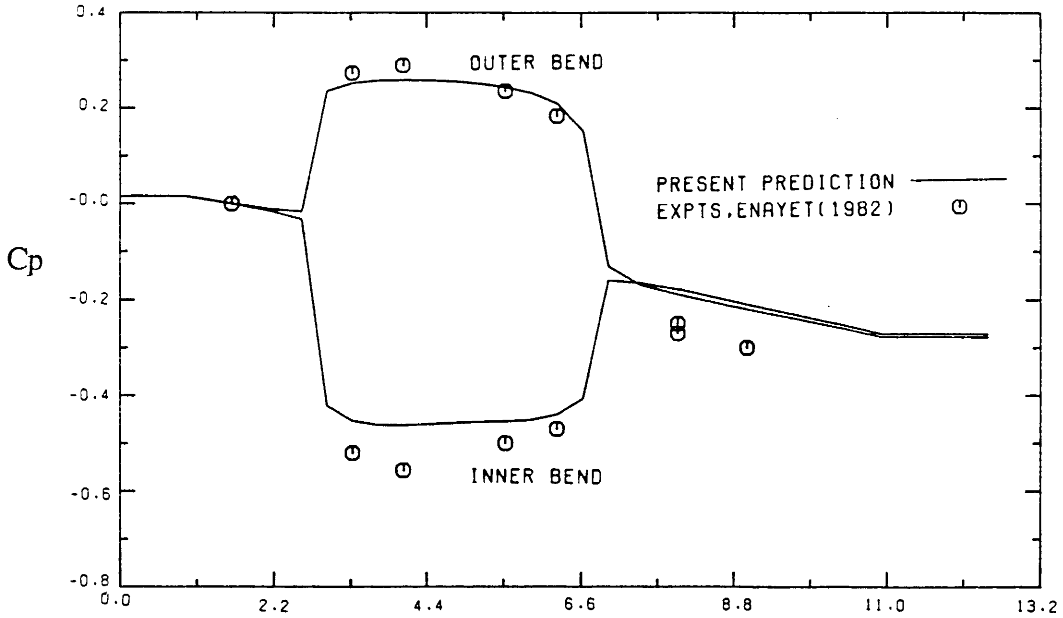

Normalized (by D) length along the duct

(b) Comparison with experiment

Fig. 5.22 90-deg bend: Static pressure distributions for Re=43,000

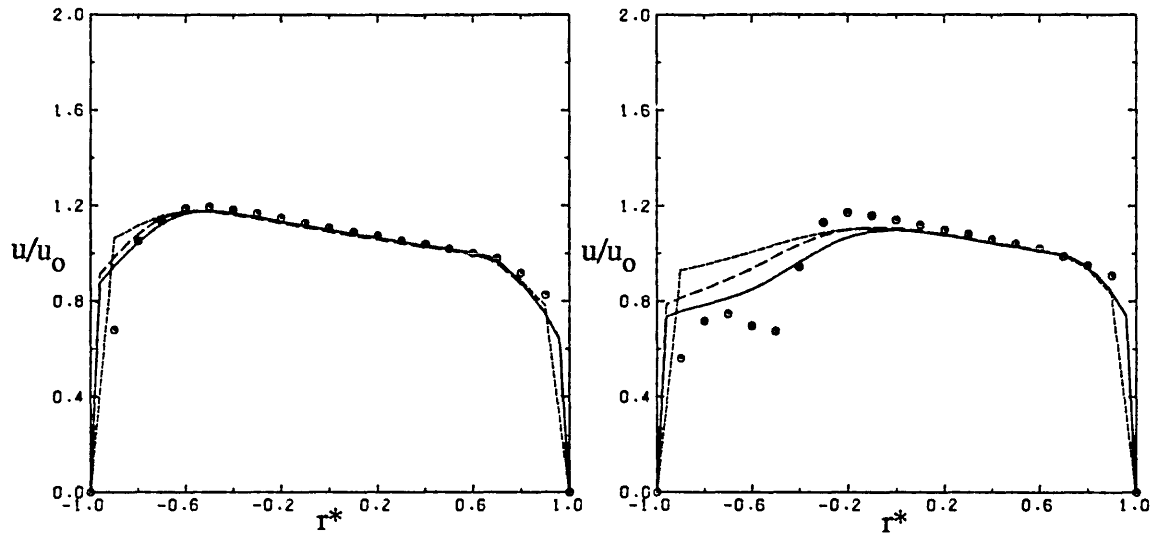

(a) θ=30 deg

(b) θ=60 deg

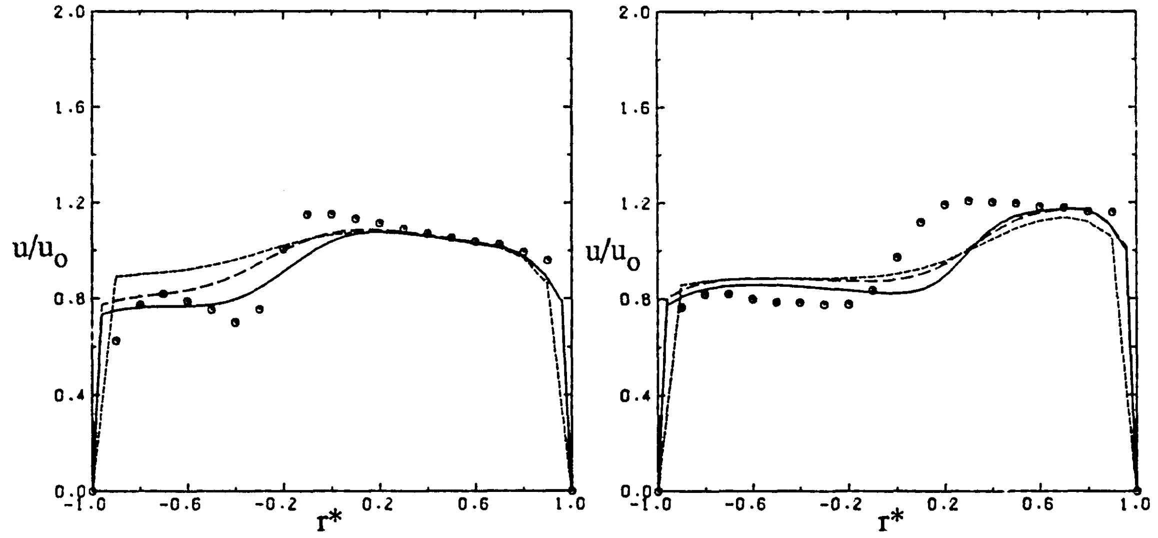

(c) θ=75 deg

(d) 1D downstream

Fig. 5.23 Streamwise velocity profiles in the symmetry plane: Grid dependence and comparison with experiment. ∘ , Expts. by Enayet et al (1982); ------- , 21x23x11; --- , 37x23x19; —— , 37x46x19 grids.

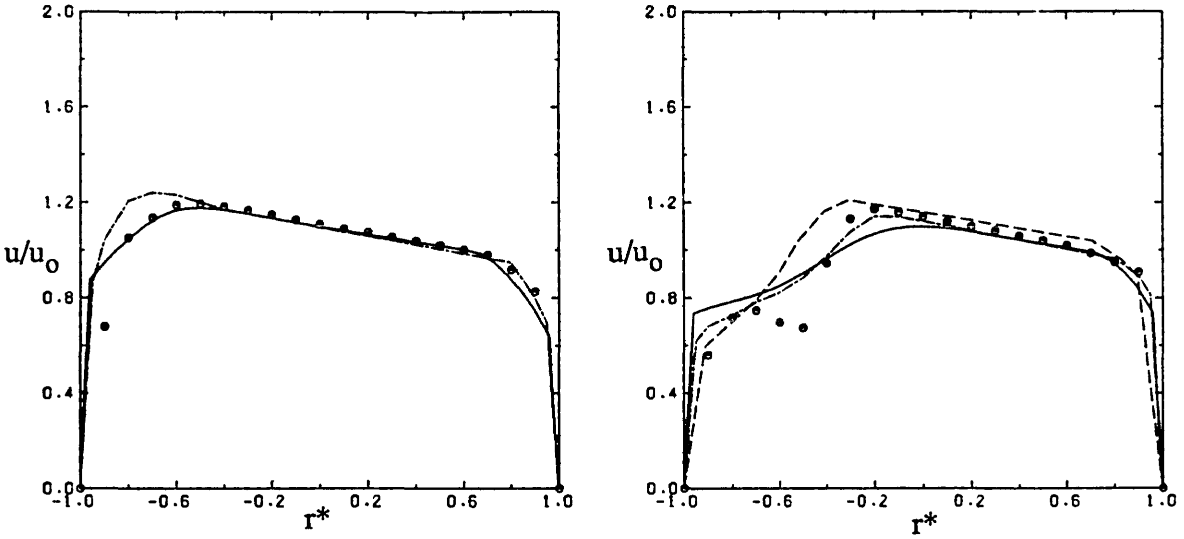

(a) θ=30 deg

(b) θ=60 deg

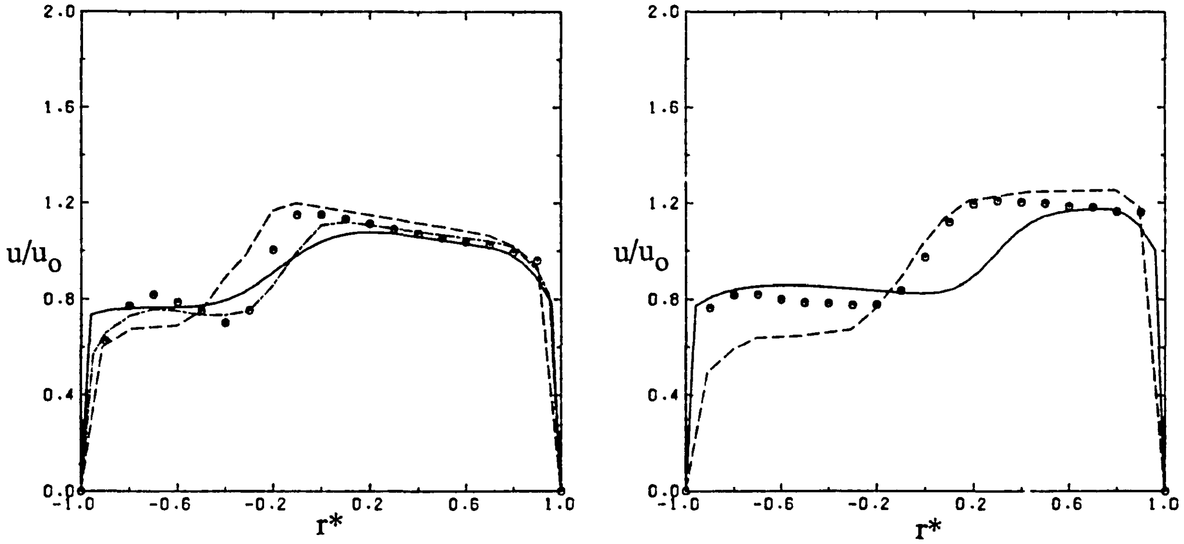

(c) θ=75 deg

(d) 1D downstream

Fig. 5.24 Streamwise velocity profiles in the symmetry plane: Comparison with other predictions and experiment. ∘ , Expts. by Enayet et al (1982);
—— , Present prediction (37x46x19); —·—·—, Anderson (1988);
- - - -, Iacovides and Launder (1984).

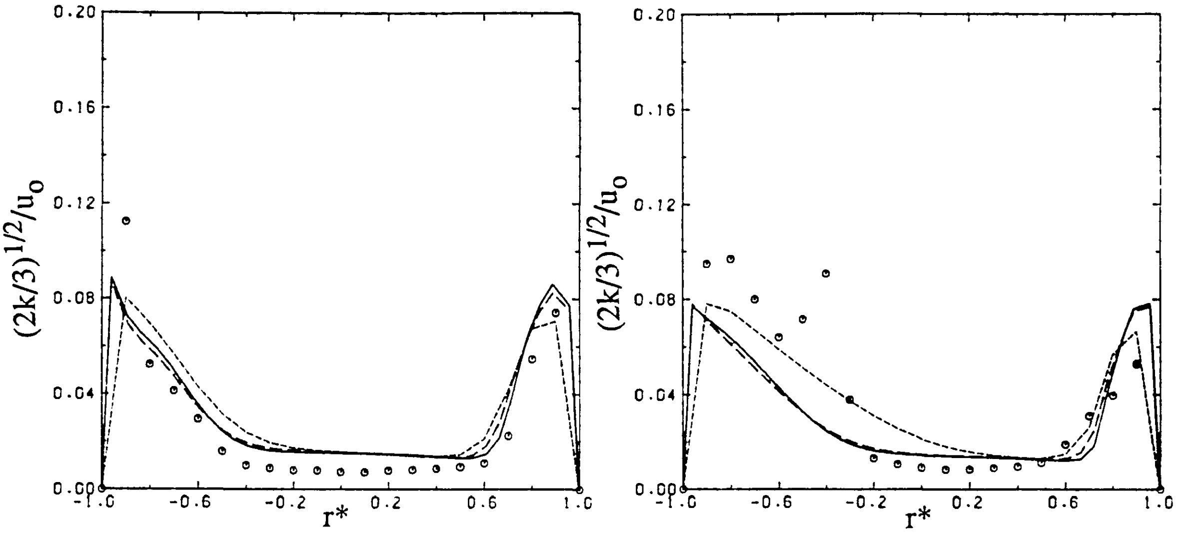

(a) θ=30 deg

(b) θ=60 deg

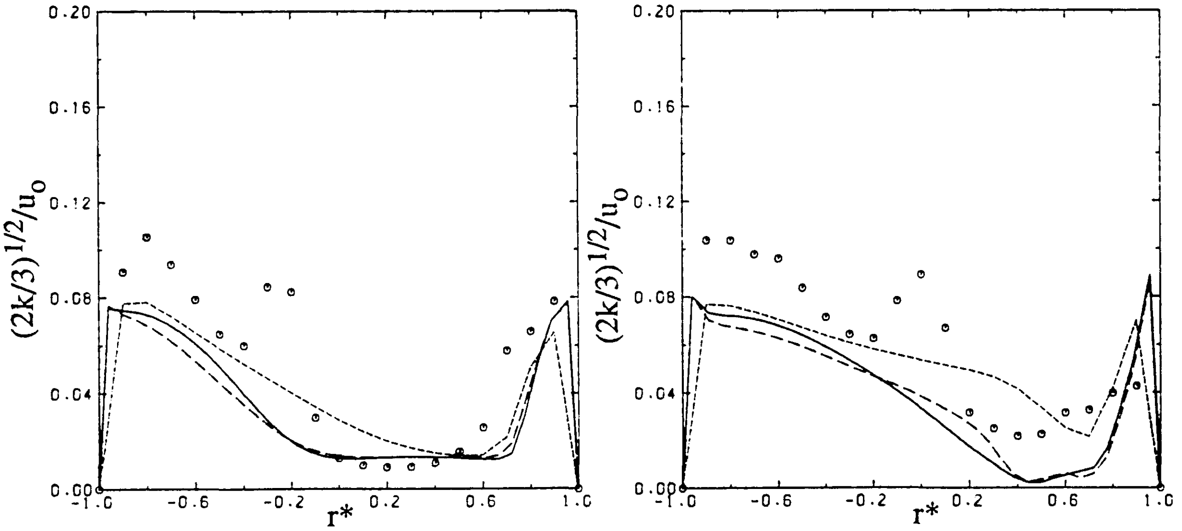

(c) θ=75 deg

(d) 1D downstream

Fig. 5.25 Profiles of turbulence intensity in the symmetry plane: Grid dependence and comparison with experiment. ⊙ , Expts. by Enayet et al (1982); ------- , 21x23x11; ----, 37x23x19; —— , 37x46x19 grids.

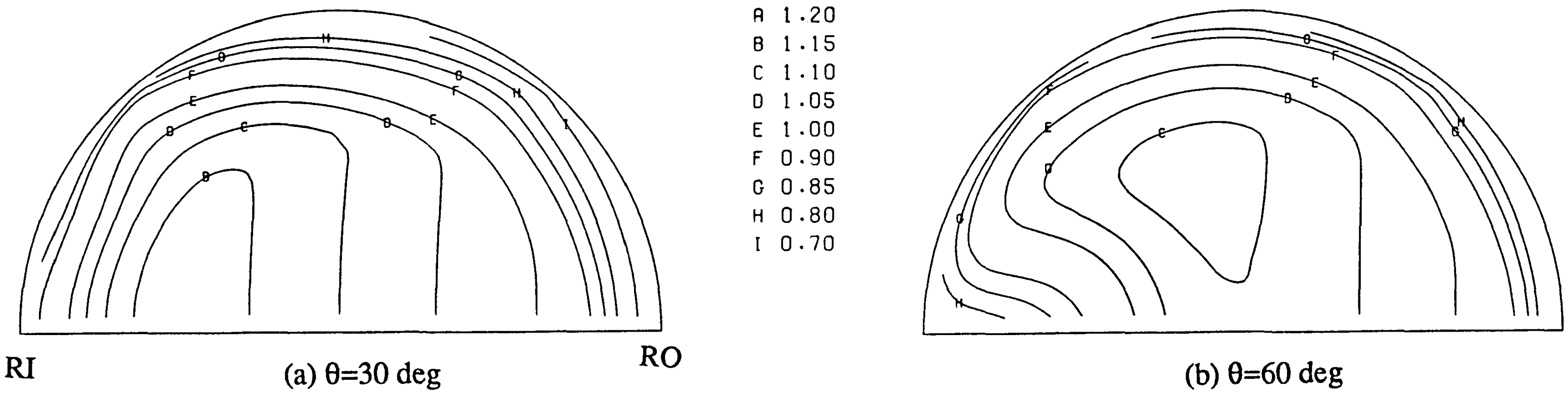

(a) θ=30 deg

(b) θ=60 deg

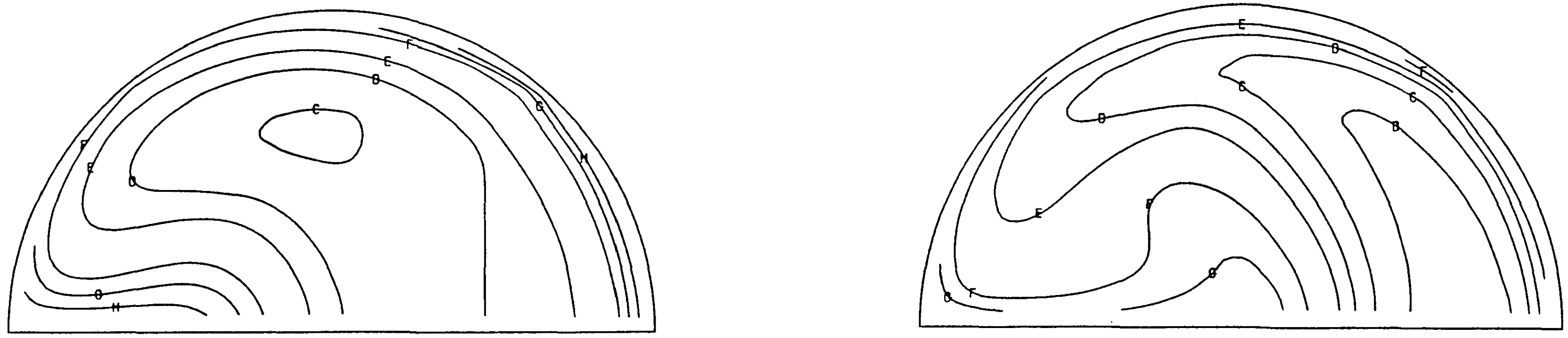

(c) θ=75 deg

(d) 1D downstream

Fig. 5.26 Contours of u/u_0 at different streamwise sections at Re=43,000

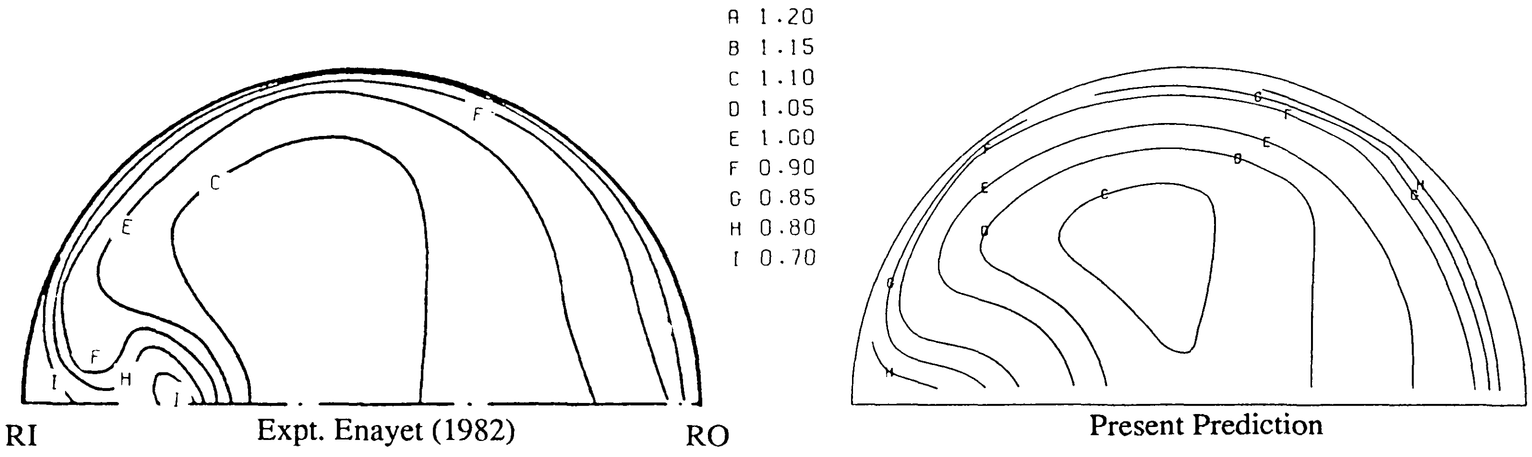

(a) θ=60 deg

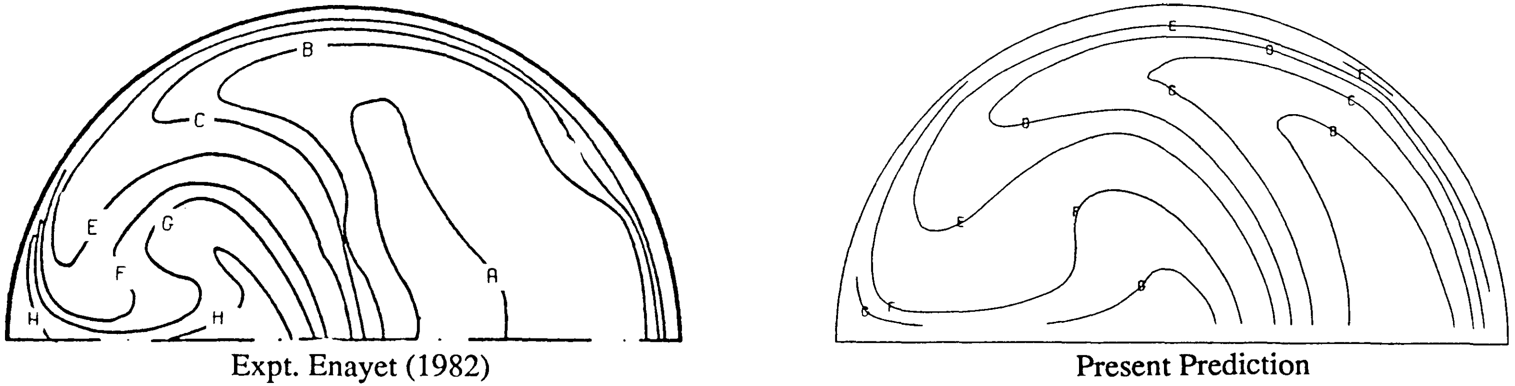

(b) 1D downstream

Fig. 5.27 Comparison of u/u_0 contours at Re=43,000

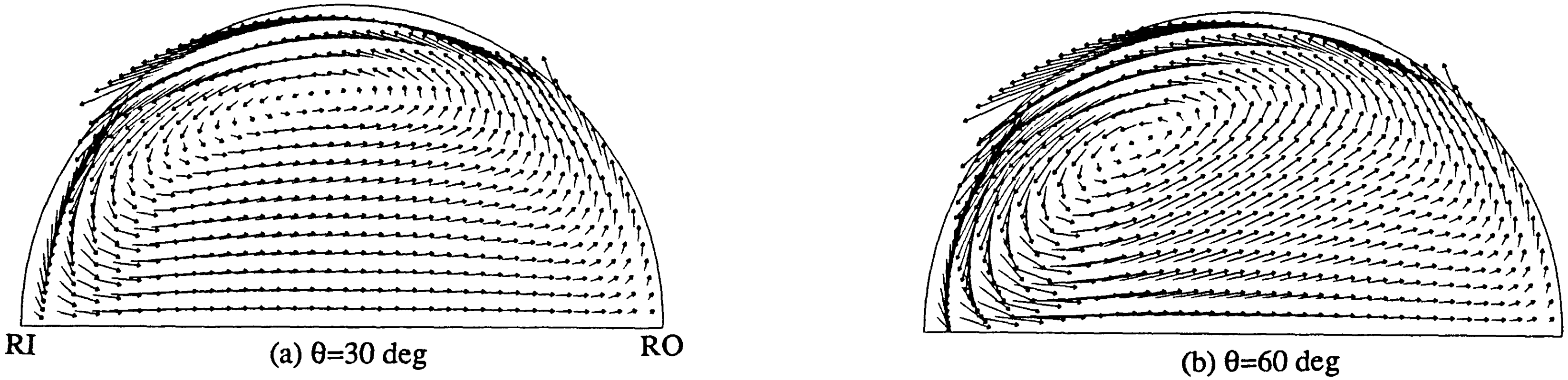

(a) θ=30 deg

(b) θ=60 deg

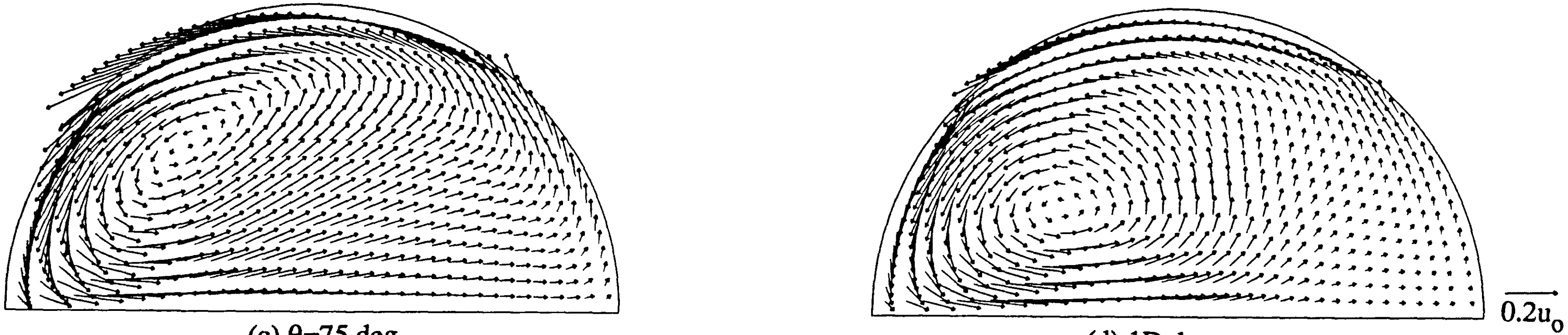

(c) θ=75 deg

(d) 1D downstream

Fig. 5.28 Secondary velocity vectors at different streamwise sections at Re=43,000

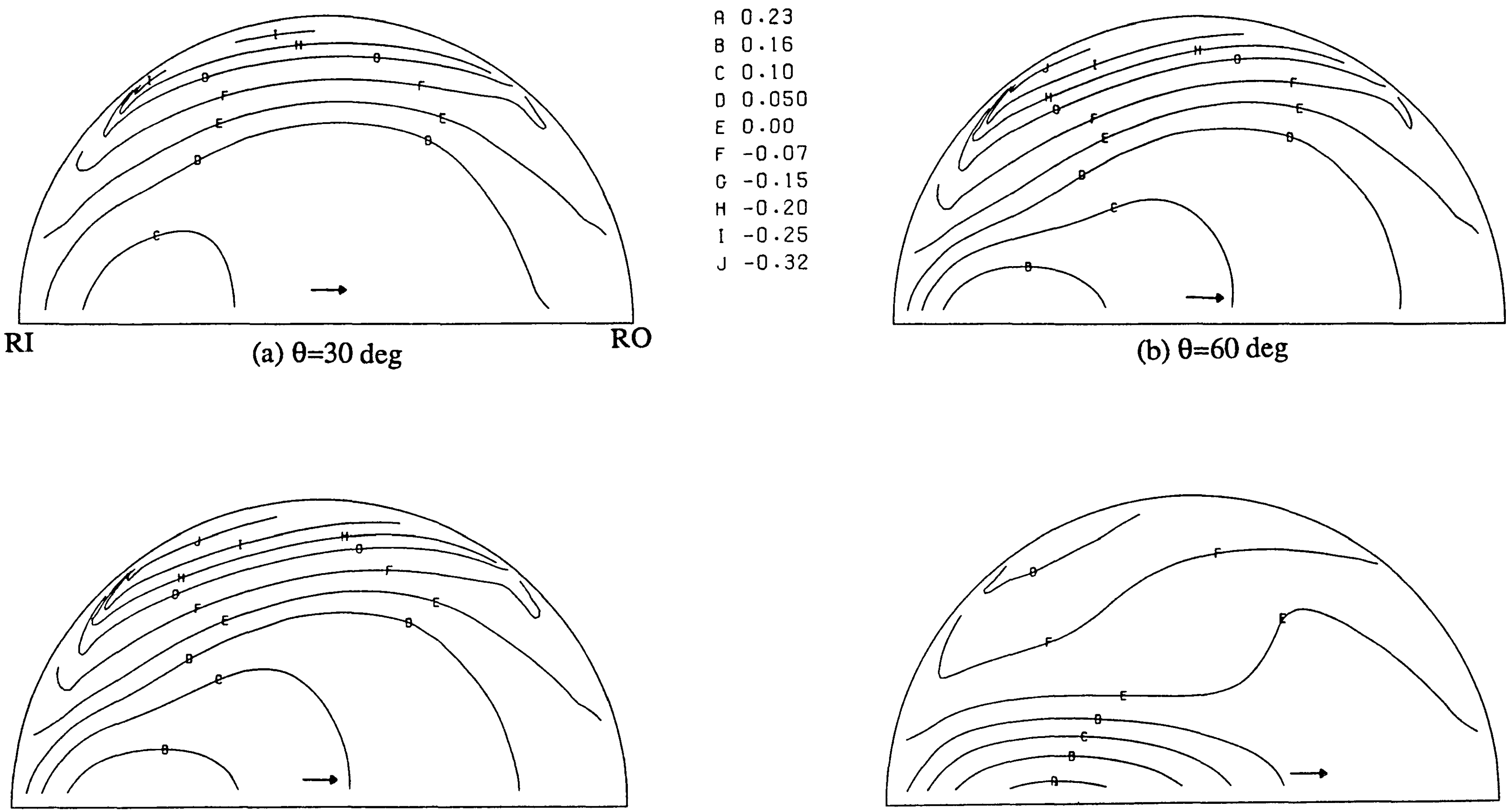

(a) θ=30 deg

(b) θ=60 deg

(c) θ=75 deg

(d) 1D downstream

Fig. 5.29 Contours of v/u_0 at different streamwise sections at Re=43,000; arrows show the positive direction of v-velocity

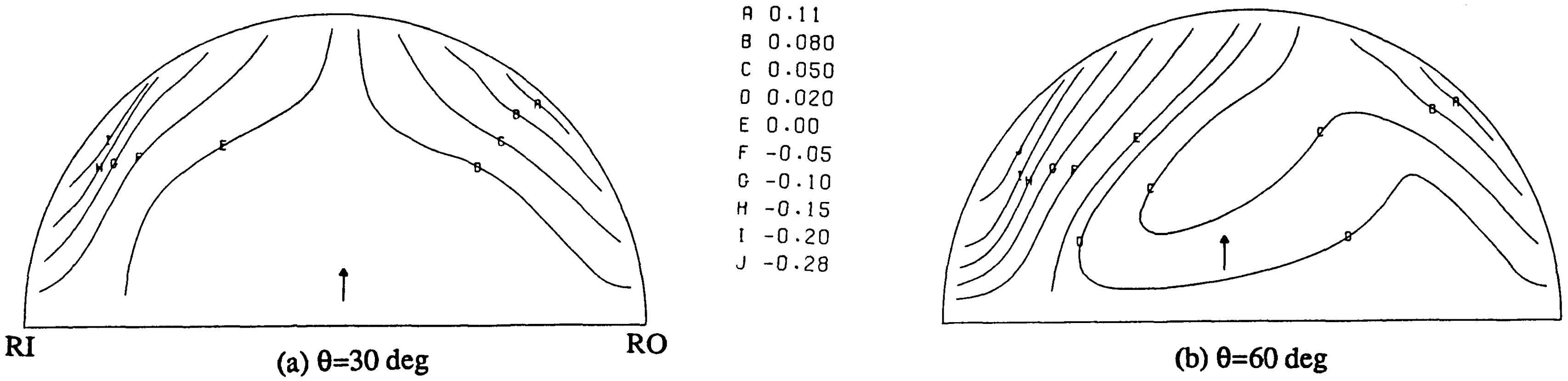

(a) θ=30 deg

(b) θ=60 deg

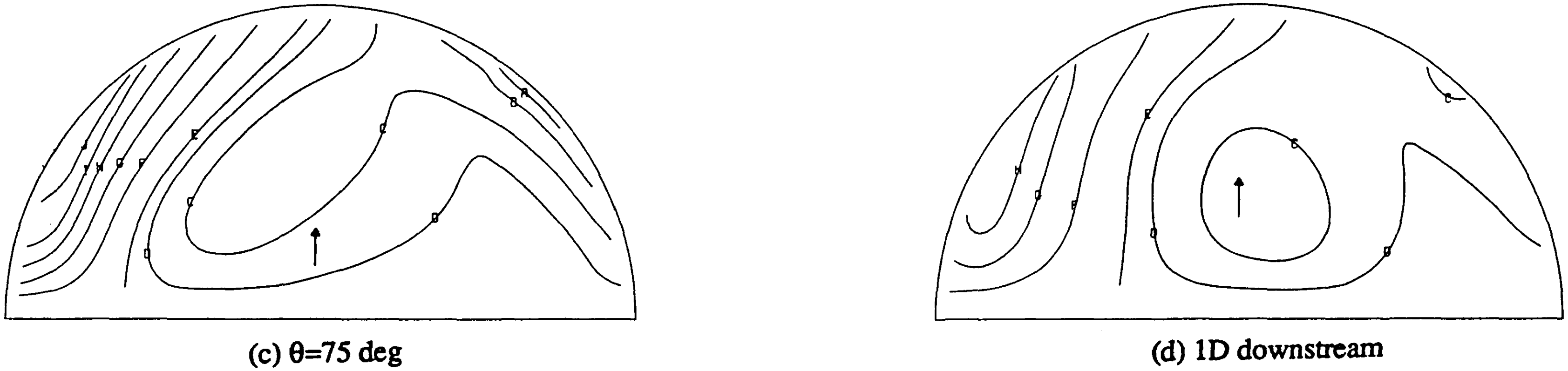

(c) θ=75 deg

(d) 1D downstream

Fig. 5.30 Contours of w/u_0 at different streamwise sections at Re=43,000; arrows show the positive direction of w-velocity

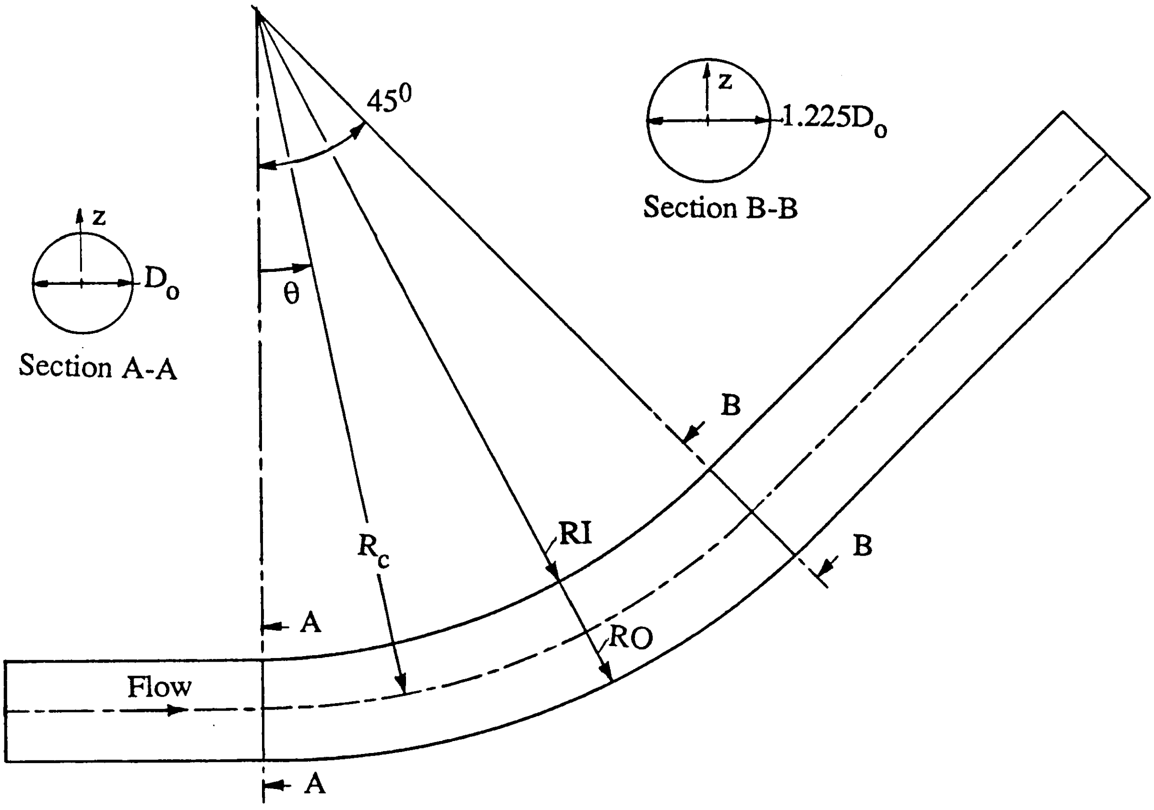

Fig. 5.31 45-deg C-diffuser: Flow configuration and definition of coordinates

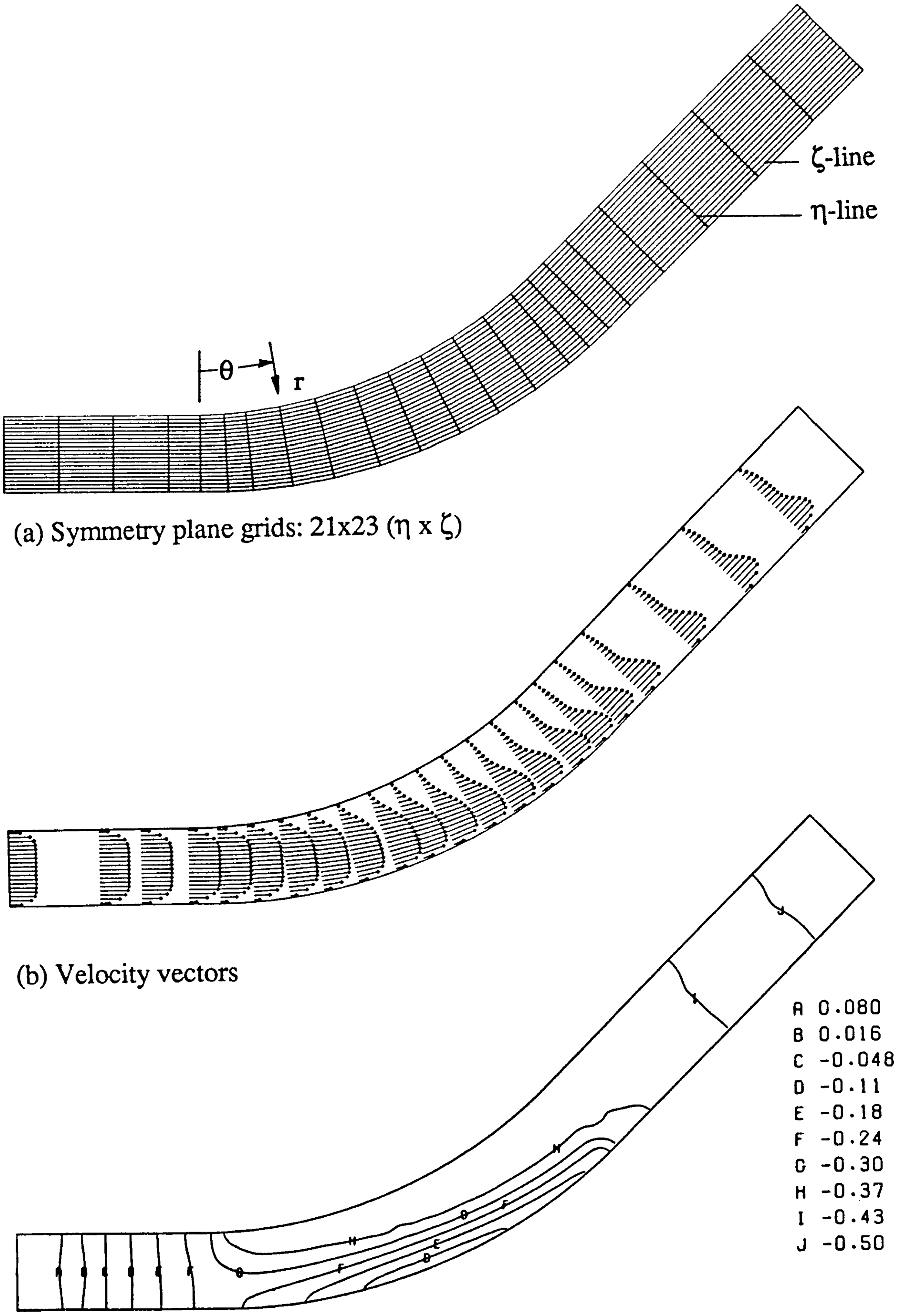

(a) Symmetry plane grids: 21x23 (η x ζ)

(b) Velocity vectors

(c) Isobars, Cp

Fig. 5.32 C-diffuser: Grids and flow characteristics in the symmetry plane at Re=790

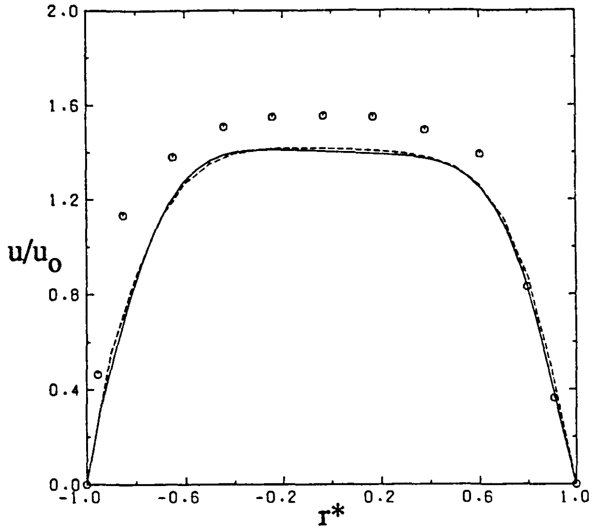

(a) θ=4 deg

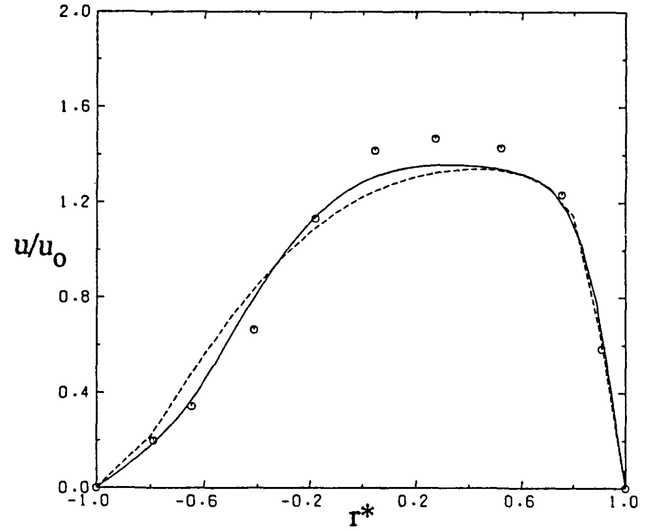

(b) θ=20.5 deg

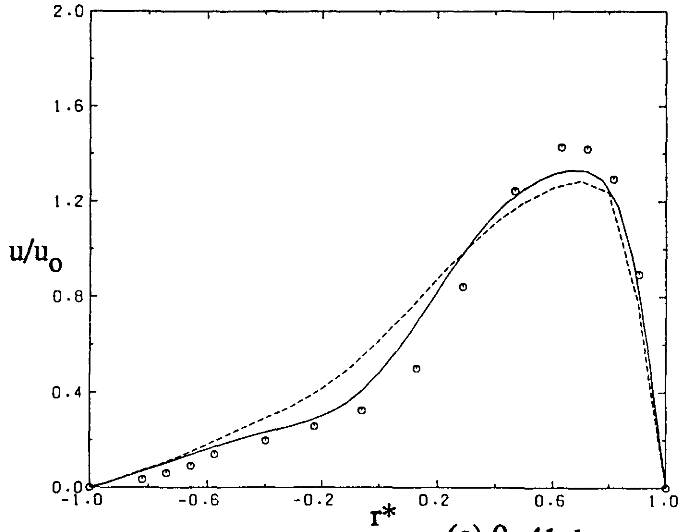

(c) θ=41 deg

Fig. 5.33 Streamwise velocity profiles in the symmetry plane: Grid dependence and comparison with experiment. ∘ , Expts. by Rojas (1986); Present predictions: -------- , 21x23x11; ——— , 37x46x19 grids.

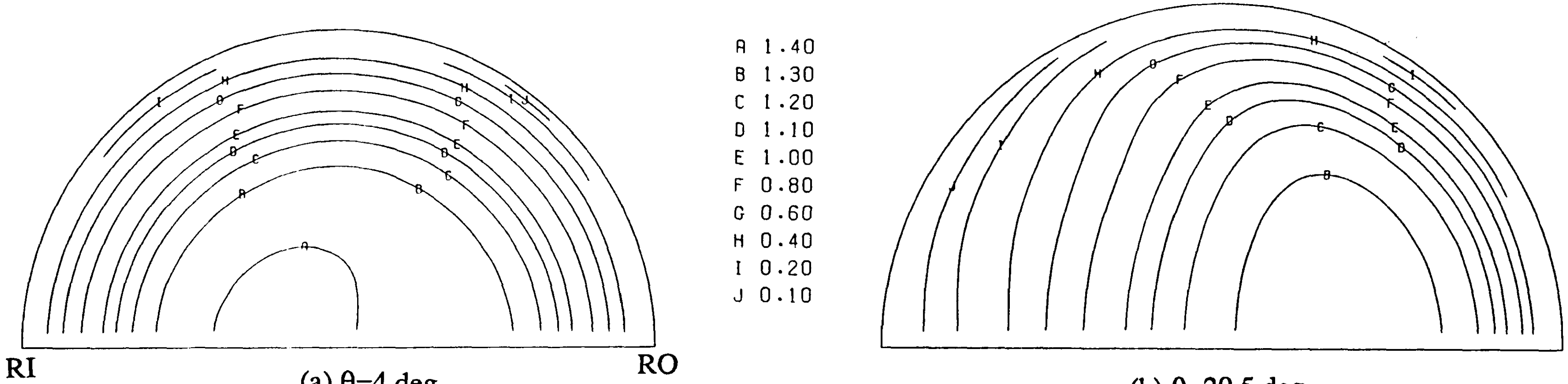

(a) θ=4 deg

(b) θ=20.5 deg

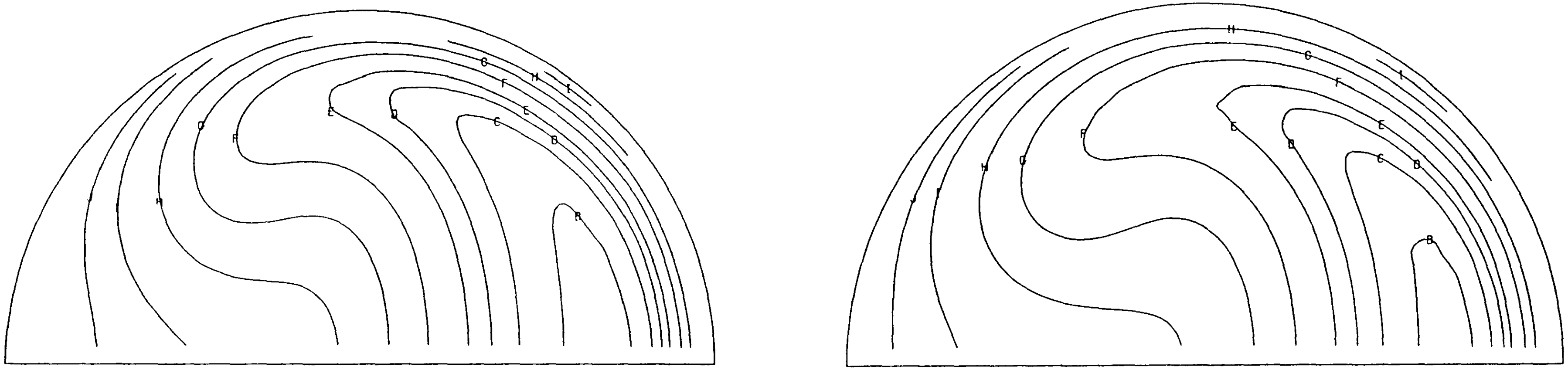

(c) θ=41 deg

(d) $1D_o$ downstream

Fig. 5.34 Contours of u/u_o at different streamwise sections at Re=790

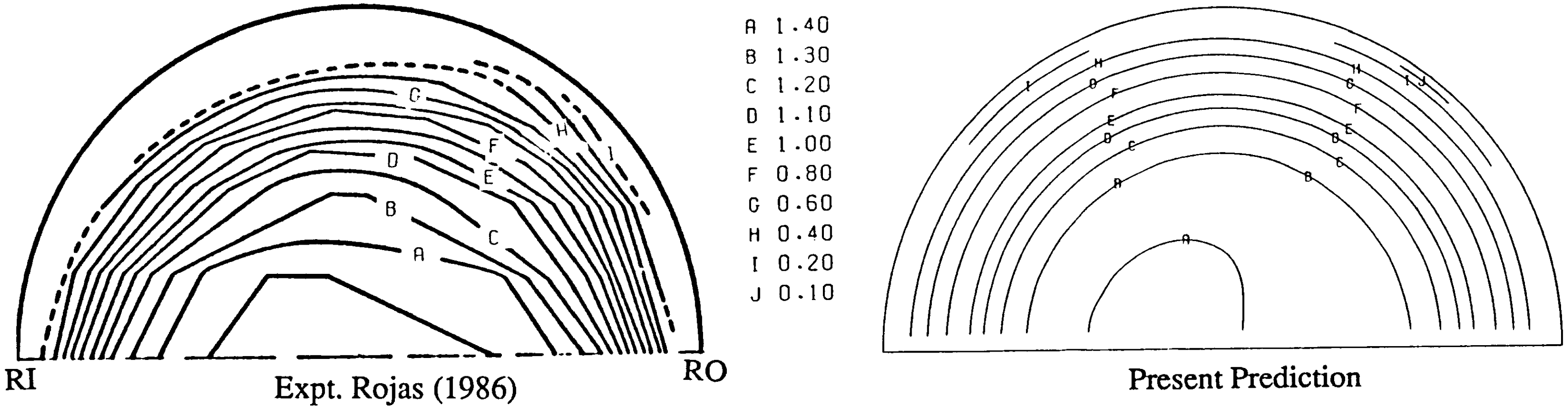

(a) θ=4 deg

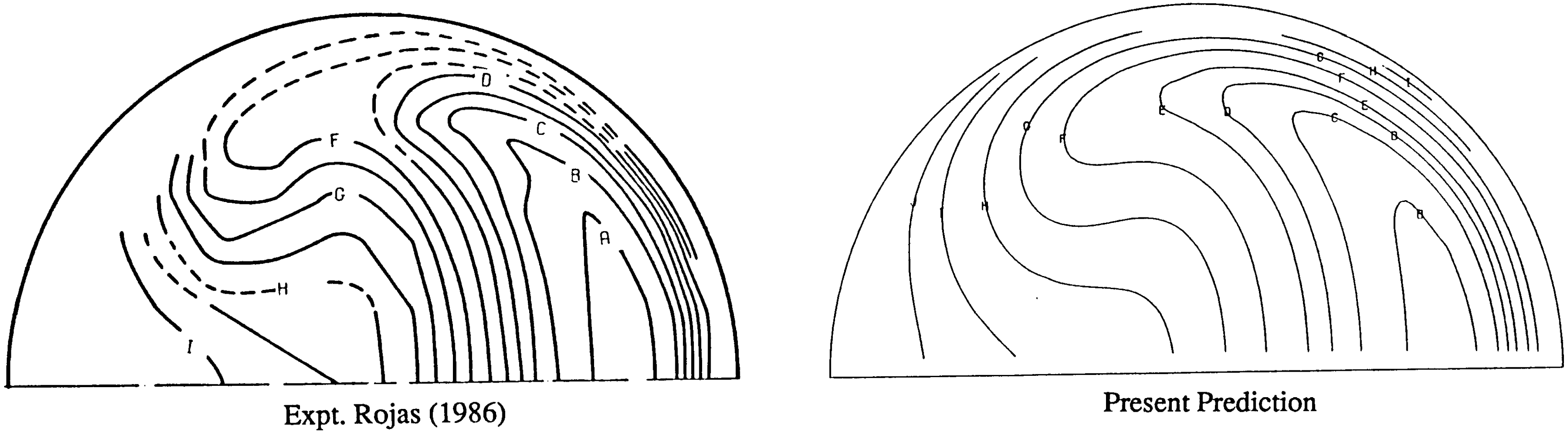

(b) θ=41 deg

Fig. 5.35 Comparison of u/u_0 contours at Re=790

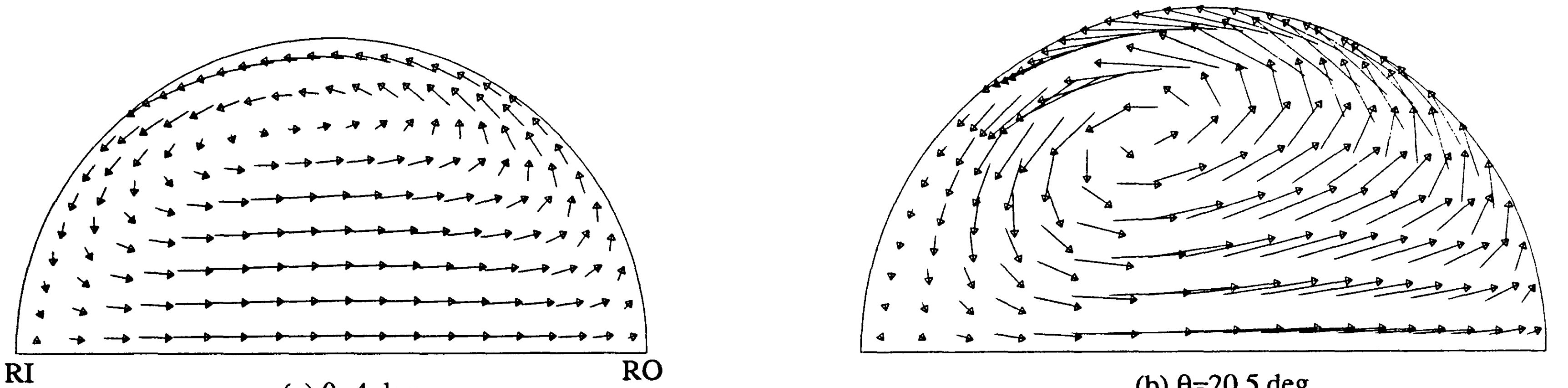

(a) θ=4 deg

(b) θ=20.5 deg

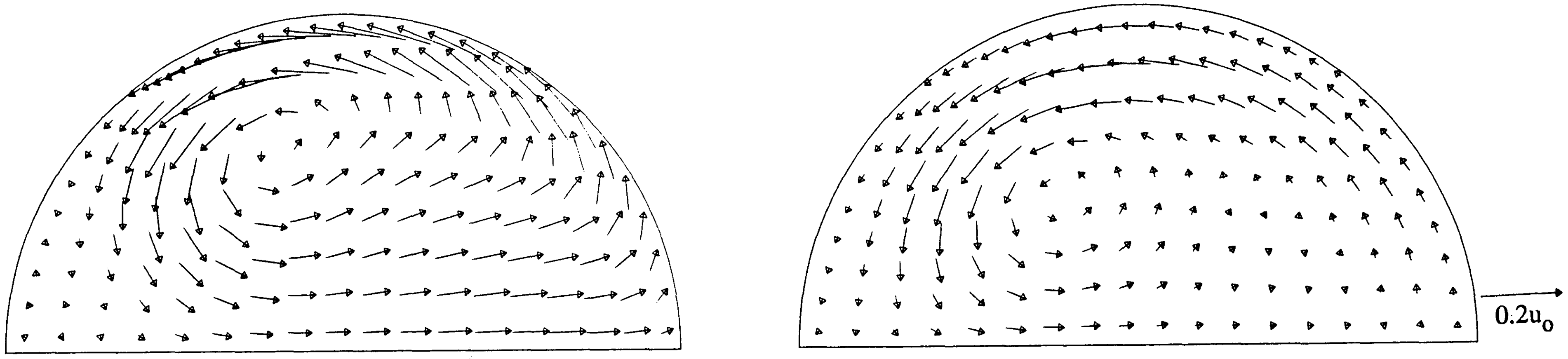

(c) θ=41 deg

(d) 1D$_o$ downstream

Fig. 5.36 Secondary velocity vectors at different streamwise sections for Re=790

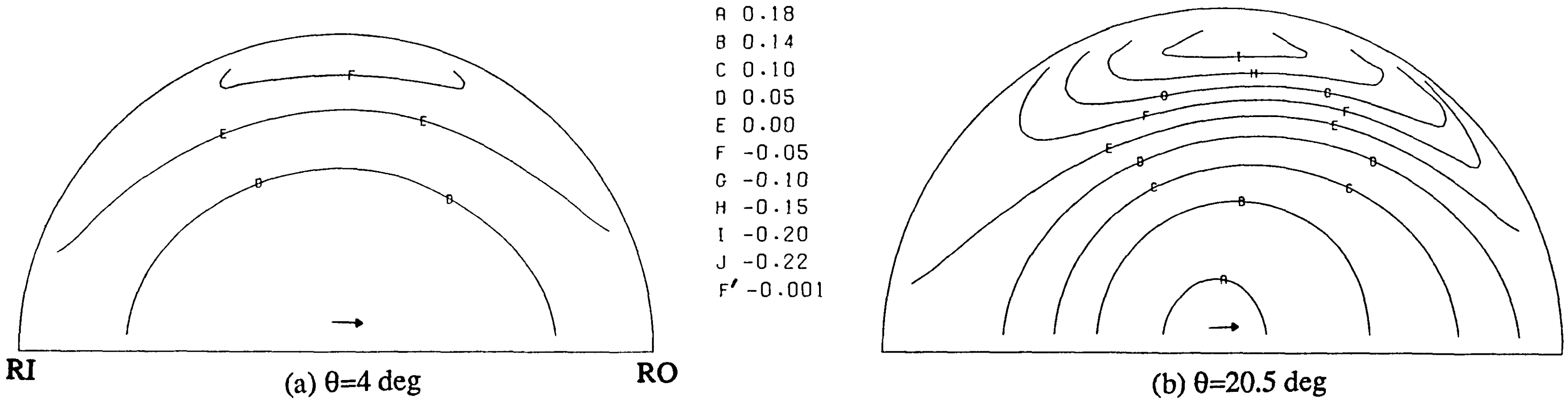

(a) θ=4 deg

(b) θ=20.5 deg

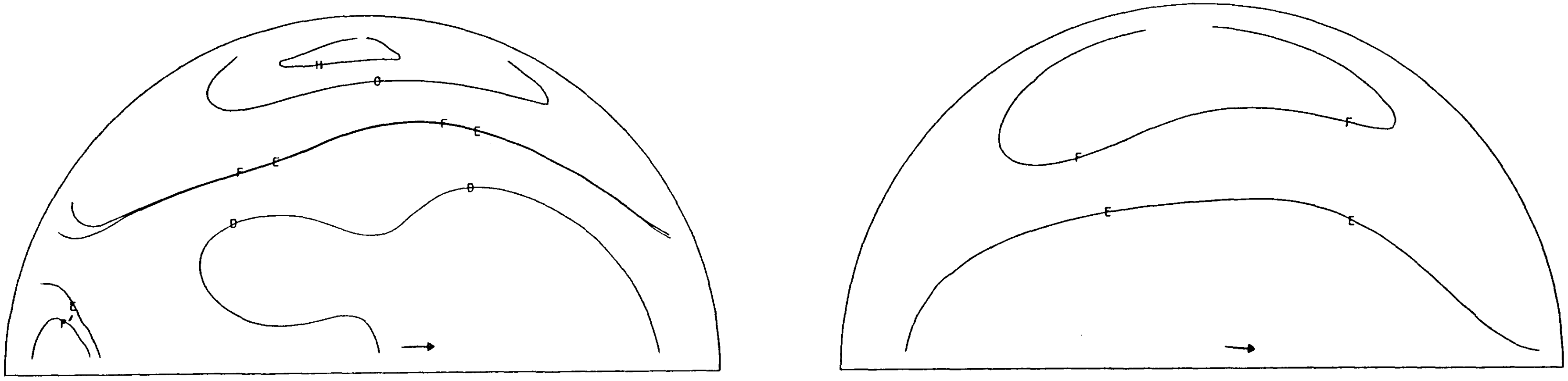

(c) θ=41 deg

(d) $1D_0$ downstream

Fig. 5.37 Contours of v/u_0 at different streamwise sections at Re=790; arrows show the positive direction of v-velocity

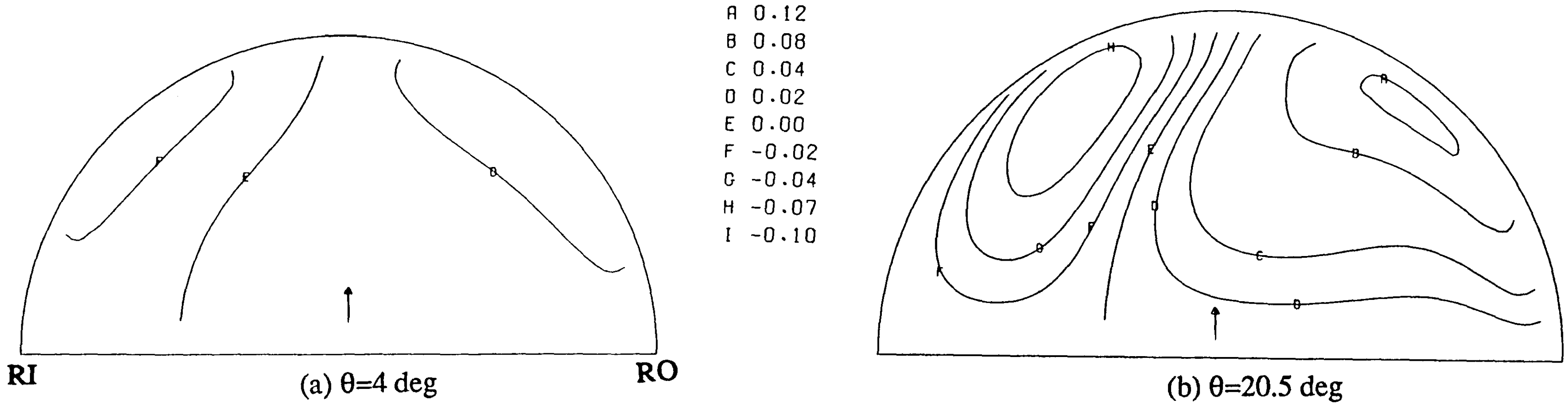

(a) θ=4 deg

(b) θ=20.5 deg

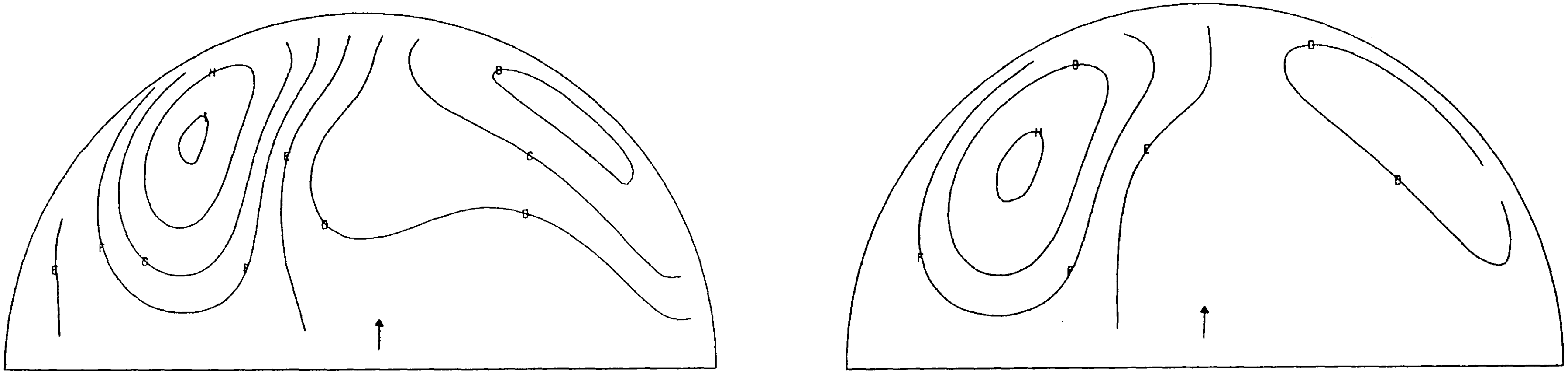

(c) θ=41 deg

(d) $1D_0$ downstream

Fig. 5.38 Contours of w/u_0 at different streamwise sections at Re=790; arrows show the positive direction of w-velocity

CHAPTER 6

FLOW THROUGH VOLUTE CASINGS

6.1 Introduction

This chapter presents the calculations of flow in two types of volute casings; one having a symmetric, circular cross-section and the other with non-symmetric, trapezoidal cross-sectional shape. For the circular case, the flow was considered to be laminar but in the second problem turbulent flow was predicted and the results are compared with available experimental data. The objectives of these studies were to understand the three-dimensional flow development pattern in volute casings as well as to demonstrate the ability of the developed numerical technique to handle volute geometries of practical interest.

In order to bridge the gap between a volute and a curved duct, flow development in a volute-like duct (hereafter referred to as trumpet shaped) is first considered in section 6.2. The main objectives were to understand the overall flow features for such a duct and to study the effect of the radius of curvature variation which has been absent in the cases considered so far (Ch.4 and Ch.5).

The above-mentioned duct was then modified (section 6.3) to simulate a symmetric, circular cross-sectional volute by allowing a radially exiting discharge flow. Since no experimental data were available for this particular flow, only qualitative comparisons were made with experimental and numerical data for flow through volutes with similar geometrical configuration. By comparing these results with those of trumpet-shaped duct of section 6.2 it was possible to isolate the effects of discharge flow on flow development in a volute.

In section 6.4, turbulent flow was predicted for a trapezoidal volute and some critical flow parameters were compared with available experimental data.

Finally, closing remarks are made in section 6.5.

6.2 Laminar Flow Through a Trumpet-shaped Duct

6.2.1 Description of the Geometry

In this section, developing laminar flow in a circular cross-sectional duct with variable curvature and variable cross-sectional area is predicted. This type of duct represents the third category of once-curved ducts mentioned in §1.1.

A schematic diagram of the duct is given in Fig.6.1. Similar to a volute casing, it has an upstream tangent (inlet duct) and a spiral section. The cross-sectional shape is circular everywhere starting from the inlet through the spiral section and upto θ=360 deg (exit). The area of cross-section A (=$0.25\pi D^2$, where D is the local diameter of the cross-section) reduces linearly in the spiral section with azimuth angle θ and at θ=360 deg the area is 5% of the area at θ=0 deg (termed the 'throat'). The radius ratio δ for the spiral section is defined as:

$$\delta = D/2RI \qquad (6.1)$$

Here, RI is the radius of the inner bend of the duct[1]. The azimuthal variation of the non-dimensional cross-sectional area, A/A_{th} (where A_{th} is the throat area) is given in Fig.6.2a and the radius-ratio is shown in Fig.6.2b. It can be seen that A/A_{th} varies linearly from 1.0 (at θ=0 deg) to 0.05 (at θ=360 deg); whereas the radius-ratio varies quadratically from 0.5 (at θ=0 deg) to 0.112 (at θ=360 deg). This value of δ is typical of small turbocharger inlet volutes (Lymberopolous, 1987).

6.2.2 Computational Details

Due to the existence of a vertical symmetry plane (z=0, Fig.6.1), only one-half of the cross-section was considered in the calculations. The number of grid nodes employed was 21x46x11 in the η, ζ and ξ directions respectively (Fig.6.3). Two different arrangements of grids (Type I and Type II) were considered for the gridding of the

---

[1] This definition of δ is slightly different to those defined in Chapters 4 and 5 (Eq. 4.3). Here, instead of using the mean radius of curvature in the denominator, the inside radius has been used. This is convenient in the sense that since the inside radius is constant all along, the value of δ indicates, apart from the tightness of the bend, the curvature of the outside radius. The radius-ratio given by Eq.4.3 will be $\delta/(1-\delta)$, if δ is defined by Eq.6.1.

cross-section. The reason for this was to further evaluate the capability of the solution technique for handling various mesh systems and levels of non-orthogonality.The particular choice of the type II mesh is related to the exit conditions from a turbocharger volute as will become clearer in a later section.

A uniform plug velocity u_0 was applied at the inlet plane of the duct, and the other two components of velocity v and w were taken to be zero. The Reynolds number of the flow was defined as:

$$Re= \rho u_0 D_{\theta=0}/\mu \qquad (6.2)$$

The value of Re was taken to be 500. The corresponding Dean number, defined as:

$$De=Re\delta^{1/2} \qquad (6.3)$$

was equal to 353.6 based on the value of δ at the throat. For the walls, the symmetry plane and exit, usual boundary conditions were applied (§3.6).

6.2.3 Results and Discussion

The velocity vectors on the symmetry plane are shown in Fig.6.4. At the entrance to the spiral section (θ=0 deg), the velocity field exhibits the typical curvature effect in terms of flow accelerated near the inner bend and decelerated near the outer. Growth of the boundary layers and the obvious effect of area-reduction can be seen in all the vectors for increasing values of the azimuth angle. Variation of the static pressure coefficient, Cp (on the symmetry plane at the inner and outer bend) defined as :

$$Cp =(p - p_{ref})/0.5\rho u_0^2 \qquad (6.4)$$

where p_{ref} is the static pressure at the inlet plane of the duct, is shown in Fig.6.5. It shows that a radial pressure gradient is set up as soon as the flow enters into the curved part of the duct. With reference to similar plots in Ch.4 (Figs.4.9, for constant curvature and constant cross-sectional ducts), these curves show that the magnitude of the radial pressure gradient increases continuously as the flow moves downstream. This is directly related to the reduction of flow-area and consequent acceleration of the flow.

The streamwise velocity (u/u_0) contours at eight azimuthal locations for the two different grid arrangements are given in Figs.6.6a-h and 6.7a-h respectively. The agreement between the two sets of calculations is remarkably good for all the contour values considering the very different degrees of non-orthogonality over the duct cross-section. The small differences which exist are due to different levels of resolution in various parts of the cross-section. The similarity between the predicted results supports the fact that the numerical errors are insignificant and the computer code is capable of handling arbitrary geometries accurately. The typical flow acceleration at entry to the duct can be clearly seen from the clustering of the velocity contours near the inner bend (Figs.6.6a and 6.7a). At this location, the maximum streamwise velocity occurs on the symmetry plane. This accelerated velocity gradually redistributes over the cross-section due to the centrifugal forces and by about θ=45 deg (Figs.6.6b and 6.7b) the contours show an axi-symmetric pattern. For all other plots, the typical curved duct contours can be observed. One major difference, however, is the displacement of the maximum streamwise velocity from the symmetry plane to an area much closer to the wall and slightly towards the inside of the cross-section. This phenomenon, which was not observed for similar flows through constant curvature ducts (Ch.4 and 5), is related to the new type of secondary velocity structure to be described in the next paragraph. The other aspect to be noted is the continuously increasing magnitude of velocities, obviously due to area reduction. A double-peak nature (Ch.4) of the streamwise velocity can be seen only at θ=135 deg plots.

The secondary velocity vectors at corresponding azimuthal locations are shown in Fig.6.8a-h (Type I mesh) and Fig.6.9a-h (Type II mesh). Again, the agreement between these two sets of results is good although the Type II results, which have more grid nodes near the inside wall, seem to resolve the strong secondary flow better. The counter-rotating vortex which is found typically in constant curvature ducts (Ch.4 and 5) can be seen to persist only upto θ=90 deg. While the inner half of the cross-section behaves throughout in an expected manner, the outer half exhibits a new behaviour in comparison to the constant curvature ducts. It can be seen that after θ=90 deg, the secondary flow which carries fluid along the symmetry plane cannot reach the outer bend smoothly. Rather it decelerates rapidly due to another opposing secondary motion coming from the outer wall and directed towards the inside. At θ=180 deg and θ=225 deg, a second weaker vortex associated with this motion can be seen in the outer half of the cross-section. The collision of the two secondary streams gives rise to a 'stagnation point' on the symmetry plane (at about the duct centre at θ=270 deg) and the net effect is the turning of the primary vortex motion towards the curved wall away from the symmetry plane. The collision point of the two secondary motions on the symmetry plane is found to shift more towards the inner bend as the flow develops. The reason for this can be ascertained by reference to the different curvature variations of the two bends (outer and inner, see Fig.6.1). While the radius of curvature of the inner bend is constant throughout, that of the outer decreases continuously with increasing values of azimuth angle. Hence, for higher values of θ, the strength of the secondary stream originating from the outer bend intensifies continuously 'pushing' the stagnation point further towards the inner bend. The occurrence of the maximum streamwise velocity away from the symmetry plane is probably due to the upwardly moving secondary flow caused by collision.

6.3 Flow Through a Symmetric, Circular Volute

6.3.1 Description of the Geometry

In this section, the computed results for laminar flow in a symmetric, circular cross-sectional volute are presented. A diagram of the volute geometry is given in Fig.6.10. The spiral part is fitted with a constant cross-sectional (area and shape) upstream section of $2R_t$ long, where R_t is the rotor-tip radius (or radius of the inner bend) as shown in Fig.6.10. The cross-sectional shape is predominantly circular everywhere except in the last 27 deg (i.e., $\theta>333$ deg), where it changes to a rectangle at the exit ($\theta=360$ deg). This has been done in order to avoid 'overlapping' (cf.Fig.6.1 and Fig.6.10) as well as to conform with a volute which possesses a 'zero-thickness' tongue-width.

The cross-sectional area A is made up of two parts (Fig.6.10b), one is circular and the other is a rectangular part having an area equal to BBx(0.5WD) (shown for half of the cross-section due to symmetry). This rectangular part of the area is constant along the azimuthal direction and at $\theta=360$ deg, the duct area A is exactly equal to BBxWD. The dimensions of BB and WD are:

$$\begin{aligned} BB&=0.05R_t \\ WD&=0.10R_t \end{aligned} \tag{6.5}$$

The non-dimensional area A/A_{th} (where A_{th} is the throat area, i.e., at $\theta=0$ deg) varies linearly over most of the azimuthal direction and is given in Fig.6.11a. The radius-ratio δ, defined as:

$$\delta=D/2R_t \tag{6.6}$$

where D is the hydraulic diameter of the cross-section, is shown in Fig.6.11b. Quicker variations of A/A_{th} and δ after $\theta=333$ deg are due to the geometrical reasons mentioned in the previous paragraph.

6.3.2 Computational Details

Again, the cross-sectional shape is symmetrical (Fig.6.10), and only one-half of the cross-section need to be considered in the calculations. Two grid systems were employed, one with 21x46x11 (in the η, ζ and ξ directions respectively) and the other with 37x46x20; the latter is shown in Fig.6.12.

As usual, a uniform plug velocity u_o was specified at the inlet plane and the radial component v and axial component w were set to zero. The Reynolds number of the flow, defined by Eq.(6.2) was taken to be 500. The corresponding Dean number based on the radius-ratio δ at the throat (θ=0 deg) was equal to 353. The flow was considered to be laminar and hence only the momentum and pressure correction equations were solved. For the symmetry plane and walls, usual boundary conditions (§3.6) were applied. Since no flow was allowed to recirculate under the tongue, wall boundary conditions were also imposed at the θ=360 deg plane (i.e., a complete 'blocked off' duct end). The boundary conditions at the volute exit plane (considered to be the same as the inner bend i.e., a circle of radius R_t, Fig.6.10) were of particular significance and the procedure followed is described below.

Boundary Conditions at Exit from the Volute

As already mentioned in Ch.1, the ideal design function of the type of volute considered in this study is twofold; one is to ensure uniformity of discharge flow in terms of flow-rate and flow-angle and the other is to maintain a constant pressure level all around the rotor-tip. Ideally, a properly designed volute should satisfy both these criteria for the designed operating environment but, as was shown in the literature survey (§1.2), the simultaneous satisfaction of these two requirements is hardly ever met.

A technique which will solve the volute-rotor system as one unit (for example, Hamed et al, 1978) can easily specify the boundary condition in terms of 'fixed pressure' because at the exit from the rotor, the pressure is usually known (often atmospheric). Since the present investigation is confined to the volute, neither the pressure (which may be known but is found to vary, see §1.2) nor the uniform flow-angle is a proper boundary condition.

Hence, in order to simulate the presence of the rotor in a rather simple manner, only the first named purpose of the volute (i.e., uniform flow rate) has been imposed into the computational procedure. This was advantageous in the sense that it is the primary criterion and the two important design parameters such as rotor-tip pressure and flow-angle variations then become a predicted outcome of the calculation.

The uniform flow rate boundary condition was imposed by specifying uniform v-velocity (radial component) over the entire volute exit plane along the azimuthal direction. For all other variables, zero-gradient boundary conditions have been applied.

This practice is clearly a gross simplification, justified only by the preliminary nature of this study and, as will be mentioned in the next chapter, this is one of the areas where more attention is needed for future work on volute flows. In their finite difference solution of flow through volute casing, Chen et al (1986) have also reported such an exit boundary treatment.

6.3.3 Presentation of Results

The velocity vectors on the symmetry plane are shown in Fig.6.13. Growth of the boundary layers on the walls and the obvious effect of discharge flow can be seen in the spiral part of the volute. The magnitude of the core flow shows uniformity on this plane upto θ=270 deg, after which significant flow acceleration can be observed.

Variation of static pressure coefficient Cp, defined by Eq.(6.4), on the symmetry plane are shown in Fig.6.14. Just after the throat (θ=0 deg) the flow experiences a favourable pressure gradient on the inside whereas on the outside it experiences an adverse pressure gradient. For the rest of the spiral section, the pressure gradient is found to be in approximate equilibrium and after θ=315 deg, it decreases very sharply. These curves resemble the corresponding figures in Ch.4 and Ch.5, but are different to those of Fig.6.5. The dissimilarities can be explained by the fact that in the case of the trumpet-shaped duct (§6.2) the total flow accelerates due to area reduction, whereas in this case the scale of acceleration is much less (for θ<315 deg) because of the radially exiting fluid stream.

The development of the streamwise velocity on the symmetry plane is given in Fig.6.15a-h. The abscissa for these plots is the non-dimensional radial distance r* measured along the symmetry plane and defined as (see Fig.6.10b):

$$r^*=(r - R_t)/(RO - R_t) \qquad (6.7)$$

The comparison of results for the two meshes used, clearly demonstrates that the grid refinement over the cross-section (from 21x11 to 37x20) did not produce significant changes. No similar comment can be made for the azimuthal direction since the mesh density could not be increased due to limitations of available computer memory. An important point to note is the profile at θ=4.5 deg (Fig.6.15a). The fine grid computation reveals an incipient separation of the streamwise component on the outer wall which is related to the adverse pressure gradient (Fig.6.14); the coarse-mesh cannot pick up this small scale detail. The effect of the sudden area-change (due to the introduction of the rectangular part of the volute cross-section as shown in Fig.6.10) can also be observed near r*=0 on the same figure. The location of the maximum streamwise velocity u/u_0 is initially ($\theta \leq 90$ deg) near the volute exit, which then changes as the maximum u-velocity migrates towards the outer bend, typical of bend flows. However, after $\theta=270$ deg, the maximum velocity is found to occur again near the volute exit i.e., near $r^*=0$. For all the profiles a large boundary layer flow can be seen to exist near the outer wall ($r^*=1.0$). The 95% thickness of this boundary layer is 20% of r^* at $\theta=4.5$ deg, it quickly drops to 13% at $\theta=90$ deg and for $\theta>90$ deg it shows a monotonic rise to 21% at $\theta=315$ deg.

The isovelocity contours of the streamwise component u/u_0 for eight azimuthal locations are shown in Fig.6.16a-h. The effect of flow-acceleration on the volute-exit side (or the inside) can be observed in the first two figures i.e., at $\theta=4.5$ and 45 deg. After that the core flow shows a tendency towards a typical bend flow pattern in that the streamwise velocity can be seen to be displaced towards the outer bend. At $\theta=135$ deg (Fig.6.16d) the maximum u-velocity is found to be shifted away from the plane of symmetry; but in the later plots ($\theta>135$ deg) it moves back onto the symmetry plane.

The secondary velocity vectors for the corresponding locations are given in Fig.6.17a-h. The effect of the discharge flow is visible in all the plots. Growth of the secondary boundary layer along the curved wall from the outer to the inner bend shows apparent similarity to corresponding plots in previous chapters. However, in this case the movement of the secondary fluid along the curved surface is caused by two physical forces. One is the radial pressure gradient caused by curvature and the other, perhaps more significant for $\theta>135$ deg, is the exiting mass flow which provides a constant 'pull'. Unlike typical bend flows, the strength of the secondary stream carrying fluid particles along the symmetry plane from inside to outside can be seen to be very small and sometimes negligible. This is why the vortex motion over the cross-section is not very clear in the figures, although a weak vortical motion of the secondary fluid can be seen in Fig.6.17b-c. This vortex clearly disappears at $\theta=180$ deg and a radially inward secondary flow continuously feeds the rotor periphery.

These differences in the secondary velocities are responsible for the atypical streamwise velocity contours (Fig.6.16a-h) in comparison to bend flows. The other important aspect is that the secondary boundary layer can be seen to exist even at the volute exit.

6.3.4 Discussions of Results

In this section, the results presented in §6.3.3 are discussed from the viewpoints of the effect of discharge flow on flow development, the effect of viscosity and the possible effects of flow parameters at volute exit. Since no experimental data were available for this test case, only qualitative comparisons were made with flow through similar geometries.

6.3.4.1 Effect of Discharge Flow

The Dean number of this flow is the same (=353) as that of the duct of §6.2. The only difference is in the exit boundary conditions. By comparing the contours of Fig.6.16a-h with the corresponding contours of Fig.6.6a-h, some distinctive features can be observed. Firstly, as a result of the discharge fluid the total flow rate does not increase significantly (at least for $\theta<270$ deg) which is very desirable from a distribution point of view. For $\theta\geq270$ deg noticeable core flow acceleration is found. This increase of core flow is due to two possible reasons. One is that the linear area variation (Fig.6.11a) may be too steep for this region to conform with the exiting flow and hence to maintain a uniform velocity profile; the second cause is the upstream effect of the larger area-reduction for $\theta>333$ deg. However, for the most part of the volute, the linear area variation is a reasonable guideline for area distribution. This is in agreement with the findings of Lymberopolous (1987), Chen et al (1986).

Secondly, the development pattern of streamwise velocities are significantly influenced by the discharge flow. Practical turbocharger volutes are often designed on the basis of obtaining a free-vortex profile (velocity x radius from the centre of the rotor=constant) in the radial direction. This profile is usually achieved at the throat by designing a proper inlet duct (Hussain, 1982), which then can be retained by proper distribution of area in the azimuthal direction. The large radial pressure gradient which occurs along the volute in practical cases is due to high mass flow rate. For this particular test case, the total flow rate is very low (u_0=0.16 m/sec) in comparison to reality. However, a profile qualitatively similar to a free-vortex flow does exist at bend entry (Fig.6.15a) and is due to the sudden imposition of a radial pressure gradient at the throat. Apart from the contour levels near the rotor side, an approximately axisymmetric flow pattern is displayed over most of the cross-section. This relatively simple nature of the contours can be explained as follows. As has been shown in previous chapters, the flow development (at least for the range of Dean numbers considered in this study) in a curved duct is determined by the secondary flows induced by curvature. For a volute, the other important factor is the discharge flow, which acts in a direction opposite to the centrifugal forces experienced by the fluid flowing in the core region. These two opposing forces are believed to be in approximate equilibrium which results in the particular pattern of the contours.

The secondary velocity at $\theta=90$ deg (Fig.6.17c) exhibits the typical primary vortex as observed for bend flows. This vortex can be seen to break up at $\theta=135$ deg and, as has been mentioned in the previous section, completely disappears at values of $\theta>135$ deg. At these stations (especially $\theta=270$ and 315 deg) a radially inward secondary flow can be seen to be gradually accelerating towards the rotor side. This behaviour was also observed (on a much more exaggerated scale) for the trumpet shaped duct of §6.2. The reasons are believed to be related to the different curvature variations of the two bends (inner and outer) as discussed in §6.2. However, since no primary vortex is present (or the secondary fluid is sucked out through the volute exit), this oncoming secondary stream from the outer wall moves unhindered towards the rotor. In their experimental work on flow through a nearly square scroll, Malak et al (1986) have also reported similar secondary velocity pattern at higher values of the azimuth angle (see Fig.1.3b).

6.3.4.2 Effect of Viscosity

The effect of viscosity can be observed from the growth of large boundary layers along the walls (Fig.6.15). As has been shown, just after the throat ($\theta=4.5$ deg) the boundary layer has a value of 20% of r^*. Also a tendency towards flow separation was observed near the outer wall. In practical flows, as commented by Tindal et al (1987), for lower overall pressure ratios across the turbine (i.e., at lower mass flow rates) the flow has a tendency towards separation near the outer wall. This behaviour is typical of bend flows. The implication of this boundary layer growth, which may be further enhanced by a possible flow separation, is the reduction of effective flow area and hence the reduction of the 'swallowing capacity' of the turbine from its design value.

6.3.4.3 Flow Parameters at Volute Exit

The flow angle α near the volute exit is defined as (see Fig.6.10):

$$\alpha=\tan^{-1}(-v/u)\ (180/\pi)\ \text{degrees} \qquad (6.8)$$

The variations of α along the azimuthal direction (on the symmetry plane and near the wall) is shown in Fig.6.18. Three different variations can be identified in these profiles. Firstly, the value of α increases sharply upto $\theta=90$ deg; secondly, in the range of $90<\theta<290$ deg, it shows a monotonic drop and thirdly, for $\theta>290$ deg, the value of α falls very quickly and then, in the last 18 deg, it displays a further sharp rise. Larger values of 'near wall' flow angle is a consequence of the boundary layer which is found to exist even at the volute exit. It should be noted that both u and v component have a reduced magnitude near the wall, but the reduction of the u-component is more than that of v, and hence the higher values of α occur there (Eq.6.8).

The increasing trend of α in the first 90 deg is due to the migration of the core flow towards the outer wall and accumulation of low velocity near the rotor (inner) side (Fig.6.15a-c). On the other hand, the decrease of α for $\theta>90$ deg is related to the increasing values of the u-component (Fig.6.15d-h) near the volute exit. The trends of α

for θ>90 deg may be compared (only qualitatively) with the predicted results of Hamed and Baskharone (1980) shown in Fig.1.4a.

The reason that the present results differ for the first 90 deg is believed to be due to the lower flow rates for the present case in comparison to those of Hamed et al (1980), who have considered flows in the compressible range. As a result, the pressure gradients of this volute are very low and hence the free vortex like flow cannot be sustained. The contours of the streamwise velocity component for laminar and turbulent flows at θ=30 deg for the 90-deg bend may be compared with each other (Fig.5.16a and 5.26a). It can be seen that the flow acceleration which takes place near the inner bend is still present for the turbulent flow but has disappeared for the laminar case.

From one-dimensional analysis (Lymberopolous, 1987) the flow angle α can be shown to be equal to:

$$\alpha=9.1\ [A/\{(R_c)_{th}WD\}]\ \text{degrees} \qquad (6.9)$$

In the above expression R_c represents the distance measured from the centre of the rotor to the centroid of the volute cross-section. For this particular volute, the value of α (using the above relation) comes out to be equal to 46 degrees, a reasonable mean of the predictions shown in Fig.6.18. Obviously, since the one-dimensional analysis does not take account of effects such as viscosity, shape etc., the deviations from α=46 degrees are clearly understandable.

The variations of flow angle can cause non-uniform loading on the turbine blades which may have a far reaching detrimental effect on the performance and life of the turbine as a whole. These aspects were discussed by several authors and have been reviewed in §1.2. The ability of the current method to provide prediction of flow angle variation is a significant improvement on simple one-dimensional analysis.

6.3.4.4 Three-dimensionality of the Flow

It is obvious from the previous results that the flow in this type of volute is strongly three dimensional in nature. All of the velocity components viz., u, v, w are significant for the most part of the cross-section and also the three-dimensionality extends upto the volute exit.

The combined effect of the streamwise component u and radial component v (near the volute exit) on the turbine performance has been shown in the previous section. Needless to say that the one-dimensional analyses are restricted to the total velocity at a very crude level, while the two-dimensional analyses (such as Lymberopolous, 1987) take care of the streamwise and radial components only. It is assumed in such calculations that the axial component w is negligible. The present computations contradict such a simplification as can be seen from the secondary velocity vectors of Fig.6.17. The azimuthal variation of w/u_0 near the volute exit is shown in Fig.6.19. It can be seen that for the most part of the volute $20< \theta<290$ deg, the w-component is essentially constant (28% of u_0). But due to the rapid area variation (and also shape) in the last part ($\theta>290$ deg) it shows substantial variations. It is not known what will be the effect of such a profile. One possibility is that, it will produce a non-uniform axial thrust on the rotor; at the very least, it may contribute to considerable disturbance of the discharge flow especially for a nozzle-less volute casing.

For symmetric volutes at a particular azimuthal location, the net effect of w can be taken to be nullified; but for non-symmetric ones such effects cannot be neglected. The origin of this component is related to the particular secondary flow pattern which is due to the shape of the cross-section and will be discussed in §6.4.4.2. The experimental results of Malak et al (1986) also show (Fig.1.3b) significant axial component at scroll exit. The recent measurements of Miller et al (1988) have also shown the three-dimensionality of the flow at the volute exit.

6.4 Flow Through a Non-symmetric, Trapezoidal Volute

In this section, turbulent flow through a volute with non-symmetric and trapezoidal cross-section is studied. This particular volute was fabricated at King's College, London and studied experimentally by Scrimshaw (1981). The predicted results are compared with experimental data in order to validate the ability of the developed code for handling flows of practical interest. It may be mentioned here that although a number of experimental works have been reported in literature (§1.2), none of them, except the one considered below, qualified as a validation test case for this study because of insufficient geometrical information supplied (for example, Malak et al, 1986), occasionally due to the proprietary nature and confidentiality of the undertaken research.

6.4.1 Description of the Geometry

Some important features of the geometry are shown schematically in Fig.6.20. The inlet duct is of length $1.575R_t$, where R_t is the rotor-tip radius (R_t=50.8 mm; this is not now identical with the inner bend radius). The cross-section at inlet is a rectangle ($0.874R_t$x$0.625R_t$), which gradually reduces to a trapezoid at the throat (θ=0 deg) (see Fig.6.20). The area at the throat A_{th} is 46.5% of the rectangular area at the inlet. All other details of the geometry were available and can be found in Scrimshaw (1981).

The cross-sectional area of the volute at θ=90 deg is shown in Fig.6.20. It consists of four surfaces and for convenience they will be referred to as follows:

PP' : Curved surface
SS' : Flat surface
PS : Inner bend or computational exit
P'S' : Outer bend

The dashed line near the inner bend represents the volute-exit or rotor-tip radius. The cross-sectional area A represents the area PP'S'S. The azimuthal distribution of the cross-sectional area A/A_{th} in the spiral part is given in Fig.6.21a. The variation can be seen to be approximately linear upto θ=225 deg, after which slight deviation from linearity is present. The radius-ratio δ defined by Eq.(6.1) is given in the adjacent Fig.6.21b.

From the geometrical point of view, this volute differs from the one studied in §6.3 in that it is non-symmetric, its cross-sectional shape is trapezoidal, the tongue (T in Fig.6.20) has a finite width and the flow area of the inlet duct is changing in the streamwise direction. However, the variations of area and radius-ratio along the azimuthal direction are essentially similar for most of the spiral part.

6.4.2 Computational Details

Two grid systems were employed for this study, one with 15x49x12 nodes (in the η, ζ and ξ directions respectively) and the other with 30x97x24 nodes as shown in Fig.6.22. For the coarser mesh it was possible to obtain full convergence whereas for the finer mesh only a partially converged solution could be obtained in the available time and computing resources. In what follows the results obtained with the coarse mesh are presented and discussed. However, some comparisons of the partially converged fine mesh solution are given in §6.4.4.3.

Again, a uniform plug inlet velocity u_0 (equal to 70.8 m/s) was specified at the inlet plane of the volute. This value was calculated from the mass flow rate specified by Scrimshaw (1981), which corresponded to an overall pressure ratio of 1.5 across the turbine. In the experimental study, the flow started from a plenum chamber and hence the specification of plug profile can be taken to be fairly accurate. The other two components of velocity v and w are believed to be small and hence were taken to be zero. Since the flow was considered to be turbulent, the turbulence intensity k and its dissipation rate ε were also necessary and in the absence of any data they were assumed as follows:

$$k_{in}=0.1\%u_o^2$$
$$\varepsilon_{in}=k_{in}^{3/2}/0.1D \qquad (6.10)$$

The Reynolds number of the flow calculated on the basis of the hydraulic diameter D at the throat and area-mean velocity was equal to $6.34\text{x}10^5$. The corresponding Dean number at the throat (Eq.6.3) was equal to $4.49\text{x}10^5$.

The other boundaries were treated in the same way as described in §6.3.2. Again, no flow was allowed to recirculate under the tongue and naturally the highest discrepancies between the prediction and experimental data were found in the vicinity of the tongue. These aspects will be discussed in §6.4.4.

6.4.3 Presentation of Results

The results are presented in the same order as the other test case described previously in the chapter. First, the velocity vectors for the whole length of the volute in a plane passing through the middle of the exit width and parallel to the flat surface (Line A-A) are shown in Fig.6.23. The initial acceleration of the flow in the converging inlet duct is obvious from the plot. At entrance to the spiral part, the vectors near the inner bend change drastically, an effect related to the particular tongue treatment used (i.e., no flow passes under the tongue). This effect can be seen to exist upto θ=45 deg, after which the vectors exhibit a pattern similar to a free-vortex flow.

In Fig.6.24 the static pressure coefficient, Cp (defined by Eq.6.4) is shown. The effects of the turning are picked up very quickly as soon as the flow enters the curved region. These curves are comparable to the pressure profiles of the 90-deg bend for the turbulent flow (Fig.5.22b) and also to those of the laminar flow through the circular volute (Fig.6.14) in the early part of the spiral section. However, significant variations appear especially in the tongue region and at around θ=315 deg. The first irregularity of pressure is a direct result of the simplification of the tongue as mentioned previously. In this case, the flow over the tongue is treated as a sudden expansion. This assumption, to some extent, simulates the real flow situation for a volute with finite tongue width such as this, but due to blocked off end at θ=360 deg it is much more exaggerated. More discussion on this is deferred until §6.4.4.1. The second irregularity occurs at θ=315 deg. This is probably related to the sudden variation of area (which is also associated with a change of shape from trapezoidal to rectangular) at this azimuthal location (Fig.6.21a). However, in general, a favourable pressure gradient can be found to exist for the most part of the volute.

The isovelocity contours of the streamwise velocity component at ten azimuthal stations (two in the inlet duct and eight in the spiral part) are given in Fig.6.25a-j. Since the inlet duct is converging, the streamwise velocity is found to accelerate in order to maintain continuity. In Station 2, which is very close to the throat, the effect of curvature can be seen very clearly from the radial gradient of the contours. As soon as the flow crosses the throat (θ=4.5 deg), this gradient is mostly retained in the part of the cross-section away from the volute exit, but a significant low velocity region can be seen to occupy the part of the volute near the inner bend. As mentioned in the previous paragraph, the accumulation of the low velocity region is due to the assumption of no flow recirculation under the tongue which renders the flow to be experiencing a sudden expansion. However, the flow does not attain a negative value (separation) perhaps due to the particular mesh density employed for this study. In the region of $90 \leq \theta \leq 225$ deg, the contour distributions show both qualitative and quantitative similarity with each other and display little change. This is due to the smooth area variation in this region and is in agreement with the pressure gradients (Fig.6.24). After $\theta > 225$ deg, the streamwise velocities are found to be decelerated. The reason is believed to be associated with the difference in the gradient of the area distribution at this azimuthal locations (Fig.6.24), and also, possibly more significant, due to the boundary condition imposed at θ=360 deg plane. What happens is that the flow has to decelerate before θ=360 deg plane such that the streamwise velocity conforms with the solid wall boundary condition. Development of the non-dimensional streamwise velocity u/u_0 along a radial plane r^* for the spiral part of the volute is shown in Fig.6.26a-h. From this figure, the effect of the tongue can be seen more clearly. It can also be observed that a large number of grids would be required in order to resolve the boundary layers along the walls.

The secondary velocity vectors at corresponding locations are given in Fig.6.27a-j. Generation of strong secondary velocities in the inlet duct (Fig.6.27a-b) is related to the change of cross-sectional shape and area. The proximity of the curved section can be seen to be picked up by the secondary velocities in the inlet duct and is evidenced by the movement of the node-like sink from the middle of the flat surface towards the inner bend (see Fig.6.27a-b). Inside the spiral part, qualitative similarity of the secondary velocities can be observed for all stations. In general, the vectors display an expected pattern. Due to the combined effect of high radial pressure gradient and discharge flow, the secondary stream moves towards the rotor accompanied by an inward acceleration due to the area reduction from the outer to the inner bend. No vortex as typically found in curved rectangular ducts (Ch.4) can be observed in any of the plots. The relatively simple pattern of the secondary velocities is probably due to the particular shape of the volute and this is why the streamwise velocity contours also showed a less complicated nature in comparison to the bend flows.

6.4.4 Comparison with Experiment and Discussion

The objective of this test case was to show the ability of the present computational procedure to predict the flow parameters of interest and also to demonstrate the ability to reveal the three-dimensional flow pattern inside volute casings. In what follows, is an assessment of the prediction in terms of critical design parameters as outlined in the literature and the possible reasons behind the differences. Based on the results presented in this chapter, the effect of area variation and cross-sectional shape is also discussed. Finally, some comparisons between the coarse and fine grid calculations are described in §6.4.4.3

6.4.4.1 Comparison with Experiment

In Fig.6.28a-b, the exit flow angle α (defined by Eq.6.8) and total/static pressure ratio P_o/p_{exit} (P_o is the total pressure at the inlet of the volute and p_{exit} is the static pressure at the volute exit) along the azimuthal direction are compared with the experimental data of Scrimshaw (1981). In general, qualitative agreement can be seen for the most part of the volute. However, in the vicinity of the tongue (i.e., θ<30 deg and θ>320 deg), large discrepancies can be observed between experimental data and computed results. The probable reasons for this are discussed below.

The qualitative dissimilarity of the predicted flow angle near the tongue region is related to the simplification of the particular tongue treatment adopted as mentioned previously. In a real situation, a certain amount of mass recirculates under the tongue and mixes with the fresh fluid stream coming from the inlet duct. Also, as reported by Scrimshaw (1981), some fluid was found to move from the rotor space into the volute which was termed as 'injection effect'; as a result of which negative values of flow angle were measured there. In this computation, no such recirculation has been allowed and hence at the tongue, a singularity (both v and u component being zero at θ=0 and 360 deg) exists on the radial plane. The imposition of constant mass flux at the computational exit sustains a high value of the v-component, whereas the streamwise velocity u gradually increases in magnitude. Hence the magnitude of the flow angle sharply drops in the first 30 deg. The opposite effect predominates for θ>320 deg.

In the region of 30< θ<320 deg, the flow angles are generally over-predicted by 2-3 degrees. From Eq.(6.9), the value of the flow angle comes out to be equal to 11.3 deg for this volute, which is still higher than the computed values and hence further away from the experimental data. One possible reason for this over-prediction (in the current calculation) could be due to neglect of compressibility. The Mach number of the velocity at volute exit computed by the current predictions is shown in Fig.6.29. It can be seen that the Mach number reaches as high as 0.5, in which range the density variation may be upto 10% (Schlichting, 1979). The effect of lowering the density would be to increase the absolute gas velocity (i.e., essentially the u-component because α is small), as a result of which the flow angle would also be less.

Similar to the flow angle, significant differences can be seen between experimental data and the present prediction for the total/static pressure ratio at the volute exit (Fig.6.28b). The measured values of static pressure show biggest irregularity at the tongue, where a large pressure drop can be seen to exist.[1] What is apparent from the comparison is that such discrepancies are mostly, if not all, reproduced qualitatively in the computations and hence this acts as a support for the present boundary condition, at least as a first-hand approach. However, the rapid pressure fluctuations within the first 10 deg could not be picked up due to the particular tongue treatment and insufficient mesh refinement. The other peak of the total/static pressure ratio is found at θ=315 deg which represents an adverse pressure gradient (a smaller value of P_o/p_{exit} means static pressure is high). The important point to note is that this pressure irregularity which occurs due to area variation (Fig.6.21a) as discussed in §6.4.3 (and is also evidenced by the experimental data), has been reproduced in the current calculations. The over-prediction of this adverse pressure gradient can be directly related to the no flow-recirculation under the tongue. For the region of $30<\theta<300$ deg, the computed P_o/p_{exit} can be seen to be less than the experimental data or in other words, the static pressure p_{exit} is over-predicted for this volute. Similar behaviour was also observed for the case of the 90-deg bend turbulent flow (Fig.5.22b). Given the mesh density for this test case, it is very difficult to make a conclusive judgement as to why this has happened, but it is probable that the turbulence model may have contributed to this discrepancy.

---

[1] This is clearly undesirable as discussed by Scrimshaw (1981) and others as reviewed in §1.2. However, the emphasis of this study is on how accurately are these irregularities reproduced in the calculations and not on what the effects might be.

6.4.4.2 Effect of Cross-sectional Shape and Area

The secondary velocity vectors for this volute demonstrate that the effect of discharge flow extends into the whole of the cross-section from the very beginning of the spiral part. In contrast, for the circular volute (§6.3), the effect of the discharge flow was found to be confined near the inner bend for $\theta<225$ deg. Although no conclusive remark can be made from the above mentioned observations because of the large difference between the flow rates, it is probable that the cross-sectional geometry is partially responsible for this. One way of quantifying the relative size of a volute is the aspect ratio (Lymberopolous, 1987), defined as:

$$f = \{A/(R_c)WD\} \tag{6.11}$$

The value of 'f' utilises the cross-sectional area A, distance from the centre of the rotor to the centroid of the cross-section R_c and the volute exit width WD and hence is an indication of how big the exit width is. For the trapezoidal volute f=1.246 and for the circular volute f=5.06 at the throat. Smaller value of the aspect ratio means that the area of discharge is relatively large in comparison to the cross-sectional area and hence it is likely that the effect of the discharge flow will be propagated more inside the cross-section as it happens for the circular volute at $\theta=225$ deg and beyond. The experimental data of Malak et al (1986) also support the above statement.

The three-dimensionality of the flow has been shown in the vector and contour plots. The axial component w/u_0 at volute exit is plotted in Fig.6.30. The magnitude is found to be fairly constant (about 10% of u_0) but is much smaller than the circular volute (Fig. 6.19). This is obviously related to the simpler shape (trapezoidal instead of circular) and larger exit width of the trapezoidal volute. A possible effect of the axial component has been mentioned in §6.3.4.4.

The variation of cross-sectional area with azimuth angle for the circular volute is linear upto $\theta=333$ deg, and for the trapezoidal volute it is (almost) linear upto $\theta=225$ deg and then it slightly deviates from linearity (see Fig.6.21a). The uniformity of the streamwise velocity contours and secondary velocity vectors in the range of $45<\theta<225$ deg for both the cases justifies that a linear area variation is a reasonable estimate for the volute design. In other azimuthal locations, significant dissimilarities were observed and the reasons have been mentioned previously. Another comment that can be made from the results is that rapid variations of area as well as shape must be avoided in order to maintain uniformity along the rotor periphery.

6.4.4.3 Note on Fine Grid Computation

It has been demonstrated in several of the calculations reported in earlier sections that successive mesh refinement reveals various delicate features of the flow by eliminating numerical errors and also by resolving the solution domain better. A similar attempt of grid refinement was undertaken for this study as has been mentioned in the beginning of the section. However, due to limitations of time and available computing resources, the fine grid computations could not be proceeded until full convergence. The level of convergence that could be reached was only about (see §3.7) $5x10^{-1}$ and the results are therefore possibly far from convergence and hence must be viewed with caution. For the sake of interest, some results of the fine grid computation are presented in Fig.6.31; the corresponding coarse mesh results are also shown for comparison.

The most obvious point to notice is the tendency towards improved resolution in the viscous layers near the walls for the case of the fine grid computation. This is clearly visible from the contours as well as from the vector plots. The secondary velocity patterns exhibit substantial similarity although the fine grid result shows the axial gradients more clearly, an effect directly related to better resolution. One major difference that exists in the secondary velocity vectors is the direction of secondary velocity near the outer surface and hence, the streamlines of the secondary velocities look different. For the greater part of the cross-section, the level of similarity is reasonably good. It can be seen from Fig.6.31c that the flow angles predicted by the fine grid computation is more than that predicted by the coarse mesh calculation and is further away from the experimental data. The reason is related to the under-prediction of the maximum streamwise velocity near the volute exit (Fig.6.31a).

From the above discussion it can be said that apart from the boundary layers, the flow field has been properly resolved and hence the discussions presented in the context of this partcular test case is restricted in the core region. However, the main objective of this particular study was validation of results and this has been demonstrated fairly well. The reasons for the discrepancies have been identified and analysed. More discussion on how the present code can be improved to model further practical flow situatuations will be mentioned in the next chapter.

6.5 Closure

In this chapter, the predicted flow field through two volute casings were presented and one of them was compared with experimental data. In order to isolate the effect of discharge velocity, flow through a trumpet shaped duct was also predicted. From the results and discussions included in this chapter, the following remarks can be made.

i) The initial parts of the volute show significant qualitative and quantitative similarity with curved duct flows. Over the later part, the curvature effects gradually diminish due to relaxation of curvature and more importantly due to the progressive shift of the effect of discharge flow towards the outer bend of the volute cross-section. Apart from the region affected by the tongue, the flow parameters computed by the present numerical scheme compare well with experimental data for the most part of the volute.

ii) The geometrical details of the volute cross-section play a major role in determining the exit parameters which may affect turbine performance. The choice of a linear area distribution may be considered as a first-hand approach in practical designs, although this may be too steep for the later part of the spiral section. It is also obvious that the area and shape variation should be as smooth as possible. Any slight irregularity in cross-section may cause significant fluctuations of flow parameters of interest.

iii) The throat region is of critical importance because the growth of the boundary layers, enhanced by the adverse pressure gradient, may reduce the swallowing capacity of the turbine. For laminar flow, an incipient separation of the streamwise velocity on the outer bend was observed at the throat.

iv) The behaviour of the secondary velocities are controlled mostly by the shape of the cross-section and also by the relative size of the exit and cross-sectional areas. Strong three-dimensionality of the flow was found to exist upto the volute exit. For both the test cases, significant variations of all three components of velocity were observed along the azimuthal direction. The effects of streamwise and radial components of velocity can have a dominating effect on the turbine performance through flow angle, while the axial component, may influence the discharge flow by means of an axial thrust on the rotor and disturbed radial flow.

The present methodology does predict the critical flow parameters reasonably well and can be used as a design tool. Of course, for better realism of the flow, several important modifications must be made and this is discussed in the next chapter.

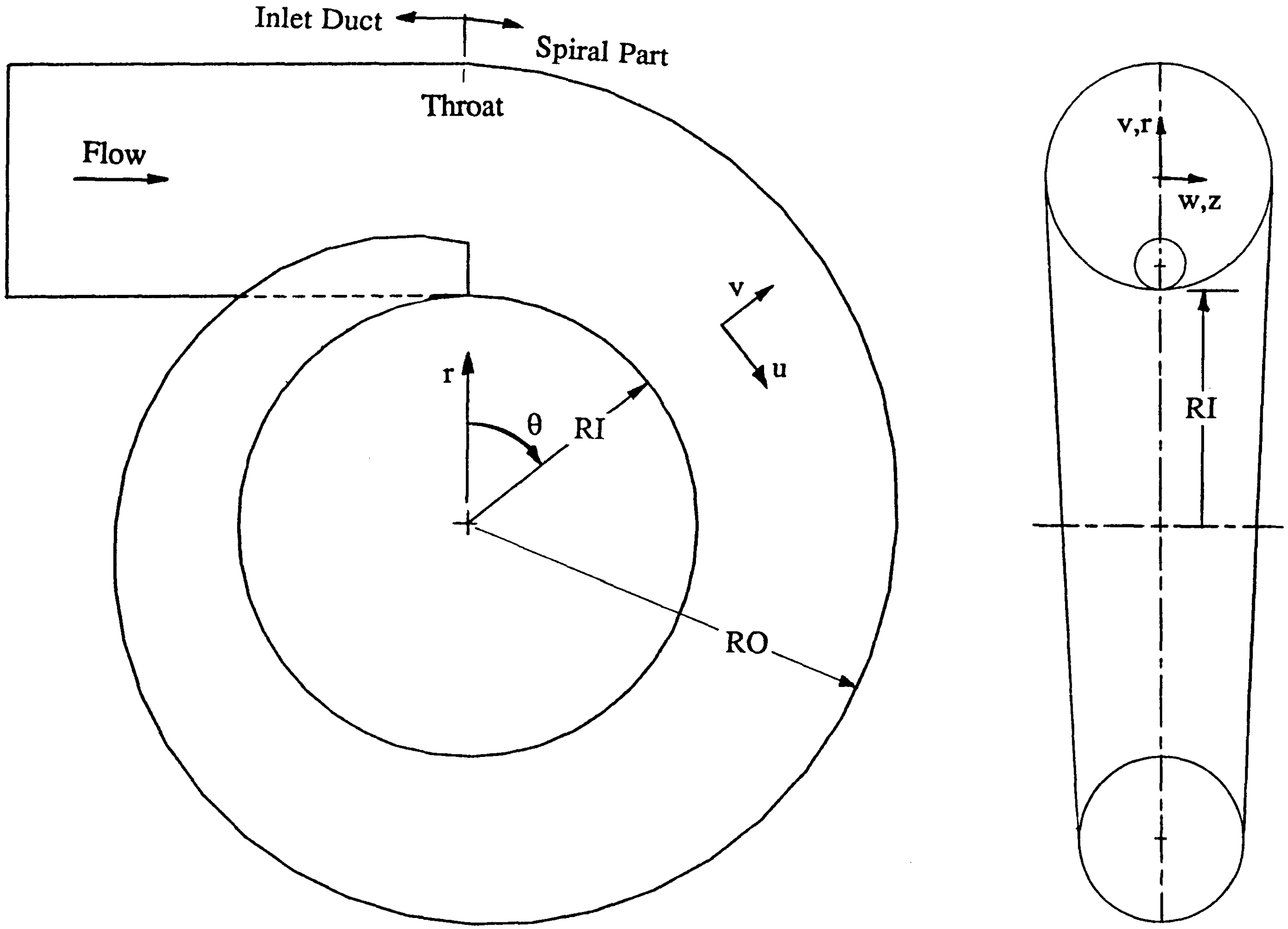

Fig. 6.1 Volute-like duct: Flow configuration and definition of coordinates

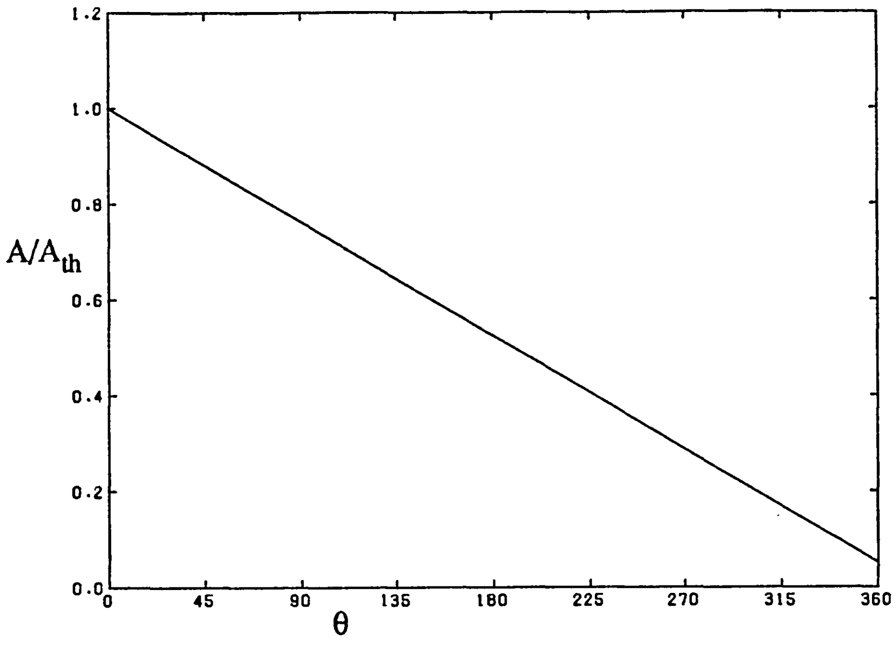

Fig. 6.2a Variation of cross-sectional area with azimuth angle

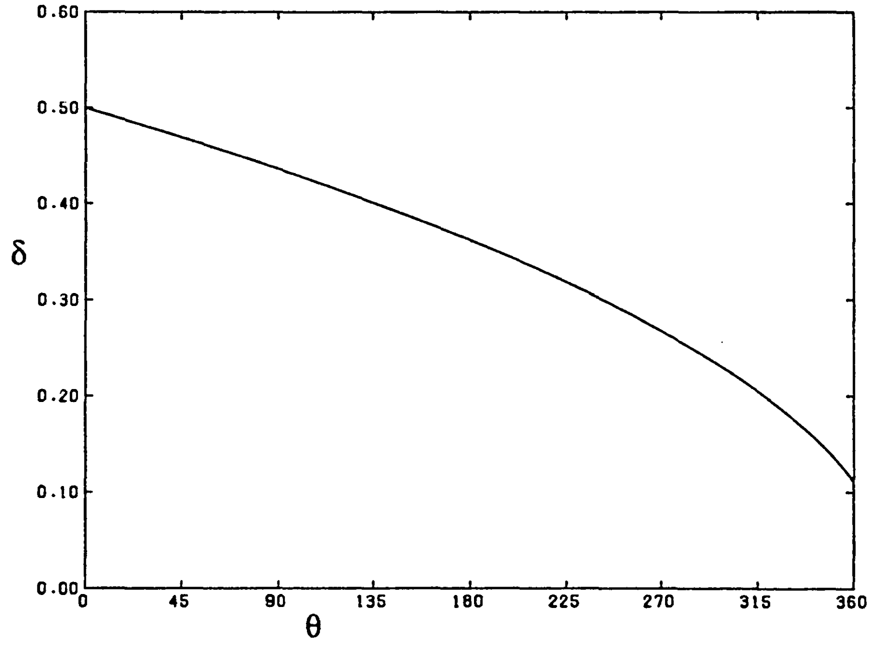

Fig. 6.2b Variation of radius-ratio with azimuth angle

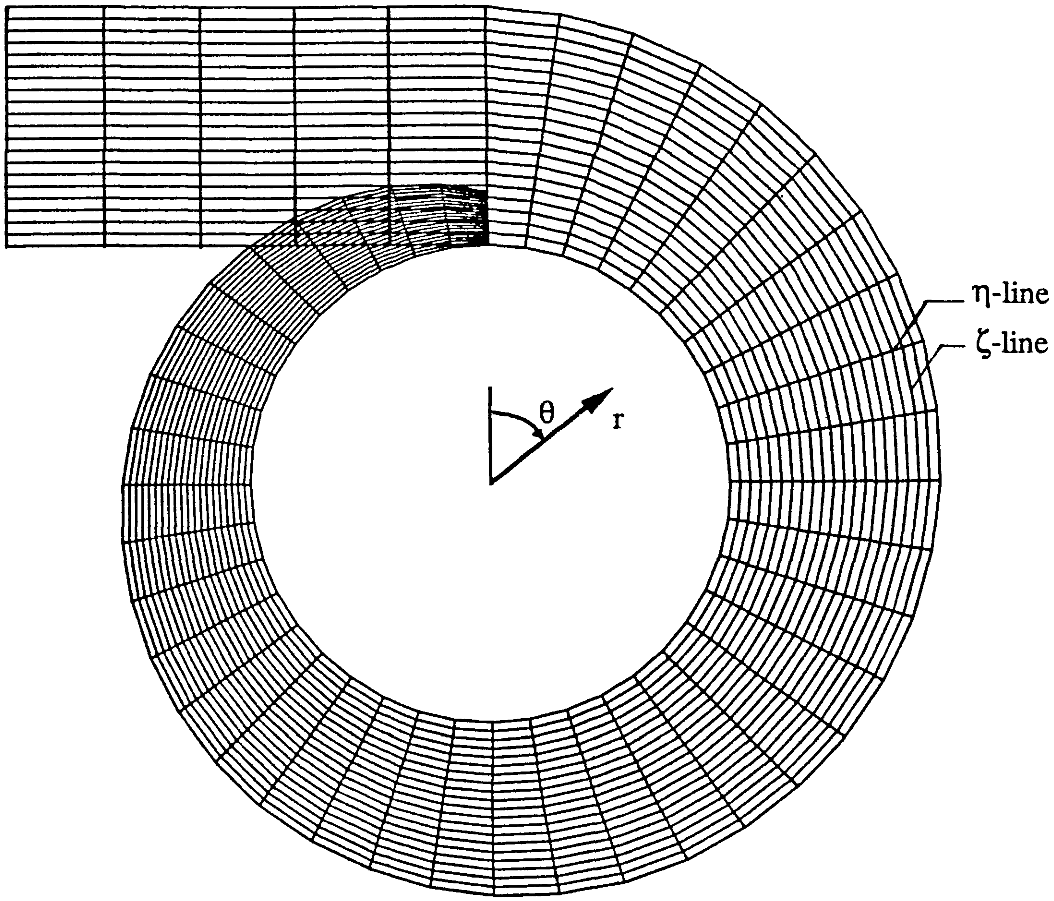

(a) Symmetry plane grids: 21x46 (η x ζ)

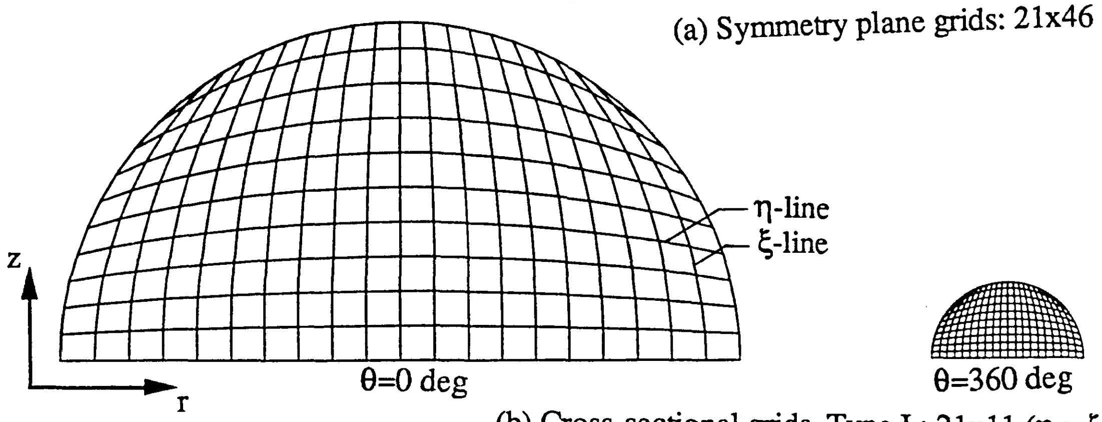

(b) Cross-sectional grids, Type I : 21x11 (η x ξ)

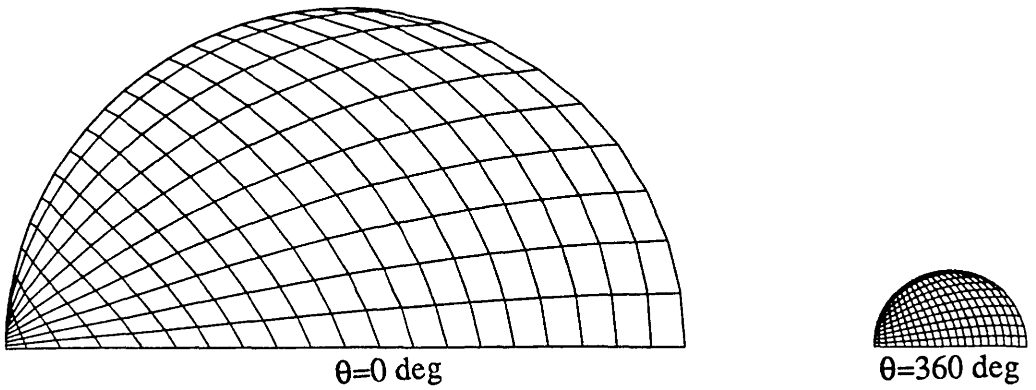

(c) Cross-sectional grids, Type II : 21x11 (η x ξ)

Fig. 6.3 Computational grids used for the volute-like duct

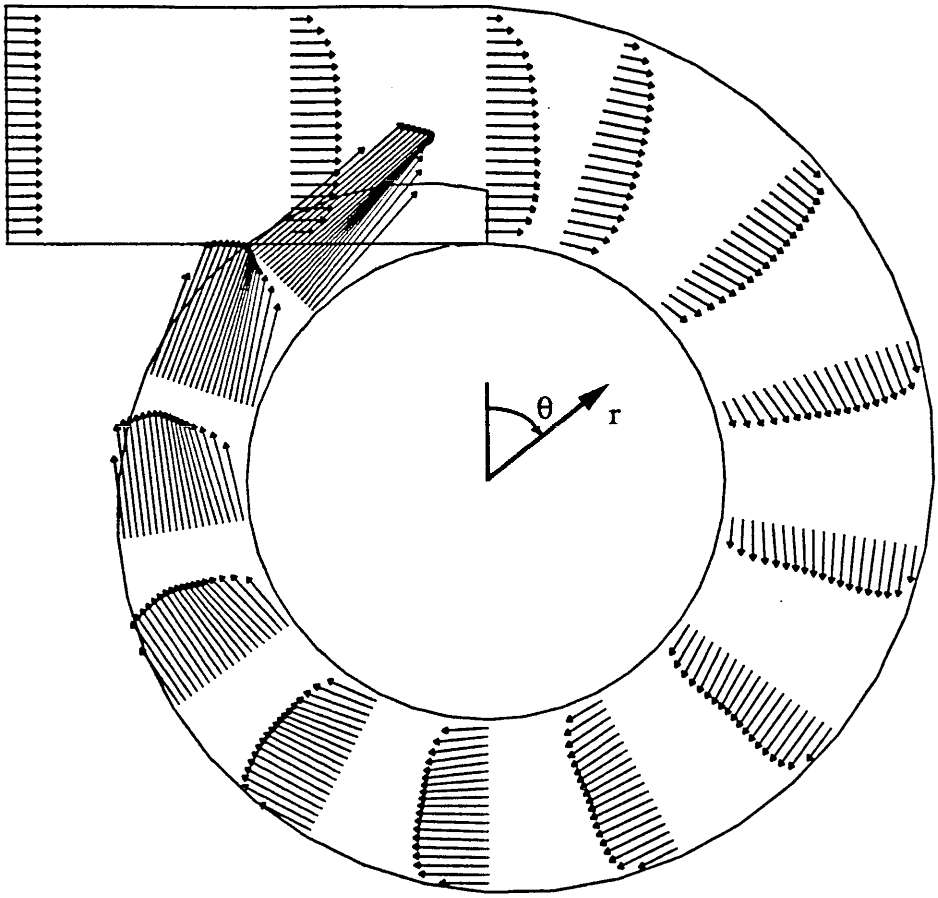

Fig. 6.4 Velocity vectors on the symmetry plane

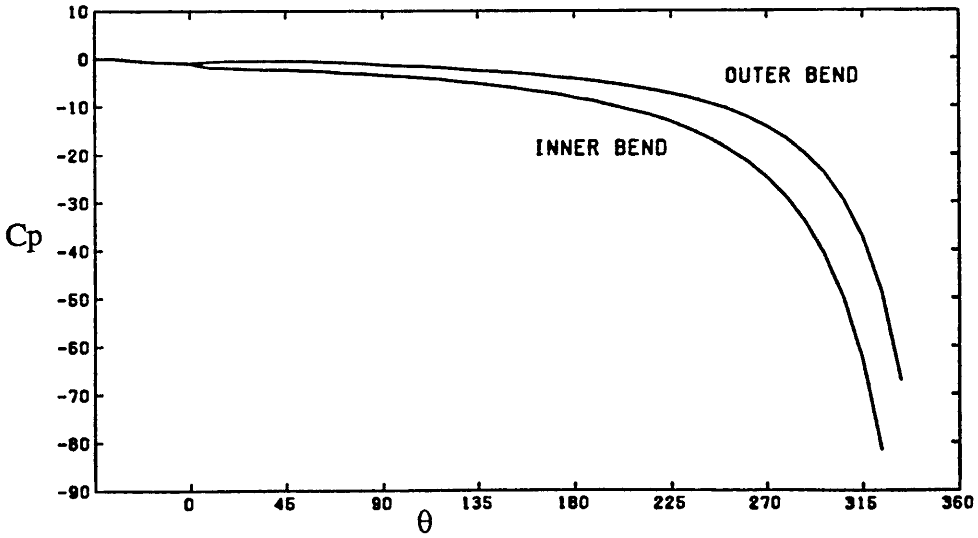

Fig. 6.5 Variation of static pressures along the duct

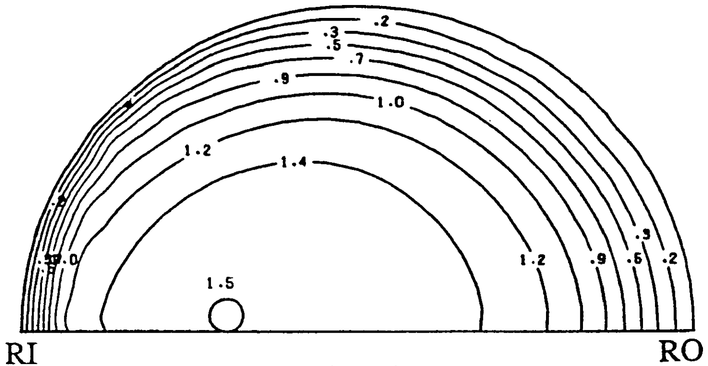

(a) θ=0 deg

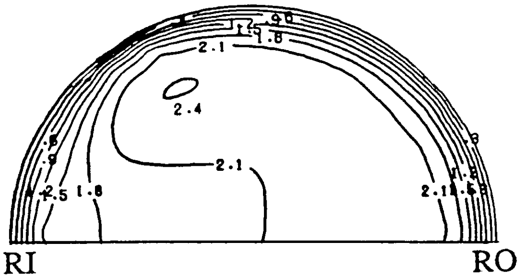

(e) θ=180 deg

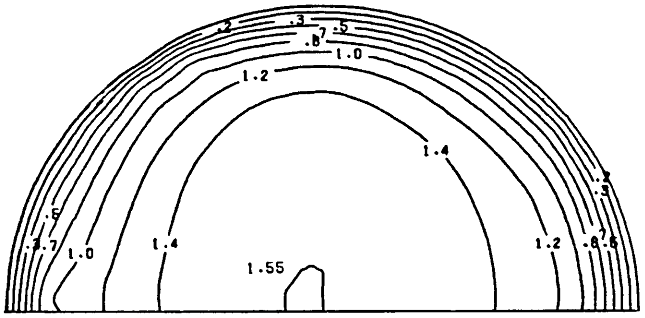

(b) θ=45 deg

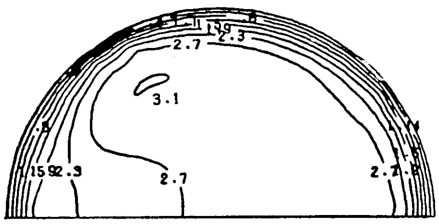

(f) θ=225 deg

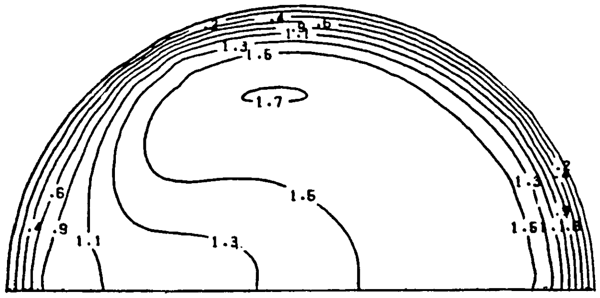

(c) θ=90 deg

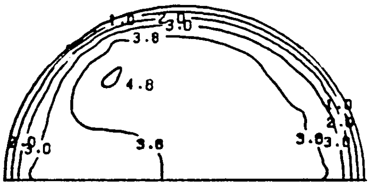

(g) θ=270 deg

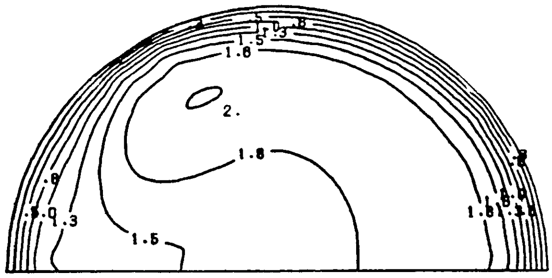

(d) θ=135 deg

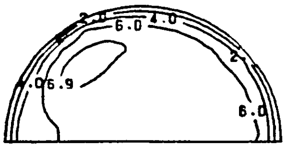

(h) θ=315 deg

Fig. 6.6 Development of streamwise velocity (u/u_o) (Type I)

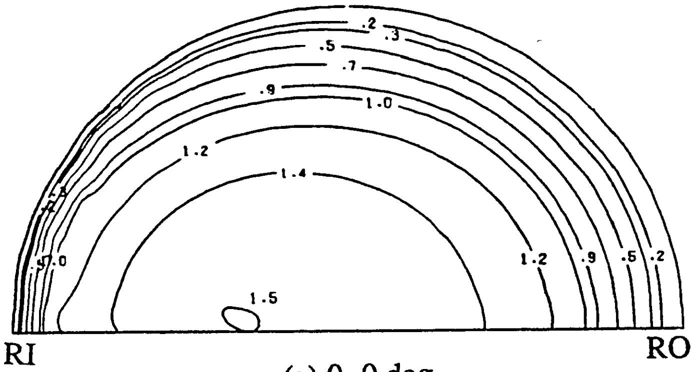

(a) θ=0 deg

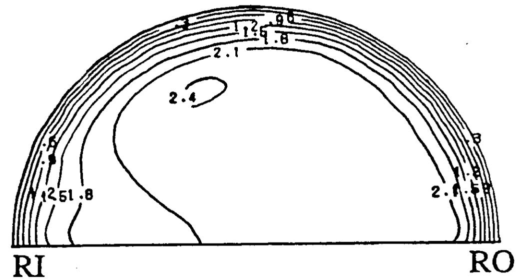

(e) θ=180 deg

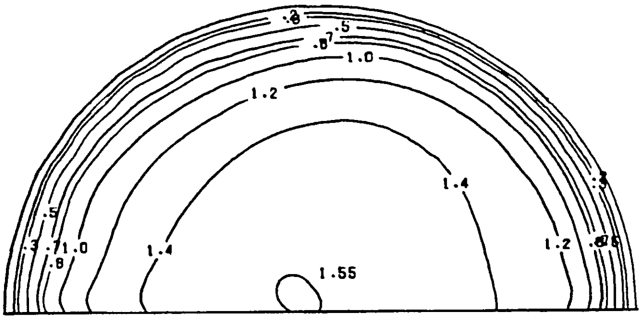

(b) θ=45 deg

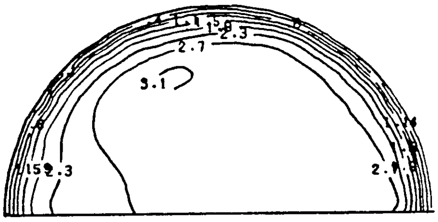

(f) θ=225 deg

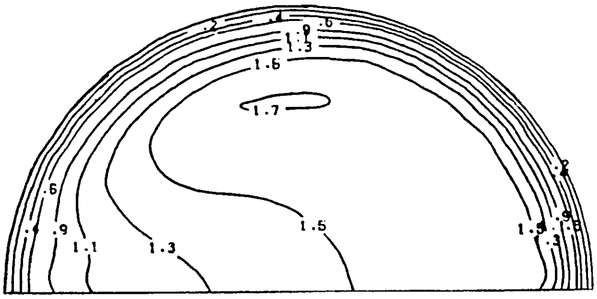

(c) θ=90 deg

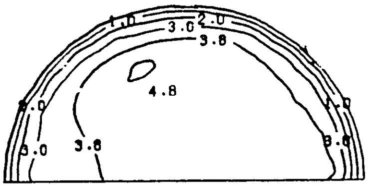

(g) θ=270 deg

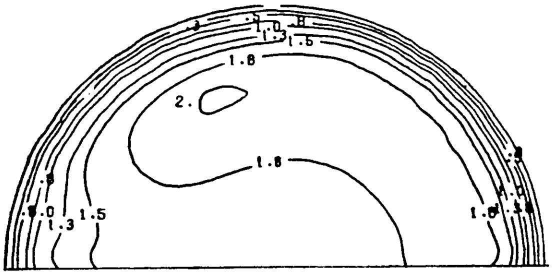

(d) θ=135 deg

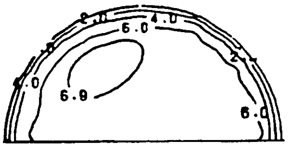

(h) θ=315 deg

Fig. 6.7 Development of streamwise velocity (u/u_0) (Type II)

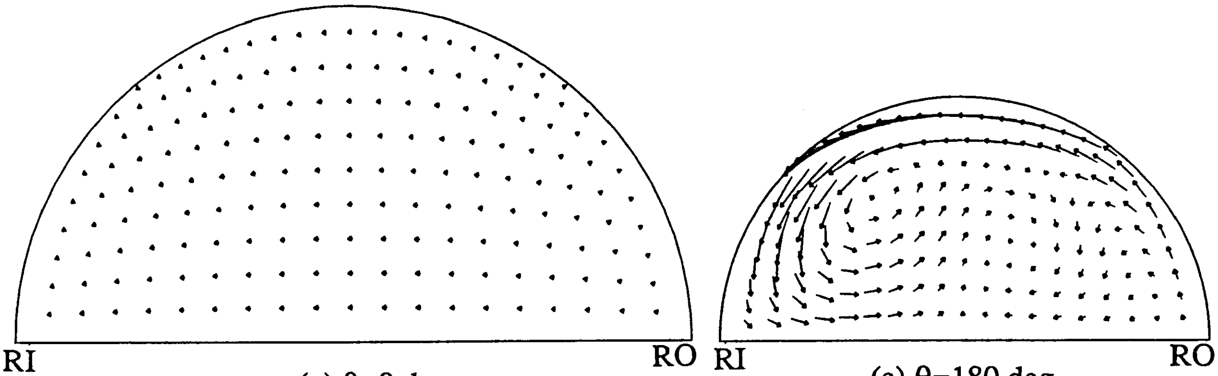

(a) θ=0 deg

(e) θ=180 deg

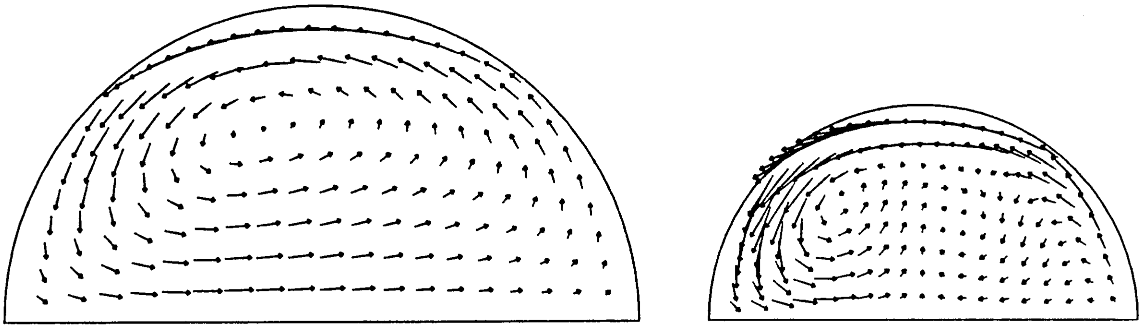

(b) θ=45 deg

(f) θ=225 deg

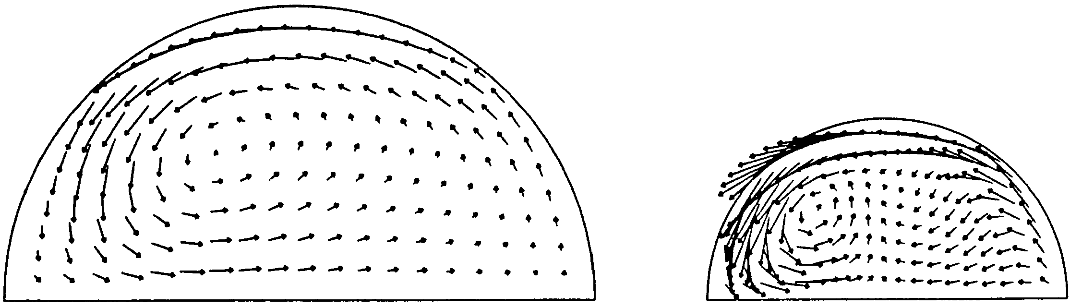

(c) θ=90 deg

(g) θ=270 deg

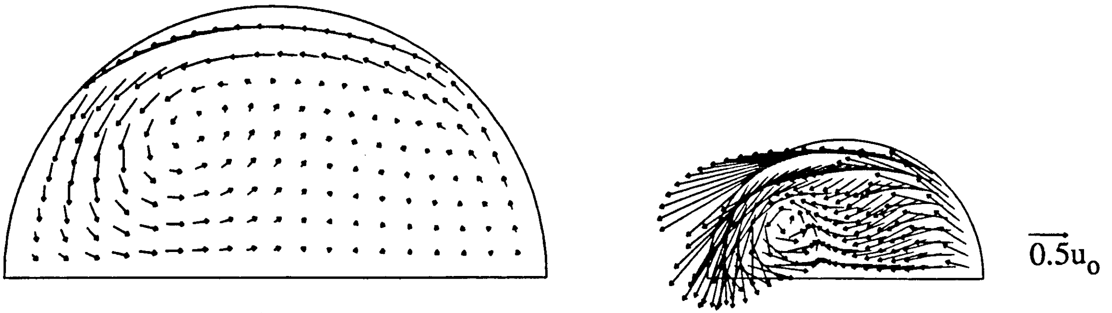

(d) θ=135 deg

(h) θ=315 deg

Fig. 6.8 Development of secondary velocity (Type I)

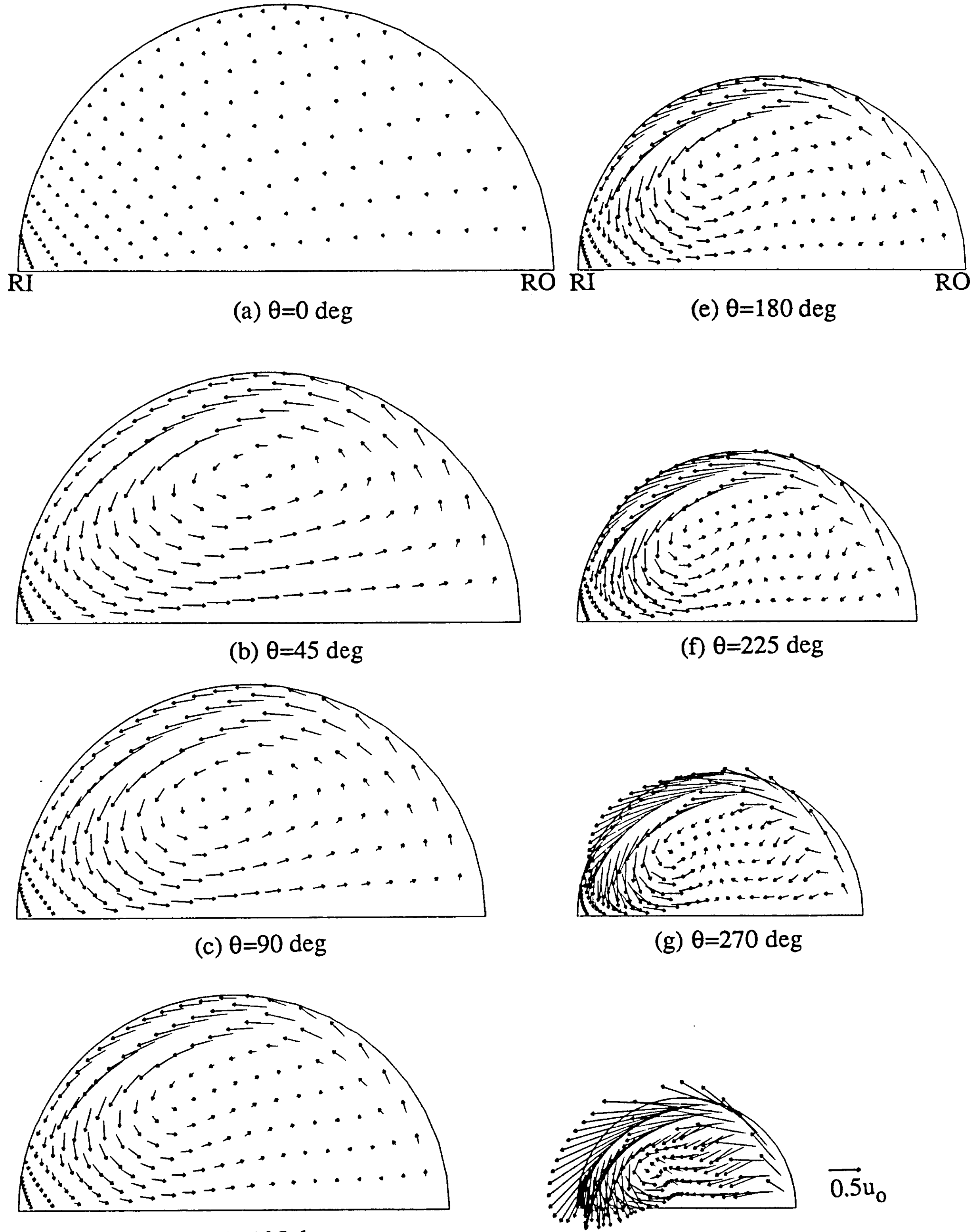

(a) θ=0 deg

(e) θ=180 deg

(b) θ=45 deg

(f) θ=225 deg

(c) θ=90 deg

(g) θ=270 deg

(d) θ=135 deg

(h) θ=315 deg

Fig. 6.9 Development of secondary velocity (Type II)

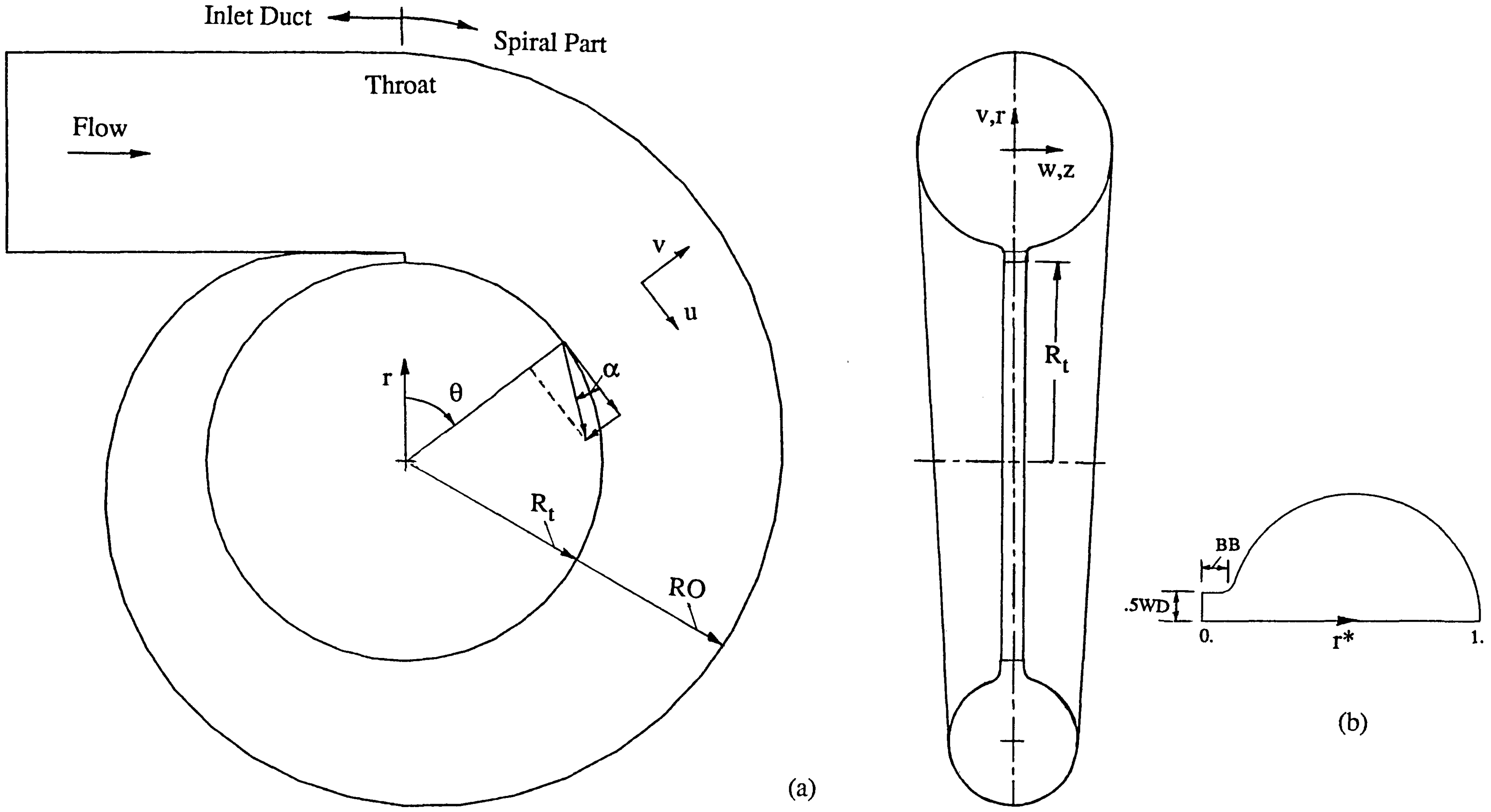

Fig. 6.10 Diagram of the symmetric, circular volute: Flow configuration and definition of coordinates

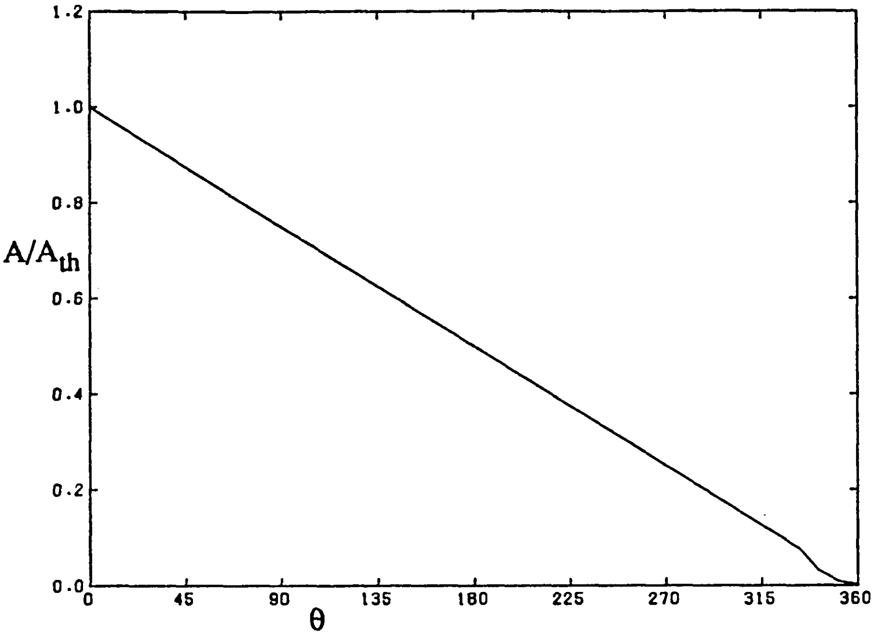

Fig. 6.11a Variation of cross-sectional area with azimuth angle

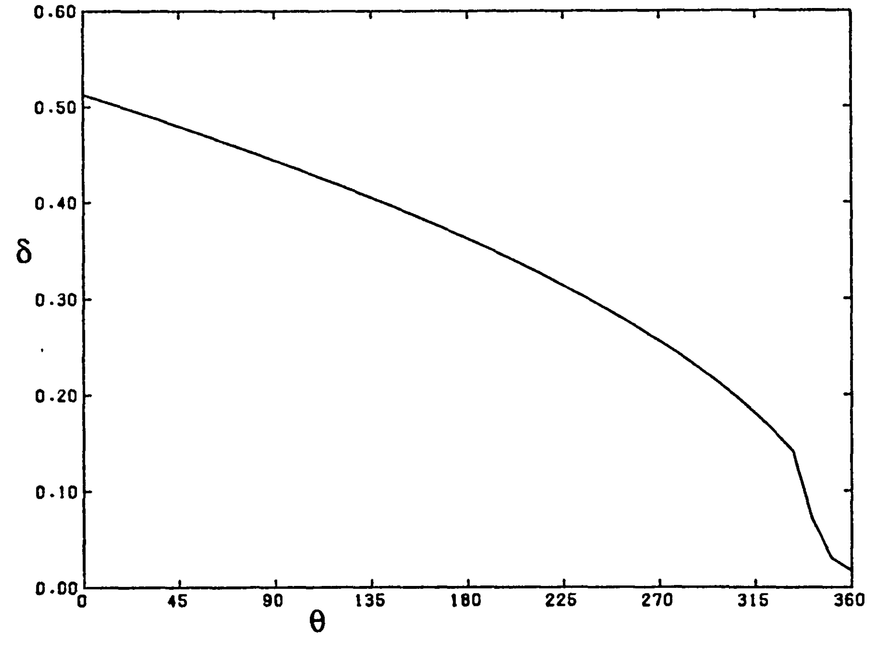

Fig. 6.11b Variation of radius-ratio with azimuth angle

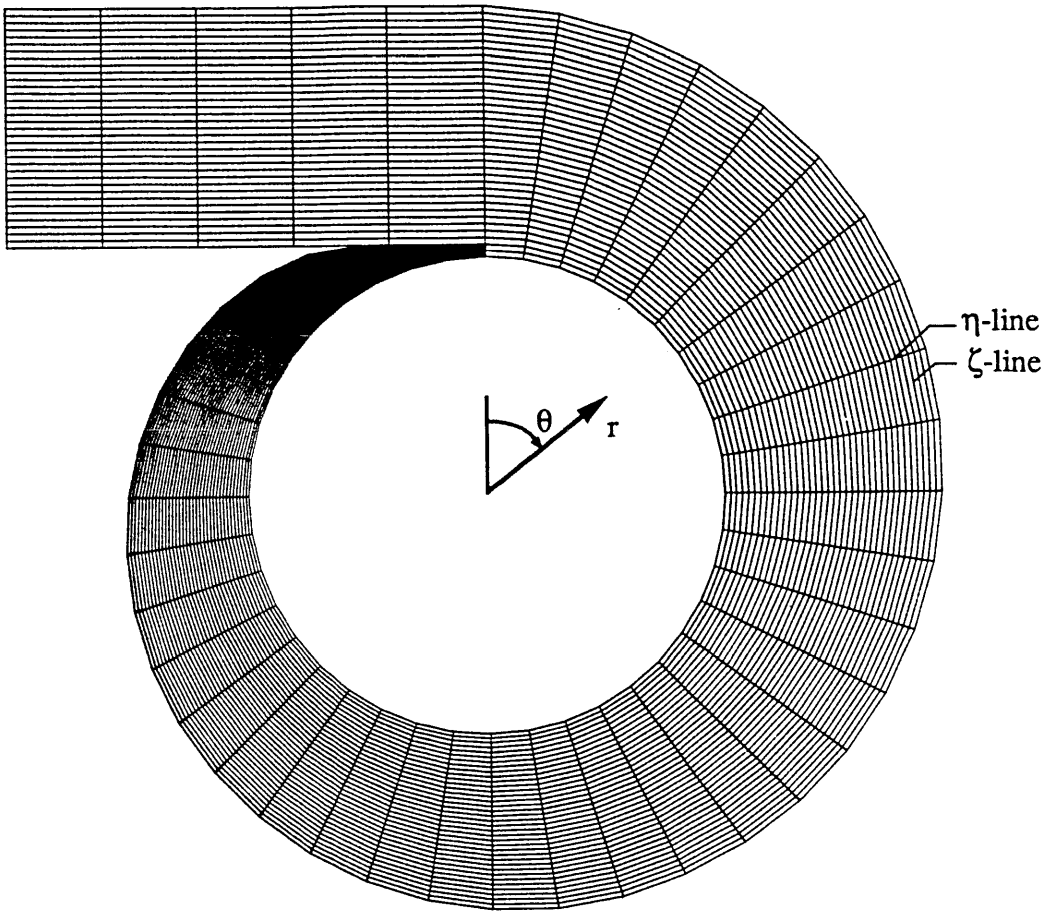

(a) Symmetry plane grids: 37x46 (η x ζ)

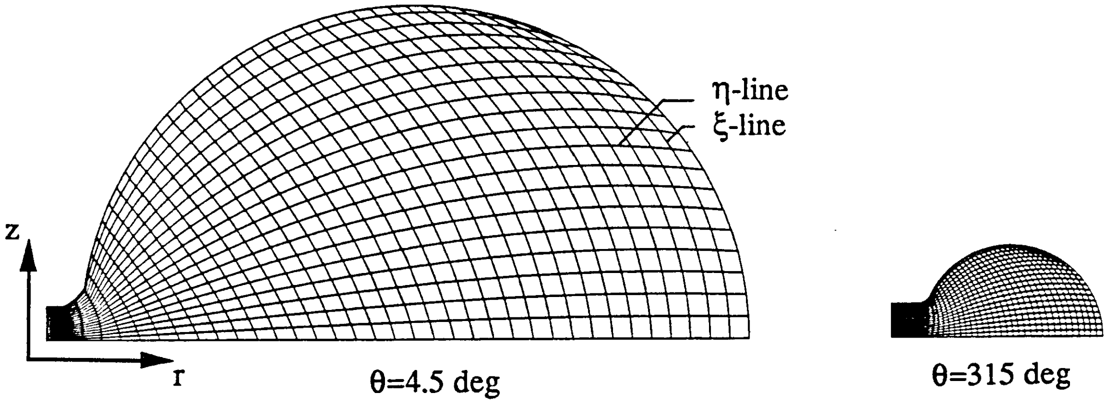

(b) Cross-sectional grids: 37x20 (η x ξ)

Fig. 6.12 Computational grids used for the symmetric, circular volute

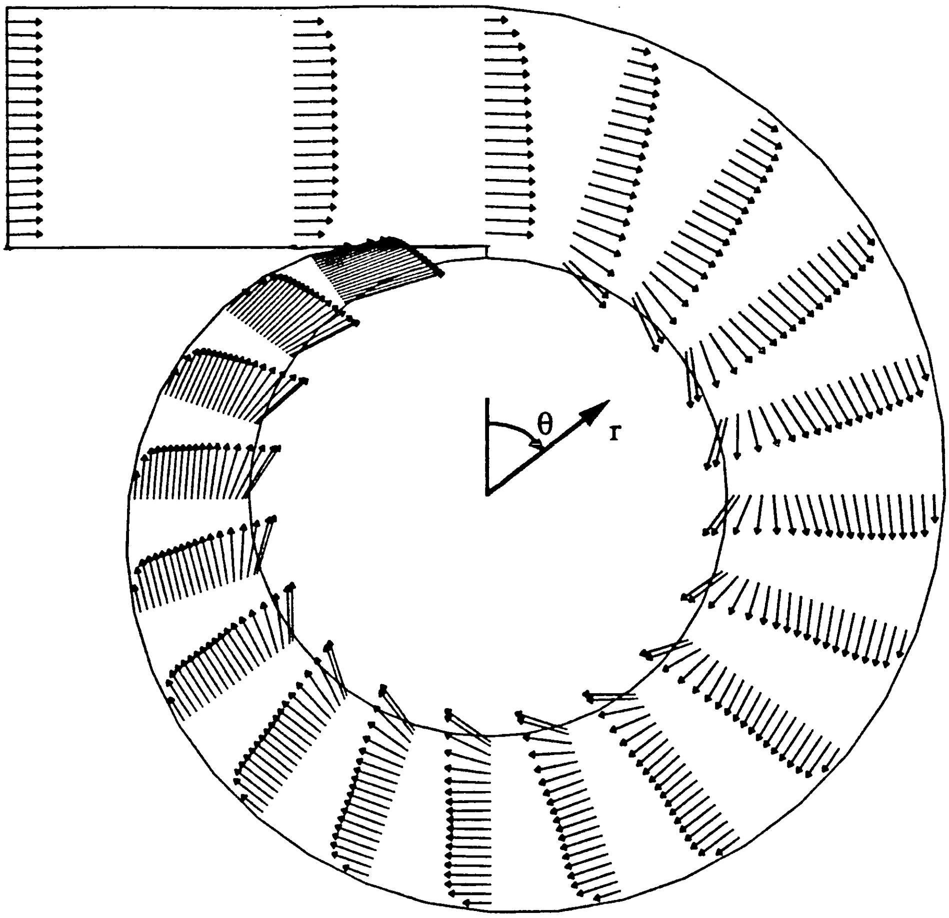

Fig. 6.13 Velocity vectors on the symmetry plane

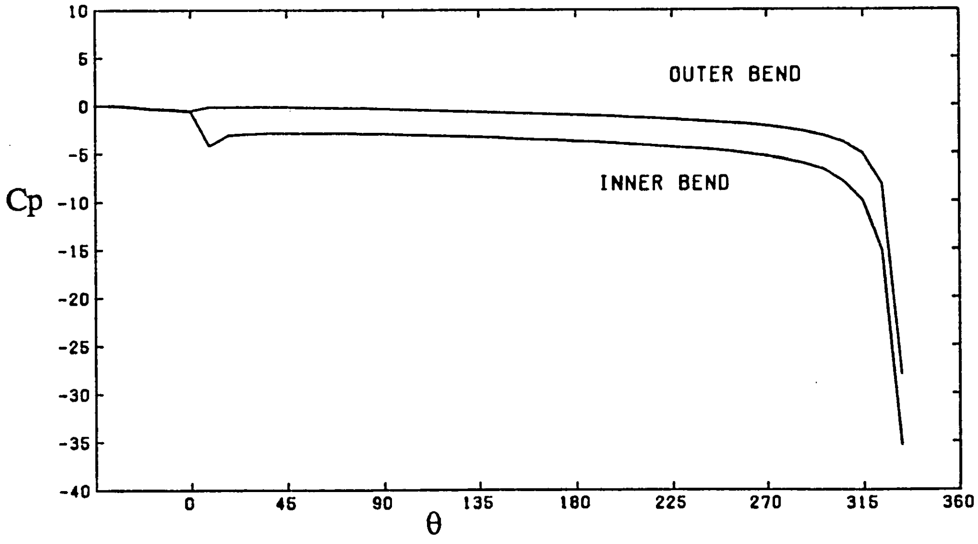

Fig. 6.14 Variation of pressure along the volute

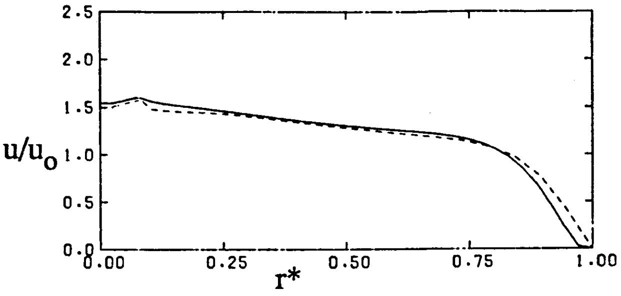

(a) θ=4.5 deg

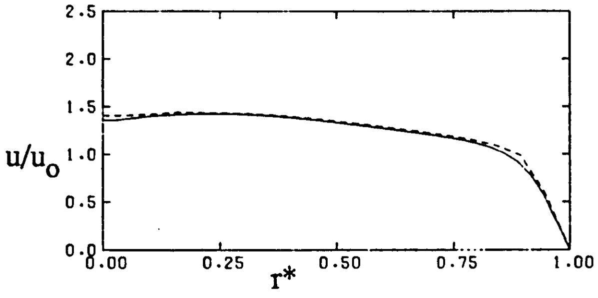

(b) θ=45 deg

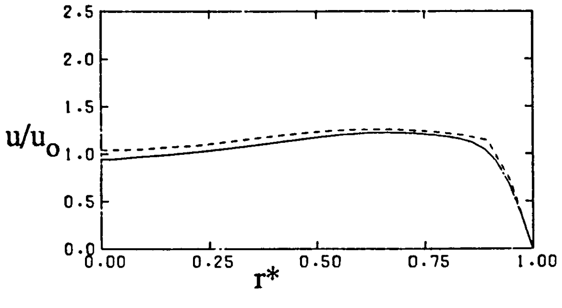

(c) θ=90 deg

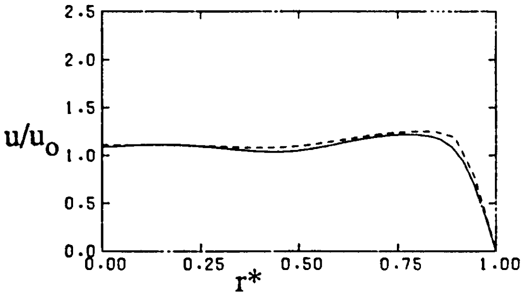

(d) θ=135 deg

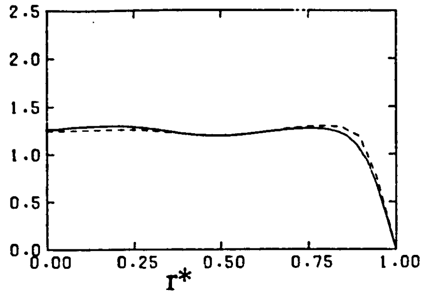

(e) θ=180 deg

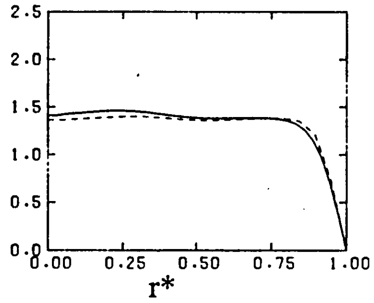

(f) θ=225 deg

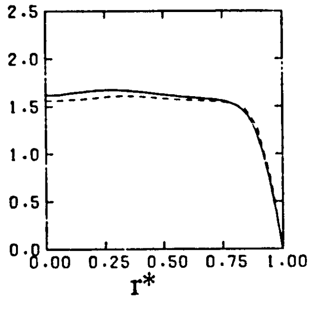

(g) θ=270 deg

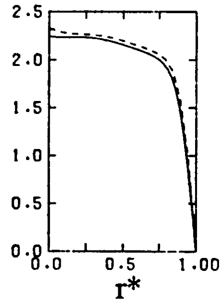

(h) θ=315 deg

Fig. 6.15 Velocity profiles in the symmetry plane at different azimuthal locations. Predictions: ------, 21x46x11 and ——, 37x46x20 grids.

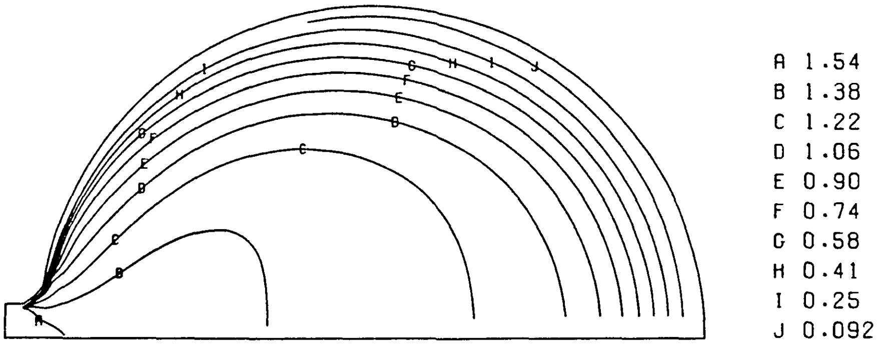

(a) θ=4.5 deg

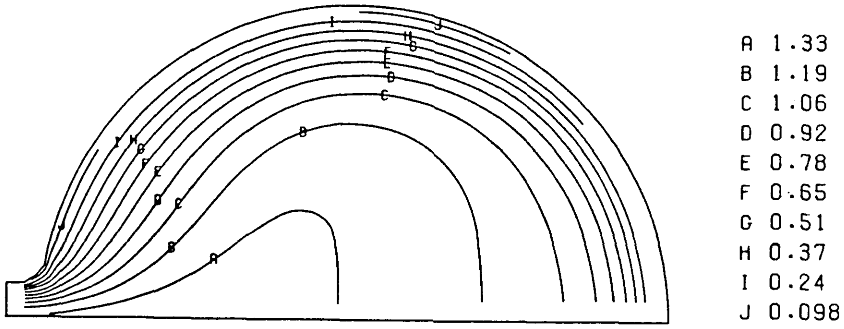

(b) θ=45 deg

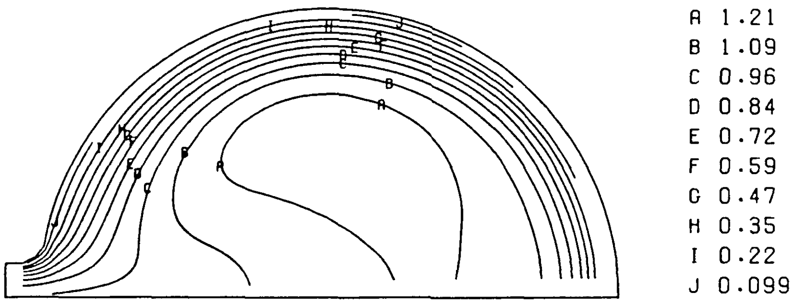

(c) θ=90 deg

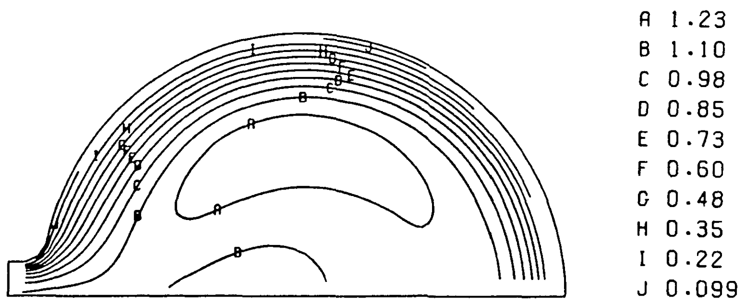

(d) θ=135 deg

Fig. 6.16 Development of streamwise velocity (u/u_0) along the volute

-- cont'd

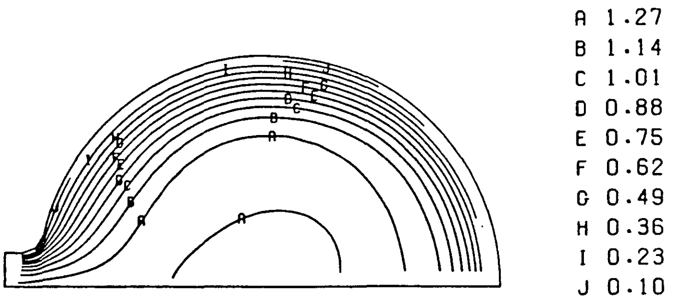

(e) θ=180 deg

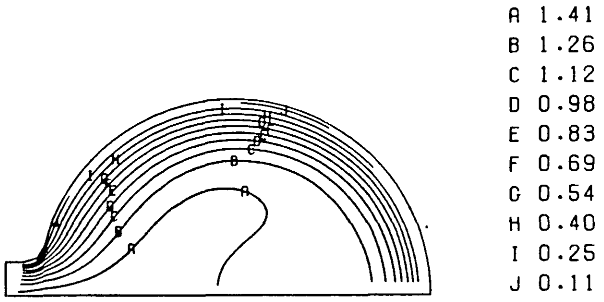

(f) θ=225 deg

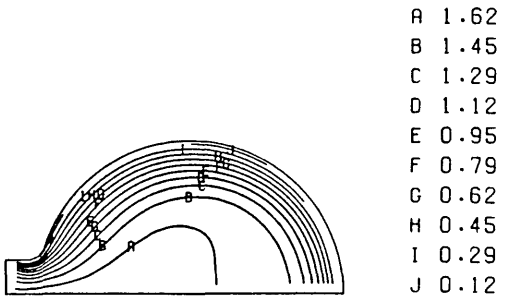

(g) θ=270 deg

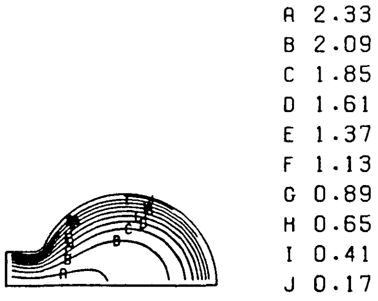

(h) θ=315 deg

Fig. 6.16 (cont'd) Development of streamwise velocity (u/u_0) along the volute

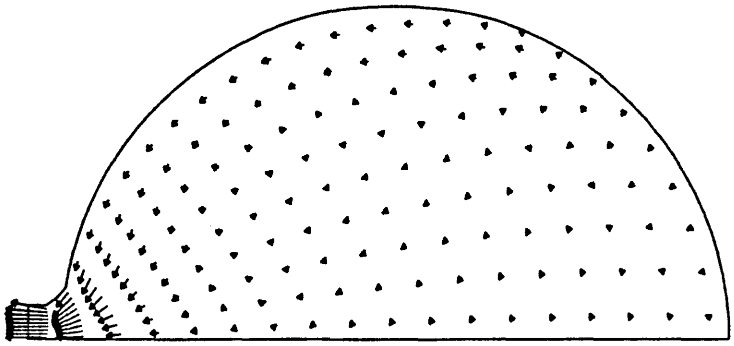

(a) θ=4.5 deg

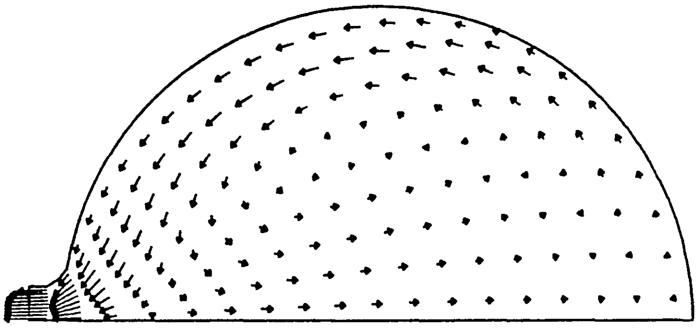

(b) θ=45 deg

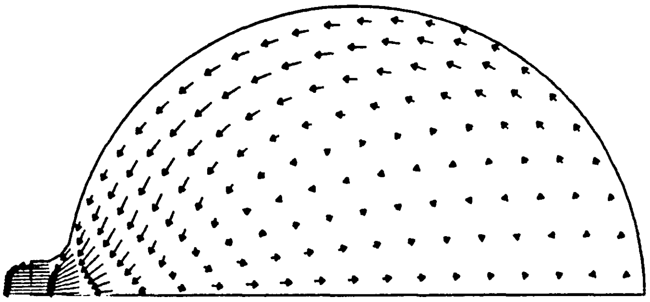

(c) θ=90 deg

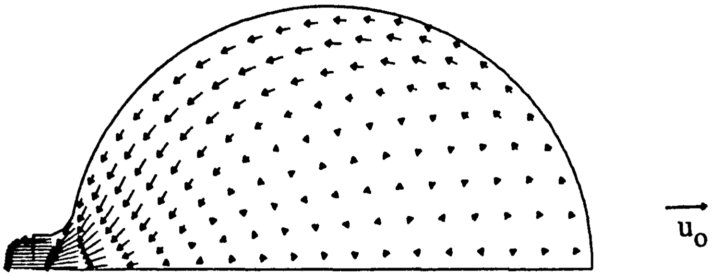

(d) θ=135 deg

Fig. 6.17 Development of secondary velocity along the volute
-- cont'd

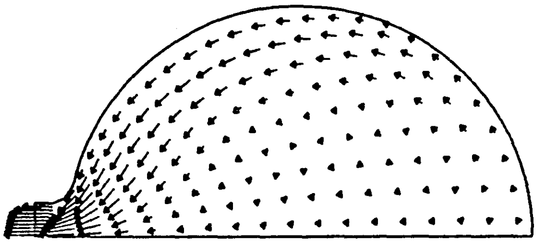

(e) θ=180 deg

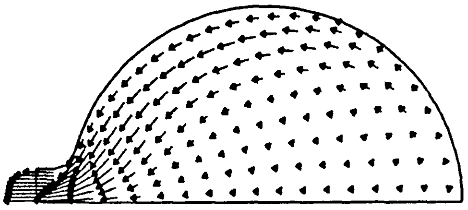

(f) θ=225 deg

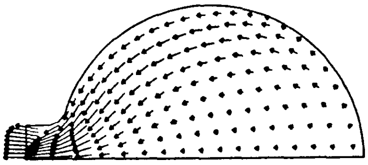

(g) θ=270 deg

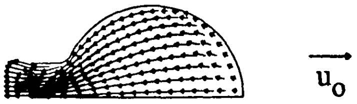

(h) θ=315 deg

Fig. 6.17 (cont'd) Development of secondary velocity along the volute

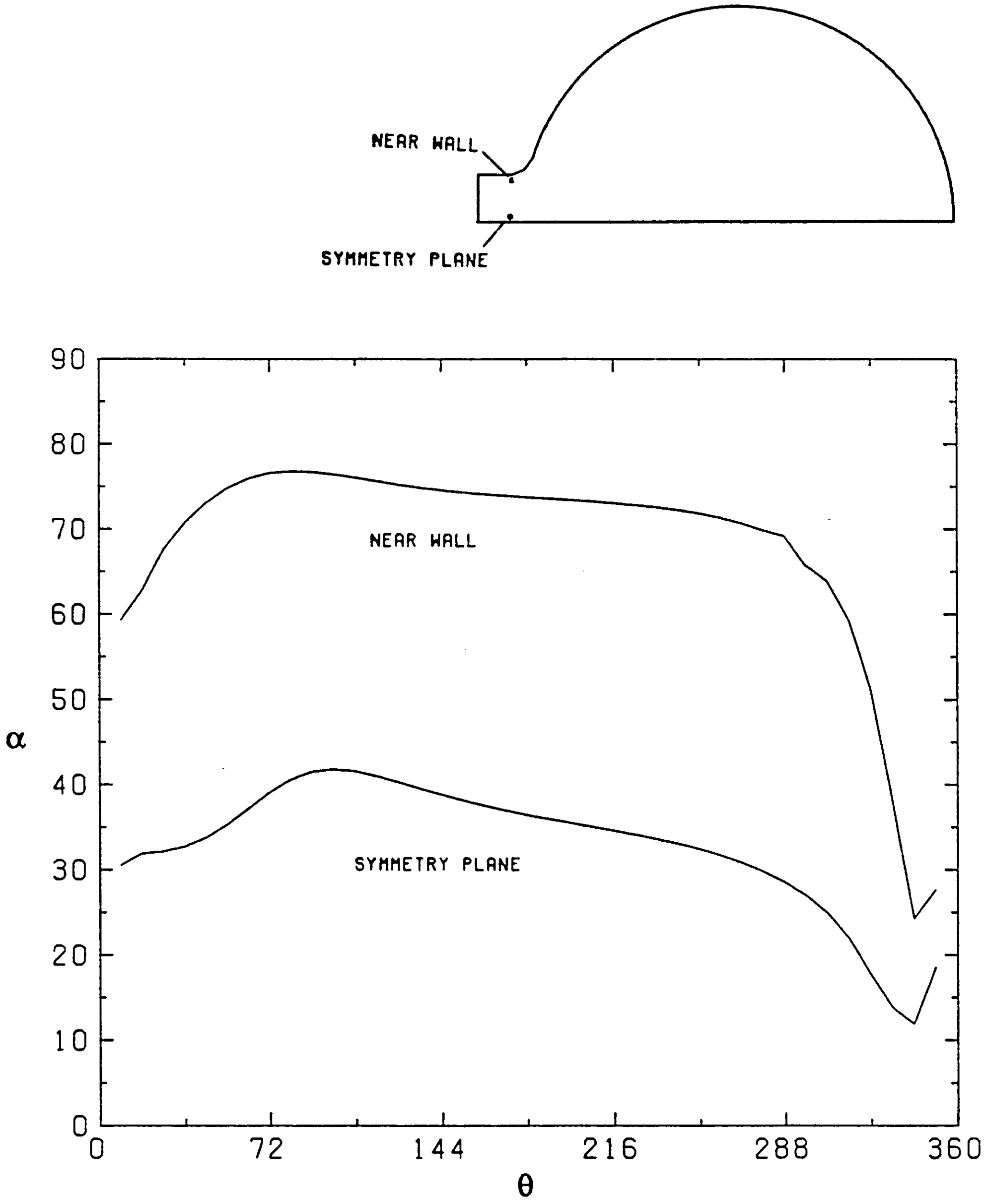

Fig. 6.18 Variation of flow angle in the azimuthal direction

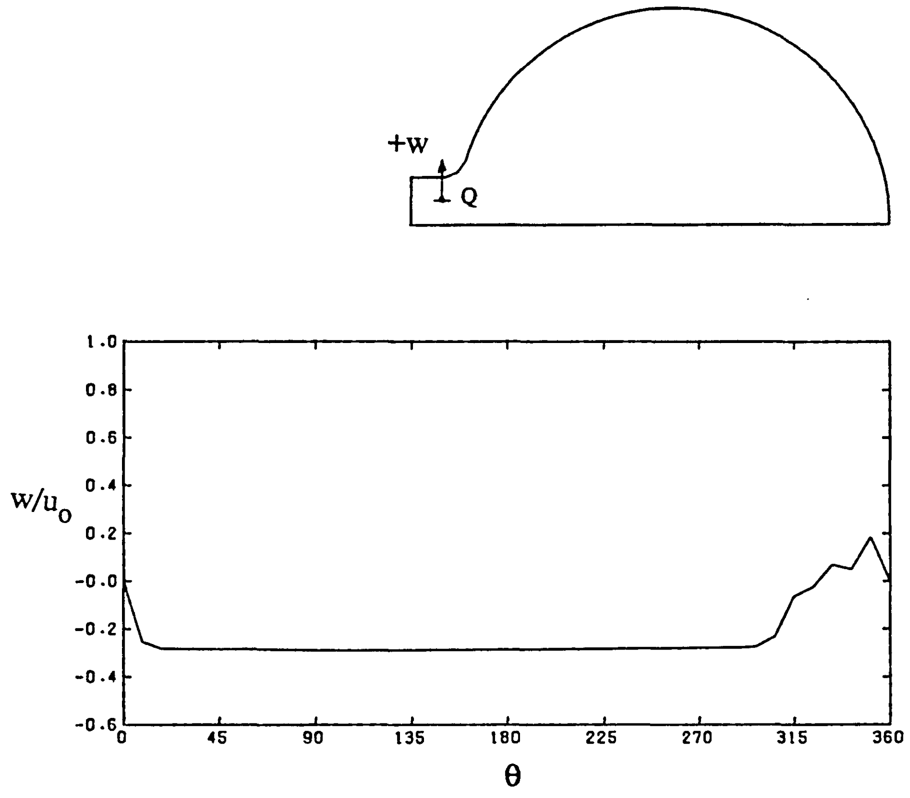

Fig. 6.19 Variation of axial velocity (w) at Q in the azimuthal direction

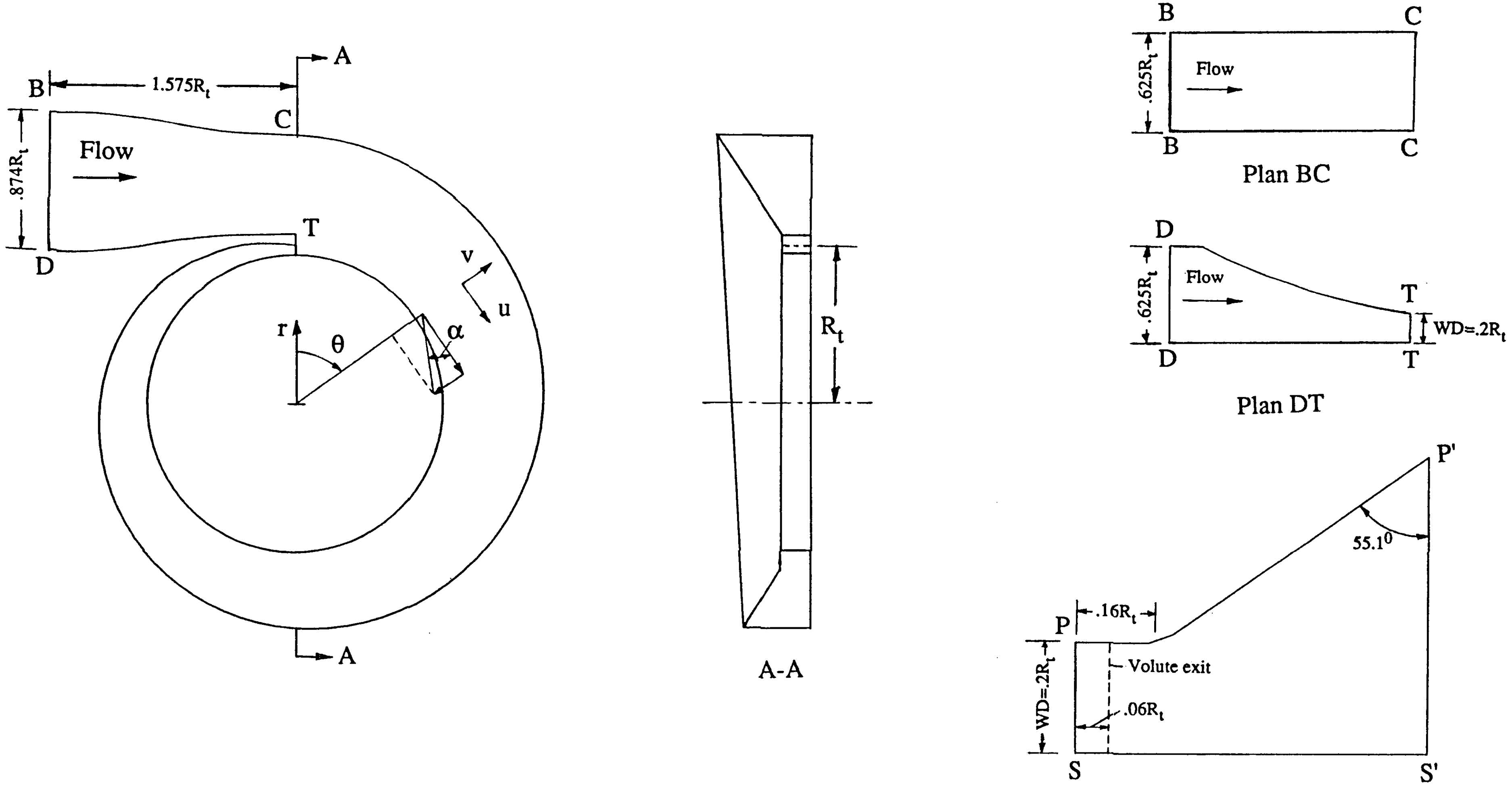

Fig. 6.20 Diagram of the non-symmetric, trapezoidal volute: Flow configuration and geometrical details

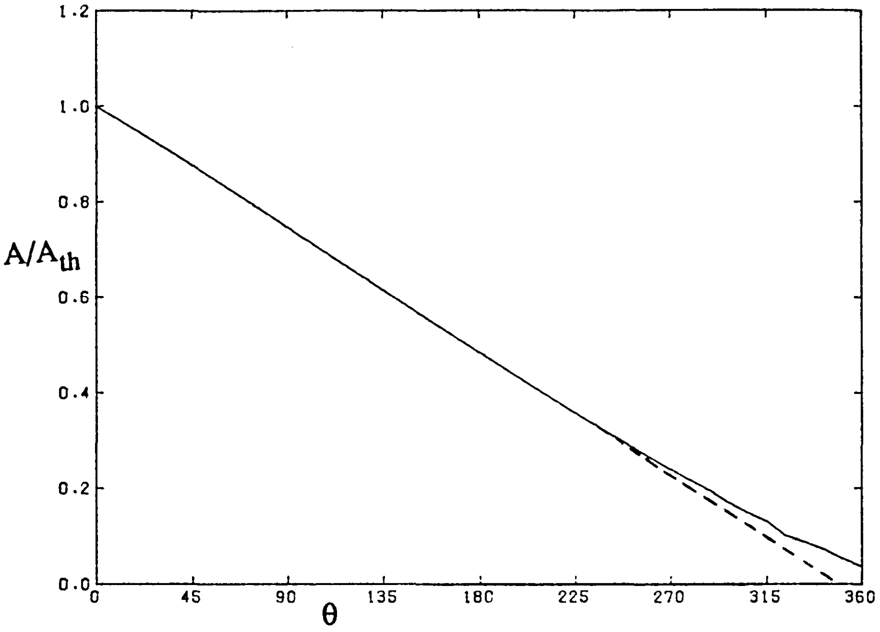

Fig. 6.21a Variation of cross-sectional area with azimuth angle (dashed line shows a linear variation)

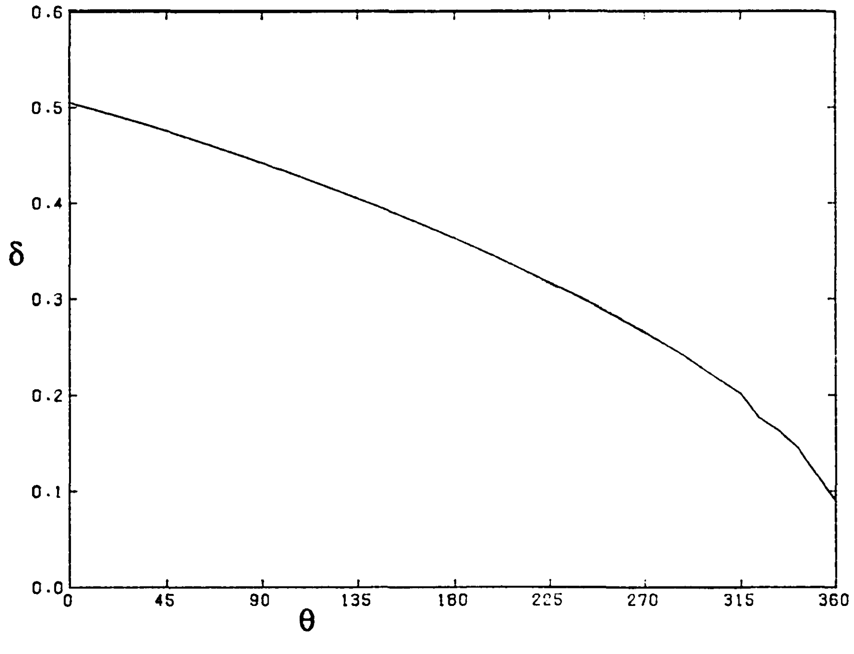

Fig. 6.21b Variation of radius-ratio with azimuth angle

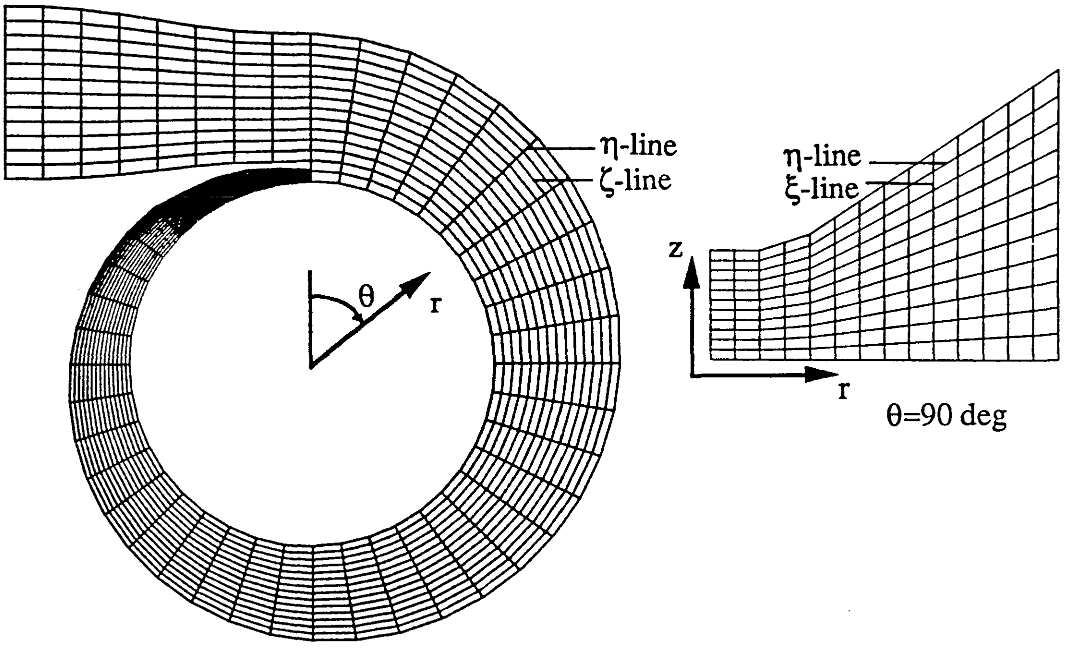

(a) 15x49x12 (η x ζ x ξ) grids

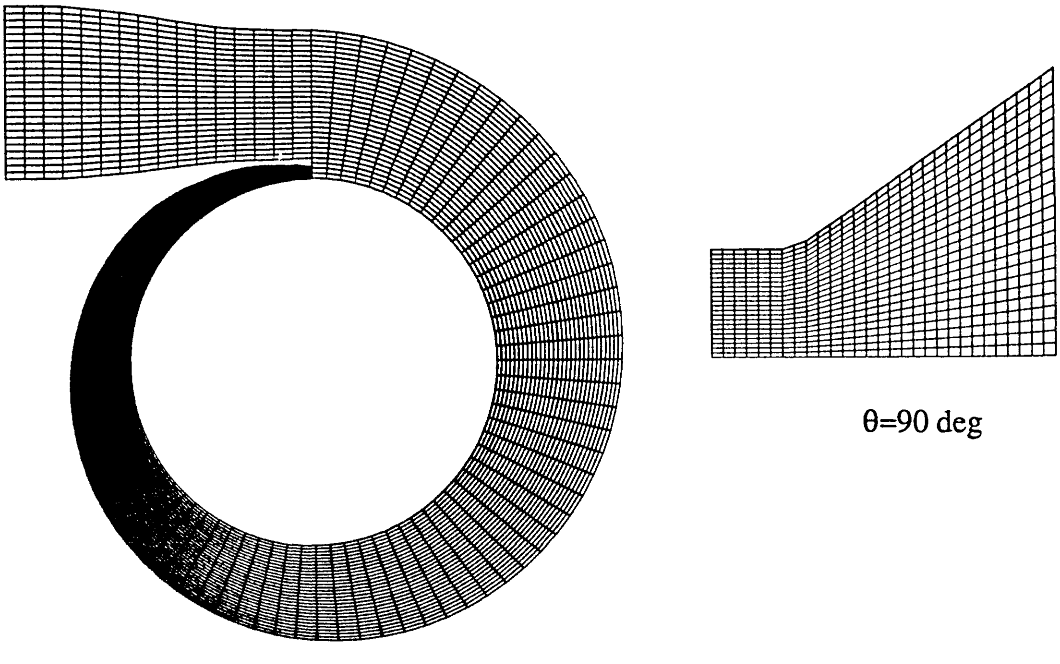

(b) 30x97x24 (η x ζ x ξ) grids

Fig. 6.22 Computational grids for the non-symmetric, trapezoidal volute

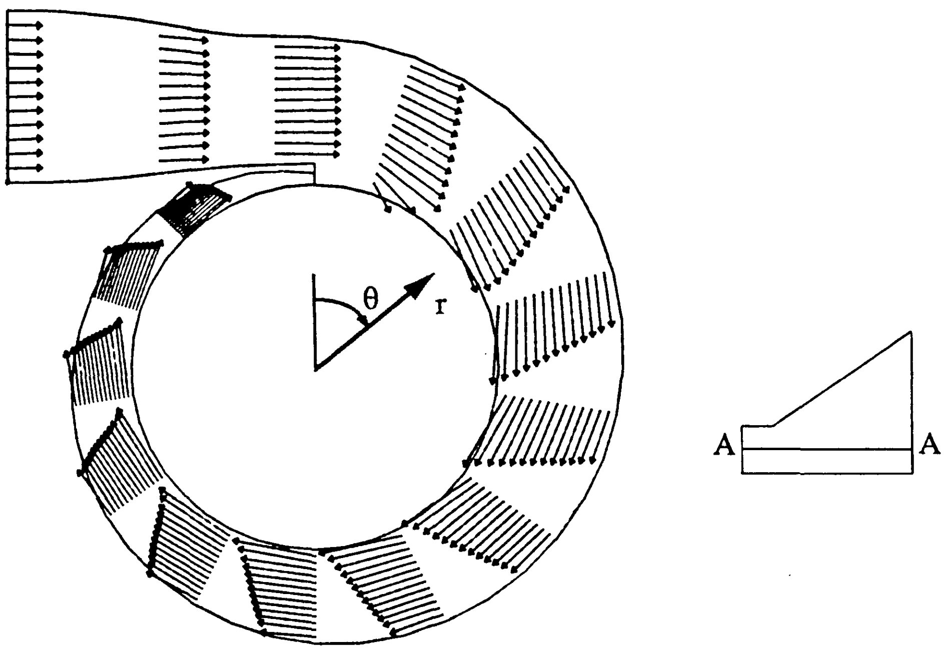

Fig. 6.23 Velocity vectors on plane A-A

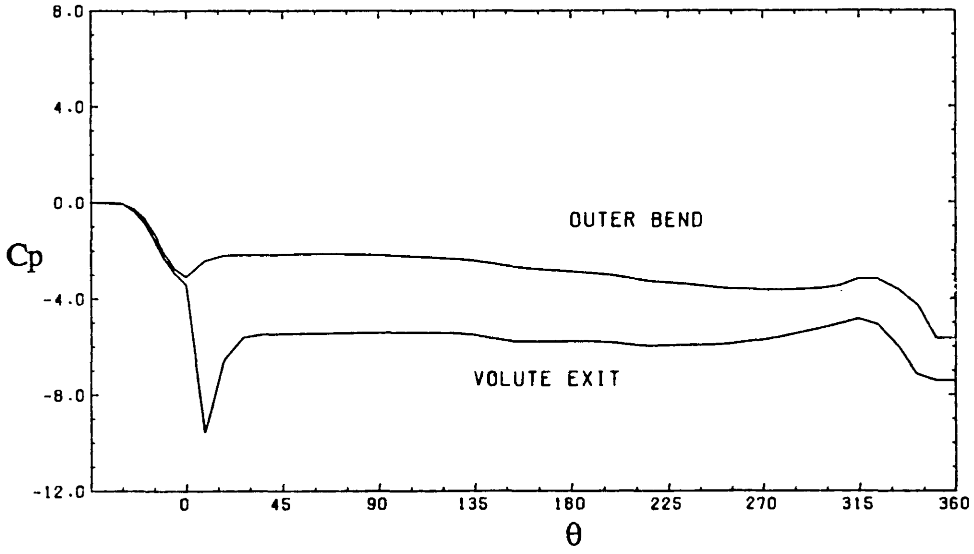

Fig. 6.24 Variation of static pressure in the azimuthal direction

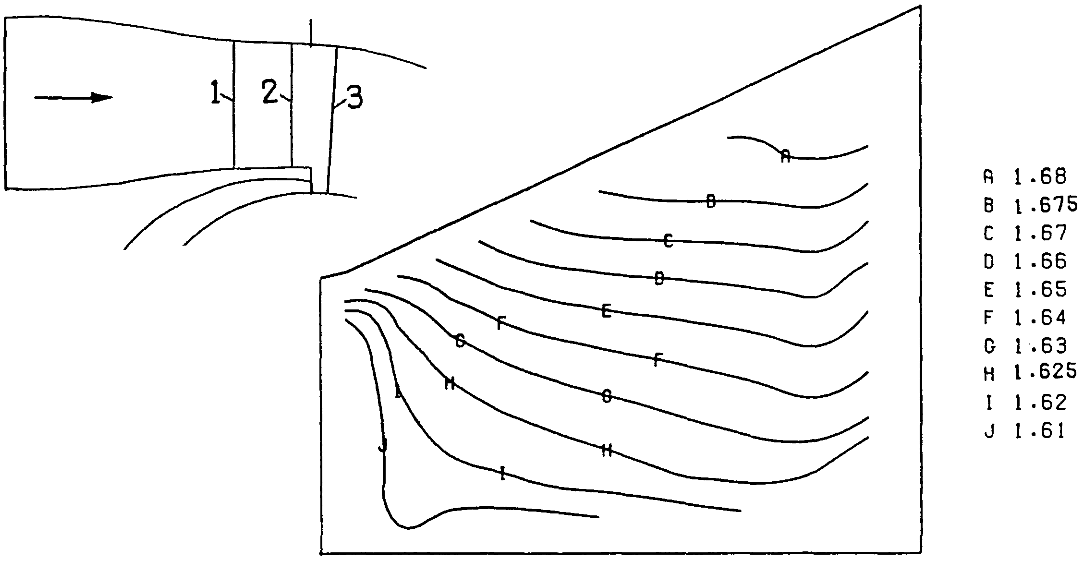

(a) Station 1

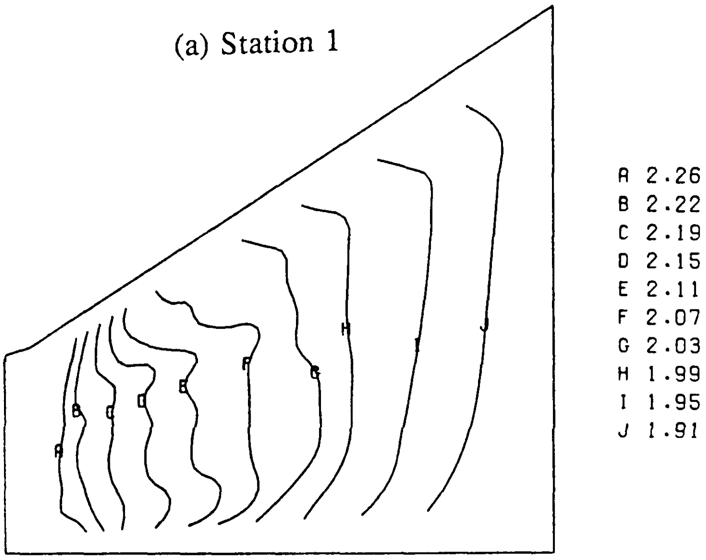

(b) Station 2

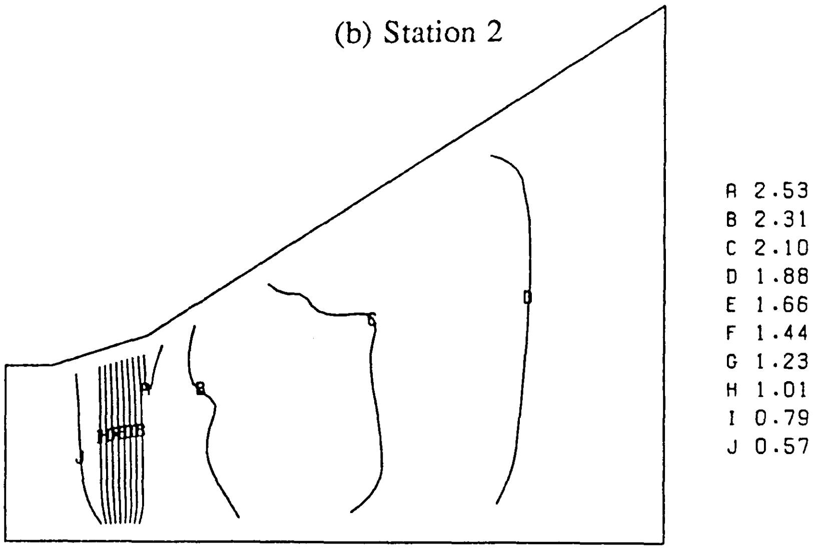

(c) Station 3, θ=4.5 deg

Fig. 6.25 Development of streamwise velocity (u/u_0) along the volute

-- cont'd

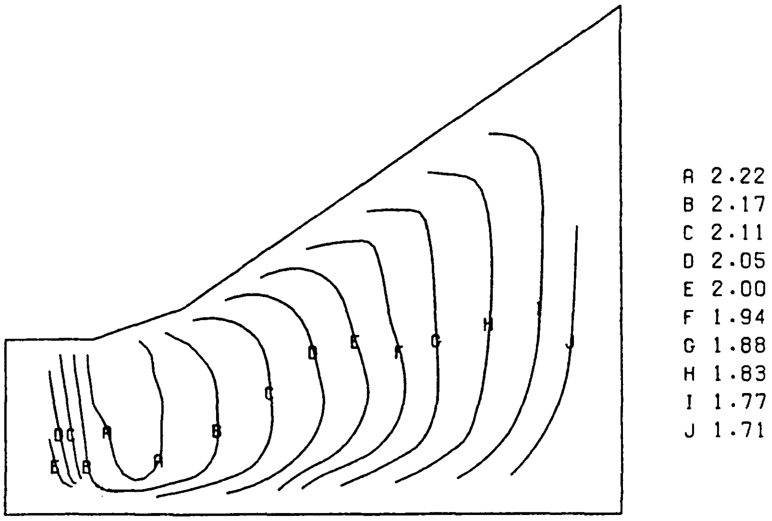

(d) θ=45 deg

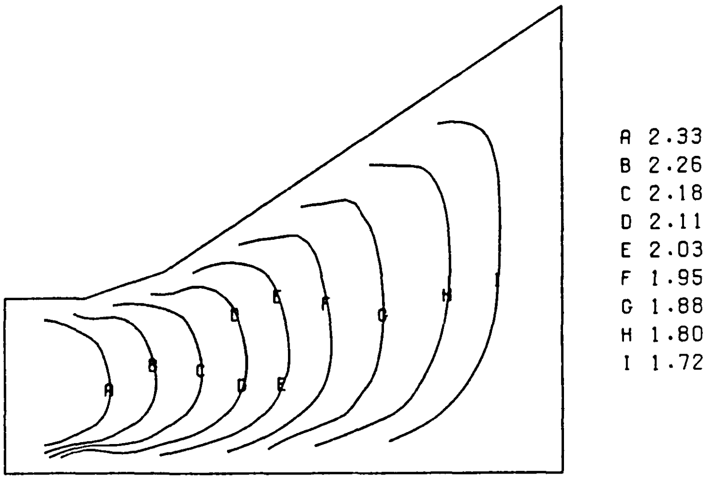

(e) θ=90 deg

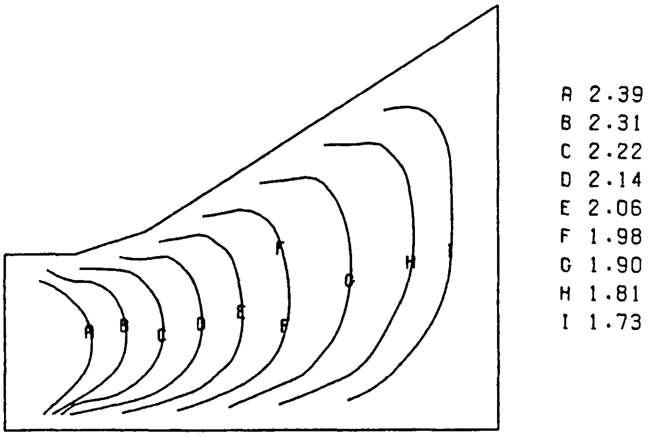

(f) θ=135 deg

Fig. 6.25 (cont'd) Development of streamwise velocity (u/u_0) along the volute

-- cont'd

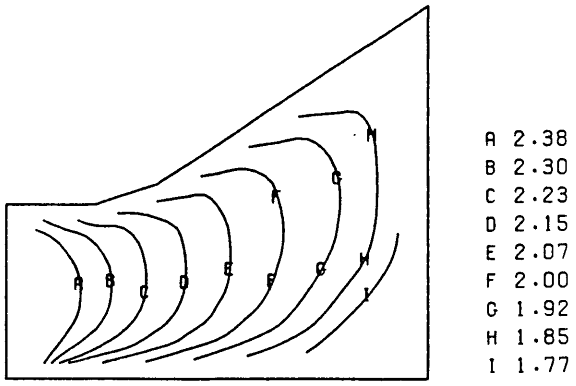

(g) θ=180 deg

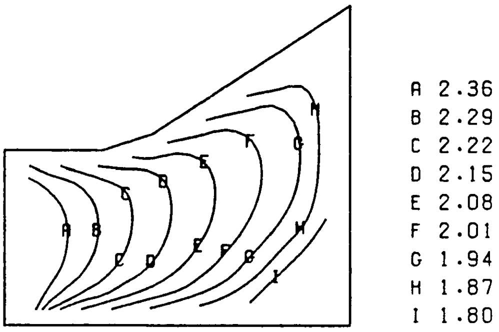

(h) θ=225 deg

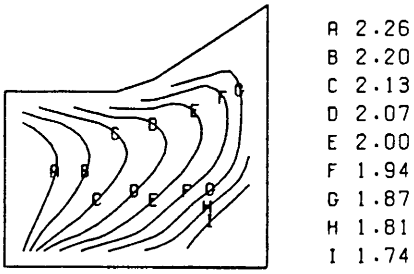

(i) θ=270 deg

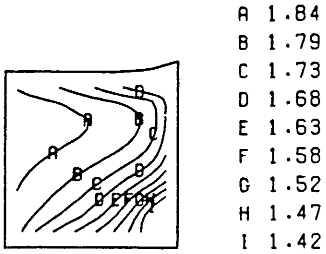

(j) θ=315 deg

Fig. 6.25 (cont'd) development of streamwise velocity (u/u_0) along the volute

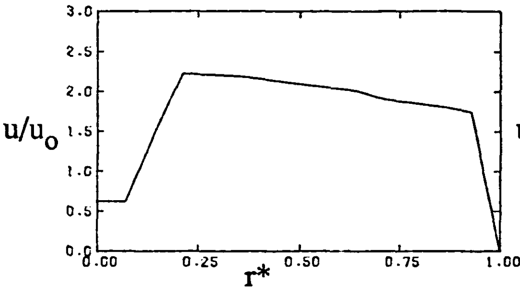

(a) θ=4.5 deg

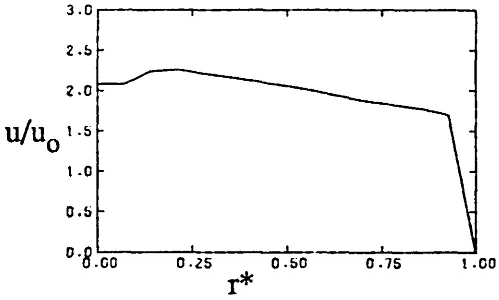

(b) θ=45 deg

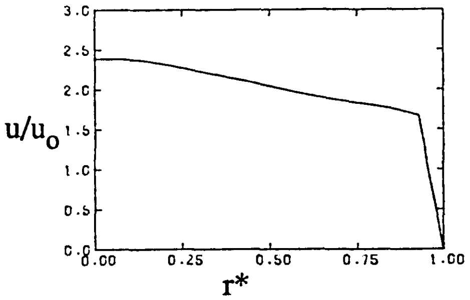

(c) θ=90 deg

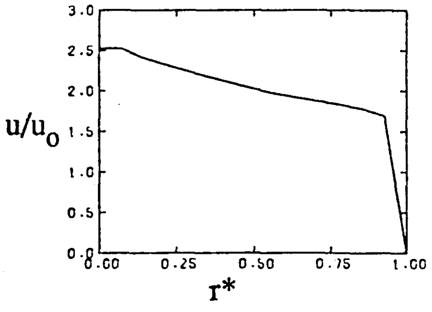

(d) θ=135 deg

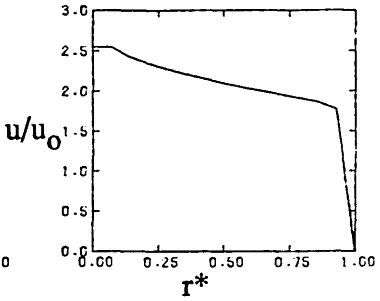

(e) θ=180 deg

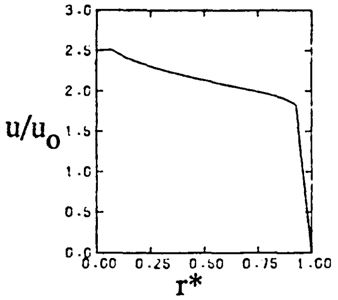

(f) θ=225 deg

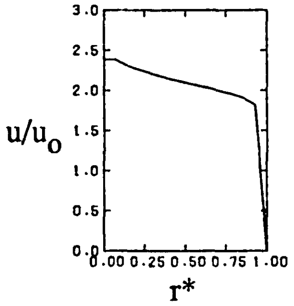

(g) θ=270 deg

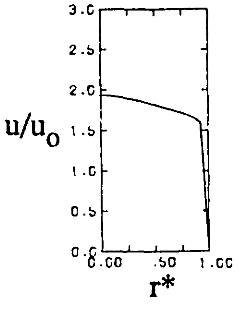

(h) θ=315 deg

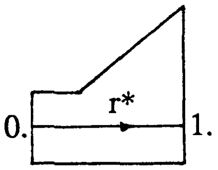

Fig. 6.26 Profiles of streamwise velocity (u/u_o) at different azimuthal locations on the plane r*

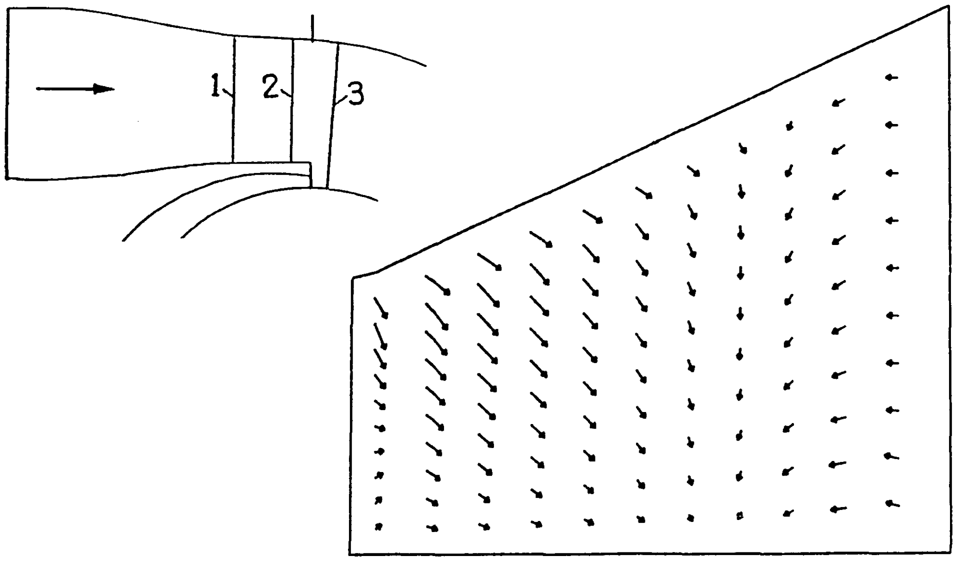

(a) Station 1

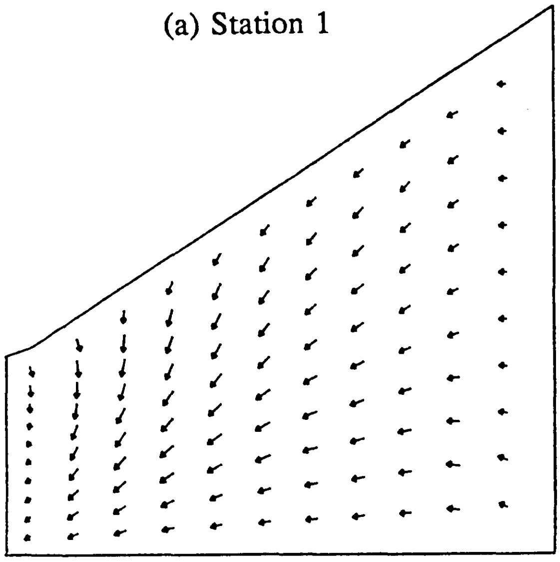

(b) Station 2

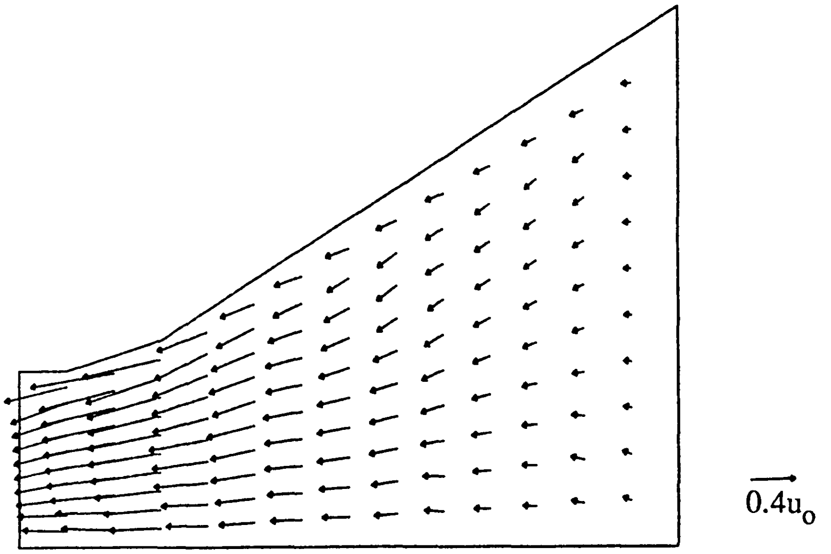

(c) Station 3, θ=4.5 deg

Fig. 6.27 Development of secondary velocity along the volute

-- cont'd

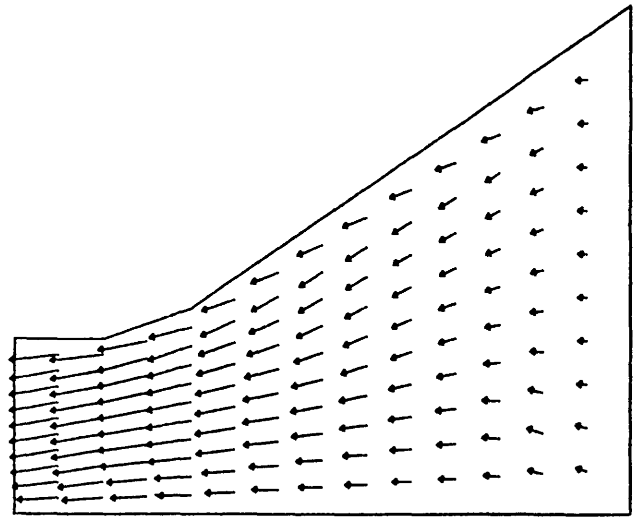

(d) θ=45 deg

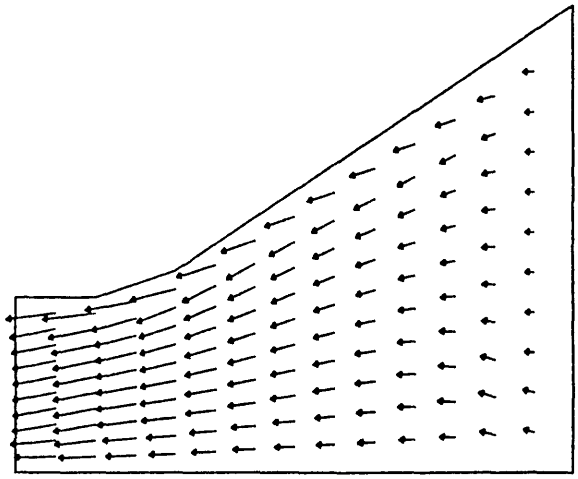

(e) θ=90 deg

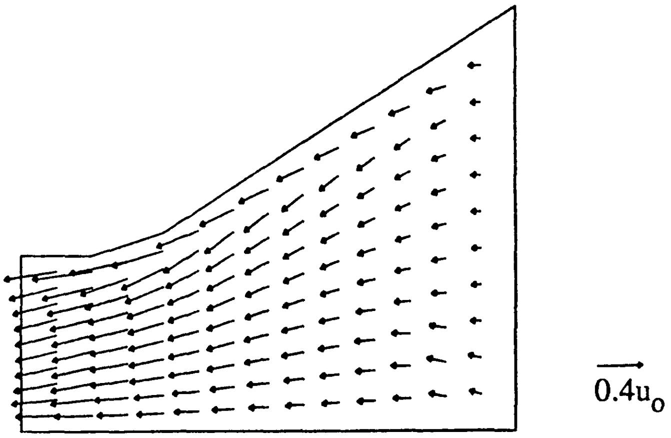

(f) θ=135 deg

Fig. 6.27 (cont'd) Development of secondary velocity along the volute

-- cont'd

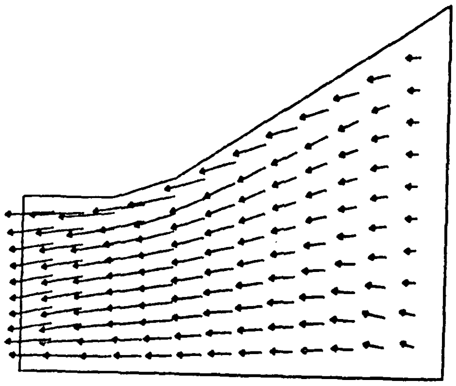

(g) θ=180 deg

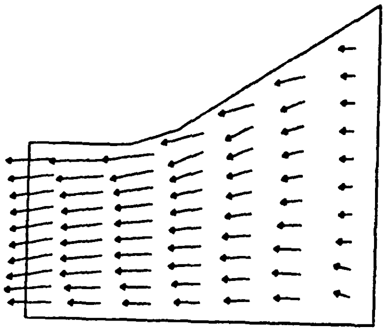

(h) θ=225 deg

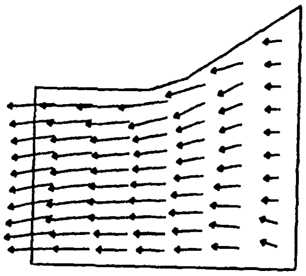

(i) θ=270 deg

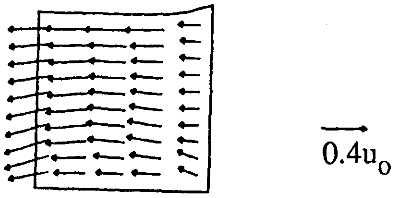

(j) θ=315 deg

Fig. 6.27 (cont'd) Development of secondary velocity along the volute

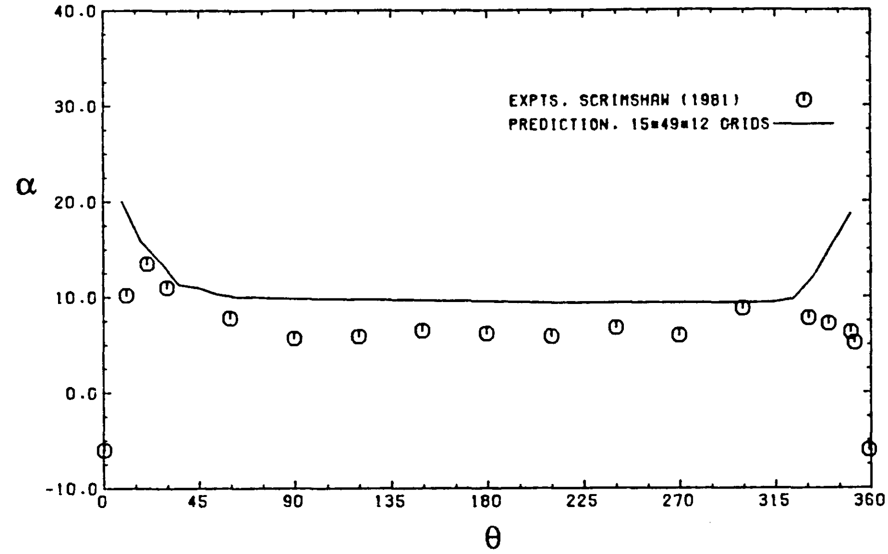

(a) Flow angle α at volute exit

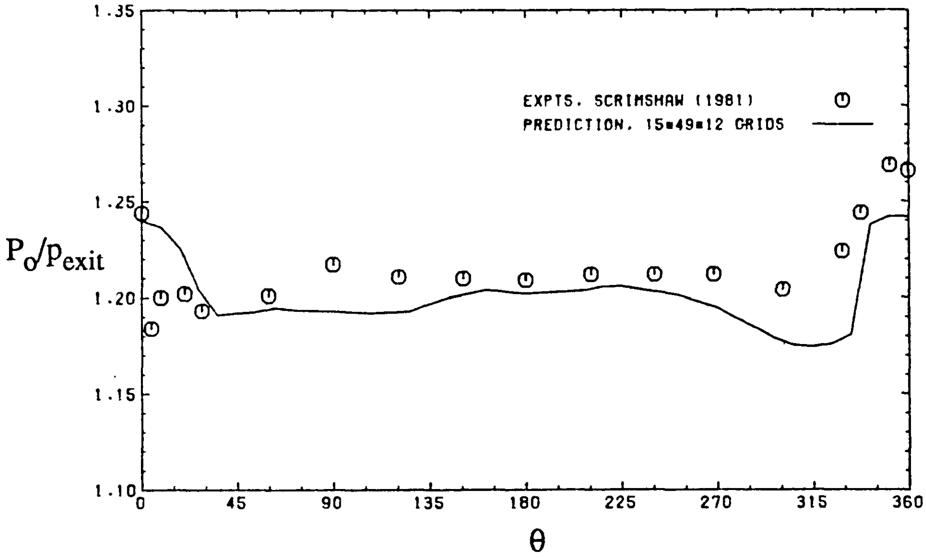

(b) Total/static pressure ratio

Fig. 6.28 Comparisons with experiment

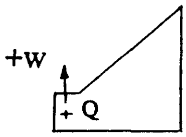

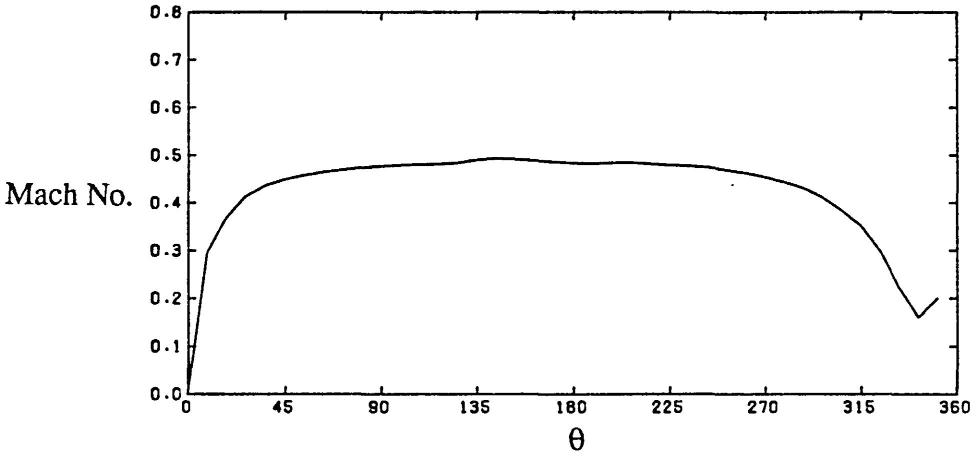

Fig. 6.29 Mach number at volute exit (Q)

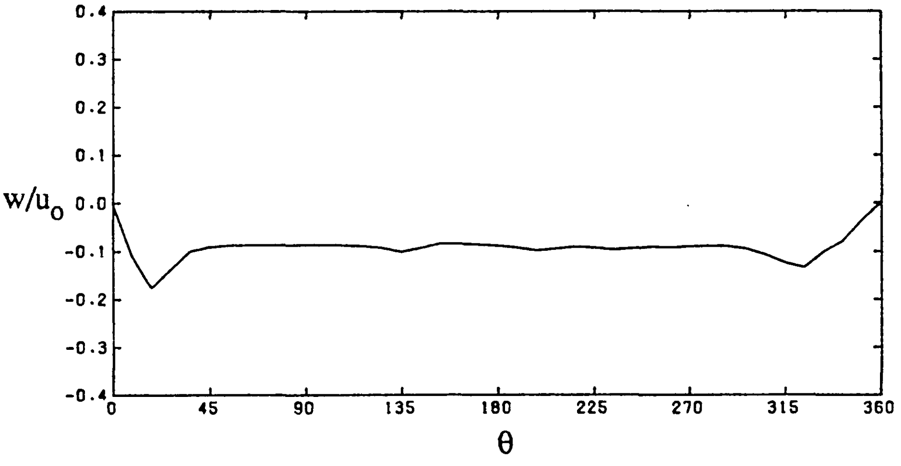

Fig. 6.30 Variation of axial velocity (w) at Q
in the azimuthal direction

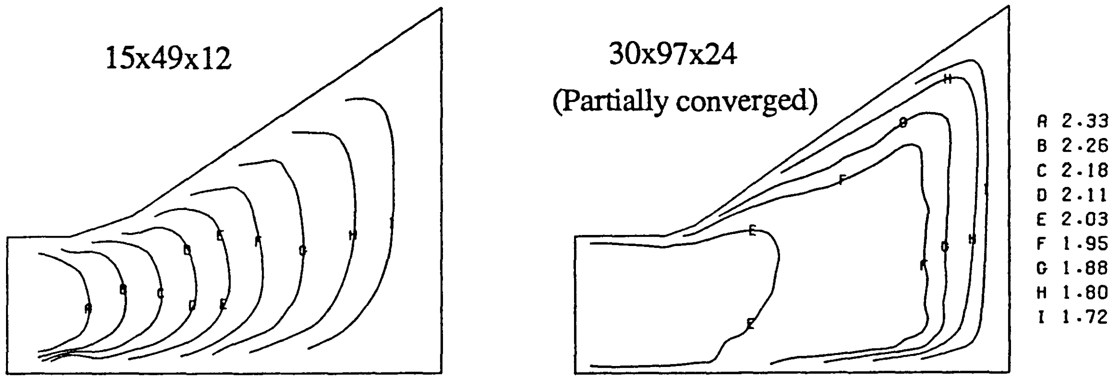

(a) u/u_0 contours at θ=90 deg

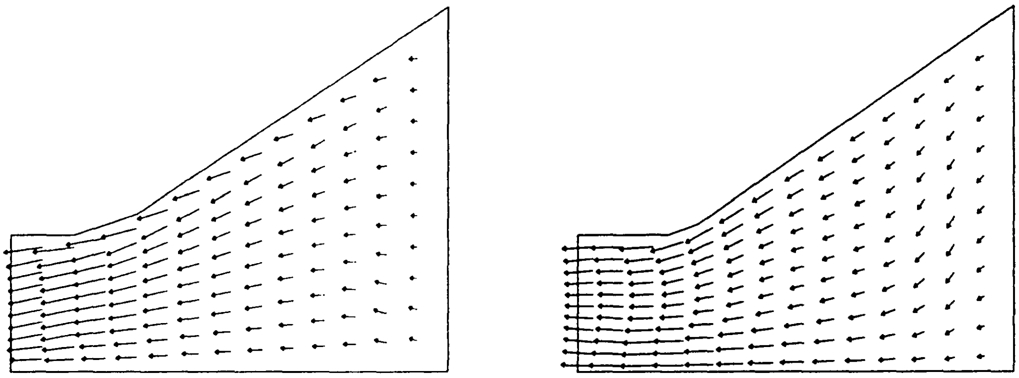

(b) Secondary velocity at θ=90 deg

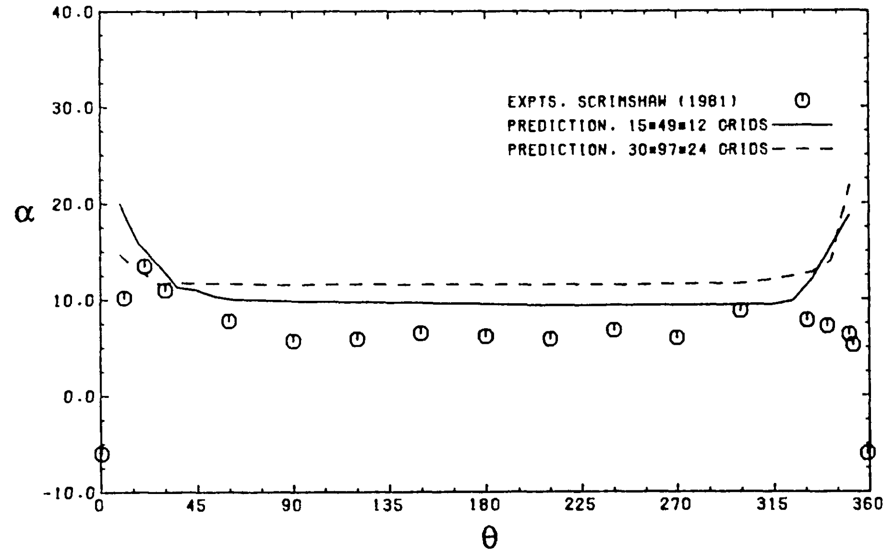

(c) Flow angle α at volute exit

Fig. 6.31 Comparison of results between coarse and fine grids

CHAPTER 7

CONCLUSIONS AND SUGGESTIONS FOR FUTURE WORK

In this chapter, a summary of what has been accomplished in the present work is highlighted. Some suggestions for future work in the light of the current study are also given in this chapter.

7.1 Summary of Achievements and Main Findings

The work presented in this thesis can be broadly divided into two parts; firstly, the development of a general computational procedure and its assessment and secondly, the study of flow in various types of curved geometries including nozzle-less, single-entry volute casings as found in typical automotive turbochargers. The achievements and findings are hence summarized under two headings.

Developed Numerical Procedure

Two different types of computer codes were developed for this study viz., one which employs the orthogonal toroidal mesh and uses grid-oriented velocity vectors and the other which employs non-orthogonal curvilinear mesh and uses fixed velocity vectors.

For both of the computer codes, the governing differential equations were derived from the general tensor form. A brief study (similar to those of Demirdzic, 1982 and Manners, 1988) has been conducted regarding the various forms of the governing transport equations and the relative merits and demerits of each other has been identified. This analysis stresses the fact that for general non-orthogonal curvilinear coordinates, a set of spatially invariant (Cartesian) base vectors will result in the simplest form of equations, but from the viewpoint of numerical solution of flow, it may suffer from decoupling problems especially when a staggered arrangement of flow variables are employed. For the study of once-curved ducts (the type of duct considered in this study), a cylindrical-polar frame of reference can very well solve this problem. By truncating some of the terms, the general equations can easily be converted into their Cartesian counterparts and in the general computational procedure (which is similar to that reported by Shyy et al, 1985), this has been done in switches by changing a control parameter. The advantage is that it can be easily used for other duct shapes such as S-diffuser or other irregular geometries found in aircraft intake systems.

The general computer code was subjected to rigorous testing by applying it to several flow situations and comparing the predicted results with analytical, numerical or experimental data of bench-mark accuracy. In general, reasonably good predictions were obtained for laminar flows which proved that the coding has been properly done. For turbulent flows, the predictions were not as good as those for laminar flows, the reasons for which are believed to be related to turbulence modelling and associated wall functions. For all cases, better results were obtained by refining the grids. The non-orthogonality of grid lines appeared to have no visible effect on the flow parameters apart from causing slower convergence rate.

Flow in Curved Ducts and Volute Casings

Based on the two most important geometrical characteristics of once-curved ducts viz., curvature and cross-section, three different types of curved ducts were identified. The programme of research was to study systematically the effects of curvature and cross-section on the flow development through various categories of ducts with the final objective of studying the flow through nozzle-less volute casings. As a result of this elaborate programme, it was possible to explain some features of the flow development inside volute casings from a more fundamental approach than has hitherto been reported.

The detailed study of laminar developing flow in constant curvature and constant cross-sectional ducts (circular and square) revealed the existence of strong secondary velocities over the cross-section which gave rise to typical helical vortices due to the superimposition of the through-flow. The intensity of these secondary velocities were found to be dominated more by curvature than by the flow rate. For the range of flow considered in this study, additional complexities in the secondary velocity structure were present at higher Dean numbers. This was evidenced by a tailed-vortex and a separation of secondary boundary layer near the inner bend. The development of streamwise velocity was found to be closely governed by the secondary velocity and hence confirms the strong coupling of the three velocity components for curved ducts. Several comparisons with experimental data and other numerical predictions for developing and fully-developed region supported the fact that the computational procedure (toroidal, grid-oriented velocity code) was robust enough to reveal most of the delicate features of such a flow.

By way of assessing the predictive ability of the general non-orthogonal computer code, the flow through constant curvature and constant/variable area ducts with upstream and downstream tangents were studied. It was observed that as the flow enters into the curved duct, it experiences a favourable pressure gradient on the inner bend and an adverse pressure gradient on the outer. At exit from the bend, opposite phenomena were observed. Further, it has been found that the removal of the radial pressure gradient in the downstream tangent is quickly reflected on the secondary velocity (more for laminar case than the corresponding turbulent flow) but the streamwise velocities were rather sluggish and hence the residual effects of secondary velocity can be seen.The secondary velocities for the 45-deg diffuser were found to be at least 10% less than that for the 90-deg bend at the same Dean number. For the case of the diffuser, the secondary boundary layer at the exit from the bend was found to separate near the inner bend of the cross-section.

Finally, flow through two volute casings were studied, one of which was compared with available experimental data. The effect of the discharge flow on flow development through a circular, symmetric volute was studied by comparing the results with a similar trumpet shaped duct at the same flow rate. The initial part of the volutes showed significant similarity with the curved duct flows considered in this study in terms of pressure gradient and secondary velocities, but at later part, the effect of the discharge flow was found to be more pronounced. For both the volutes, all three components of velocity were found to be significant near the volute exit. While the radial and streamwise components of velocity can affect the flow angle which is an important design parameter, the other component can also influence the proper running of the turbine. The strength and pattern of secondary flow are largely determined by the cross-sectional shape. The predicted results compared fairly well with experimental data and the reasons for the discrepancies were identified and discussed. The level of agreement suggests that the developed code can be used as a design tool for volute casings.

7.2 Suggestions for Future Work

During the course of discussion, several important points have emerged which need further consideration. This is true for both the numerical procedure as well as for modelling volute flows. For convenience of presentation, and also in line with the achievement summary, these are enumerated under two headings.

Numerical Procedure

i) For this study, only the hybrid differencing scheme has been used for approximation of convection terms. However it is known that for high flow rates, it switches to upwind differencing scheme which suffers from the problem of numerical diffusion. This has also been confirmed by the present work. So, higher order differencing schemes such as

QUICK or LUDS etc., need urgent attention for this methodology. This is particularly important for three dimensional flows, where improved accuracy by successive grid refinement is not always possible due to computer limitations.

ii) The grid generation techniques should also be improved. The transfinite mappings followed in this study was found to provide limited flexibility and the grid properties were very difficult to control in some regions of the flow domain. The use of more advanced procedures such as solution of Poisson's Equation with weighing functions may be used for better gridding of the domain.

iii) Application of other turbulence models and the treatment of the near wall region is also of critical importance for curved ducts. It may be mentioned here that the maximum discrepancies between prediction and experimental data were observed for the case of the turbulent flow through a 90-deg bend. Several turbulence models are available in literature but apart from the most widely used k-ε eddy-viscosity model, none of them was tried in the present work due to time limitation and the uncertainty associated with the fact that using a higher order turbulence model such as Reynolds Stress Model cannot guarantee better predictions. However, these aspects need thoughtful consideration especially with the increased complexity of the coordinate system used in this study.

Flow Through Volutes

There are several points which should be considered in future research on volute.

i) The treatment of the exit boundary is of utmost importance. Either a scroll-rotor system should be solved as a single unit or a boundary condition simulating a rotor should be implemented. The type of boundary condition reported in this thesis is a crude one although one reference could be found in literature which employed such a boundary treatment. By extending the volute cross-section towards the inside of the rotor, a 'fixed pressure' boundary condition may be tried. Again, since the experimental data are usually reported at the volute exit, the comparisons obtained by applying such a boundary condition is also subjected to criticism.

ii) It has been mentioned in Chapters 1 and 6 that the detailed information of flow inside the volutes are very rare. The quality of a prediction method for a highly complex flow configuration such as this cannot be conclusively judged if there is any uncertainty about the geometry. The compared results in this thesis are for flow parameters around the volute exit only and are typical of the data available in literature. Reliable experimental data especially the velocity components inside the volute cross-section along with inlet flow variables and detailed information about the geometry are of utmost necessity.

iii) The effect of compressibility should be included when simulating flows of practical interest. The present algorithm (SIMPLE) needs to be updated (Karki and Patankar, 1989) for the prediction of transonic flows which are common for turbocharger volutes. The fluid which flows through such volute is at a higher temperature and hence an energy equation may also be tried.

iv) The treatment of the tongue needs special consideration. This is possible by employing finer meshes near the tongue and allowing some sort of recirculating flow under it. The mixing of the two streams should be handled in a way such that the amount of flow recirculation becomes a predicted outcome.

v) Twin-entry volute casings are often used for turbochargers and the present methodology may be extended for simulation of flow through such volute casings. The wall separating the two sections of twin-entry volutes can be handled by blocking some of the computational nodes.

7.3 Final Remarks

The objectives of the present research work as mentioned in chapter 1 have been generally achieved. A numerical procedure was developed which can be used for successful prediction of flow in nozzle-less, single-entry volute casings as found in automotive turbochargers. This code is capable of handling flow through complex three-dimensional geometries of practical interest. Various minute details of flow development in once-curved ducts were revealed as a result of this work. Such details may be of importance to flow designers as well as can provide insights towards better understanding of complicated flows. However, there is considerable room for improvements and these are given as suggestions for future work.

REFERENCES

Adler V.M. (1934)
'Stromung in gekrummten Rohren', Z. Angew. Math. Mech., Vol. 14, p. 257.

Agrawal Y., Talbot L., Gong K. (1978)
'Laser anemometer study of flow development in curved circular pipes', J. Fluid Mech., Vol. 85, pp. 497-518.

Anderson B.H. (1988)
'CFD application to subsonic inlet airframe integration', von Karman Institute for Fluid Dynamics, Lecture Series 1988-04, Rhode Saint Genese, Belgium.

Aris R. (1962)
Vectors, Tensors and the Basic Equations of Fluid Mechanics, Prentice-Hall, Inc., Englewood Cliffs, N.J.

Austin L.R., Seader J.D. (1973)
'Fully developed viscous flow in coiled circular pipes', AIChE J., Vol. 19, p. 85.

Azzola J., Humphrey J.A.C., Iacovides H., Launder B.E. (1986)
'Developing turbulent flow in a U-bend of circular cross-section: Measurement and computation', J. Fluids Engg., Vol. 108, pp. 214-221.

Barnard M.C.S., Benson R.S. (1969)
'Radial gas turbines', Proc. I. Mech. E., Vol. 183, Pt.3N.

Barua S.N. (1963)
'On secondary flow in stationary curved pipes', Q. J. Mech. Appl. Maths., Vol. 16, p.61.

Baskharone E.A. (1984)
'Optimization of the three-dimensional flow path in the scroll-nozzle system of a radial inflow turbine', Tran. ASME, J. Engg. for Gas Turbines and Power, Vol.106, pp.511-515.

Berger S.A., Talbot L., Yao L.-S. (1983)
'Flow in curved pipes', Ann. Rev. Fluid Mechanics, Vol. 15, p. 461.

Bhinder F.S. (1970)
'Investigation of flow in the nozzle-less spiral casing of a radial inward-flow gas turbine', Proc. I. Mech. Engrs., Vol. 184, Pt.3G(II).

Bovendeerd P.H.M., van Steenhoven A.A., van de Vosse F.N., Vossers G. (1987)
'Steady entry flow in a curved pipe', J. Fluid Mechanics, Vol. 177, p. 233.

Braaten M.E., Shyy W. (1986)
'Three dimensional analysis of the flow in a curved hydraulic turbine draft tube', General Electric Company, Corporate Research and Development, Report No. 86CRDO37.

Chen S-R., Lee S.S., Huang Y.M. (1986)
'A mathematical model for the analysis of fluid flow in a scroll', Tran. ASME, J. Fluids Engg., Vol. 108, pp.6-11.

Cheng K.C., Lin R-C., Ou J-W. (1976)
'Fully developed laminar flow in curved rectangular channels', Trans. ASME, J. Fluids Engg., ser I, Vol. 98(1), p. 41.

Chorin A.J. (1967)
'A numerical method for solving incompressible viscous flow problems', J. Comp. Phys., Vol. 2, No.1, p. 12.

Collins W.M., Dennis S.C.R. (1975)
'The steady motion of a viscous fluid in a curved tube', Q. J. Mech. Appl. Maths., Vol. 28, p. 133.

Coupland J., Priddin C. (1986)
'Modelling the flow and combustion in a production gas turbine combustor', Turbulent Shear Flows, Vol. 5, Eds L Bradbury et al, Springer Verlag.

Dean W.R. (1927)
'Note on the motion of fluid in a curved pipe', Phil. Mag., Vol. 20, p. 208.

Demirdzic I. A. (1982)
A finite volume method for computation of fluid flow in complex geometries, PhD Thesis, University of London.

Denton J.D. (1975)
'A time marching method for two- and three-dimensional blade to blade flow', ARC R.&M. No. 3775.

Ellison L.F., Partridge J.M. (1978)
'Vane vibration in radial flow turbochargers', I. Mech. Engrs., c 76/78.

Enayet M.M., Gibson M.M., Taylor A.M.K.P., Yianneskis M. (1982)
'Laser doppler measurements of laminar and turbulent flow in a pipe bend', NASA Report, CR3551.

Ghia K.N., Ghia U. (1983)
'Advances in grid generation', ASME conference on Appl. Mech. Bio-Engg. and Fluids Engg., FED-5.

Gibson M.M., Jones W.P., McGuirk J.J., Whitelaw J.H. (1988)
'Lectures on turbulence models for Computational Fluid Dynamics', Department of Mechanical Engineering, Imperial College, London.

Gosman A.D., Ideriah F.J.K. (1976)
'TEACH-T : A general computer program for two-dimensional, turbulent, recirculating flows', Fluids Section, Department of Mechanical Engineering, Imperial College, London.

Gosman A.D., Pun W.M., Runchal A.K., Spalding D.B., Wolfstein M. (1969)
Heat and Mass Transfer in Recirculating Flows, Academic Press, London.

Greenspan A. D. (1973)
'Secondary flow in a curved tube', J. Fluid Mechanics, Vol. 57, p. 167.

Gubarev A.V., Fillipov G.A. (1961)
'Bladeless guide vane for centripetal turbines', British Library Translation Ref: AD600 TT-11698 (64-141).

Hamed A., Baskharone E. (1980)
'Analysis of three dimensional flow in a turbine scroll', Tran. ASME, J. Fluids Engg., Vol. 102, pp.297-301.

Hamed A., Baskharone E., Tabakoff W. (1978)
'A flow study in radial inflow turbine scroll-nozzle assembly', Tran. ASME, J. Fluids Engg., Vol. 100, pp.31-36.

Humphrey J.A.C., Iacivides H., Launder B.E. (1985)
'Some numerical experiments on developing laminar flow in circular sectioned bends', J. Fluid Mechanics, Vol. 154, p. 357.

Hussain M. (1982)
Investigation of flow in the nozzle-less volute casing of a centripetal gas turbine, PhD thesis, The Hatfield Polytechnique, School of Engineering, Division of Mechanical & Aeronautical Engineering, U.K.

Iacovides H., Launder B.E. (1984)
'The computation of momentum and heat transport in turbulent flow around pipe bends', Proc. 1st UK National Heat Transfer Conference, Vol. 2, 1097, I. Chem. Engrs. Symposium Series 86.

Ito H. (1959)
'Friction factors for turbulent flows in curved pipes', ASME Trans., J. Basic Engg., Vol. 81D, No.2, p. 123.

Ito H. (1969)
'Laminar flow in a curved pipe', Z. Angew. Math. Mech., Vol. 49, p. 653.

Jones W.P., Launder B.E. (1972)
'The prediction of laminarisation with a two-equation model of turbulence', Int. J. Heat and Mass Transfer, Vol. 15, p.301.

Karki K.C., Patankar S.V. (1989)
'Pressure based calculation procedure for viscous flows at all speeds in arbitrary configurations', AIAA Journal, Vol. 27, No.9, pp.1167-1174.

Kastner L.J., Bhinder F.S. (1975)
'A method for predicting the performance of a centripetal gas turbine fitted with a nozzle-less volute casing', ASME Paper No.75-GT-65.

Khalil I.M., Weber H.G. (1984)
'Modelling of three dimensional flow in turning channels', Trans. ASME, J. Engg. Gas Turbine & Power, Vol. 106, No. 3, p. 682.

Koutmos S.P., McGuirk J.J. (1983)
'Numerical calculation of the flow in annular combustor dump diffuser geometries', Fluids Section Report, FS/83/36, Mech. Engg. Dept., Imperial College, London.

Koutmos S.P., McGuirk J.J., Priddin C.H., Sodha M.N. (1990)
'Numerical investigation of the flow within a turbofan lobed mixer', to appear in AIAA, J. Propulsion and Power.

Lai K.Y.M. (1982)
Numerical analysis of fluid transport phenomena, PhD Thesis, University of London.

Laufer J. (1954)
'The structure of turbulence in fully developed pipe flow', NACA Rep.1174.

Launder B.E., Spalding D.B. (1974)
'The numerical computation of turbulent flows', Comp. Meth. Appl. Mech. and Engg., Vol. 3, p. 269.

Leonard B.P. (1979)
'A stable and accurate convective modelling procedure based on quadratic upstream interpolation', Comp. Meth. Appl. Mech. Engg., Vol. 19, pp.59-98.

Lymberopolous N. (1987)
Flow in single and twin-entry radial turbocharger turbine volutes, PhD Thesis, University of London.

Malak M.F., Hamed A., Tabakoff W. (1986)
'Three-dimensional flow measurements in a radial inflow turbine scroll using LDV', ASME Paper No. 86-GT-122.

Malin M. R., Younis B. A. (1989)
'Calculation of turbulent buoyant plumes with Reynolds stress transport closure', Proc. of the 3rd International PHOENICS Users' Conference.

Manners A. (1988)
The calculation of flows in gas turbine combustion systems, PhD Thesis, University of London.

McConalogue D.J., Srivastava R.S. (1968)
'Motion of fluid in a curved tube', Proc. R. Soc., London, A 307, p. 37.

McGuirk J.J. (1988)
'3D combustor predictions - A comparison of equilibrium and laminar flamelet chemistry models', AGARD, Combustion and Fuels in Gas Turbine Engines, Conference Proceedings No.422.

Miller E.C., L'Ecuyer M.R., Benisek E.F. (1988)
'Flow field surveys at the rotor inlet of a radial inflow turbine', Trans. ASME, Vol.110, pp. 552-561.

Mori Y., Uchida Y., Ukon T. (1971)
'Forced convective heat transfer in a curved channel with a square cross section', Int. J. Heat and Mass Transfer, Vol. 14, p. 1787.

Murata S., Miyake Y., Inaba T. (1976)
'Laminar flow in a curved pipe with varying curvature', J. Fluid Mechanics, Vol. 73,p.735.

Nakayama A. (1985)
'A numerical method for solving momentum equations in generalized coordinates (Its application to three-dimensional separated flows)', Trans. ASME, J. Fluids Engg., Vol. 107, pp. 49-54.

Nandakumar K., Masliyah J.H. (1982)
'Bifurcation in steady laminar flow through curved tubes', J. Fluid Mechanics, Vol. 119, pp. 475-490.

Olson D.E., Snyder B. (1985)
'The upstream scale of flow development in curved circular pipes', J. Fluid Mechanics, Vol. 150, pp. 139-159.

Patankar S.V. (1980)
Numerical Heat Transfer and Fluid Flow, McGraw-Hill, New York.

Patankar S.V., Spalding D.B. (1972)
'A calculation procedure for heat, mass and momentum transfer in three dimensional parabolic flows', Int. J. Heat and Mass Transfer, Vol. 15, pp. 1787-1806.

Pedley T.J. (1980)
The Fluid Mechanics of Large Blood Vessels, Cambridge University Press.

Peric M. (1985)
A finite volume method for the prediction of three-dimensional fluid flow in complex ducts, PhD Thesis, University of London.

Rhie C.M. (1985)
'A three dimensional passage flow analysis method aimed at centrifugal impellers', Computers and Fluids, Vol. 13, No. 4, pp. 443-460.

Roache P.T. (1976)
Computational Fluid Dynamics, Hermosa Publishers, Albuquerque, New Mexico.

Rojas-Mendez J.A. (1986)
Flow and heat transfer characteristics of diffusing-curved-ducts, PhD Thesis, University of London.

Sani R.L., Gresho P.M., Lee R.L., Griffiths D.F. (1981)
'The cause and cure (?) of the spurious pressures generated by certain FEM solutions of the incompressible Navier-Stokes equations', Int. J. Num. Meth. Fluids, Vol. 1, pp.17-43 and 171-204.

Schlichting H. (1979)
Boundary Layer Theory, McGraw-Hill Book Company, New York.

Scrimshaw K.H. (1981)
Scale effects in small geometrically similar radial gas turbines with particular reference to blade-less volute phenomena, PhD Thesis, University of London.

Shyy W., Tong S.S., Correa S.M. (1985)
'Numerical recirculating flow calculation using a body-fitted coordinate system', Numerical Heat Transfer, Vol. 8, p. 99.

Singh M.P. (1974)
'Entry flow in a curved pipe', J. Fluid Mechanics, Vol. 65, p. 517.

Soh W.Y., Berger S.A. (1984)
'Laminar entrance flow in a curved pipe, J. Fluid Mechanics, Vol. 148, p. 109.

Sokolnikoff I. S. (1964)
Tensor Analysis, J. Wiley and Sons, Inc., New York.

Spalding D.B. (1972)
'A novel finite-difference formulation for differential expressions involving both first and second derivatives', Int. J. Num. Meth. Engg., Vol. 4, p. 551.

Stewartson K., Cebeci T., Chang K.C. (1980)
'A boundary -layer collision in a curved duct', Q. J. Mech. Appl. Maths.,Vol. 33, p. 59.

Tabakoff W., Sheoran Y., Kroll K. (1980)
'Flow measurements in a turbine scroll', Trans. ASME, J. Fluids Engg., Vol.102, pp.290-296.

Tabakoff W., Vittal B.V.R., Wood B. (1984)
'Three-dimensional flow measurements in a turbine scroll', Trans. ASME., J. Engg. Gas Turbines and Power, Vol. 106, pp.517-522.

Talbot L., Wong S.J. (1982)
'A note on boundary -layer collision in a curved pipe', J. Fluid Mechanics, Vol. 122, p. 505.

Tennekes H., Lumley J.L. (1972)
A First Course in Turbulence, MIT Press.

Tindal M.J., Williams T.J., Khalil A.I. (1987)
'Flow in the volutes of small radial turbines', Trans. ASME, Paper No. 87-ICE-48.

Thompson J. (1876)
'On the origin of winding of rivers in alluvial plains, with remarks on the flow of water round bends in pipes', Proc. R. Soc., London, A 25, p. 5.

Van Dyke M. (1978)
'Extended Stokes series: laminar flow through a loosely coiled pipe', J. Fluid Mechanics, Vol. 86, p. 129.

Vinokur M. (1974)
'Conservation equations of gasodynamics in curvilinear coordinate systems', J. Comp. Physics, Vol. 14, p.105.

Ward-Smith A.J. (1980)
Internal Fluid Flow, Claredon Press, Oxford.

Watson N., Janota M. (1982)
Turbocharging the Internal Combustion Engine, The MacMillan Press.

Wilkes N.S., Thompson C.P. (1983)
'An evaluation of higher-order upwind differencing for elliptic flow problems', CSS 137, AERE Harwell.

Yao L.S., Berger S.A. (1975)
'Entry flow in a curved pipe', J. Fluid Mechanics, Vol. 88, p. 339.